Dependence of Radiant Optical Magnetization on Material Composition

by

Elizabeth F. C. Dreyer

A dissertation submitted in partial fulfillment
of the requirements for the degree of
Doctor of Philosophy
(Electrical Engineering)
in the University of Michigan
2018

Doctoral Committee:

Professor Stephen C. Rand, Chair
Professor Pallab Bhattacharya
Professor Jinsang Kim
Professor Karl Michael Krushelnick
Professor Herbert Graves Winful

nosce te ipsum, puella stellarum

Elizabeth F. C. Dreyer

efcloos@umich.edu

ORCID iD: 0000-0003-2558-2097

DEDICATION

To my parents, who encouraged me to dream big dreams.
To my husband, who helped those dreams take flight.

ACKNOWLEDGEMENTS

A PhD is not the result of one researcher, working alone in a basement for years, only to emerge at the end with a fully formed dissertation. Rather, it takes a village to support the researcher along the way. I am grateful for my village. I am forever thankful to:

- My husband Patrick, for being my rock.
- My family - especially my parents, Mike and Cheri; my brother, Stephen; and my in-laws, Bill and Sally - for believing in me, even if you don't always know what I do.
- God, for sustaining my faith throughout this trial.
- My friends at University of Michigan - especially Laura and Heather - for motivating me to keep going, and making the journey worthwhile.
- My hometown friends - Allie, Mary, Natalie, Brooke, and Andrew - for everything.
- My research colleagues - Alex, Will, Mike, Ayan, Hengky, Manish, Theresa, Laura, Long, Krishnandu, Ayesheshim, and Tuan - for all of the big and small things in the lab.
- My research adviser and thesis committee, for giving me feedback over the years and enabling this dissertation to be the best possible version.
- The EECS support staff - especially Car, Amy, Greg, and José - for pushing me, helping me, and making ERB and EECS better places to be.
- The College of Engineering staff - especially Kim, Tiffany, Shira, and Andria - for giving me countless opportunities to give back to the UM community.
- Other UM offices - especially WISE, CEW, CAPS - for being there when I needed it.
- The Science, Technology, and Public Policy certificate program, for teaching me how to be a responsible scientist, and citizen, in society.
- My extracurricular organizations - especially Society of Women Engineers and the Optics Society at UM - for giving me the opportunity to be more than just a researcher.
- Michigan Technological University - especially the Electrical & Computer Engineering Department - for providing me with the foundation to thrive in grad school. Go Huskies!

Finally, thank you to all the adults who took time to encourage my curiosity. Thank you to Rochester Community Schools - especially Mr. Mattick, my 6th grade Math teacher, who had me skip to 7th grade math; Mr. Thuma, my AP Physics teacher, who encouraged me to make my career in Science; and the Hart Middle School librarian who let me check out my own books. Thank you to everyone who believed in me.

PREFACE

This dissertation is submitted for the degree of Doctor of Philosophy at the University of Michigan. The research described herein was conducted under the supervision of Professor S. C. Rand in the Department of Electrical Engineering and Computer Science, University of Michigan, between September 2012 and March 2018.

The majority of the research conducted for this thesis was part of an international research collaboration, led by Dr. Rand at the University of Michigan. The literature review in Chapter 1 is my original work. In Chapter 2, the quantum theory was primarily developed by A. A. Fisher, with additional symmetry analysis done by me. The initial atomic classical theory was developed by W. M. Fisher. P. M. Anisimov provided the torque-enhanced molecular model. In Chapter 3, the experimental apparatus was built in collaboration with W. M. Fisher and A. A. Fisher. My significant contributions were alignment, sample preparation, and data acquisition. The classical simulation was entirely my original work. In Chapter 4, A. A. Fisher collected the data for the tetrachloride series and GGG intensity-dependent scattering. I collected the data for the orthosilicate series and Quartz. The spectroscopy data was collected by M. T. Trinh and K. Makhal. The experimental analysis was entirely my original work, along with the simulation results. In Chapter 5, the predictions from the optical susceptibility were generated by A. J.-T. Lou. The rest of the analysis was my own. Portions of the results of this thesis appear in publication as noted in the citations and Chapter 5.

This material is based upon work supported by the National Science Foundation (NSF) Graduate Research Fellowship under Grant No. F031543 and the Air Force Office of Scientific Research (AFOSR) under Grant No. FA9550-14-1-0040. Any opinion, findings, and conclusions or recommendations expressed in this material are those of the author and do not necessarily reflect the views of the NSF or AFOSR.

TABLE OF CONTENTS

LIST OF FIGURES

LIST OF TABLES

LIST OF APPENDICES

LIST OF ABBREVIATIONS

cps counts per second

ED Electric Dipole

EM electromagnetic

FOM Figure of Merit

GGG Gadolinium Gallium Garnet

IFE inverse Faraday effect

LOM Lorentz oscillator model

MD Magnetic Dipole

M-E Magneto-Electric

ND Neutral Density

NLO Nonlinear Optics

NMR Nuclear Magnetic Resonance

ODE Ordinary Differential Equation

PMT Photo-multiplier Tube

PT Parity-Time

TEOS Tetraethyl Orthosilicate

TMOS Tetramethyl Orthosilicate

TPOS Tetrapropyl Orthosilicate

UV Ultraviolet

UV-VIS Ultraviolet-Visible

QD quadrupole

VB-CT valence-bond charge-transfer

ABSTRACT

The realization of strong optical magnetism in nominally "non-magnetic" media could lead to novel forms of all-optical switching, energy conversion, or the generation of large (oscillatory) magnetic fields without current-carrying coils. By advancing understanding of radiant optical magnetization, the research reported in this thesis contributes progress toward these prospects.

Experiments and simulations were performed of light scattering in natural dielectrics at non-relativistic optical intensities. The goal was to understand which molecular factors influenced the magnitude of induced magnetic dipole scattering in isotropic materials. The intensity dependence and spectra of cross-polarized scattering in several transparent molecular liquids (CCl_4, $SiCl_4$, $GeCl_4$, $SnCl_4$, $SiBr_4$, TMOS, TEOS, TPOS) and crystalline solids (GGG, Quartz) were found to agree with predictions of quantum theory. Additionally, evidence was found for the expected proportionality between the intensity of radiant magnetization and the electric dipole transition moment, together with an inverse proportionality with respect to molecular rotation frequency. By comparing spectra in molecular liquids, it was found that spectral features in the cross-polarized scattering were uniquely attributable to high-frequency librations of magneto-electric (M-E) origin. In solids, optically-induced magnetic scattering in solids reached the same intensity as Rayleigh scattering, far below relativistic conditions. Additionally, all four channels predicted by the quantum theory for second-order (2-photon) M-E processes at the molecular level were observed in experiments on GGG crystals.

Two theoretical contributions are presented in this thesis. The first is an extension of the classical Lorentz Oscillator Model from an atomic to a molecular picture. It includes the effect of torque exerted by the optical magnetic field on excited state orbital angular momentum, resulting in an enhancement in the magnetization achievable under non-relativistic conditions in molecular or condensed matter systems. Temporal dynamics are predicted for the first time, taking into account molecular composition. Secondly, the torque Hamiltonian of quantum theory is shown to obey Parity-Time (PT) symmetry, indicating that M-E effects should occur universally. Lastly, results from classical and quantum mechanical models are compared and found to be in very satisfactory agreement.

CHAPTER 1

Introduction

Since the earliest days of civilization, humanity has been fascinated by light and how it interacts with the physical world. Many have sought to not only understand light, but harness its power for science, for medicine, and for art. Philosophers in ancient Greece established the foundations of optics, the study of light [1]. A millennia later, Ibn al-Haytham became the founder of modern optics through his use of experimental techniques to understand vision and refraction of lenses [2]. Scientists such as Newton [3], Huygens, Young, Fresnel [4], and countless others throughout the 18th, 19th, and 20th centuries sought to answer the questions of *"what is light?"* and *"what happens when light meets matter?"*. Their study of phenomena such as reflection and refraction would later be called linear optics. Although the answer to *"what is light?"* is now known (hint: it's both a particle and a wave!), the question of *"what happens when light meets matter?"* continues to be an active area of research. Despite the numerous useful technologies these light-matter interactions have allowed, there is still boundless opportunity for new technologies enabled by new light-matter interactions.

There is always an interaction of some sort when light meets matter. Light can be scattered off a surface, reflected off a mirror, refracted by a lens, or stimulate the emission of more light. The exact phenomenon depends on both the characteristics of the material (structure, chemistry, color) and of the light (wavelength, intensity, polarization). In general, light-matter interactions can be classified by either the combination of material and optical properties required or by what happens when the light and matter interact. For example, low (high) intensity light usually leads to linear (nonlinear) effects. Piezo-optic light-matter interactions are those where light causes the material to compress or expand. Magneto-electric effects are those where magnetic and electric properties of the material are coupled by light.

This thesis seeks to add to the understanding of light-matter interactions. The goal is to attempt an answer to the questions: Are magneto-electric effects possible at the molecular level? How do chemical properties affect such processes? How fast do these effects

occur? This research has primarily sought to understand the dependency of radiant optical magnetization on material composition.

This thesis is organized as follows: Chapter 1 presents an overview of nonlinear optics, especially metamaterials, material symmetries, light scattering, and optical magnetization. It is found that the theory of radiant optical magnetization is a continuation of decades of light-matter interaction work that can be described by the Lorentz oscillator model. Chapter 2 discusses the theory of radiant optical magnetization using both classical and quantum mechanical models. Additionally, a connection is drawn between magneto-electric nonlinear optical susceptibilities and all-electric ones, opening up new areas of physical chemistry research. Chapter 3 is devoted to the experimental design for ultrafast laser experiments as well as classical modeling. Chapter 4 showcases the results of both the experiments and classical simulations. Also included is a comparison of experiments and theory using a "figure of merit". Finally, Chapter 5 summarizes all the experimental work conducted in this thesis and discusses the conclusions. It is found that magneto-electric effects are possible at the molecular level and this thesis discusses their dependence on material composition and time. Finally, appendices are included for the MATLAB code for the classical model and experimental control.

1.1 Overview

It is well known that an electromagnetic (EM) wave incident on a linear dielectric medium induces an electric dipole. Similarly, the magnetic portion of the wave may cause a magnetic dipole to form, though this is typically ignored due to the electric dipole approximation, which suggests that the magnetic field has little effect on the charges within a material with no special magnetic properties [5]. The electric dipole approximation describes the probability of radiative transitions occuring as a result of a light-matter interaction. It suggests that the probability of a Magnetic Dipole (MD) transition is 10^5 times more *unlikely* than that of a Electric Dipole (ED) transition.

However, when the effect of the magnetic field is included in the Lorentz oscillator model (LOM) as part of the force term, the inversion symmetry of the material is broken and new and surprisingly strong phenomena are predicted [6]. These phenomena are optical magnetization, magneto-electric rectification, and harmonic generation. In addition to this classical explanation of the phenomena, these effects can also be derived exactly using a doubly-dressed state quantum theory [7]. This thesis focuses entirely on the phenomenon of optical magnetization induced by non-relativistic optical fields through a novel (magneto-electric) nonlinear mechanism.

1.1.1 Metamaterials

Although no work using metamaterials was pursued during this dissertation, many useful analogs can be taken from the field. An overview of metamaterials is given in this section along with explanations for how it can help in understanding the mechanism for radiant optical magnetization in natural, homogenous, dielectric materials.

In general, the field of metamaterials seeks to design and fabricate structured materials with the desired magnetic and electric response properties not normally found in nature [8]. By using sub-wavelength structures, the magnetic and electric response of materials can be tuned to produce varied effects. Metamaterials can be classified into four groups based on how they modify the electric permittivity ϵ and magnetic permeability μ of materials. These four groups and the materials they are usually found in are [9, 10]:

- $\epsilon > 0, \mu > 0$, found in natural and structured dielectrics
- $\epsilon < 0, \mu > 0$, found in plasmas in certain frequency ranges
- $\epsilon > 0, \mu < 0$, found in gyrotropic magnetic materials in certain frequency ranges
- $\epsilon < 0, \mu < 0$, found in artificially produced materials only

All of the materials examined in this thesis are from the first category where ϵ and μ are both positive.

One interesting application of metamaterials in optics is negative index materials ($n = \sqrt{\epsilon\mu} < 0$). Negative index materials can theoretically enable imaging at sub-wavelength resolution [11]. Currently, negative index materials have been designed using photonic crystals [12, 13, 14, 15], optical transmission lines [16], and nano-fishnet structures [17, 18]. Nano-fishnet structures are an intriguing solution. Since it is usually difficult to obtain both electric and magnetic resonances in the same frequency range, nano-fishnet structures combine a non-resonant background structure with a resonant magnetic structure [11]. Experimentally, this has been achieved by sandwiching a magnetic resonator between metal films [19] or by using an array of metal strips of varied lengths [20].

Most metamaterial designs achieve negative refractive index by enhancing the magnetic response of a material system [11]. One technique to do this is the split-ring resonator. Although initially demonstrated in the microwave regime [10, 21], the resonators were successfully scaled to optical frequencies [22, 23, 24, 25]. Other techniques include a staple-like structure facing a metallic mirror [17] and an array of paired silver strips. The magnetic response in the strips is the result of "asymmetric currents in the metal structures induced by the perpendicular magnetic-field component of light" [26].

All of the aforementioned methods rely on an external structure to constrain charges and force a large interaction with the magnetic field component of light. This is the most obvious in the split-ring resonator structure shown below in figure 1.1.

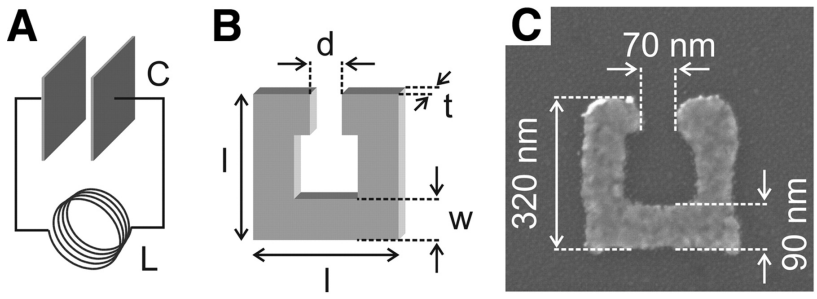

Figure 1.1: Illustration of the analogy between a conventional LC circuit (A), consisting of an inductance L, a capacitance C, and the single SRRs used here (B). l, length; w, width; d, gap width; t, thickness. (C) An electron micrograph of a typical SRR fabricated by electron-beam lithography. The thickness of the gold film is t = 20 nm. For normal incidence, where the magnetic field vector B lies in the plane of the coil, the electric field vector E of the incident light must have a component parallel to the electric field of the capacitor to couple to the LC circuit. This allows the coupling to be controlled through the polarization of the incident light. Reprinted with permission from reference [27].

In this structure, polarized light incident on the split-ring resonator induces a circulating electric current in the ring via the force of the electric field [24, 25]. This electric current causes a magnetic-dipole moment normal to the split-ring resonator plane. Dynamic magneto-optics, described in section 1.3, does the same thing, only without relying on external structure. Instead, the Lorentz force in the Lorentz oscillator model is responsible for driving the electron in a c-shaped motion (see figures 2.1 and 4.20). This allows for magneto-electric effects in natural, unstructured, homogeneous materials.

1.2 Nonlinear optics

Radiant optical magnetization has previously been shown to be dependent on the square of the applied electric field strength [6]. This means that it grows nonlinearly with the intensity of the incident light and thus is a nonlinear optical effect. Therefore, by understanding the larger field of nonlinear optics, one can better understand what radiant optical magnetization is and, just as importantly, what it is not. This section provides a review of relevant topics in nonlinear optics such as light scattering, material symmetry, and other types of optically-induced magnetization.

Material response to an applied optical electric field has been extensively characterized, enabling the development of devices that have revolutionized the field of Photonics. One way to describe material response to an applied optical electric field is through the electric susceptibility, χ [28]. Responses can be broken into two categories: linear and nonlinear effects. Linear effects include common optical phenomena such as absorption, reflection, refraction, and phase shifting [29]. Nonlinear effects include, for example, second harmonic generation, frequency-mixing, optical Kerr effect, and Raman amplification. Linear effects are described by $P = \epsilon_0 \chi^{(1)} E(\omega)$, where P is the induced polarization, ϵ_0 is the electric permittivity of free space, and $E(\omega)$ is the applied electric field. In this case, the applied electric field is the electric field component of light. Similarly, some nonlinear effects can be described as $P_{NL} = \epsilon_0 \chi^{(2)} E(\omega) E(\omega)$. In this specific case, two applied electric fields are needed resulting in a second-order or quadratic effect. In general, nonlinear optical effects can be made up of any number of applied electric and *magnetic* fields, limited only by the material response, $\chi^{(n)}$, which enables the effects to occur.

The field of nonlinear optics was established in 1961 with the discovery of second-harmonic generation by Peter Franken et al. at the University of Michigan [30]. This discovery was enabled by the invention of the first laser by Theodore Maiman in 1960 [31]. Up until then, a strong enough source of light had not existed with which to reliably observe nonlinear effects. Ever since, nonlinear optics has given rise to many interesting and important studies of light-matter interaction. One such interaction of interest is light scattering, which is described in the first subsection. In the second subsection, comments are given on the influence of material symmetry on light-matter interactions. Other topics in optical magnetization, such as ultrafast demagnetization and the inverse Faraday effect, are discussed in the final subsection.

1.2.1 A brief history of light scattering

Light scattering is one of the oldest and most important areas of study within nonlinear optics [28, 32, 33]. Although scientists have been studying light-matter interactions since the 1800s, it was not until the advent of the laser that light sources were intense enough and narrow-band enough to accurately discriminate between different phenomena. This section provides a brief overview of different types of light scattering and motivates the study of magneto-electric light scattering.

Broadly speaking, light scattering can be broken into two categories: elastic and inelastic scattering. In elastic scattering, the scattered light is of the same frequency as the light used to stimulate the material. In inelastic scattering, the scattered light can be the same or

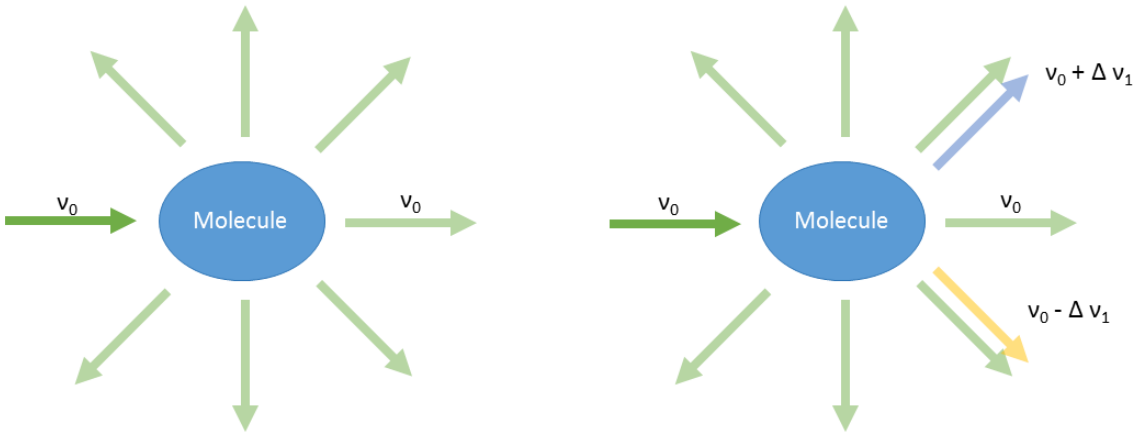

Figure 1.2: Depictions of (l) elastic and (r) inelastic light scattering.

shifted in frequency. See figure 1.2 for a comparison of elastic and inelastic scattering.

1.2.1.1 Elastic light scattering

The three main types of elastic light scattering are Mie, Tyndall, and Rayleigh scattering [34]. These processes scatter light at the same frequency as incident light, but do so in different directional patterns. Suppose an electromagnetic wave polarized in the $\hat{x}$-direction is propagating in the $\hat{z}$-direction. Whereas Rayleigh scattering scatters light uniformly in the plane of propagation ($\hat{y}$-$\hat{z}$ plane) and in a cosine-squared pattern out of the plane, Mie and Tyndall scattering scatter light more strongly in the direction of forward propagation of the incident light. This change in direction is due to the size of the particles from which light is being scattered (particle size: Rayleigh $<$ Mie $<$ Tyndall). In the experiments described within this thesis, only Rayleigh scattering is of concern. The large particles needed for Tyndall and Mie scattering are removed by filtering samples through 0.9μm Millipore filters.

1.2.1.2 Inelastic light scattering

Inelastic light scattering covers a broad array of phenomena and processes [33]. These can be broken up into effects that are very near to or harmonics of the incident frequency and those which have larger non-harmonic frequency shifts. It can be further divided into stimulated and spontaneous effects [32]. Some examples of spontaneous near-frequency or harmonic effects are:

- *Hyper-Rayleigh scattering*, where the scattered frequency is twice the incident fre-

quency ($\nu_s = 2\nu_0$) [35, 36, 37].

- *2^{nd} Hyper-Rayleigh scattering*, where the scattered frequency is thrice the incident frequency ($\nu_s = 3\nu_0$) [38].

Spontaneous effects scatter light incoherently in all directions. Stimulated effects most often scatter light coherently in the forward or backward directions. Whereas stimulated effects often have rules of wave-vector matching, spontaneous effects do not [35]. Additionally, stimulated effects are usually much more intense that spontaneous effects. Some examples of stimulated near-frequency effects are:

- *Second-harmonic generation*, where the scattered frequency is twice the incident frequency ($\nu_s = 2\nu_0$) [30].

- *Stimulated Rayleigh scattering*, where the scattered spectrum is a broadened version of the incident spectrum ($\nu_s = \nu_0, \Delta\nu_{s,fwhm} > \Delta\nu_{0,fwhm}$) [39].

- *Stimulated Rayleigh-Wing scattering*, where the scattered spectrum is broadened on the Stokes side of the incident spectrum due to orientation fluctuations of individual molecules ($\nu_s = \nu_0, \Delta\nu_s = \Delta\nu_0 + 1/(\tau 2\pi c)$) [28, 40].

- *Stimulated Thermal Rayleigh scattering*, where the scattered spectrum is broadened on the anti-Stokes side of the incident spectrum due to parametric coupling between light and acoustic waves ($\nu_s = \nu_0, \Delta\nu_s$) [33, 41].

The other types of inelastic light scattering are stimulated Raman scattering and stimulated Brillouin scattering. Raman scattering arises from a molecular scattering process followed by an electronic, vibrational, vibration-rotational, or a pure rotational transition [33, 42]. Brillouin scattering is generated through the interaction of the incident light with an elastic acoustic wave within the material [32, 43]. Both Raman and Brillouin scattering can be two-photon processes. Meaning, they can be thought of as a two-step change in molecular energy involving an intermediate state. Some examples of Raman scattering include:

- *Stimulated rotational Raman scattering*, where the scattered frequency is $\nu_s = \nu_0 - \Delta\nu_{rot}$. Typical values of $\Delta\nu_{rot}$ for small molecules are about 0.1 to 10 cm^{-1} (for example, 0.356 cm^{-1} for NF_3) [44, 45].

- *Stimulated vibrational Raman scattering*, where the scattered frequency is $\nu_s = \nu_0 - \Delta\nu_{vib}$. Typical values of $\Delta\nu_{vib}$ are hundreds of wavenumbers for all but the smallest molecules (for example, the symmetric stretching of $SiCl_4$ is 424 cm^{-1}) [44, 46].

- *Stimulated electronic Raman scattering*, where the scattered frequency is $\nu_s = \nu_0 - \Delta\nu_e$. Values of $\Delta\nu_e$ can be as large as ~8000 to ~25000 cm^{-1} [32].

- *Stimulated hyper-Raman scattering*, where the scattered frequency is $\nu_s = 2\nu_0 - \Delta\nu_{rs}$. $\Delta\nu_{rs}$ can be any of the aforementioned Raman processes [47, 48].

- *Stimulated spin-flip Raman scattering*, where the scattered frequency is $\nu_s = \nu_0 - \Delta\nu_{sf}$. $\Delta\nu_{sf}$ is the transition between the Zeeman-splitting sublevels of electrons in a semiconductor [49].

1.2.1.3 Higher order and multiple scattering

Additional types of light scattering in nonlinear optics include contributions from higher-order scattering and collisional events. In light scattering, low-order optical interactions in liquids, like the ones described above, are governed by the electric dipole approximation [50, 51, 52]. In general, the spatial component of a radiating electromagnetic field can be considered in its expanded form as

$$e^{i\mathbf{k}\cdot\mathbf{r}} = 1 + i\mathbf{k}\cdot\mathbf{r} - \frac{1}{2}(\mathbf{k}\cdot\mathbf{r})^2 + ..., \tag{1.1}$$

where **k** is the wavevector and **r** a spatial coordinate vector. The electric dipole approximation assumes that the wavelength of the radiating field ($\lambda = 2\pi/|\mathbf{k}|$) is much greater than the physical scale **r**, enabling the approximation of

$$e^{i\mathbf{k}\cdot\mathbf{r}} \approx 1. \tag{1.2}$$

In other words, the electric dipole approximation assumes that the product of the radius a of the scatterer and the wavenumber of light ($k = 2\pi/\lambda$) satisfies $ka << 1$. A major result of the electric dipole approximation is that, due to evaluation of the selection rules, almost all scattered radiation should be from an electric dipole transition. Therefore, when the electric dipole approximation is well-obeyed, such as in molecular liquids like carbon tetrachloride at visible wavelengths and low intensities, little-to-no higher-order radiation should be observed.

When the electric dipole (ED) approximation fails, as it does for example when the ED moment is zero by virtue of a quantum mechanical selection rule, magnetic dipole (MD), quadrupole (QD), and higher order interactions may be the leading terms of the multipole expansion. Rather than MD and QD transitions being 10^5 and 10^8 times more unlikely, respectively, than an ED transition, they can become the dominant moments of

the material system. Another situation in which the dipole approximation fails is for visible light interactions when the radius of the scatter approaches or exceeds the wavelength λ. Examples of this include nanoparticle suspensions [53] and agglomerates [54].

Transitions enabled by the breakdown of the electric dipole approximation are not relevant to this work because the electric dipole approximation is *valid* in all of our samples. This work uses molecular liquids where the average scatterer has a radius of $a < 1$ nm, and the wavelength of incident light is 800 nm. Also, their principal resonances are well-known to be electric dipole in character. Therefore, the electric dipole approximation is well-obeyed. The magnetic dipole radiation observed in chapter 4 is due to a new non-linear (2-photon) process that alters the symmetry of the material and introduces magnetic response in a fashion reminiscent of metamaterials.

Collisional events can also alter light scattering in important ways. The scattered radiation from colliding molecules reflects not only internal molecular characteristics but also changes in their electronic structure caused by collision. Examples include dipole-induced dipole effect, molecular frame distortions, and depolarized-light orientation scattering.

Dipole-induced dipole effects occur during collisions when the applied electric field induces a dipole moment in one molecule and then the field from that dipole induces an additional dipole in a neighboring molecule [55]. This interaction [56, 57, 58, 59] is generally accepted as the primary driver of depolarized scattering in noble gases [60]. Frommhold summarizes the results for Helium, Neon, Argon, Krypton, and Xenon in his 1981 review article [61], showing dipole-induced dipole scattering is strong even in low-density gases.

Earlier in 1971, Bucaro and Litovitz investigated depolarized light scattering in atomic liquids (Xenon, Argon) and molecular liquids which were isotropic (CCl_4, $SnBr_4$), moderately anisotropic ($CHCl_3$, C_6H_{12}, C_5H_{12}, C_2H_5OH, C_2H_3OH, H_2O, NH_3), and highly anisotropic (Br_2, CS_2) [55]. They sought to answer if the collision-induced anisotropy observed in gases carries over to the liquid state, and if so in what manner. They discovered that although the small depolarization in the atomic liquids and molecular liquids could be attributed to the dipole-induced dipole effect, it was suppressed in anistropic liquids. Instead, molecular frame distortion drives the depolarization.

Molecular frame distortion is a change in the polarizability of a molecule due to a collision [55, 62]. Shelton and Tabisz studied the isotropic molecules of CH_2, CF_4, CCl_4, and SF_6 in 1980 and confirmed that molecular frame distortion makes only a very small contribution to their polarizability [62]. Stevens et al. also studied depolarization in CCl_4 and $GeCl_4$ in 1982 and concurred that molecular frame distortion contributed negligibly to collision-induced polarizability [63]. For a more in-depth overview on collision-induced scattering from tetrahedral molecules, see Neumann and Posch's 1985 article [64].

If a molecule is anisotropic, such as CS_2, the depolarization of the scattered light can be caused by more than collision-induced effects. Its orientation can also change with time. This is known as the reorientational optical Kerr effect [32, 65]. The electric field of the incident light re-orients the molecule by exerting electric torque on the anisotropic polarization of the molecule. The energy required to reorient depends on thermal collisions with other molecules and the viscous damping of the medium. The amount of energy required to reorient the molecule then determines the frequency of the scattered light. Shapiro and Broida studied fluctuations in orientations of CS_2 in 1967. They mixed CS_2 with CCl_4 and compared the reorientation as a function of the concentration of CS_2. They found that the scattered radiation was about 60 times weaker in CCl_4 than in CS_2.

A more generalized way to specifically discuss depolarized light scattering in liquids is as being caused by a "fluctuation in the optical anisotropy of the medium" [63]. Madden proposed this "molecular dynamics" theory in 1978 as a way to describe Rayleigh scattering from spherical molecules [66]. He incorporated the aforementioned effects along with new dependencies on material viscosity and self-diffusion as contributions to the optical anisotropy. This generalized theory allowed for Chappell et al. to explore the effect of viscosity and shear waves on the depolarized light spectrum of liquid triphenylphosphite in 1981 [67]. They discovered that changes in microscopic stress can contribute to the optical anisotropy and lead to so-called Rytov doublets which correspond to shear-orientational modes. Shear wave contributions are only present in media composed of anisotropic molecules [68].

A final type of light scattering is multiple scattering [69]. Weiss and Adler determined in 1981 that multiple scattering is negligible for inert gases at liquid densities [70]. Multiple scattering is most prevalent in solutions with high amounts of absorption or when the scatterer particle size causes Mie scattering rather than Rayleigh scattering [71].

In the experiments detailed in this thesis, molecular frame distortions, shear waves and depolarized-light orientation scattering can be ignored when dealing with isotropic molecules. Dipole-induced dipole scattering contributes a small fixed amount of depolarization in tetrahedral molecules such as carbon tetrachloride. This is discussed further in the next section. Multiple scattering can also make a fixed contribution to depolarization, but only in materials of significant opacity, which does not apply to the transparent media studied in this work.

1.2.1.4 Polarization-sensitive light scattering experiments

Polarization-sensitive light scattering experiments permit the analysis of scattering mechanisms. They control both the polarization state of the incident light as well as analyze

the polarization state of the scattered light. Scattered light is often analyzed at 90 degrees from the direction of propagation of the incident beam for convenience in reducing background noise, but in this work, the 90 degree geometry offers a unique separation of electric and magnetic effects. More detail on the importance of this specific detection geometry is provided in section 3.1.

The first known polarization-sensitive light scattering experiment to identify a magnetic dipole transition was in 1939 by O. Deutschbein [72]. Deutschbein performed experimental studies on the processes of light emission. He noted that knowledge of the radiated field, such as the directional dependence of the intensity and polarization state, makes it possible to learn about the material structure. In his experiment, he excited Europium-salts using UV-light and used a combination of input polarizer and signal analyzer and a four-step procedure to distinguish radiation from electric and magnetic dipole transitions. The results in this thesis are consistent with Deutschbein's method.

Before the popularization of the laser, most polarization-sensitive light scattering experiments used filtered lines of a mercury-arc lamp to probe material systems. One example is the work by Kratohvil et al., where they used the 436 and 536 nm lines of Mercury to examine the depolarization of Rayleigh scattering [73]. They sought to predict the scattering response (Rayleigh ratio) of a liquid based on other measurable quantities such as the refractive index, wavelength of light, isothermal compressibility and the pressure derivative. In terms of scattered intensities, the Raleigh ratio is defined as $R_u = (V_v + H_v + V_h + H_h)/2$. These correspond to combinations of the incident polarization state and analyzer, namely $V_u, H_u, V_v, V_h, H_h, H_v$. The subscripts designate the polarization state of the incident beam (u - unpolarized, v - vertically, and h - horizontally polarized), and R, V, and H refer to the total Rayleigh ratio and its vertical and horizontal components, respectively. The depolarization ratio, ρ_u or D_u, equals $(H_h + H_v) / (V_v + V_h)$.

Once the laser became common, scientists were able to probe material systems using narrower-band and higher intensity light. Terhune et al. noted that nonlinear light scattering "provides an important tool for the study of molecular structures and their interactions in liquids" [36]. Throughout the rest of the 20th century, scientists examined the cross-polarized light spectrum (H_v or $I_{VH}(\omega)$) from spherical-top molecules such as carbon tetrachloride [55, 63, 74]. Scientists such as Gabelnick & Strauss, Buacaro & Litovitz even noted a Stokes-broadening in the "depolarized" Rayleigh spectra of CCl_4, attributing it to anisotropic fluctuations of the liquid. Experiments just comparing the Rayleigh spectrum (V_v) to the H_v spectrum eventually became known as dynamic or depolarized light scattering experiments [75, 76, 77, 78].

Now, in the modern era, light scattering is generally analyzed in terms of the differential

cross section, $\partial\sigma/\partial\Omega$, and the polarization ratio, ρ_0 [79]. ρ_0 is defined as the ratio of the horizontally-to-vertically polarized light scattered at 90 degrees. Theoretically its value is related to sample properties by

$$\rho_0 = \frac{6\gamma^2}{45a^2 + 7\gamma^2} \tag{1.3}$$

where a is the mean polarizability and γ is the anisotropy of the molecule. If a molecule is perfectly isotropic, $\rho_0 = 0$, and there is no horizontal component to the scattered light. The total Rayleigh scattered cross-section is

$$\sigma = \frac{32\pi^2(n-1)^2}{3\lambda^4 N^2}\left(\frac{6+3\rho_0}{6-7\rho_0}\right), \tag{1.4}$$

where λ is the incident wavelength, n is the refractive index, and N is the number density of the molecule (molecules/m^3).

The total detected power collected in a scattering experiment is the integral of the differential cross section, $\partial\sigma/\partial\Omega$, over the solid angle subtended by the collection optics, $\Delta\Omega$. Including the efficiency, η of the collection optics, the incident intensity of light I_{inc}, and the multiplier effect of the number of scatterers in the observation volume NV, the detected power is

$$P_{DET} = \eta I_{inc} NV \int \frac{\partial\sigma}{\partial\Omega} d\Omega. \tag{1.5}$$

The differential scattering cross section, $\partial\sigma/\partial\Omega$, is determined by the geometry of the experiment. For the experiments considered in this section where the laser propagates along the x-axis, is polarized along the z-axis, and light is collected at 90 degrees along the y-axis, the differential scattering cross sections for vertically- and horizontally- polarized detected light are

$$\frac{\partial\sigma_V}{\partial\Omega} = \frac{3\sigma}{8\pi}\left(\frac{2-\rho_0}{2+\rho_0}\right) \tag{1.6}$$

and

$$\frac{\partial\sigma_H}{\partial\Omega} = \frac{3\sigma}{8\pi}\left(\frac{\rho_0}{2+\rho_0}\right). \tag{1.7}$$

The results from a select number of 90-degree polarization-sensitive light scattering experiments, including those mentioned above, are shown in table 1.1. Note that the polarization ratios are defined as $\rho_v = H_v/V_v$ and $\rho_h = V_h/H_h$. The depolarization ratio is $\rho_u = (1 + 1/\rho_h) / (1 + 1/\rho_v) = (H_h + H_v) / (V_v + V_h)$. A lower value of ρ_u indicates that less light is being "depolarized" into the cross-polarization channel.

In 2007, N. L. Sharma searched for contributions to optical scattering in liquids and nanoparticle suspensions beyond the electric dipole approximation [53]. Rather than only

Table 1.1: Comparison of 90-degree polarization-sensitive light scattering experiments.

Material	Intensity (W/cm^2)	λ_0 (nm)	Arb. Units V_v	V_h	H_h	H_v	ρ_v	ρ_h	ρ_u	Ref.
CCl_4	$< 10^2$	633							0.0012	[74]
	$< 10^2$	633							0.053	[80]
	$< 10^2$	633	9	0.75	0.75	1.5	0.08	0.5	0.23	[53]
	$< 10^0$	546	10	0.33	0.30	0.32	0.03	1.1	0.0570	[73]
H_2O	$< 10^2$	633							0.092	[80]
	$< 10^0$	546	2.1	0.11	0.11	0.13	0.06	1.0	0.1060	[73]
Fused quartz	$< 10^2$	488					0.04			[76]
	$< 10^2$	1064	7.7			0.60	0.08			[81]

taking points for two input and two output polarization states (V_v, V_h, H_h, H_v), he mapped out the full polarization patterns for CCl_4, C_6H_6, and polystyrene nanospheres. Polarization mapping is done by fixing the polarization state of the detected scattered light and iterating through possible polarization states for the incident light. This results in data sets for V_i and H_i, where i is an incident linear polarization state between 0 and 360 degrees.

Although Sharma's initial experiments inspired later experiments at the University of Michigan which discovered transverse optical magnetization [82], his results for scattering in carbon tetrachloride were found to be anomalous. By looking at table 1.1, it is possible to compare the depolarization ratio from the Sharma experiment to others in the literature. His depolarization ratio, ρ_u, is four times larger than that of Wahid and two orders of magnitude greater than that of Gabelnick within the same power range. One possible cause for this large scattering is contamination by suspended nanoparticles in what were assumed to be pure liquids. Metal nanoparticles for example support magnetic modes whereas in dielectric liquids like CCl_4, the electric dipole approximation is well-obeyed at low light intensities.

1.2.2 Comments on material symmetry

The symmetry of a material is often the most important consideration when predicting the dependence of light-matter interactions on material composition. As will be discussed below, before effects of temperature, pressure, viscosity, or optical resonances can be considered, the symmetry of the material must support the interaction. The first section here covers the standard symmetries seen in nonlinear optics and discusses how symmetry can allow or disallow certain effects. The second section looks at a specific type of symmetry, Parity-Time, and how it is enabling new and exciting advances within optics.

1.2.2.1 Standard symmetries of nonlinear optics

The symmetry of a material is the primary driver of how it will respond to light. Below are the 5 main types of discrete symmetries in physics [83]:

- *Spatial inversion (or Parity transformation), $x \rightarrow -x$*, where a material system can be reflected along a plane and maintain its original structure, i.e. mirror symmetry. Geometrically, a square has four planes of mirror symmetry.
- *Rotational symmetry*, where a material system can be rotated and maintain its original structure. Geometrically, a square has spatial rotation symmetry for 90 degree rotations whereas an equilateral triangle has spatial rotation symmetry for 120 degree rotations.
- *Time reversal transformation, $t \rightarrow -t$*, where an interaction with a material system can be done backwards in time and the result does not change.
- *Permutation symmetry*, where a material system contains more than one identical particle and their locations can be swapped with no effect.
- *Charge conservation*, where an interaction with a material system does not change the charge of its particles.

Each of the above symmetries have different levels of importance in each branch of optics. Spatial inversion and rotational symmetry are the most common symmetries in conventional nonlinear optics. Spatial inversion and time reversal transformation, combined, are important in quantum optics and are referred to as "Parity-Time (PT) symmetry". Permutation symmetry is also important in quantum optics. Each electron within a system at the same energy level and spin state is indistinguishable from any other, allowing for electrons to be treated as interchangeable. Lastly, charge conservation, combined with parity and time inversion symmetry, is mainly used in quantum field theory [84].

Spatial inversion and rotational symmetry combined form the 32 crystallographic point groups that are the foundation of nonlinear optics. Using the Hermann-Mauguin notation, the point groups are listed in table 1.2. Note that centrosymmetric materials are those which possess inversion symmetry.

In the work presented within this thesis, materials which are either cubic or centrosymmetric are of primary interest. Since centrosymmetric materials do not support second-order all-electric nonlinear optical effects, this allows observed second-order magneto-electric effects to be properly characterized. The cause of this prohibition of even-ordered

Table 1.2: Hermann-Mauguin descriptions of crystallographic point groups, where n = n-fold rotation axis, 1 = nothing, m = reflection, -1 = inversion, $\bar{n}$ = n-fold rotation + inversion axis, n/m = n-fold rotation + reflection axis [85].

	Point Group	
Crystal Class	Centrosymmetric	Non-centrosymmetric
Cubic	$m3$, $m\bar{3}m$	23, 432, $\bar{4}3m$
Hexagonal	$6/m$, $6/mmm$	6, $\bar{6}$, 622, $6mm$, $\bar{6}m2$
Trigonal	$\bar{3}$	3, 32, $3m$, $\bar{3}m$
Tetragonal	$4mm$, $4/mmm$	4, $\bar{4}$, $4/m$, 422, $\bar{4}m2$
Monoclinic	$2/m$	2, $\bar{2}$
Orthorhombic	mmm	222, $mm2$
Triclinic	$\bar{1}$	1

phenomena is that the polarization must change sign if all of the electric field vectors change sign [86, 87]. Mathematically, the polarization is represented as

$$P_i^{(2)} = \epsilon_0 \sum_{jk} \chi_{ijk}^{(2)} E_j E_k \qquad (i, j, k = x, y, z). \tag{1.8}$$

For inversion symmetry to hold, the polarization must change sign when all of the electric field vectors do.

$$-P_i^{(2)} = \epsilon_0 \sum_{jk} \chi_{ijk}^{(2)} (-E_j)(-E_k) \tag{1.9}$$

Therefore,

$$-P_i^{(2)} = (-)(-)\epsilon_0 \sum_{jk} \chi_{ijk}^{(2)} (E_j)(E_k) = +P_i^{(2)}. \tag{1.10}$$

The only way for $-P_i^{(2)} = P_i^{(2)}$ to be true is for all 27 elements of the $\chi_{ijk}^{(2)}$ tensor to be zero. Therefore, centrosymmetric materials cannot support second-order all-electric optical effects. In table 1.2, 10 out of the 32 point groups are centrosymmetric.

For cubic materials, only diagonal elements of the nonlinear optical susceptibility tensor are non-zero, i.e. $\chi_{xxx}^{(2)}$, $\chi_{yyy}^{(2)}$, and $\chi_{zzz}^{(2)} \neq 0$. Therefore, the direction of the nonlinear polarization must be in the same direction as the electric field vectors.

$$P_i^{(2)} = \epsilon_0 \sum_{ii} \chi_{iii}^{(2)} E_i E_i \qquad (i = x, y, z). \tag{1.11}$$

In the experiments described in this thesis, the geometry of the experiments is such that the scattered light is in a different direction than that of the incident electric field vectors.

Therefore, any even-ordered nonlinear signals that are observed must not be due to an all-electric process.

Two additional symmetries to consider in nonlinear optics are *intrinsic* permutation symmetry and Kleinman symmetry [28]. Both are a type of permutation of the $\chi^{(2)}$ indices and optical frequencies involved in a problem. Intrinsic permutation symmetry requires that any permutation of indices must be accompanied by a permutation of frequencies:

$$\begin{aligned}\chi^{(2)}_{ijk}(\omega_3 = \omega_1 + \omega_2) &= \chi^{(2)}_{jki}(\omega_1 = -\omega_2 + \omega_3) = \chi^{(2)}_{kij}(\omega_2 = -\omega_3 - \omega_1) \\ &= \chi^{(2)}_{ikj}(\omega_3 = \omega_2 + \omega_1) = \chi^{(2)}_{jik}(\omega_1 = \omega_3 - \omega_2) \\ &= \chi^{(2)}_{kji}(\omega_2 = -\omega_1 + \omega_3)\end{aligned} \tag{1.12}$$

Kleinman symmetry, on the other hand, allows for permutation of indices without a permutation of frequencies:

$$\begin{aligned}\chi^{(2)}_{ijk}(\omega_3 = \omega_1 + \omega_2) &= \chi^{(2)}_{jki}(\omega_3 = \omega_1 + \omega_2) = \chi^{(2)}_{kij}(\omega_3 = \omega_1 + \omega_2) \\ &= \chi^{(2)}_{ikj}(\omega_3 = \omega_1 + \omega_2) = \chi^{(2)}_{jik}(\omega_3 = \omega_1 + \omega_2) \\ &= \chi^{(2)}_{kji}(\omega_3 = \omega_1 + \omega_2)\end{aligned} \tag{1.13}$$

Whereas intrinsic permutation symmetry is allowed near to and far away from material resonances, Kleinman symmetry only applies far off resonance. Both are useful for simplifying problems using nonlinear optical susceptibilities, as will be seen in section 2.3.

An additional characteristic of nonlinear susceptibility tensors to note is how those tensors behave when mixed fields are a part of the nonlinear process. Recall that the nonlinear optical susceptibility, χ, is a tensor whose rank is determined by the order of the nonlinear optical process. For example, in $P^{(2)}_{NL} = \epsilon_0 \chi^{(2)} E(\omega) E(\omega)$, $\chi^{(2)}$ is a rank-3 tensor. If the nonlinear effect is magneto-electric as described by $P^{(2)}_{NL} = \epsilon_0 \chi^{(2)}_{ME} E(\omega) H^*(\omega)$, the nonlinear optical susceptibility $\chi^{(2)}_{ME}$ must be a rank-3 pseudo-tensor instead. The main differences between a tensor and a pseudo-tensor are in how they transform under inversion of coordinates. Whereas a tensor preserves its sign under inversion, a pseudo-tensor reverses sign. Although the symmetries discussed above are specific to tensors, similar results can be derived for pseudo-tensors [85, 88].

1.2.2.2 PT symmetry in optics

As mentioned earlier, Parity-Time symmetry is a relatively new and important area of quantum optical research. Since first explored by Bender and Boettcher in 1998 [89], it has led to numerous applications in optics [90, 91, 92, 93], NMR [94], microwave cavities [95],

lasers [96, 97, 98], and acoustic systems [99, 100]. There is also work being done in Bose-Einstein condensates [101], trimer lattices [102], and metamaterials [103, 104]. The most exciting work, however, involves the creation of optical diodes via PT-symmetric whispering gallery microcavities [105], fiber networks [106], and integrated photonic devices [107, 108]. The creation of optical diodes opens the doors to all-optical circuits.

In quantum mechanics, a system can be described by the use of a Hamiltonian, an operator which describes the total energy of a system [109]. Before Bender and Boettcher's 1998 paper, it was thought that a Hamiltonian must be Hermitian in order to have real energy eigenstates with real eigenvalues (a real spectrum) [110]. Real energy eigenstates means that the states of the system can be measured. Bender and Boettcher showed that a non-Hermitian Hamiltonian will still have real eigenvalues if it is P-T symmetric, meaning that the Hamiltonian commutes with the time reversal operator $\hat{T}$ and the parity operator $\hat{P}$:

$$\hat{P}\hat{T}\hat{H} = \hat{H}\hat{P}\hat{T} \tag{1.14}$$

Conventionally, Hermitian Hamiltonians describe isolated systems whereas non-Hermitian Hamiltonians "govern the behavior of systems in contact with the environment" [111]. PT-symmetric Hamiltonians describe systems that are in contact with their environments, but in such a balanced way that the gain from and loss to the environment are exactly balanced.

The parity and time reversal operators can be expressed in terms of their actions upon the real space coordinate r, time t and linear momentum $p = dr/dt$. A parity reversal operation inverts the sign on all spatial coordinates [109]. Under parity reversal, r and t transform as $\hat{P}(\hat{r}) = -\hat{r}$ and $\hat{P}(\hat{t}) = \hat{t}$. Linear momentum transforms as $\hat{P}(\hat{p}) = -\hat{p}$. These transformations result in polar vectors such as electric field to change sign, but for axial vectors such as the magnetic field to not [110]. Any operator has spatial inversion symmetry if $\hat{P}(\hat{H}) = \hat{H}$ or rather:

$$\hat{H}(\hat{\mathbf{p}}, \hat{\mathbf{r}}, t) = \hat{H}(-\hat{\mathbf{p}}, -\hat{\mathbf{r}}, t), \tag{1.15}$$

where $\mathbf{p}$ is linear momentum, $\hat{\mathbf{r}}$ is position, and t is time.

A time reversal operation reverses the sign on all temporal coordinates. Under time reversal, r and t transform as $\hat{T}(\hat{r}) = \hat{r}$ and $\hat{T}(\hat{t}) = -\hat{t}$. Linear momentum transforms as $\hat{T}(\hat{p}) = -\hat{p}$. These transformations result in quantities that depend linearly on time, such as momentum, to change sign, but for time-independent quantities to not. Additionally, the imaginary number, i, changes sign in order to preserve uncertainty. Any operator has time

inversion symmetry if $\hat{T}(\hat{H}) = \hat{H}$ or rather:

$$\hat{H}\left(\hat{\mathbf{p}}, \hat{\mathbf{r}}, \hat{t}\right) = \hat{H}^{*}\left(-\hat{\mathbf{p}}, \hat{\mathbf{r}}, \hat{t}\right), \tag{1.16}$$

where * represents the complex conjugate of the Hamiltonian.

Under combined time and parity operations, r and t transform as $\hat{P}\hat{T}(\hat{r}) = -\hat{r}$ and $\hat{P}\hat{T}(\hat{t}) = -\hat{t}$. Linear momentum transforms as $\hat{P}\hat{T}(\hat{p}) = \hat{p}$ since it depends linearly on both position and time. Any operator has parity-time (PT) inversion symmetry if $\hat{P}\hat{T}(\hat{H}) = \hat{H}$ or rather:

$$\hat{H}\left(\hat{\mathbf{p}}, \hat{\mathbf{r}}, \hat{t}\right) = \hat{H}^{*}\left(\hat{\mathbf{p}}, -\hat{\mathbf{r}}, -\hat{t}\right). \tag{1.17}$$

In general, parity-time symmetry in a system means that loss and gain are *exactly balanced* [112]. Later in section 2.2.2, the magnetic-interaction Hamiltonian in magneto-electric scattering is shown to be PT-symmetric, indicating that magneto-electric effects are universal.

1.2.3 Ultrafast demagnetization and the inverse Faraday effect

In addition to light scattering, the area of most interest and relevance to this thesis is optical magnetization. Optical magnetization is the process whereby magnetic dipoles are generated within a material by light. Optical magnetization has potential applications in magnetic domain imagery [113], ultrafast magnetic data storage using ultrafast pulses [114], and the inducement of negative permeability in dielectric materials [115]. Optical magnetization interactions can be classified based on the frequency of the dipoles generated in the interaction, and their orientation in space. The inverse Faraday effect (IFE) is studied chiefly in paramagnetic materials, ultrafast demagnetization experiments in ferro- and ferri-magnetic materials, and metamaterials rely on carefully engineered sub-wavelength structures to manipulate magnetic properties.

The IFE is the process by which longitudinal (non-radiative) DC magnetization is induced in a transparent medium by a circularly-polarized high-frequency electromagnetic wave [33, 116, 117]. The IFE has been observed in paramagnetic samples such as Eu^{2+}:CaF_2, diamagnetic glasses, and liquids such as C_6H_6 and CS_2 [117, 118]. Although all materials can exhibit IFE, it is very weak in nonmagnetic materials. This effect is not relevant to the present work because linear polarization is used exclusively in our experiments and static magnetic fields cannot radiate to produce light scattering signals at all.

Ultrafast demagnetization experiments are similar to traditional IFE in their result, but rely on a different mechanism. Although circularly-polarized light is involved in both,

ultrafast demagnetization experiments are influenced by quantum mechanical transition probabilities and by thermodynamics under different experimental conditions [119]. They are performed exclusively on ferrimagnetic or ferromagnetic materials. Materials tested include GdFeCo microstructures [120, 121], TbFe alloys [122], GdFeCo alloys, TbCo alloys, Pt/Co multilayers [123], and nanostructured nickel silicide on a Si (100) surface [124]. These materials enable the magnetization to be switched quickly using an all-optical technique. This may allow a magnetic memory to be created using light to read and record information instead of electricity.

Optical magnetization can also be mediated by the direct excitation of magnetic dipole resonances in either atomic or nanosphere systems. Kasperczyck et al. excited the magnetic dipole transition in Eu^{3+} ions embedded in Y_2O_3 nanoparticles [125]. The use of an azimuthally polarized beam allowed for the unambiguous excitation of the MD transition due to the lack of the electric field at focus. The MD or ED transitions could be excited depending on the laser wavelength tuning. Brewer et al. excited the magnetic dipole transition within the $4f$ shell of europium ions on the same transition studied by Deutschbein. At high input intensities, they succeeded in observing nutation oscillations between the ground and excited ionic levels [126]. Strong magnetic resonances have also been excited in silicon nanoparticles with diameters around 200 nm, which showed a response in the visible range [127]. It was also present in Eu^{3+} and Gd^{3+} doped β-$NaYF_4$ nanocrystal systems [128]. In the present work, no exotic polarizations or nanoparticles were used.

1.3 Dynamic magneto-optics in natural materials

Observations of elastic light scattering were reported in 2007 from homogeneous liquids in which the intensities of cross-polarized components were as high as one-fourth the Rayleigh scattered components in the same media [82, 129]. The experiments, performed at a scattering angle of 90 degrees as shown in figure 1.3, allowed electric and magnetic contributions to the scattering to be separated using orthogonal analyzers. These experiments explored the magneto-electric response of carbon tetrachloride (CCl_4) using three different laser systems and experimental conditions (See table 1.3).

Table 1.3: Summary of experimental parameters from 2007 scattering experiments [82].

Laser	Rep. Rate	Pulse width	Intensity
Ti:Al_2O_3 amplifier	1 kHz	150 fs	$\leq 10^{10}$ W/cm^2
Ti:Al_2O_3 oscillator	80 MHz	100 fs	2.2×10^{10} W/cm^2
Argon	CW	CW	5×10^4 W/cm^2

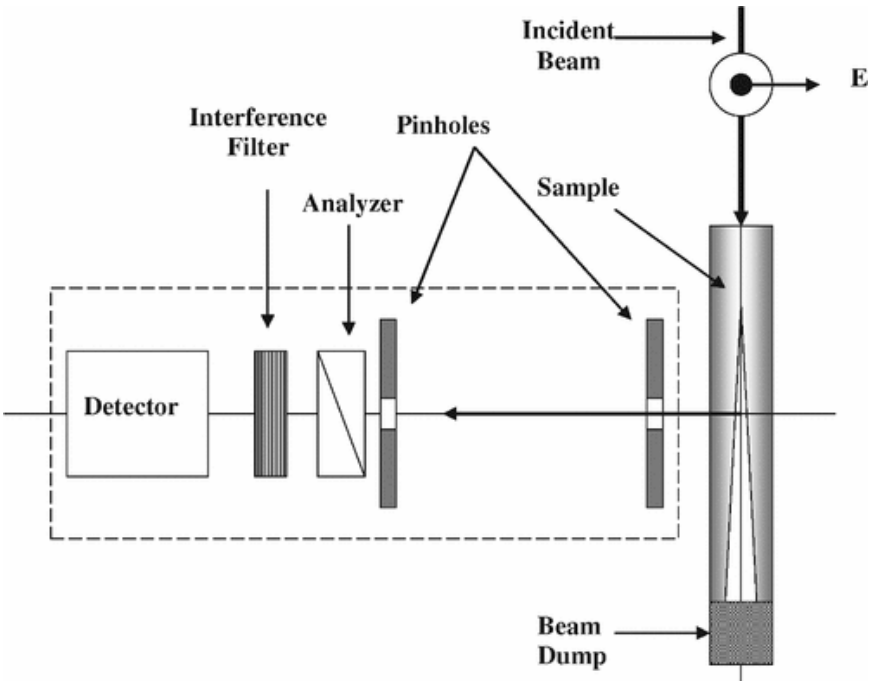

Figure 1.3: Schematic diagram of the experimental geometry used to map electric dipole and magnetic dipole radiation patterns by scanning polarization in the transverse plane of the incident light. Reprinted with permission from reference [82].

The first experiment, which used a Ti:Al_2O_3 amplified laser system, examined CCl_4 above the threshold for white-light generation with an excitation wavelength of 775 nm and the signal was detected at 640 nm. The sample was illuminated through the upper meniscus of a cylindrical sample holder. The maximum ratio between magnetic dipole and electric dipole scattering intensities was 0.22 ± 0.05. However, this value was later determined to be limited by detector saturation and, in the present work, even higher values are reported [130]. A second experiment, which used a Ti:Al_2O_3 oscillator laser system, switched to a rectangular sample holder that enabled the illumination through the side of a sample in a horizontal geometry. The excitation and detection wavelengths were both 810 nm. Experiments at lower intensities using a continuous wave argon laser failed to produce any significant magnetic dipole scattering at all. From these early experiments, one main conclusion can be drawn, namely that magnetic dipole scattering can be induced at non-relativistic intensities and exceed the limit imposed by the multipole expansion.

Experiments in 2008 made preliminary investigations of magnetic scattering in materials such as water and benzene that showed the same behavior as the original carbon tetrachloride samples [131]. Using the amplified Ti:Al_2O_3 source at intensities well below the threshold for white-light generation ($I << 2 \times 10^{10}$ W/cm^2), a transition from negligible magnetic scattering at low incident intensities to intense signal levels at higher intensities

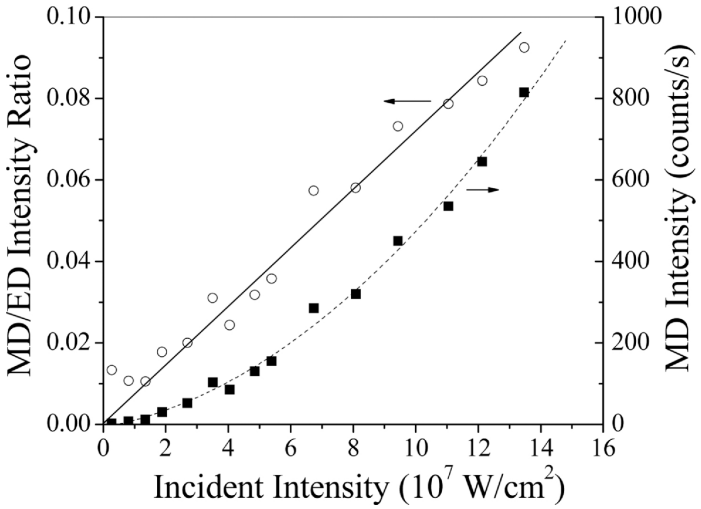

Figure 1.4: Experimental intensity of magnetic dipole scattering versus input intensity in CCl_4. The solid (dashed) curve is a linear (quadratic) regression through the data. Reprinted with permission from reference [131].

was observed. Figure 1.4 shows a scattered intensity ratio of 0.08 around intensities of 1.4×10^8 W/cm^2 in CCl_4 for example.

It should be noted that in these experiments, possible origins of these signals as collisionally-rotated electric dipoles, quadrupoles, or chirally-rotated Rayleigh components were carefully eliminated using limiting apertures and polarization analysis. The only remaining conclusion for dipolar signals polarized perpendicular to the Rayleigh component were that they were indeed caused by induced magnetic-dipole scattering.

After these early experimental successes [82, 131], initial classical and quantum mechanical models of the interactions were proposed. Between 2009 and 2011, W. Fisher presented a basic model for the interaction using the classical Lorentz oscillator model (LOM) that includes the Lorentz term ($\overline{v} \times \overline{B}$) [6, 132, 133]. This theory is described further in section 2.1.1. The numerical results obtained from solving this complete LOM showed that large amplitude, magnetically induced charge displacements at zero frequency and at twice the driving frequency arise when the Lorentz term is retained. Parametric instability in the equations of motion drives the effect to completion. In his quantum theory, S. Rand presented a density matrix theory which modeled radiant optical magnetization as a "mixed" type of nonlinearity proportional to the product of the electric- and magnetic-field strengths of light. These models have since been refined [7, 134] and are discussed in later sections.

The first signals in solids were observed in Gadolinium Gallium Garnet in 2013 [135]. Remarkably, the magnetic dipole scattered intensity was as large as the electric dipole

scattered intensity. Later, Yttrium Aluminum Garnet and Quartz showed the same large response [130]. In the present research, scattering results have been extended to additional liquids including ethylene glycol [135], carbon tetrachloride analogs, and benzene derivatives. These are discussed in chapter 4 and reference [136].

During this time, rapid progress was made on understanding magneto-electric phenomena as a quantum mechanical process. Recent work shows that at moderate intensities the magnetic field of light breaks the inversion symmetry of centrosymmetric media [7, 134]. State mixings that account for the unexpected appearance of all three nonlinearities are shown in figure 1.5, where some of the admixtures of the dressed states are written out explicitly. Doubly-dressed state theory is an extension of dressed atom theory [137]. Dressed atom theory is a technique where the complete Hamiltonian of a system (including interactions) is diagonalized and the new eigenstates, or dressed states, of the system are found. Once these states and their energies are known, the total system state is found to be a superposition of these eigenstates. The eigenstates of the complete Hamiltonian are referred to as "dressed" states because the complete Hamiltonian included the conventional molecule-field Hamiltonian as well as an interaction Hamiltonian. In light-matter interactions, the electric field of light serves as the interaction. So, the atomic or molecular system can be thought of as being "dressed" or "mixed" by the electric field. In doubly-dressed state theory, the base Hamiltonian is dressed by two separate fields. In this case, the atom is dressed first by the electric field-component of light and then by the magnetic field-component. Once the system is mixed, the analysis can proceed. During the second dressing of the system by the magnetic field, the inversion symmetry is broken. Nonlinear moments caused by this change in symmetry are also shown in figure 1.5 as double-headed arrows connecting admixed components with appropriate angular momenta.

The key features of the quantum mechanical theory developed in reference [7] are the magnetic interaction Hamiltonian and the molecular model. The initial quantum theory developed by S. Rand in 2008 [131] and expanded in 2014 [134] was an atomic model, which did not fully account for the enhanced value of induced magnetization. A new molecular model is capable of predicting enhancement of the optical magnetization by analyzing the effect of optical magnetic torque, which converts electronic angular momentum to rotational angular momentum of the molecules as they return to the ground state. This "ground state" quantum model bears many similarities to a classical model in which the electric field simply initiates charge motion and the magnetic field deflects the charge to create novel nonlinear response including optical magnetization. See figure 1.5 for a diagrammatic explanation. A more complete explanation of the quantum mechanical model is described in section 2.2.

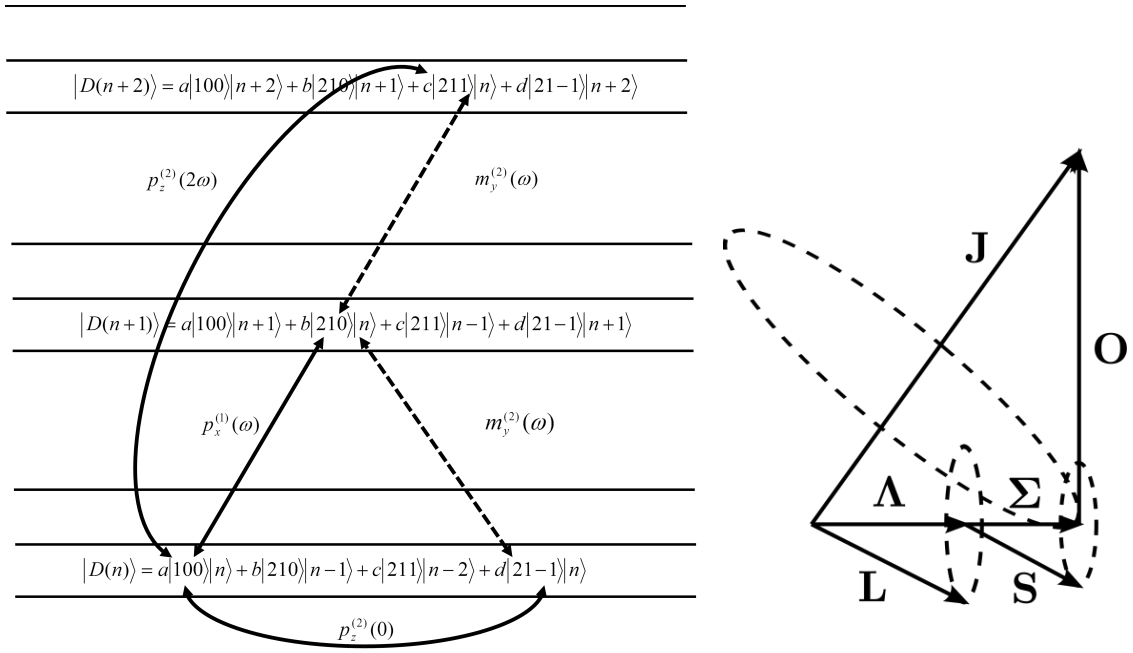

Figure 1.5: (Left) Second-order dressed state mixings that account for three new, quadratic magneto-electric nonlinearities allowed in centro-symmetric (as well as non-centrosymmetric) dielectric media. (Right) An angular momentum diagram for a molecular model in which the internal (L) and external (O) angular momenta excited by the optical H field can be exchanged in a ΔJ=0 transition that becomes 2-photon resonant through rotational excitation of the molecular ground state.

Experiments in this dissertation were performed to understand the dependency of radiant optical magnetization on molecular parameters. A key finding was that second-order magneto-electric dynamics can account for unpolarized scattering from high-frequency librations previously ascribed to first-order collision-induced or third-order, all-electric processes. Connections of magneto-electric effects to all-electric ones were also uncovered through theoretical analysis, opening the door to rational design of materials to optimize Magneto-Electric (M-E) effects at the molecular level. An overview is given in section 2.3 and fully detailed in reference [138].

CHAPTER 2

Theory of Radiant Optical Magnetization

This chapter details the theoretical origins of radiant optical magnetization and its associated processes. The first section focuses on the classical origins of magneto-electric effects using the Lorentz oscillator model. Although the Lorentz oscillator model itself is not new, its application to radiant optical magnetization is. In 2009, W. M. Fisher et al. proposed including the Lorentz term into the force term of the oscillator function [132]. Now, the model is further extended by including the effect of torque exerted by the optical magnetic field on the excited state orbital angular momentum. This enhances the magnitude of the magnetic dipole moment [139]. The second section provides comments on the doubly-dressed state quantum mechanical model published by Fisher et al. [7, 134]. The results of this model as well as its parity-time symmetry are discussed. The final section explores the connections of the magneto-electric nonlinear optical susceptibility to the third-order all-electric susceptibility elements [138].

2.1 Classical theory

2.1.1 Background on Lorentz Oscillator Model

The standard model used to relate the atomic structure of a medium to its optical properties is a mechanical one in which the active electron is depicted as a small mass attached to a fixed nuclear mass by a spring. In the atomic version of such a Drude-Lorentz model, the position of an electron is determined by classical equations of electron motion with respect to a stationary equilibrium point (See reference [34] for example),

$$\frac{d^2\overline{r}\,(t)}{dt^2}+\gamma\frac{d\overline{r}\,(t)}{dt}+\omega_0^2\overline{r}\,(t)=\frac{\overline{F}\,(t)}{m}. \tag{2.1}$$

In the simplest case, the force here is an applied electric field of the form, $\overline{F}\,(t)=q\overline{E}\,(t)=qE_x\cos(\omega t)$ and the motion is restricted along the x-axis. The equation of motion can be

rewritten then as:

$$\ddot{x} + \gamma\dot{x} + \omega_0^2 x = \frac{q}{m} E_x \cos(\omega t). \tag{2.2}$$

This is an ordinary differential equation which has a solution of the form, $x(t) = x_0 \times \cos(\omega t - \varphi)$. Substituting the characteristic solution into the equation of motion gives the value of x_0 and φ.

$$x_0 = \frac{qE_x/m}{\sqrt{\left(\omega_0^2 - \omega^2\right)^2 + \gamma^2\omega^2}} \tag{2.3}$$

$$\varphi = \arctan\left(\frac{\gamma\omega}{(\omega_0^2 - \omega^2)}\right) \tag{2.4}$$

The Lorentz oscillator model lets one derive physically relevant properties such as index of refraction, absorption, dispersion, and polarization.

Despite the many things that can be learned from the simple Lorentz oscillator model, it was discovered to have two main drawbacks. The first was that light is simply not a time-dependent electric field; it is an electromagnetic wave. Therefore, one must include both the electric *and magnetic* field components of light into the force term of the equations as $\overline{F}(t) = q\left(\overline{E} + \overline{v} \times \overline{B}\right)$.

Once the Lorentz force was included in the force term, solving these equations provided the conventional electric polarization, $P(\omega)$, as well as three new magneto-electric nonlinearities shown in figure 2.1: a charge separation, $p(0)$; a second harmonic generation, $p(2\omega)$; and a radiant optical magnetization, $m(\omega)$. $p(0)$ is a new sort of optical Hall effect [140, 141], since a dielectric displacement is induced by an optical magnetic field. W. M. Fisher showed that these equations are complex Mathieu equations, a specialized case of the Hill equations [133].

The second limitation of the simple Lorentz oscillator model was that it did not capture any molecular dynamics of the system. Since it was hypothesized that rotation was a key component of the magnetization [131], it was logical to allow the model to rotate. Extending the model to be a homonuclear diatomic molecule made the rotation physically meaningful. This extension to the molecular domain opened the door to understanding the complex dynamics of Dynamic Magneto-Optics, including the enhancement of the magnetization.

2.1.2 Derivation of the torque model

In the case of a rotating molecule, the equilibrium point undergoes rotational motion and therefore cannot be used as a fixed point of reference. Instead, the origin of the coordinate system must coincide with the center-of-mass of the molecule. This introduces a

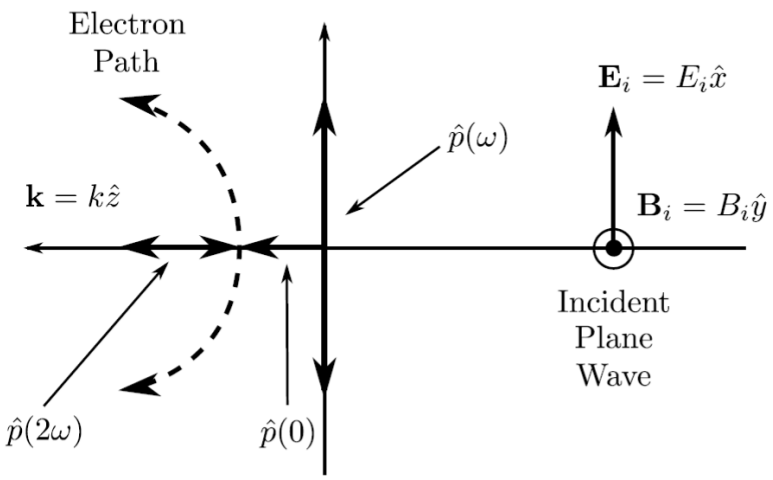

Figure 2.1: Motion of electron

new degree of freedom, namely rotation about the center-of-mass, and permits the applied magnetic field to exert torque on molecules that acquire angular momentum.

The displacement of the electron from equilibrium is taken to be $\overline{r} = \overline{\xi} - \overline{r}_A$, where $\overline{r}_A$ specifies the point of equilibrium. This also designates the point of attachment of the electron on its spring in the classical picture shown in figure 2.2, whereas $\overline{\xi}$ specifies electron position with respect to the center-of-mass. The applied fields cause excursions and librations about the point of equilibrium. Hence, the equation of motion with respect to the center-of-mass is

$$\frac{d^2\overline{\xi}\,(t)}{dt^2} + \gamma\frac{d\overline{\xi}\,(t)}{dt} + \omega_0^2\left(\overline{\xi} - \overline{r}_A\right) = \frac{\overline{F}\,(t)}{m}, \tag{2.5}$$

where ω_0 and γ are the resonant frequency and damping constants of the Hooke's Law oscillator, and m is the electron effective mass. $\overline{F}\,(t)$ is the external force acting on the oscillator. It has the form

$$\overline{F}\,(t) = q\left(\overline{E} + \overline{v} \times \overline{B}\right), \tag{2.6}$$

where q is the change, $\overline{E}$ and $\overline{B}$ are the applied fields oriented along x and y respectively, and $\overline{v}$ is the velocity.

In equation 2.5, the internal restoring force experienced by the electron has been written as $\overline{F}_i\,(t) = -m\omega_0^2\overline{r}\,(t)$. Whenever the electron is out of equilibrium, the molecule experiences an equal but opposite reaction force, $\overline{F}_r = \overline{F}_i$, applied to the point of equilibrium. That is, the electron exerts a torque on the molecule given by

$$\overline{T} = \overline{r}_A \times \left(m\omega_0^2\overline{r}\right) = m\omega_0^2\overline{r}_A \times \overline{\xi}. \tag{2.7}$$

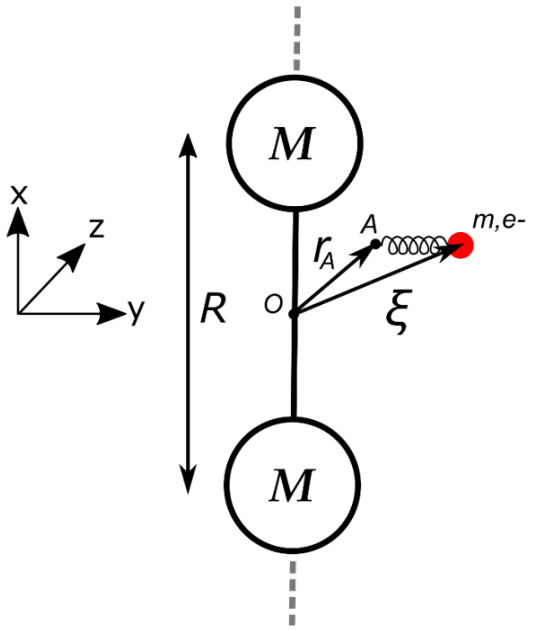

Figure 2.2: Model of a homonuclear diatomic molecule, together with the coordinate system and position vectors $\overline{\xi}$ and $\overline{r}_A$ specifying electron position and point of equilibrium respectively.

This torque modifies the components of angular velocity in a fashion that depends on the moment of inertia about each Cartesian axis. For a homonuclear diatomic molecule, there are two distinct moments of inertia denoted by

$$I_{\perp} = I_y = I_z \tag{2.8}$$

$$I_{//} = I_x \tag{2.9}$$

The torque due to the reaction force is therefore capable of creating components of angular velocity in all three directions [142] according to

$$I_{//}\frac{d\Omega_x}{dt} = T_x, \tag{2.10}$$

$$I_{\perp}\frac{d\Omega_y}{dt} = T_y, \tag{2.11}$$

$$I_{\perp}\frac{d\Omega_z}{dt} = T_z. \tag{2.12}$$

Note that for the specific initial condition $\overline{r}_A(0) = r_A\widehat{y}$, the torque in equation 2.7 develops components only along $\widehat{x}$ and $\widehat{z}$, since $\overline{r}_A \times \overline{\xi}$ in equation 2.7 has no components along

$\widehat{y}$. That is, $T_y(0) = 0$. According to equations 2.10 and 2.12, the non-vanishing torque components in this case alter linear velocities in the $\widehat{y}$-$\widehat{z}$ and $\widehat{x}$-$\widehat{y}$ planes as time progresses. Motion is therefore inherently three-dimensional in the model. The same conclusion is reached for an initial condition of $\overline{r}_A(0) = r_A\widehat{z}$. However, for an initial condition of $\overline{r}_A(0) = r_A\widehat{x}$, corresponding to a point of equilibrium located on the axis of the molecule, torque has no effect on the dynamics since $\overline{r}_A(0) \times \overline{\xi}(0) = 0$. Consequently, to investigate the role of torque in this model, all calculations were performed using the initial condition, $\overline{r}_A(0) = r_A\widehat{y}$.

In the general case, the exertion of torque by the displaced electron causes the molecule to rotate. This in turn changes the position of the equilibrium or attachment point, as described by the equation

$$\frac{d\overline{r}_A(t)}{dt} = \overline{\Omega}(t) \times \overline{r}_A(t) \tag{2.13}$$

where $\overline{\Omega}(t)$ is the angular velocity of the molecule.

The quantities of main interest here are the instantaneous values of the induced polarization, $\overline{P}(t)$, and the optical magnetization, $\overline{M}(t)$. Their definition in terms of the given coordinate system are

$$\overline{P}(t) = e\overline{\xi}(t), \tag{2.14}$$

$$\overline{M}(t) = -\frac{e}{2m}\overline{L} = -\frac{e}{2}\overline{\xi}(t) \times \frac{d\overline{\xi}(t)}{dt}. \tag{2.15}$$

To summarize, the system of equations needed to be solved are

$$\frac{d^2\overline{\xi}(t)}{dt} + \gamma\frac{d\overline{\xi}(t)}{dt} + \omega_0^2\left(\overline{\xi}(t) - \overline{r}(t)\right) = \frac{e}{m}\left(\overline{E}(t) + \frac{d\overline{\xi}(t)}{dt} \times \overline{B}(t)\right), \tag{2.16}$$

$$\overline{T} = \overline{r}_A(t) \times \omega_0^2 m\left(\frac{d\overline{\xi}(t)}{dt} - \frac{d\overline{r}_A(t)}{dt}\right), \tag{2.17}$$

$$\frac{d\overline{r}_A(t)}{dt} = \overline{\Omega} \times \overline{r}_A(t). \tag{2.18}$$

Correspondingly, the dipole moments using the equation solutions are

$$\overline{M}_y^{(2)}(\omega) = \left[-\frac{e}{2}\overline{\xi}(t) \times \frac{d\overline{\xi}(t)}{dt}\right]_y, \tag{2.19}$$

$$\overline{P}_z^{(2)}(0) = [e\overline{\xi}(t)]_z, \tag{2.20}$$

$$\overline{P}_x^{(1)}(\omega) = [e\overline{\xi}(t)]_x. \tag{2.21}$$

2.2 Quantum mechanical model

2.2.1 Derivation of the quantum mechanical model

Fundamentally, magneto-electric scattering is a quantum mechanical process. The classical model of section 2.1 consists of a homonuclear diatomic molecule (symmetric top) assumed to have a 1-photon ED resonance at frequency ω_0. To formulate the corresponding quantum theory, the quantization axis is taken to lie along the axis of the molecule [45] and, without loss of generality, it may be assumed to be parallel to the electric field (i.e. along $\hat{x}$). A linearly-polarized light field of frequency ω propagates along $\hat{z}$ with a small 1-photon detuning of $\Delta^{(e)} = \omega_0 - \omega$. Based on the procedure outlined in reference [7], there is a ED transition from the uncoupled product state $|1\rangle = |1,0,0\rangle\,|0,0\rangle\,|n\rangle$ to $|2\rangle = |2,1,0\rangle\,|1,0\rangle\,|n-1\rangle$ as shown in figure 2.3. Each uncoupled product state is composed of the uncoupled electronic states, $|\alpha, L, m_l\rangle$; the molecular rotational states, $|O, m_e\rangle$; and the single-mode Fock state, $|n\rangle$. The ED transition from $L = 0$ to $L = 1$ is followed by a MD transition between the uncoupled product state $|2\rangle = |2,1,0\rangle\,|1,0\rangle\,|n-1\rangle$ to $|3\rangle = |2,1,-1\rangle\,|1,1\rangle\,|n\rangle$, that is a change of $m_l = 0$ to $m_l = 1$. These uncoupled product states are eigenstates of the molecule-field Hamiltonian,

$$\hat{H}_{mf} = \hat{H}_m + \hat{H}_f = \frac{\hbar\omega_0}{2}\hat{\sigma}_z + \frac{\hat{O}^2}{2I} + \hbar\omega\hat{a}^+\hat{a}^- \tag{2.22}$$

with eigenenergies $E_i\,(i = 1, 2, 3)$ defined by $\hat{H}_{mf}\,|i\rangle = E_i\,|i\rangle$. $\hat{O}^2/2I$ designates kinetic energy of molecular rotation perpendicular to the internuclear axis with moment of inertia

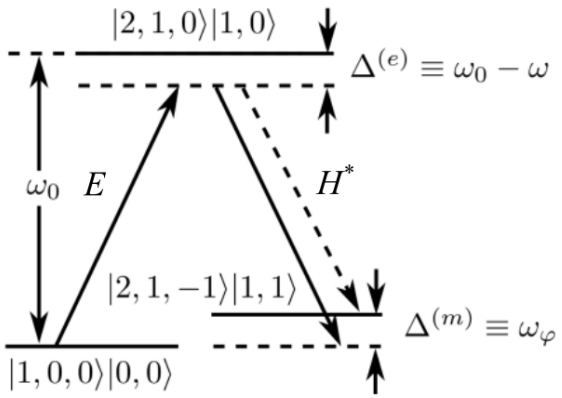

Figure 2.3: Energy levels of the molecular model showing the 2-photon transition (solid arrows) driven by optical E and H^* fields. The dashed downward arrow depicts a magnetic de-excitation channel that becomes an option if the excitation bandwidth exceeds ω_ϕ.

I. The quantized form of the interaction Hamiltonian is

$$\hat{H}_{int} = \hat{H}_{int}^{(e)} + \hat{H}_{int}^{(m)} = \hbar g\left(\hat{\sigma}^{+}\hat{a}^{-} + \hat{\sigma}^{-}\hat{a}^{+}\right) + \hbar f\left(\hat{L}'_{-}\hat{O}'_{+}\hat{a}^{+} - \hat{L}'_{+}\hat{O}'_{-}\hat{a}^{-}\right). \tag{2.23}$$

Primes on the orbital $\left(\hat{L}'_{\pm} \equiv \hat{L}_{\pm}/\hbar\right)$ and rotational angular momentum operators $\left(\hat{O}'_{\pm} \equiv \hat{O}_{\pm}/\hbar\right)$ indicate division by $\hbar$. The prefactors are $\hbar g = -\mu_0^{(e)}\xi$ and $\hbar f = -\mu_0^{(m)}\xi/c$, where $\mu_{eff} \equiv i\left(\frac{m_e\omega_0}{4m_N\omega_c}\right)\mu_0^{(m)}$ is the effective magnetic moment and $\xi \equiv \sqrt{\hbar\omega/2\epsilon_0 V}$ is the electric field per photon. Therefore, the full Hamiltonian for magneto-electric processes is the combined molecule, field, and interaction components:

$$\hat{H} = \frac{\hbar\omega_0}{2}\hat{\sigma}_z + \frac{\hat{O}^2}{2I} + \hbar\omega\hat{a}^{+}\hat{a}^{-} + \hbar g\left(\hat{\sigma}^{+}\hat{a}^{-} + \hat{\sigma}^{-}\hat{a}^{+}\right) + \hbar f\left(\hat{L}'_{-}\hat{O}'_{+}\hat{a}^{+} - \hat{L}'_{+}\hat{O}'_{-}\hat{a}^{-}\right). \tag{2.24}$$

For completeness, the solution of the Hamiltonian is shown below in figure 2.4 for the 3-state basis introduced above and also for a more complete 4-state basis that includes the state $|211\rangle\,|11\rangle\,|n\rangle$ as in reference [7]. It is found that at low intensities, the square of the nonlinear magnetic moment $(\langle\hat{m}\rangle^2)$ is quadratic with respect to input intensity. At higher input intensities, $\langle\hat{m}\rangle^2$, which is proportional to the magnetization that is experimentally measured in section 4.1 and classically modeled in section 4.2, has a cubic dependence. Once it saturates with the polarization, the magnetization maintains a linear dependence on intensity.

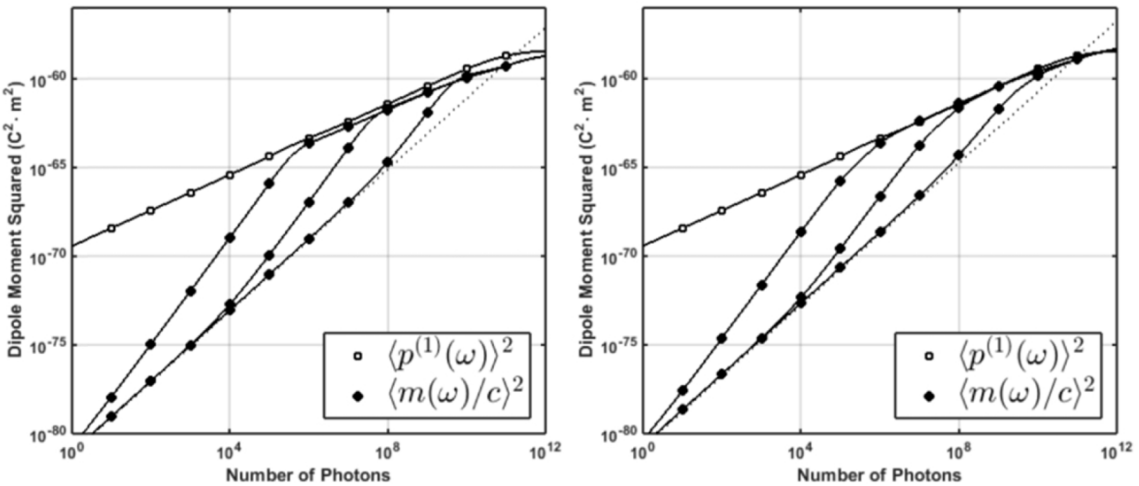

Figure 2.4: Squared values of the total magnetic moment and the first order electric dipole moment versus the number of incident photons in a (a) 3-state model and (b) a 4-state model. In both figures separate curves are shown for $\langle\hat{m}\rangle^2$ with rotational frequencies (left to right) of ω_ϕ/ω_0=10^7, 10^5, 10^3. Reprinted with permission from reference [7].

2.2.2 Parity-time symmetry of the magnetic interaction Hamiltonian

In this section, the symmetry properties of the quantized magneto-electric Hamiltonian are examined under reversal of time and space coordinates. It is shown that although neither parity nor time-reversal symmetry is obeyed on an individual basis, the combination of time and space inversion is a valid dynamic symmetry for M-E interactions. Thus, systems that evolve according to this Hamiltonian are PT symmetric.

The magnetic portion of the interaction Hamiltonian in equation 2.23 that governs the second step of magneto-electric interactions at the molecular level is

$$\hat{H}_{int}^{(m)} = \hbar f\big(\hat{L}'_{-}\hat{O}'_{+}\hat{a}^{+} - \hat{L}'_{+}\hat{O}'_{-}\hat{a}^{-}\big). \tag{2.25}$$

As shown below, the magnetic dynamics described by this Hamiltonian obey parity (P) and time (T) reversal symmetry only in combination. To establish this result, the effects of applying P and T symmetries to the individual operators in $\hat{H}_{int}^{(m)}$ are determined.

The operators $\hat{L}$ and $\hat{O}$, governing orbital and rotational angular momentum respectively, transform identically under time reversal and spatial inversion [143]. Hence, it is sufficient to analyze the transformation properties of only one of them, say $\hat{L} = \hat{r} \times \hat{p}$, using its representation is terms of the real space coordinate r and the linear momentum $p = dr/dt$ of the charge in motion. Now, the motion variables themselves obey the transformations $\hat{P}(\hat{r}) = -\hat{r}$; $\hat{T}(\hat{r}) = \hat{r}$, and $\hat{P}(\hat{p}) = -\hat{p}$; $\hat{T}(\hat{p}) = -\hat{p}$. Consequently, it is straightforward to determine the effects of applying parity and time-reversal operators to an angular momentum operator.

$$\begin{aligned}
\hat{P}\big(\hat{L}_{\pm}\big) &= \hat{P}\big[\hat{L}_x \pm i\hat{L}_y\big] \\
&= \hat{P}\big[\,(\hat{y}\hat{p}_z - \hat{z}\hat{p}_y) \pm i\,(\hat{z}\hat{p}_x - \hat{x}\hat{p}_z)\,\big] \\
&= \big[\,(-\hat{y})\,(-\hat{p}_z) - (-\hat{z})\,(-\hat{p}_y)\,\big] \pm i\big[\,(-\hat{z})\,(-\hat{p}_x) - (-\hat{x})\,(-\hat{p}_z)\,\big] \\
&= -\hat{L}_{\pm}
\end{aligned} \tag{2.26}$$

$$\begin{aligned}
\hat{T}\big(\hat{L}_{\pm}\big) &= \hat{T}\big[\hat{L}_x \pm i\hat{L}_y\big] \\
&= \hat{T}\big[\,(\hat{y}\hat{p}_z - \hat{z}\hat{p}_y) \pm i\,(\hat{z}\hat{p}_x - \hat{x}\hat{p}_z)\,\big] \\
&= \big[\,(\hat{y})\,(-\hat{p}_z) - (\hat{z})\,(-\hat{p}_y)\,\big] \mp i\big[\,(\hat{z})\,(-\hat{p}_x) - (\hat{x})\,(-\hat{p}_z)\,\big] \\
&= -\hat{L}_{\mp}
\end{aligned} \tag{2.27}$$

Similarly, the optical field raising and lowering operators may be represented by the canonical variables q and p according to $\hat{a}^{\mp} = \sqrt{\frac{\omega}{2\hbar}}\left(\hat{q} \pm i\frac{\hat{p}}{\omega}\right)$ [109]. Hence, the field

transformations are similarly determined by space and momentum properties.

$$\begin{aligned}\hat{P}\big(\hat{a}^{\mp}\big) &= \hat{P}\left[\sqrt{\frac{\omega}{2\hbar}}\left(\hat{q} \pm i\frac{\hat{p}}{\omega}\right)\right] \\ &= \left[\sqrt{\frac{\omega}{2\hbar}}\left((-\hat{q}) \pm i\frac{(-\hat{p})}{\omega}\right)\right] \\ &= -\hat{a}^{\mp} \neq \hat{a}^{\mp}\end{aligned} \tag{2.28}$$

$$\begin{aligned}\hat{T}\big(\hat{a}^{\mp}\big) &= \hat{T}\left[\sqrt{\frac{\omega}{2\hbar}}\left(\hat{q} \pm i\frac{\hat{p}}{\omega}\right)\right] \\ &= \left[\sqrt{\frac{\omega}{2\hbar}}\left((\hat{q}) \mp i\frac{(-\hat{p})}{\omega}\right)\right] \\ &= \left[\hat{a}^{\mp}\right]^{+} \neq \hat{a}^{\mp}\end{aligned} \tag{2.29}$$

Combining the results of equations 2.26-2.29, the magnetic part of the Hamiltonian is found to transform as follows:

$$\begin{aligned}\hat{P}\left(\hat{H}_{int}^{(m)}\right) &= \hat{P}\left[\hbar f \hat{L}'_{-}\hat{O}'_{+}\hat{a}^{+} + \hbar f^{*}\hat{L}'_{+}\hat{O}'_{-}\hat{a}^{-}\right] \\ &= \left[\hbar f\big(-\hat{L}'_{-}\big)\big(-\hat{O}'_{+}\big)\big(-\hat{a}^{+}\big) + \hbar f^{*}\big(-\hat{L}'_{+}\big)\big(-\hat{O}'_{-}\big)\big(-\hat{a}^{-}\big)\right] \\ &= -\hat{H}_{int}^{(m)} \neq \hat{H}_{int}^{(m)}\end{aligned} \tag{2.30}$$

$$\begin{aligned}\hat{T}\left(\hat{H}_{int}^{(m)}\right) &= \hat{T}\left[\hbar f \hat{L}'_{-}\hat{O}'_{+}\hat{a}^{+} + \hbar f^{*}\hat{L}'_{+}\hat{O}'_{-}\hat{a}^{-}\right] \\ &= \left[\hbar f\big(-\hat{L}'_{+}\big)\big(-\hat{O}'_{-}\big)\big(\hat{a}^{-}\big) + \hbar f^{*}\big(-\hat{L}'_{-}\big)\big(-\hat{O}'_{+}\big)\big(\hat{a}^{+}\big)\right] \\ &= -\hat{H}_{int}^{(m)} \neq \hat{H}_{int}^{(m)}\end{aligned} \tag{2.31}$$

$$\begin{aligned}\hat{P}\hat{T}\left(\hat{H}_{int}^{(m)}\right) &= \hat{P}\hat{T}\left[\hbar f \hat{L}'_{-}\hat{O}'_{+}\hat{a}^{+} + \hbar f^{*}\hat{L}'_{+}\hat{O}'_{-}\hat{a}^{-}\right] \\ &= \left[\hbar f\big(-\big)^{2}\hat{L}'_{+}\big(-\big)^{2}\hat{O}'_{-}\big(-\hat{a}^{-}\big) + \hbar f^{*}\big(-\big)^{2}\hat{L}'_{-}\big(-\big)^{2}\hat{O}'_{+}\big(-\hat{a}^{+}\big)\right] \\ &= \hat{H}_{int}^{(m)}\end{aligned} \tag{2.32}$$

According to equations 2.30 and 2.31, the magnetic interaction Hamiltonian does not obey either spatial inversion or time reversal symmetry separately. However, in equation 2.32, it is invariant under the combined symmetry operations of parity and time reversal.

2.2.3 Predictions of magneto-electric scattering completion time

When studying light scattering processes, it is important to understand the physical components which control the duration and magnitude of each process. By understanding the

relative order of magnitude of the time it takes for a specific process to go to completion, dynamic processes can be analyzed and compared. Below, the magneto-electric scattering completion time is determined from the quantum mechanical model.

Torque is the mechanism which is responsible for enhancing the induced magnetization. As shown in figure 2.5, the magnetic field of light acts upon the molecule and causes a semi-circular deflection in the electron path. The magnitude of magnetization is equal to the product of an induced electric current and the area over which it is spread. In an atomic model, there is no enhancement. In a molecular model, the magnetic field can torque upon the molecule and cause a rotation. The area increases when internal angular momentum is converted to external angular momentum (similar to the Einstein-de Haas effect [144]).

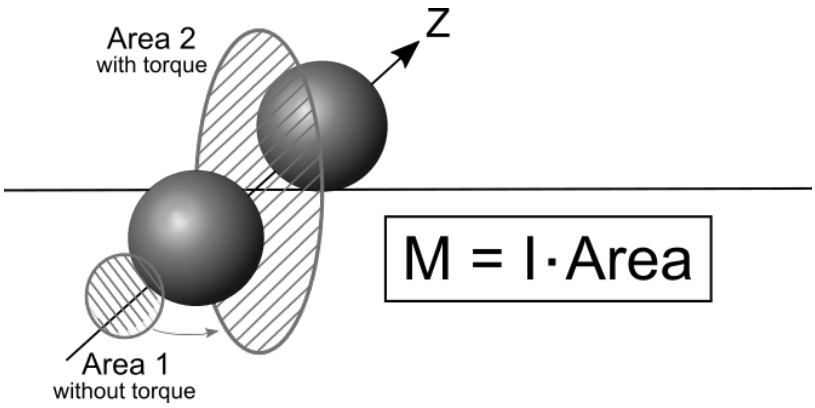

Figure 2.5: Diagram showing the magnetic enhancement.

The completion time is considered to be the time it takes for the magnetic torque to transfer the angular momentum of the electron to an orientation perpendicular to the molecular axis [7]. If the rotational angular momentum $\overline{O}$ is due to torque $\overline{T}$ exerted by a magnetic field on internal angular momentum $\overline{L}$, it accumulates with time classically according to

$$\overline{O} = \int_0^{\Delta t} \left(\frac{d\overline{O}}{dt} \right) dt. \tag{2.33}$$

Also, if total angular momentum $\overline{J} = \overline{L} + \overline{O}$ is conserved, its time derivative is zero. Thus,

$$d\overline{J}/dt = d\left(\overline{L} + \overline{O}\right)/dt = 0, \tag{2.34}$$

and

$$\overline{O} = -\int_0^{\Delta t} \left(\frac{d\overline{L}}{dt} \right) dt. \tag{2.35}$$

The equation of motion for rotations is $\overline{T} = d\overline{L}/dt$ in a fixed reference frame. Magnetic torque is given by $\overline{T} = \overline{m} \times \overline{B}$, where $\overline{m}$ is the magnetic moment due to circulation of

charge at the optical frequency (as in figure 2.5). The expression for $\overline{O}$ becomes

$$\overline{O} = -\int_0^{\Delta t} \left(\overline{m} \times \overline{B}\right) dt. \tag{2.36}$$

Conventionally, the magnetic moment, $\overline{m}$, can be expressed in terms of the internal angular moments, $\overline{L}$, as $\overline{m} = -e\overline{L}/2m_e$ (like in equation 2.15). However, once the transfer of angular momentum is taken into account, an enhanced expression of $\overline{m}$ can be used. The enhancement (as shown in figure 2.5) is the ratio of area 2 to area 1. Converting from area to frequency via moment of inertia, one finds that the enhancement is $\eta = \omega_0/\omega_\phi$, where ω_0 is the optical resonance frequency and ω_ϕ is the molecular rotation frequency. This results in an enhanced magnetic moment

$$\overline{m} = \frac{\eta e \overline{L}}{2m_e}. \tag{2.37}$$

Thus, the rotational angular momentum is given by the integral

$$\overline{O} = -\int_0^{\Delta t} \left(\frac{e\eta}{2m_e}\right) \left(\overline{L} \times \overline{B}\right) dt. \tag{2.38}$$

In a classical setting, the initial angular momentum is time dependent. It can be assumed that $\overline{L}$ and $\overline{B}$ have forms similiar to that of the electric field $\overline{E} = \frac{1}{2}\left(\overline{E}_0 e^{i\omega t} + \overline{E}_0^* e^{i\omega t}\right)$. Then, the slowly-varying envelope approximation [145] of the rotational angular momentum yields

$$\overline{O} = -\left(\frac{e\eta}{2m_e}\right)\left(\frac{2\overline{L}_0 \times \overline{B}_0^*}{4}\right)\Delta t. \tag{2.39}$$

The momentum transfer time interval, Δt, may be estimated from equations 2.38 and 2.34 by setting the time-integrated torque equal to the orbital angular momentum available for transfer ($\hbar$). That is,

$$\Delta\overline{L} = \left(\frac{e\eta}{2m_e}\right)\left(\frac{\overline{L}_0 \times \overline{B}_0^*}{2}\right)\Delta t = \hbar. \tag{2.40}$$

Setting $\overline{L} = \hbar$ also, and solving for Δt, one finds

$$\Delta t = \frac{4m_e}{e\eta B_0^*} = \frac{4m_e c}{e\eta E_0}. \tag{2.41}$$

If an applied electric field strength of $E \approx 10^8$ V/m is assumed, the magneto-electric

scattering completion time is approximated as

$$\Delta t \approx 135 fs. \tag{2.42}$$

2.3 Optical susceptibilities for magneto-electric effects

The discovery of the magneto-electric nonlinearities (magnetization $M_y(\omega)$, rectification $P_z(0)$, and second harmonic generation $P_z(2\omega)$) calls for a more complete description of nonlinear response that includes second- and third-order M-E contributions ($\chi^{(2)}_{ME}$ and $\chi^{(3)}_{ME}$), as well as conventional first ($\chi^{(1)}$), second ($\chi^{(2)}$), and third-order ($\chi^{(3)}$) all-electric terms in equations 2.43 and 2.44.

$$\begin{aligned} P_{NL} = \epsilon_0 \left\{ \chi^{(1)} E(\omega) + \chi^{(2)} E(\omega) E(\omega) + \chi^{(3)} E(\omega) E(\omega) E(\omega) + ... \right\} \\ + (1/c) \left\{ \chi^{(2)}_{ME} H(\omega) E(\omega) + \chi^{(2)}_{ME} E(\omega) H(\omega) E(\omega) + ... \right\} \end{aligned} \tag{2.43}$$

$$M_{NL} = \left\{ \chi^{(2)}_{ME} E(\omega) H(\omega) + \chi^{(2)}_{ME} E(\omega) H(\omega) E(\omega) + ... \right\} \tag{2.44}$$

In the subsequent two subsections, the constitutive relations for the M-E processes of interest (P_{NL} and M_{NL}) are compared with those of all-electric four-wave mixing. The goal is to take into account the axial nature of the magnetic field by converting expressions for M-E processes into ones expressed exclusively in terms of equivalent electric fields, such that all input and output fields have the same polar character. This allows for a direct comparison of M-E and all-electric nonlinearities. The procedure is first outlined for M-E rectification in Section 2.3.1, and it is then applied to M-E magnetization in Section 2.3.2.

2.3.1 Magneto-electric polarization

In this section, the second-order contribution to polarization P in equation 2.45, which is driven jointly by the electric field E and the magnetic field H of light in a centrosymmetric medium, is considered. It is governed by χ_{ME}, or more specifically the set of coefficients χ^{eme}_{ME} that relate the k-component of P to the driving fields H^*_l and E_m according to $P^2_k = (1/c)\, \chi^{eme}_{xyz}(0; -\omega, \omega)\, H^*_y E_x$, where k, l, m specify Cartesian coordinates, and the summation convention for repeated indices applies [146]. The convention is used that all the frequencies in the argument of the susceptibility add to zero. The factor of (1/c) in this constitutive relation has been introduced to ensure that the susceptibility has SI units of m/V, which will facilitate its comparison with any other all-electric susceptibility. The input field can be specialized to the case that is a plane wave of the form

$\overline{E} = \widehat{x}\,(E/2)\,exp\,[-i\,(\omega t - kz)] + c.c.$, polarized along x and propagating along z. In addition, it is assumed that only a single term contributes to $P_z^2\,(0)$ because the fields do not commute in M-E interactions [147]. With these assumptions, the M-E rectification polarization is

$$P_z^2\,(0) = (1/c)\,\chi_{zyx}^{eme}\,(0;-\omega,\omega)\,H_y^*\,(-\omega)\,E_x\,(-\omega) \tag{2.45}$$

In equation 2.45, the vector on the left is determined by the combination of a vector and a psuedovector on the right, through the third rank *psuedotensor* element χ_{xyz}^{eme}. To make possible a direct comparison between χ_{xyz}^{eme} and an equivalent all-electric susceptibility, the pseudovector field H_y^* must be replaced by an equivalent electric field, consistent with Maxwell's equations. Faraday's law dictates the equivalence relation

$$H_y^* = -E_x^*/\eta_0. \tag{2.46}$$

Here η_0 is the electromagnetic impedance, which is taken to be that of vacuum [148]. By substituting equation 2.46 into 2.45, the longitudinal polarization becomes

$$P_z^2\,(0) = -\epsilon_0\chi_{zyx}^{eme}\,(0;-\omega,\omega)\,E_x^*\,(-\omega)\,E_x\,(-\omega)\,. \tag{2.47}$$

Note here that although the psuedovector H_y^* was replaced by the equivalent field $-E_x^*/\eta_0$, the indices of the element χ_{zyx}^{eme} do not change since it is a scalar magneto-electric element specified by the original fields and their orientations. The polarization $P_0^{(2)}$ is non-vanishing, unlike the corresponding second-order polarization based purely on electric field inputs in centrosymmetric media. In the later case, inversion symmetry prohibits rectification, whereas the magneto-electric process in equations 2.45 and 2.47 induces non-centrosymmetry. The resulting induced birefringence contributes to the third-order polarization, as shown next.

Now, it is possible to proceed to connect the second-order, M-E rectification element $\chi_{zyx}^{eme}\,(0;-\omega,\omega)$ to the third-order susceptibility element $\chi_{zzxx}^{(3)}\,(-\omega;\omega,-\omega,\omega)$ (or γ). First, note that the rectification polarization produces a surface charge density $\sigma_z^{(2)}$ given by $\sigma_z^{(2)} = P_z^{(2)}\,(0)$. Simultaneously, the M-E interaction breaks the inversion symmetry of the medium [134], rendering it electro-optic. $\sigma_z^{(2)}$ is indistinguishable from the surface charge density produced by dielectric response to a static field $E_z\,(0)$ applied along the z-axis, identical to the charge which would appear on a dielectric spacer in a capacitor. Therefore, $\sigma_z^{(2)} = \epsilon_0\chi_{eff}\,(0)\,E_z\,(0)$, where the dielectric response is represented for the moment as an effective susceptibility $\chi_{eff}\,(0)$ at zero frequency. Since $\sigma_z^{(2)} = P_z^{(2)}\,(0)$, an

alternative to equation 2.47 for the M-E polarization is

$$P_z^2(0) = -\epsilon_0 \chi_{eff}(0) E_z(0). \tag{2.48}$$

Equating equations 2.47 and 2.48 determines the dimensionless effective susceptibility to be

$$\chi_{eff}(0) = -\chi_{zyx}^{eme}(0; -\omega, \omega) E_x^*(-\omega) E_x(\omega) / E_z(0). \tag{2.49}$$

As the result of dynamic symmetry-breaking, the static dielectric properties of the medium are altered in second order due to induced electro-optic behavior, whereas in centrosymmetric media subjected to purely electric interactions a change of permittivity requires application of the square of a static electric field as in the DC Kerr effect [149].

Next, note that a polarization at the optical frequency arises from the mixing of the static rectification field $E_z(0)$ with a probe field $E_z(\omega)$ according to

$$P_z(\omega) = \epsilon_0 \chi_{zzz}^{(eee)}(-\omega; \omega, 0) E_z(\omega) E_z(0). \tag{2.50}$$

Assuming the frequencies may be permuted (noting that all fields in 2.50 are electric), this equation may be written in the form

$$P_z(0) = \epsilon_0 \chi_{zzz}^{(eee)}(0; -\omega, \omega) E_z^*(-\omega) E_z(\omega). \tag{2.51}$$

The matrix element $\chi_{zzz}^{(eee)}(0; -\omega, \omega)$ vanishes in centrosymmetric media, so it can only be an effective susceptibility which is non-vanishing here as the result of the magneto-electric interaction. To evaluate $\chi_{zzz}^{(eee)}(0; -\omega, \omega)$, equation 2.51 must be compared with equation 2.47 which also gives the M-E rectifcation polarization. By assuming that the driving field intensities are the same ($\|E_x\| = \|E_z\|$ or $I_x = I_z$) and equating the polarizations in equations 2.47 with 2.51, one finds that

$$\chi_{zzz}^{(eee)}(0; -\omega, \omega) = -\chi_{zyx}^{(eme)}(0; -\omega, \omega). \tag{2.52}$$

The physical meaning of equation 2.52 is that, provided $I_x = I_z$, the induced electro-optic effect has the same magnitude as the induced rectification so their coefficients are equal apart from sign.

The susceptibility $\chi_{eff}(0)$ is determined by the static dielectric constant according to $\epsilon_{zz}(0)/\epsilon_0 \equiv \epsilon_r(0) = 1 + [\chi_{eff}(0)]_{zz}$. Hence, equation 2.49 yields the following expression

for the static field $E_z(0)$.

$$E_z(0) = \left(\frac{P_z^{(2)}(0)/\epsilon_0}{(\epsilon_r(0)-1)} \right) = \left(\frac{\chi_{zyx}^{(eme)}(0;-\omega,\omega) E_x^* E_x}{(\epsilon_r(0)-1)} \right) \tag{2.53}$$

Upon substitution of equations 2.52 and 2.53, equation 2.50 for the third order polarization becomes

$$P_z^{(3)}(\omega) = \epsilon_0 \left\{ \frac{\left[\chi_{zyx}^{(eme)}(0;-\omega,\omega)\right]^2}{(\epsilon_r(0)-1)} \right\} E_z(\omega) E_x^*(-\omega) E_x(\omega). \tag{2.54}$$

$P_z^{(3)}(\omega)$ in equation 2.54 is a nonlinear M-E polarization driven by the three optical fields on the right. Note that $\chi_{zyx}^{(eme)} \neq 0$ even in centrosymmetric media, so this polarization is non-vanishing. For comparison, the third-order polarization developed in response to purely electric z-polarized probe and x-polarized pump waves [33], which is also non-vanishing under inversion symmetry, is

$$P_z^{(3)}(\omega) = \epsilon_0 \chi_{zzxx}^{(3)}(-\omega;\omega,-\omega,\omega) E_z(\omega) E_x^*(-\omega) E_x(\omega) \tag{2.55}$$

Note that the coefficients in equations 2.54 and 2.55 are both scalar tensor elements describing the longitudinal electric polarization induced by the same three electric input fields. Moreover, in centrosymmetric media, there are no other contributions to the third-order polarization driven by optical electric fields. That is, in equations 2.54 and 2.55, the input and output fields are unique and identical in form. The scalar coefficients relating these input and output fields are therefore the same in the two equations. Thus, an equivalence relation for M-E rectification is obtained by equating coefficients.

$$\left\{ \frac{[\chi_{zyx}^{(eme)}(0;-\omega,\omega)]^2}{(\epsilon_r(0)-1)} \right\} = \chi_{zzxx}^{(3)}. \tag{2.56}$$

Equation 2.56 is valid when pump and probe intensities are equal (i.e. $E_x^* E_x = E_z^* E_z$ or $I_x = I_z$). It indicates that the cascading of the M-E rectification with an electro-optic response in centrosymmetric media produces a Kerr-like nonlinearity governed by $\chi_{zzxx}^{(3)}$. In non-centrosymmetric media, similar effects are well-known in which all-electric rectification combined with the electro-optic effect gives rise to large effective nonlinear refractive index contributions [149]. In the present case, however, a magneto-electric interaction is required to break the inversion symmetry of the medium dynamically, and simultaneously

produce rectification. This makes possible an effectively third-order polarization in centrosymmetric media, one that is uniquely mediated by the M-E interaction but that adds directly to the all-electric contribution, also governed by $\chi^{(3)}_{zzxx}$. This outcome applies universally to dielectric materials of any symmetry, but it should be noted that other cascaded nonlinearities may also contribute to M-E nonlinear susceptibilities [150]. In summary, equation 2.56 indicates that the off-diagonal susceptibility element $\chi^{(3)}_{zzxx}$ determines the magnitude of the coefficient for magneto-electric rectification. Conversely, the magneto-electric susceptibility $\chi^{(eme)}_{zyx}$ contributes to nonlinear refraction.

2.3.2 Magneto-electric magnetization

A relationship can also be established between susceptibility elements for magneto-electric magnetization and third-order, all-electric susceptibility elements. However, in this case the nonlinearity is not cascaded because the dominant term of the magnetization is third order from the outset as discussed below.

Second-order magnetization induced by an electromagnetic wave, of the form

$$M_{NL} = \chi^{mme} H^* E, \tag{2.57}$$

vanishes in centrosymmetric media because elements of $\chi^{(mme)}$ with repeated indices are zero. This can readily be shown using symmetry analysis of this tensor. the requirement for $\chi^{(mme)}$ to be non-vanishing is that $\chi^{(mme)'} = \chi^{(mme)}$, where the prime represents the symmetry transformation. That is,

$$\chi^{(mme)'} = \Delta_m S_m \chi^{(mme)} \Delta_m S_m^+ S_e^+, \tag{2.58}$$

where $S_e = S_m = \begin{bmatrix} -1 & 0 & 0 \\ 0 & -1 & 0 \\ 0 & 0 & -1 \end{bmatrix}$ are the spatial inversion operators for the magnetic and electric fields and $\Delta_m = -1$ is the determinant of S_m. However, evaluation of equation 2.58 yields

$$\chi^{(mme)} = -\chi^{(mme)}. \tag{2.59}$$

Hence, all matrix elements of the susceptibility must be zero. Second-order transverse magnetization is thereby prohibited in centrosymmetric media, unless the interaction itself breaks the inversion symmetry. While dynamic symmetry-breaking does take place in M-E interactions [134], allowing optical magnetization that is quadratic with respect to the input field, the quadratic contribution to the magnetic moment is much smaller than the cubic

term at moderate intensities [7]. For this reason, the second-order interaction mediated by symmetry-breaking will be ignored in the analysis here.

In third order, similar symmetry analysis prohibits the process $M^{(3)} = \chi^{(mmme)} HH^*E$. In this case, the susceptibility transforms according to

$$\chi^{(mmme)} = \Delta_m S_m \chi^{(memm)} \Delta_m S_m^+ \Delta_m S_m^+ S_e^+ = -\chi^{(mmme)}. \tag{2.60}$$

Hence in the presence of spatial inversion symmetry, all matrix elements vanish. On the other hand, the process $M^{(3)} = \chi^{(meme)} EH^*E$ yields a different result. The inversion transformation yields

$$\chi^{(meme)'} = \Delta_m S_m \chi^{(meme)} S_e^+ \Delta_m S_m^+ S_e^+ = \chi^{(meme)}. \tag{2.61}$$

Since $\chi^{(meme)'} = \chi^{(meme)}$, the susceptibility for magneto-electric magnetization is non-vanishing under inversion symmetry.

A connection can now be made between the all-electric third-order susceptibility $\chi^{(3)}$ and the M-E susceptibility $\chi^{(meme)}$ which describes optical magnetization of the form

$$M_{NL} = \chi^{meme} EH^*E. \tag{2.62}$$

Proceeding as in the last section, the magnetic field in equation 2.62 is replaced by an equivalent electric field specified by equation 2.46. This yields

$$M_y^{(3)} = \left\{ \frac{-\chi_{yxyx}^{(meme)}}{\eta_0} \right\} E_x E_x^* E_x. \tag{2.63}$$

Note that equation 2.63 still contains the psuedo-vector $M_y^{(3)}$ on the left. $M_y^{(3)}$ is an axial field which, like H, must be expressed in terms of an equivalent electric field for the purpose of comparing with a third-order, all-electric polarization. For this purpose, Ampere's Law may be used to relate the curl of M to the time derivative of an electric polarization. In insulators, this yields [131, 151]

$$\overline{\nabla} \times \frac{\overline{B}}{\mu} = \epsilon_0 \frac{\partial \overline{E}}{\partial t} + \frac{\partial P}{\partial t} + \overline{\nabla} \times \overline{M}. \tag{2.64}$$

When the input fields are weak, and $\mu = \mu_0 (1 + \chi_m) \cong \mu_0$, the induced magnetization makes a relatively small contribution to B. Under these conditions, the left-hand side of equation 2.64 can be ignored while retaining it as a source term on the right. The first two

terms in equation 2.64 then cancel, with the result that

$$0 = \frac{\partial P}{\partial t} + \overline{\nabla} \times \overline{M}. \tag{2.65}$$

For the field geometry of interest here, with the electric field oriented along x, an equivalent polar field for M is thereby determined to be,

$$-\left(\frac{\partial P}{\partial t}\right)_x = \left(\overline{\nabla} \times \overline{M}\right)_x. \tag{2.66}$$

Both P and M are expressible as plane waves, so the derivatives in 2.66 are readily evaluated. Equation 2.66 thereby becomes $-\left(\partial P_x/\partial t\right) = \left(\partial M/\partial z\right)_x$ and simplifies to

$$M_y(t) = -\left(\partial z/\partial t\right) P_x(t) = -cP_x(t), \tag{2.67}$$

where $c \equiv \partial z/\partial t$ is the phase velocity of light. The minus sign in 2.67 indicates that the magnetic moment M is diamagnetic in character. Upon substitution of equation 2.67 into equation 2.63, one finds the expression for third-order polarization equivalent to magnetization driven by equivalent electric fields.

$$P_x^{(3)}(\omega) = \epsilon_0 \chi_{yxyx}^{(meme)} E_x(\omega) E_x^*(-\omega) E_x(\omega). \tag{2.68}$$

This expression may be immediately compared with that for all-electric four-wave mixing with co-polarized pump and probe waves [152], namely

$$P_x^{(3)}(\omega) = \epsilon_0 \chi_{xxx}^{(3)} E_x(\omega) E_x^*(-\omega) E_x(\omega). \tag{2.69}$$

Equating equations 2.68 and 2.69 provides an equivalence relation between the nonlinear susceptibilities governing magnetization and four-wave mixing.

$$\chi_{yxyx}^{(meme)} = \chi_{xxxx}^{(3)} \tag{2.70}$$

The expressions in equations 2.56 and 2.70 establish specific relationships between M-E and third-order all-electric susceptibilities which are nonzero in all crystal classes. Due to extensive prior work on measurement and prediction of third-order susceptibility elements, including analysis of the relationship between structure and function at the molecular level, these connections allow for formulation of guidelines for detailed design of M-E materials at the molecular level. The equivalence relations also imply that M-E rectification and magnetization are universally allowed in dielectric materials of arbitrary crystal symmetry.

CHAPTER 3

Methods

This chapter discusses the methods used for exploring the effects of radiant optical magnetization. The experimental approach is described in section 3.1, which is primarily a continuation of methods described previously in papers [6] and other theses [136, 153]. Furthermore, the simulation methods used for the classical torque-enhanced Lorentz oscillator model are described in section 3.4. A second-order ordinary differential equation solver was used in MATLAB to evaluate the system of equations described in subsection 2.1.2.

3.1 Experimental design

At its core, the experimental design for detecting magneto-electric scattering is that of a light scattering experiment. Light scattering experiments, such as those used to detect Rayleigh scattering are a well-established way of detecting how light interacts with materials. Often, light scattering experiments are used to measure parameters such as Rayleigh scattering cross-sections [79, 154]. If the input polarization of light is controlled and varied, light scattering experiments also can be used to "map out" radiation patterns of electric dipoles [50].

The procedure for characterizing electric dipole scattering is quite simple. Suppose vertically-polarized light ($\hat{x}$-polarized) is incident upon a material. The light excites the electrons in the molecules and causes them to oscillate at the same frequency as the applied electric-field component of the light, just like the Lorentz oscillator model described in section 2.1. These induced electric dipoles radiate energy outwardly in the classic $\sin^2(\theta)$ pattern. Specifically, if the detection distance is much larger that the wavelength of light, the radiated fields are

$$\bar{B} = -\frac{\mu_0 p_0 \omega^2}{4\pi c}\left(\frac{\sin\theta}{r}\right)\cos\left[\omega\left(t - r/c\right)\right]\hat{\phi} \tag{3.1}$$

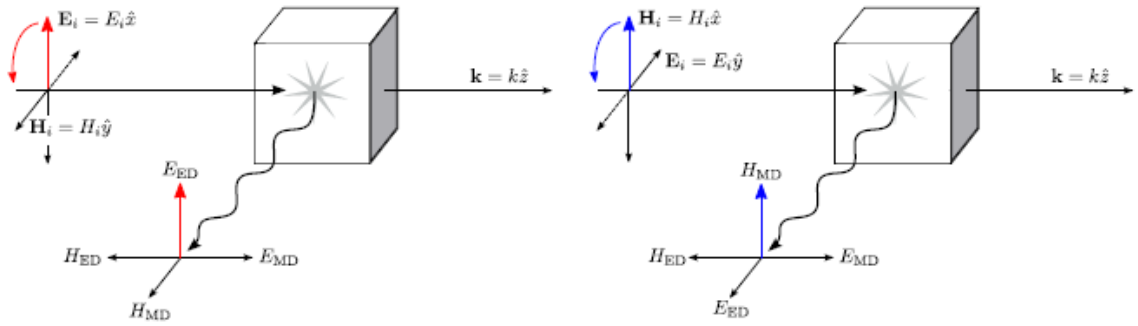

Figure 3.1: 90° light scattering geometry used in detecting (l) electric and (r) magnetic dipole radiation. Reprinted with permission from reference [136].

and

$$\bar{E} = -\frac{\mu_0 p_0 \omega^2}{4\pi}\left(\frac{\sin\theta}{r}\right)\cos\left[\omega\left(t - r/c\right)\right]\hat{\theta}, \tag{3.2}$$

where $\hat{r}$ is the radial unit vector, $\hat{\theta}$ is the polar angle unit vector measured from the $\hat{z}$ axis, and $\hat{\phi}$ is the axial angle unit vector measured from the $\hat{x}$ axis. The time-averaged Poynting vector is then

$$\left\langle \bar{S} \right\rangle = \left(\frac{\mu_0 p_0 \omega^2}{4\pi}\right)^2 \left(\frac{\sin^2\theta}{r^2}\right)\hat{r}. \tag{3.3}$$

Therefore, the maximum radiation can be detected when $\theta = 90°$, by placing the detector along the $\hat{y}$-axis within the $\hat{y}$-$\hat{z}$ plane, as shown in figure 3.1. If the incident light is rotated to be horizontally-polarized ($\hat{y}$-polarized), a minimum will then be detected. A vertically-oriented linear polarizer can thus be used to "map out" electric dipole radiation.

Now suppose that one wants to detect a vertically-oriented magnetic dipole instead of a vertically-oriented electric dipole. In this case, energy is radiated again in a $\sin^2(\theta)$ pattern. In the far field, the radiated fields are

$$\bar{B} = -\frac{\mu_0 m_0 \omega^2}{4\pi c^2}\left(\frac{\sin\theta}{r}\right)\cos\left[\omega\left(t - r/c\right)\right]\hat{\theta} \tag{3.4}$$

and

$$\bar{E} = -\frac{\mu_0 m_0 \omega^2}{4\pi c}\left(\frac{\sin\theta}{r}\right)\cos\left[\omega\left(t - r/c\right)\right]\hat{\phi}. \tag{3.5}$$

The time-averaged Poynting vector is then

$$\left\langle \bar{S} \right\rangle = \left(\frac{\mu_0 m_0 \omega^2}{4\pi c}\right)^2 \left(\frac{\sin^2\theta}{r^2}\right)\hat{r}. \tag{3.6}$$

Therefore, as shown on the right side of figure 3.1, the maximum radiation can be de-

tected when $\theta = 90°$, by placing the detector along the $\hat{y}$-axis within the $\hat{y}$-$\hat{z}$ plane. However, since the detector detects electric fields, the detected light with be horizontal in its electric-field polarization. Therefore, a horizontally-oriented linear polarizer can be used to select any magnetic dipole radiation. Incident horizontally-polarized light ($\hat{y}$-polarized) will be detected at a maximum. If the incident light is rotated to be vertically-polarized ($\hat{x}$-polarized), a minimum will then be detected.

As mentioned above, the optimal location of detection is when $\theta = 90°$. Although this condition is satisfied anywhere within the $\hat{y}$-$\hat{z}$ plane, along the $\hat{y}$-axis is the only location where the two radiation patterns are distinguishable by polarization analysis. As shown in figure 3.2, the polarization of the light radiated from the magnetic and electric dipoles is parallel in the direction of propagation ($\hat{z}$-axis), and therefore indistinguishable. This results in the need for an experiment that can only detect light at $90°$ from the direction of propagation in order to properly distinguish between electric and magnetic dipole radiation. Ideally, light will only be detected from exactly at $\theta = 90°$. However, that is impractical because an infinitely small collection angle would result in an infinitely small signal. If the collection angle is too big, radiation from the non-desired dipole will be detected in addition to the desired one. Appendix C of reference [136] calls this out-of-plane scattering. It is referred to as possible polarization leakage in table 3.2.

To be explicit in detection, the major difference between distinguishing between the two dipole radiation patterns is the optimal orientation of the analyzer. Table 3.1 summarizes which dipole component is detected based on input and output polarization of light. The polarization abbreviation follows the convention established by Kratohvil in reference [73]. Other common polarization abbreviations include I_{VV} and VV.

Table 3.1: Comparison of detected dipole radiation by input and output polarizations.

Polarization of Incident Light	Polarization of Detected Light	Polarization Abbreviation	Dipole Detected
Vertical	Vertical	V_v	ED Max.
Horizontal	Vertical	V_h	ED Min.
Horizontal	Horizontal	H_h	MD Max.
Vertical	Horizontal	H_v	MD Min.

In practice, our light scattering experiment consisted of the following components: a method to change the incident power (half-wave plate + polarizer or Neutral Density (ND) filter wheel); a method to rotate the incident polarization (half-wave plate); a method to control the analyzed polarization of the scattered light (polarizer); and a method to detect the amount of light scattered (photomultiplier tube or photodiode). Although slightly

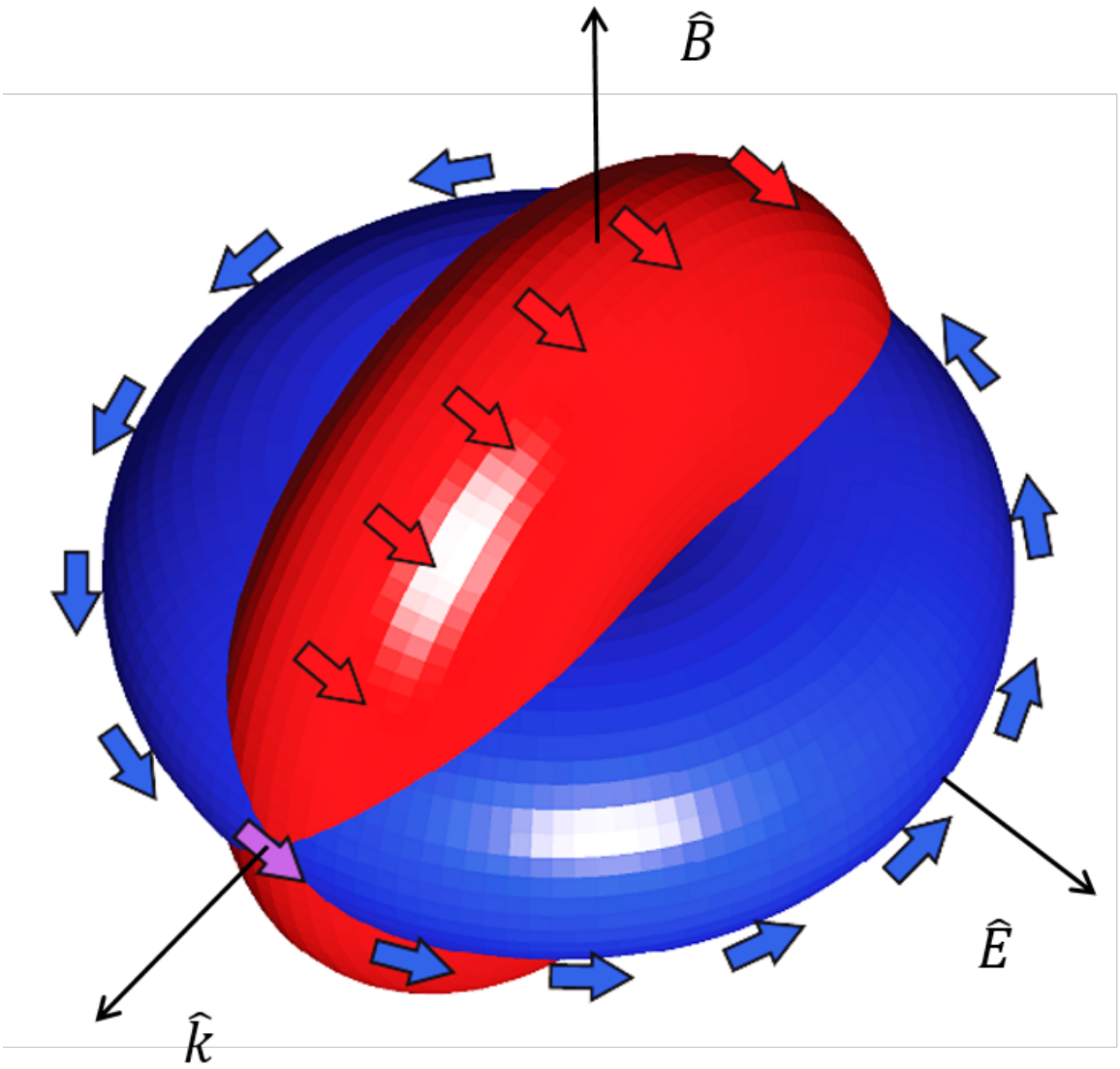

Figure 3.2: Radiation and polarization from electric (Red) and magnetic (Blue) dipoles generated by a plane wave of light. The purple arrow indicates that the polarizations of the two dipoles are parallel, and therefore indistinguishable, along the forward direction. Reprinted with permission from reference [153].

different components were used, all variations of the experiment used the basic geometry shown in figure 3.3. Note that the narrowband interference filter normally used in our light scattering experiments was omitted to record spectrally resolved scattering data.

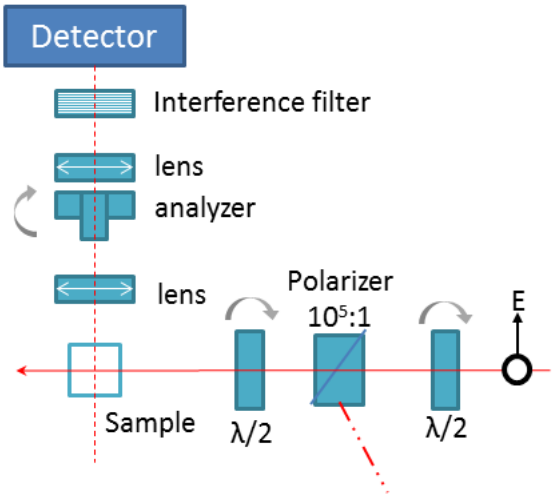

Figure 3.3: Basic geometry of magneto-electric scattering experiments.

3.1.1 Summary of experimental parameters

Magneto-electric scattering has been studied using various laser sources. The full comparison of system specifications is shown in table 3.2. The first laser source was a Clark-MXR CPA-2001. This laser provided a large amount of energy per pulse, enabling the use of a flat-top beam. However, its 1 kHz repetition rate limited the data collection range (See appendix D of reference [136]). The second laser source, the Coherent Vitara-HP, provided an increased repetition rate but lower energy per pulse, resulting in a need to focus the beam in order to reach the desired intensity range. The third laser source was an Amplitude Aurora system. It provided a larger repetition rate than the Clark-MXR CPA-2001 and large enough energy per pulse that focusing of the beam was unnecessary. The Amplitude system was used for both intensity-dependent dipole and spectroscopic measurements.

The values in table 3.2 were calculated using the following equations. See appendix C and F of reference [136] for their derivations. Note that W_x and W_y are the measured values of the $1/e^2$ beam full-width and that the $FWHM_t$ is the measured value from the MIIPS pulse compressor.

Collection angle (°)	$\theta = \arctan\left(D/2R\right)$
Collection solid angle (Ω)	$d\Omega = D^2/16R^2$

Table 3.2: Comparison of specifications of magneto-electric scattering experiments.

Laser Model	**CPA2001**	**Vitara-HP**	**Aurora**
Laser Source	Clark-MXR	Coherent	Amplitude
Pulse length ($FWHM_t$)	150 fs	15 fs	30 fs
Center wavelength	775 nm	800 nm	800 nm
Bandwidth	5 nm	60 nm	30 nm
Repetition rate	1 kHz	80 MHz	10 kHz
Avg. Power @ Exp.	560 mW	440 mW	1 W
Energy @ Exp.	56 μJ	5.5 nJ	100 μJ
Focus lens	None	200 mm	None
Input beam dia. ($W_x \times W_y$)	2.1 cm $\times$ 1.6 cm	1.02 cm $\times$ 1.64 cm	1.5 cm
Input beam aperture	3.5 mm	None	5 mm
Illuminated volume	3.5 mm	0.2 mm $\times$ 0.124 mm	5 mm
Collection lens (f1) (R)	150 mm	50 mm	150 mm
Collection magnification	x1	x3	x1
Iris diameter (D)	3.5 mm	5 mm	3 mm
Collection angle	0.67°	2.86°	0.57°
Collection solid angle ($d\Omega$)	3.4E-5 Ω	6.3E-4 Ω	2.5E-5 Ω
Polarization leakage	0.0068%	0.125%	0.005%
Collection spot size	$\sim$3 mm	$\sim$25 μm	$\sim$3 mm
Normalized Illumin. area	1.03 cm^2	76.1E-6 cm^2	0.69 cm^2
Energy density per pulse	54.4 $\mu J/cm^2$	72.3 $\mu J/cm^2$	145 $\mu J/cm^2$
Peak intensity	3.41E8 W/cm^2	4.53E9 W/cm^2	4.54E9 W/cm^2

Polarization leakage (%)	$\frac{\|E_{//}\|^2}{\|E_\perp\|^2} = \frac{2-3\cos(D/2R)+\cos^3(D/2R)}{1-\cos^3(D/2R)}$
Max. intensity	$I_{max} \approx$ *Avg. Power / (Rep. Rate)(Beam Area)(Pulse Duration)*
Pulse duration (s)	$\sigma_t = \sqrt{2\pi} FWHM_t / \left(2\sqrt{2\ln 2}\right)$
Beam area (cm^2)	$A = \pi r^2 = \pi \left(5/16\right)^2 W_x W_y$
Pulse energy (J)	$\epsilon =$ *Avg. Power / Rep. Rate*
Pulse energy per area (J/cm^2)	$\frac{\epsilon}{A} = \frac{\textit{Average Power}}{\textit{Rep. Rate}} \left(\frac{16}{5}\right)^2 \frac{1}{W_x W_y}$
Intensity (W/cm^2)	$I_{max} = \frac{\epsilon}{A\sigma_t} = \frac{\epsilon}{A} \frac{2\sqrt{2\ln 2}}{\sqrt{2\pi} FWHM_t} = \frac{\epsilon}{A} \frac{0.9394}{FWHM_t}$

3.1.2 Procedures and calibration

In a light scattering experiment, care must be taken in construction, alignment, and calibration in order to ensure the integrity and repeatability of the experiment. Section 3.1.2.1 details the construction of the experiment and the necessary equipment. Section 3.1.2.3

discusses the specific calibration of the optics and their positions.

3.1.2.1 Equipment overview

The table below details the equipment, part numbers, and suppliers for the large components used in this experiment. Note, that there are two different detection schemes listed in the table, based on light levels.

Table 3.3: Experimental Electronics

Device	Company	Part #	Quantity
Photodiode	EG&G	FND-100	1
Current Amplifier	DL Instruments	DL1212	1
Lock-In Amplifier	Stanford Research Sys.	SR810	1
PMT	Burle	C31034A	1
PMT Refrigerated Housing	Products for Research		1
Current Preamplifier	Stanford Research Sys.	SR550	1
Photon Counter	Stanford Research Sys.	SR400	1
Spectrograph	Andor	Shamrock500i	1
CCD	Andor	iXon 885	1
Single-axis stepper motor controller/driver	Newport	SMC100PP	2
360 Rotation Stage	Newport	PR50PP	2
USB Wheel	Picard Industries		1
USB Shutter	Picard Industries		1
Power Meter	Thorlabs		1

The equipment detailed in table 3.3 were characterized according to their respective user manuals and procedures. First, the linearity of the power meter and the precision of the intensity control were verified. The intensity control relied on one of two methods. The first method used a computer controlled half-wave plate and a stationary polarizer. The half-wave plate rotated the incident polarization of light and a percentage of it was passed by the polarizer. The exact percentage was determined by Malus' Law [155]. The second method was simply a computer-controlled reflective neutral density filter that attenuated the beam based on its angle. Using the second method, the linearity of both the power control method as well as the detection systems were verified. Figure 3.4 shows that the detection system had a linear response over 3 decades of input power.

The other important calibration was finding the zero-positions of the polarizer and waveplates. The zero position was an index on the SMC100PP rotation stages that was used for the controlling computer program. For example, the zero location on the polarizer was the location where vertically-polarized light was maximally transmitted. 90 units

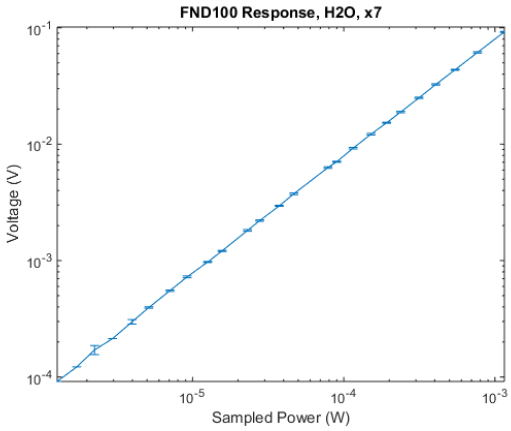

Figure 3.4: Response of detection system.

away from that location was where horizontally-polarized light was maximally transmitted. A full discussion on the calibration process is detailed in Appendix A.

3.1.2.2 Detector stabilization

When using a Photo-multiplier Tube (PMT) as the detector, special procedures must be followed to ensure accurate, sensitive, and unsaturated signal detection. The PMT described below is a C31034A [156] from BURLE Electron Tubes and was housed inside a refrigerated case from Products for Research. The steps for detector stabilization were:

1. **Temperature Stabilization**: Let PMT chill for at least 2 hours.

2. **Signal Analysis**: Analyze output electronic signal using oscilloscope, amplify if needed, and snub any ringing.

3. **PMT 1-photon Peak**: Find the "1 photon" peak by running a differential voltage scan of the signal using the SR400 gated photon counter.

The temperature stabilization was important because it lowered the level of electronic noise in the PMT. As shown in figure 3.5, the counts per second of the noise was over 20,000 counts per second (cps) when the chiller for the PMT was initially turned on. After about 2 hours of chilling, the count rate decreased to less than 20 cps. After 29 hours of chilling, the average number of dark counts was 6 cps with a standard deviation of 3 cps. Figure 3.6 shows the dark count rate distribution over a 200 second window after the PMT had chilled for 29 hours.

Snubbing is the process of adding a t-shaped 50 Ohm BNC connector and a short BNC cable with a less than 50 Ohm terminator to the output of the PMT in order to improve the

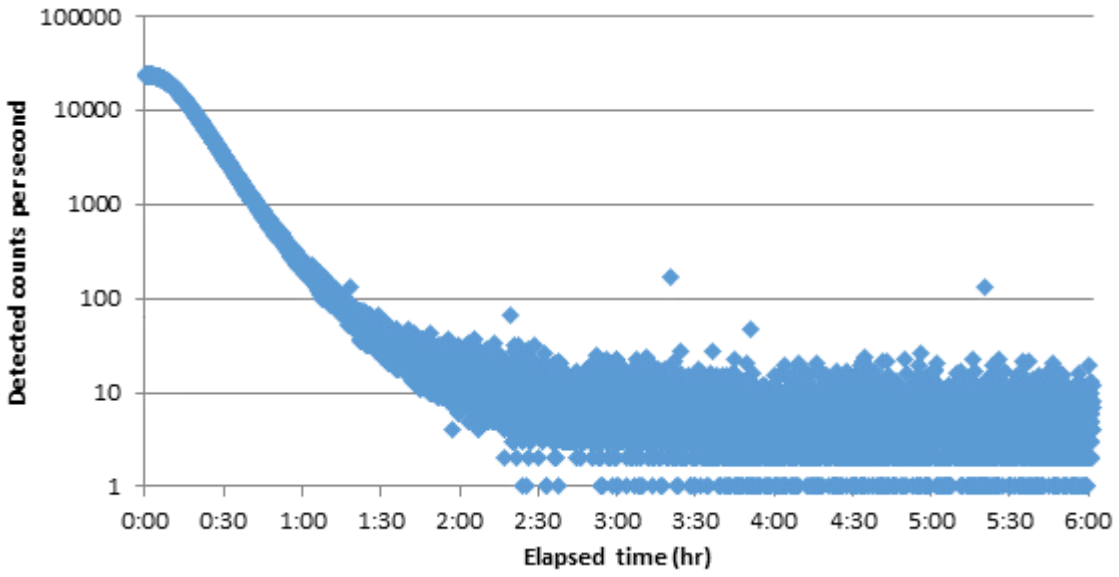

Figure 3.5: Dark count rate of C31034A after the chiller was activated. Taken using the SR400 with a discriminator of -18 mV, x5 amplification, 1800 V high voltage bias after being off for 4 days time.

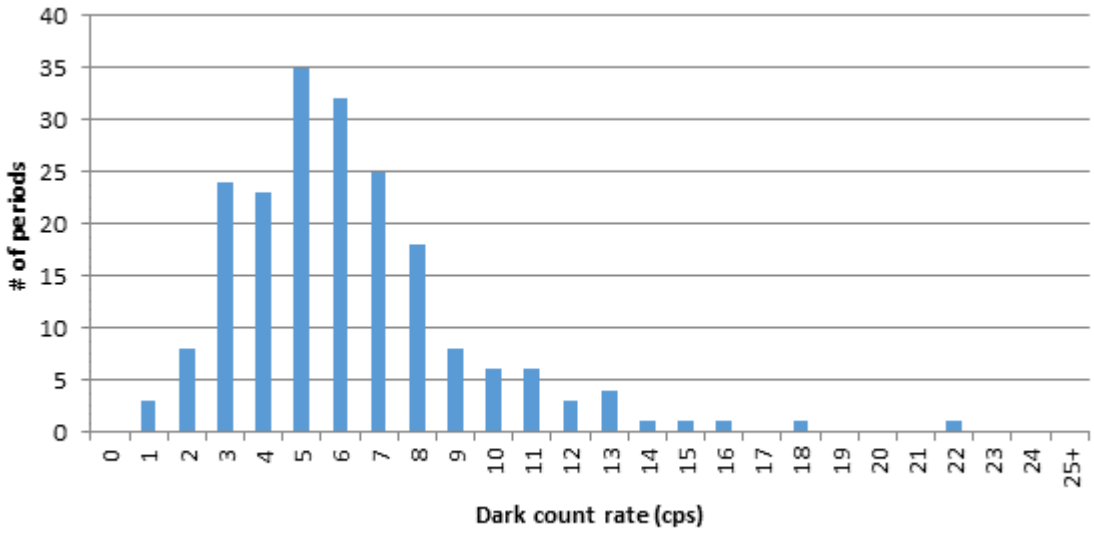

Figure 3.6: Dark count rate distribution of C31034A after the chiller was activated for 29 hours, over a 200 second window. Taken using the SR400 with a discriminator of -18 mV, x5 amplification, 1800 V high voltage bias.

shape of the output pulse. Snubbing was done before the preamplifier and both reduced ringing and increased the pulse rise-time. The output of this BNC network was connected to an oscilloscope. The length of the BNC cable was varied until it was at the correct length for the reflected signal to cancel the anode signal ringing.

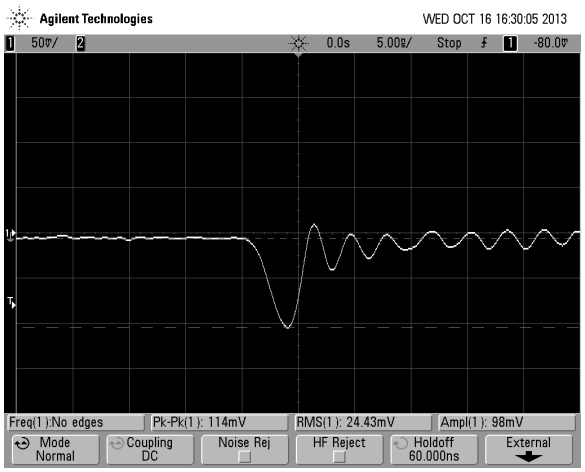

Figure 3.7: Waveform from C31034A, 5x Amp, Terminated Signal.

Once the PMT signal had been appropriately terminated, the discriminator height was determined. This process is called plateauing and used the SR400 Gated Photon Counter manufactured by Stanford Research Systems of Sunnyvale, California [157]. To find the discriminator voltage, the count rate of the PMT as a function of discriminator voltage was measured. The correct voltage was the one at which the voltage level "plateaued". As shown in figure 3.8, the optimal discriminator voltage for the C31034A PMT operating with a x5 amplification and a 1800 V bias was -0.018 V since this was the location where the plateau ended. For further study on PMTs, refer to reference [158].

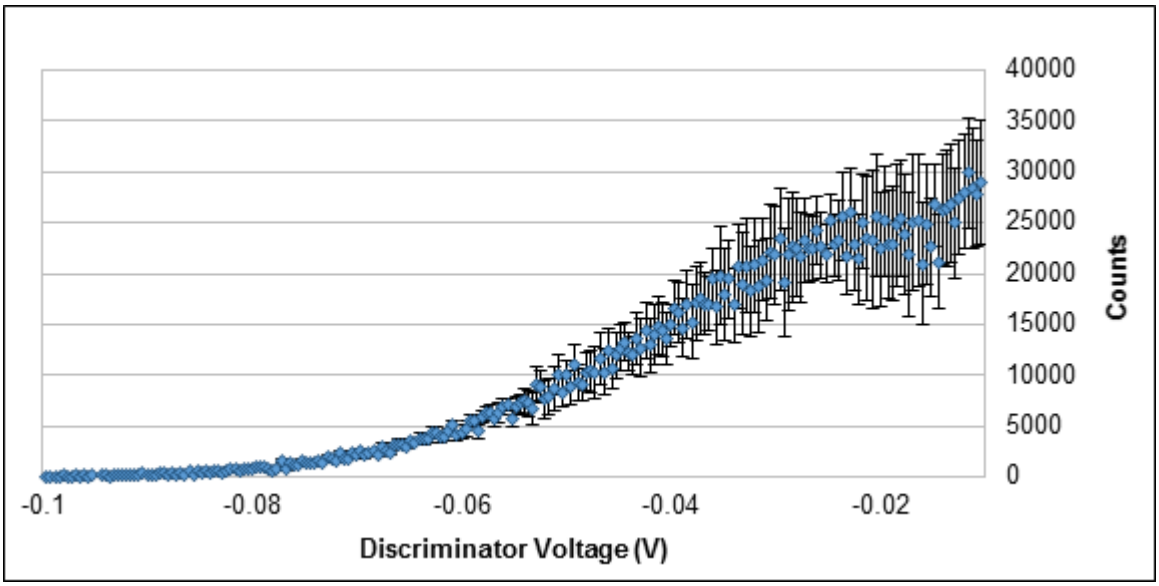

Figure 3.8: Plateauing of the C31034A PMT with 5x Amp and 1800 V bias.

3.1.2.3 Optical alignment techniques

The alignment of the experiment was one of the most crucial steps in ensuring an operational and accurate experiment. The two arms of the experiment (source & signal) needed to be precisely orthogonal to each other. Due to the nature of Rayleigh scattering and the orthogonality of the electric (ED) and magnetic (MD) dipoles, 90 degrees is the only angle at which the ED and MD are completely separable. Figures 3.9, 3.10, and 3.11 show three variations of experimental set-ups with labels on each of the components. Note the option for spectral analysis in figure 3.11.

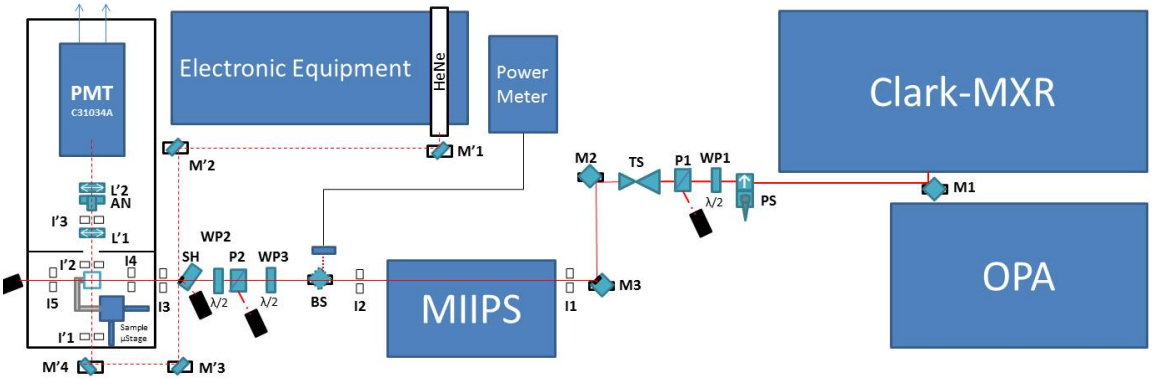

Figure 3.9: Schematic for magneto-electric scattering experiment. L = lens, I = iris, WP = waveplate, P = polarizer, SH = shutter, TS = telescope, PS = periscope, M = mirror, AN = analyzer, primes indicate alignment beam path.

The first part of the alignment was to align the source and signal arms. With every step of the alignment, the beam was made parallel to the holes on the table. This ensured that every beam path was orthogonal. For the rough alignment, a fabricated metal alignment block was used. This block had a alignment grid with 1/4" spacing along with a set of holes precisely drilled at a intersection point. This mount also had four holes on its base which could be placed over 1/4-20 set-screws secured into the table. The four holes enabled placement of the alignment holes either on a table hole line or between two sets of holes. This block was used repeatably throughout the alignment procedure to ensure a level and parallel beam, assuming that the table was flat and the holes were drilled correctly. Although not perfect, this alignment technique was sufficient for initial set-up.

After the initial set-up of the experiment, the overlap of the beam with the alignment irises was verified each day. This was done using a beam camera from Thorlabs. The most important irises were those immediately before and after the sample. The beam camera was placed behind the iris and the iris was closed down. If the iris closed down around the peak beam intensity shown on the beam camera, the beam was in the correct location. If

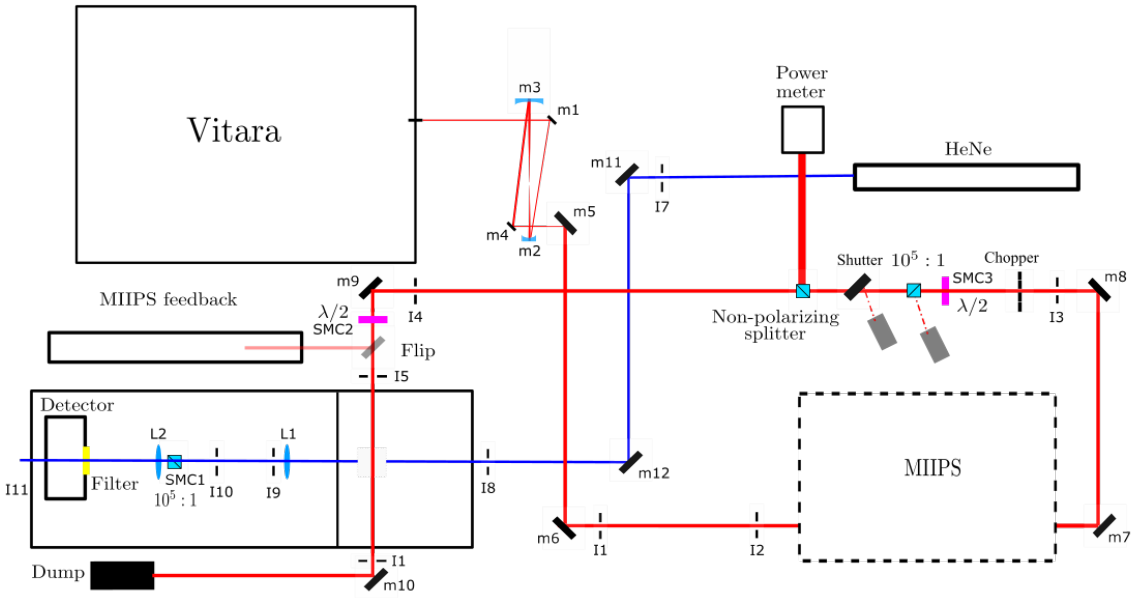

Figure 3.10: Schematic for magneto-electric scattering experiment. L = lens, I = iris, $\lambda/2$ = rotatable half-wave plate, 10^5:1 = polarizer, M = mirror, SMC = computer-controlled rotation stage, blue line indicates alignment path.

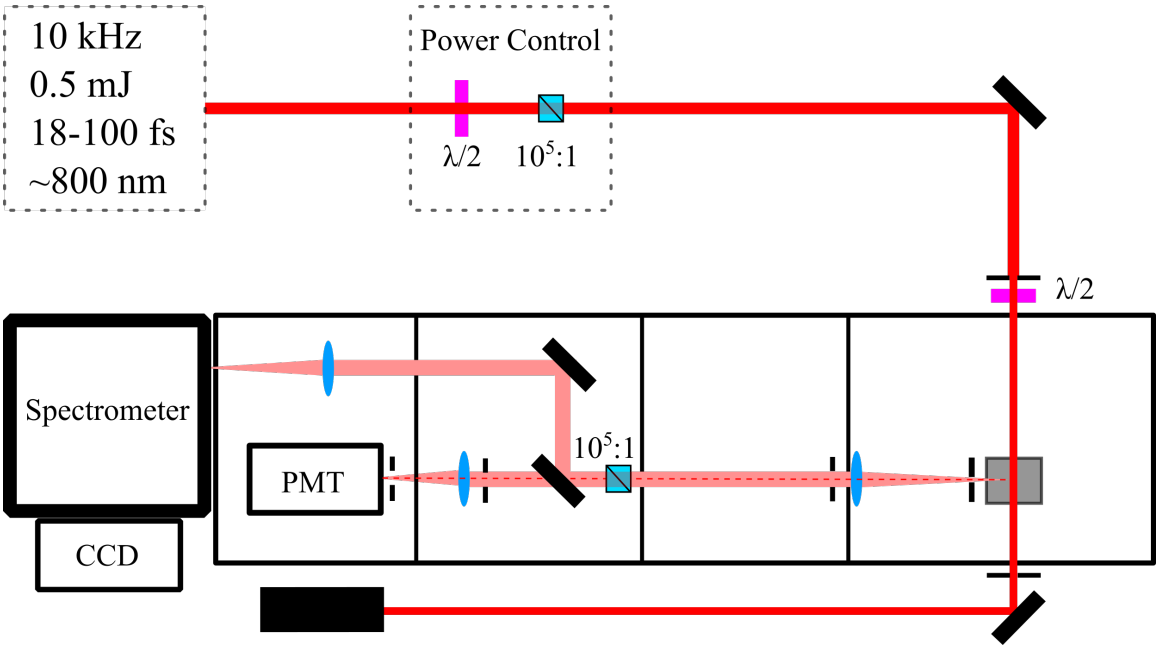

Figure 3.11: Schematic for magneto-electric scattering and spectrum experiment. $\lambda/2$ = rotatable half-wave plate, 10^5:1 = polarizer.

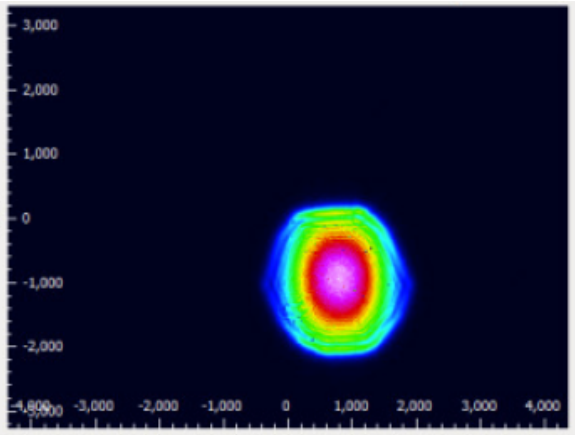

Figure 3.12: Example of beam profile during beam camera alignment.

the beam was not perfectly centered, the turning mirrors were adjusted. The beam camera alternated between the two iris locations until the beam went through both of them. An example of the beam is shown in figure 3.12.

The experiments also had the option of either compensating for dispersion to make time-bandwidth-limited pulses or adding additional linear chirp to lengthen pulses. Most experiments either used bandwidth-limited pulses or no compensation at all. For reference, MIIPS is a method used to measure the spectral phase of a femtosecond laser pulse. Instead of relying on interferometry like other methods (e.g. FROG, SPIDER), MIIPS takes advantage of the fact that second harmonic generation (SHG) involves the simultaneous sum of multiple frequencies [159, 160]. The phase between multiple paths to generate a particular SHG frequency determines if they add up constructively (if the phase is zero) or destructively (if the phase is pi).

The next crucial part of the alignment was that of the detector and sample. The detector (a FND-100 photodiode in this case) was first aligned by eye to make sure the scattering path (as indicated by the HeNe alignment beam) was centered on the detector. To verify the alignment, the HeNe alignment beam was attenuated and incident on the detector. Then, the detector was moved vertically and horizontally to find the optimal position. After using the HeNe, the same detector movement was repreated using a highly-scattering sample and the main laser beam. Figure 3.13 shows the results of these methods. It was found that both the HeNe and Vitara methods of alignment resulted in the same maximal signal position. The geometry of the two beams is evident in the horizontal positioning of the detector. Whereas the HeNe beam is a defined Gaussian laser beam positioned straight onto the detector, the Vitara beam is passing through a sample. The trapezoidal shape is due to the size of the limiting aperture of the collection system.

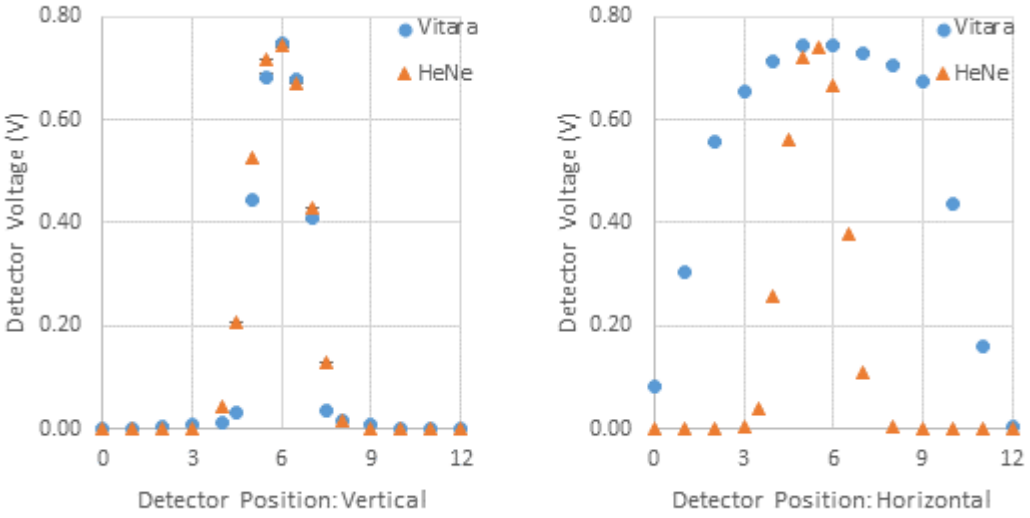

Figure 3.13: (l) Vertical and (r) Horizontal alignment of the detector comparing two alignment methods.

Additionally, the effects of different polarizations on the alignment were checked as shown in figure 3.14. This was important because the experiment relied on comparing vertically-polarized scattered light with horizontally-polarized light. In each case, a suspension of Coffeemate powdered non-dairy coffee creamer in distilled water was used as the scattering source. Note that the same overall pattern is seen as in figure 3.13. The maximum location of vertically-polarized and horizontally-polarized light overlapped for both changes in the vertical and horizontal positioning of the detector. The slight difference in shape is due to the different vertical scales in the figure for the different polarizations.

The next piece of alignment was to verify that the detection arm was unable to see any scattering from the wall of the cuvette (See figure 3.15). When running the experiment, the edge-wall scattering can contribute significantly to the H_h signal [161]. This is because the air:quartz:liquid interface can serve as a kind of mirror reflecting laser light towards the detector. In fact, if a mirror is placed at 45 degrees in the main beam, one will detect polarized dipole patterns of equal magnitude (See figure 3.16). Fortunately, this signal will depend linearly on the intensity of the beam and can be minimized by geometry. In figure 3.15, there is no limiting aperture in the detection system allowing for the edge-wall scattering to be seen. Since the V_v scattered light is stronger within the sample, the ratio of H_h to V_v scattered light can become arbitrarily large when looking at the sample edge. Therefore, *a limiting aperture is absolutely critical* in order to prevent edge-wall scattering from interfering with the detection of magneto-electric scattering.

Finally, after alignment of the main laser beam path, the detection optics and the detec-

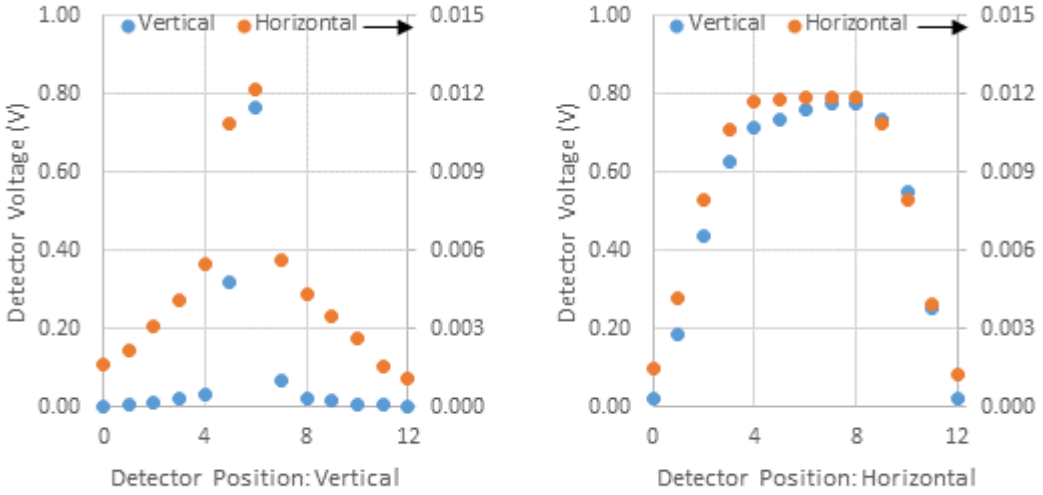

Figure 3.14: (l) Vertical and (r) Horizontal alignment of the detector comparing alignment using V_v and H_h scattered light.

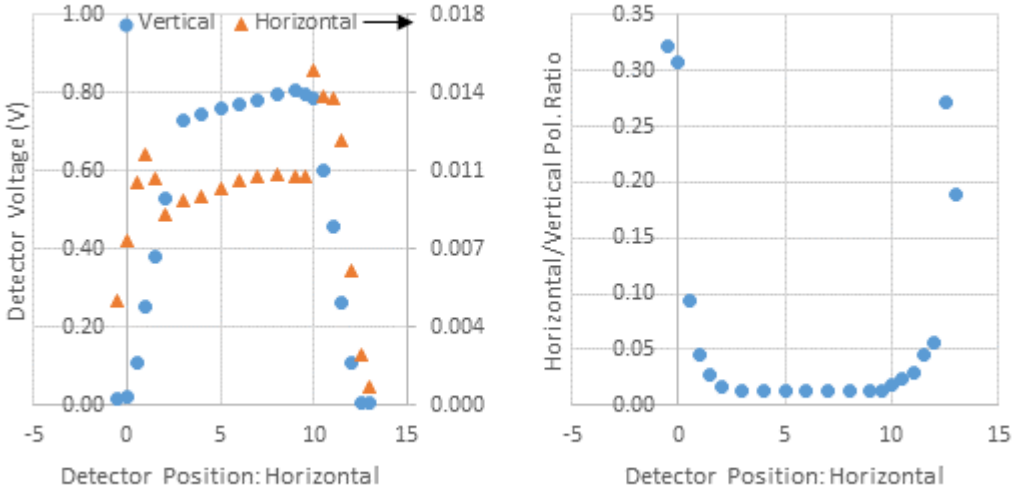

Figure 3.15: (l) Horizontal alignment of the detector comparing alignment using V_v and H_h scattered light without a limiting aperture. (r) Ratio of H_h to V_v scattered light.

tor position, the sample was placed on the sample holder stage and aligned. The stage had tip/tilt adjustments along with XYZ precision. The procedure followed was:

1. Place the sample on the sample stage.

2. Adjust the vertical height and horizontal position of the sample until the laser beam passes through the sample without clipping.

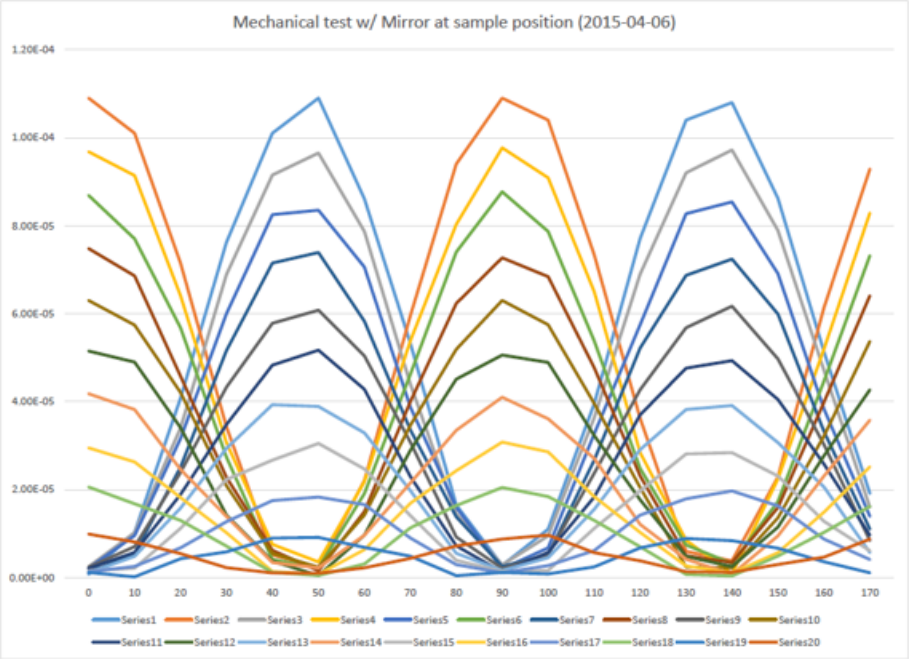

Figure 3.16: Cartesian plot of vertically- and horizontally-polarized light reflected off a 45 degree mirror through the detection optics.

3. Using the IR viewer, look at the back reflection of the source laser beam. Slightly adjust the sample until the back reflection is perfectly coincident with the source beam.

4. Examine the back reflection of the HeNe laser. Again, adjust the sample until the back reflection is perfectly coincident with the HeNe beam.

5. Check the first back reflection again. Continue adjusting until both back reflections are coincident with their source lasers.

3.1.3 Special considerations of a focused beam

Due to the limited energy per pulse compared to the other two laser sources, the Vitara laser beam had to be focused. Ideally, one wants the highest amount of intensity and the largest illumination area. These criteria are in direct opposition to each other. Fortunately, the effects of the illumination area can be minimized by controlling the size of the collection spot size. Assuming an incident beam waist (the $1/e^2$ beam full-width) of W_x = 1022 μm and W_y = 1636 μm as well as a pulse length ($FWHM_t$) of 15 fs, table 3.4 was calculated to compare possible focusing options. In considering collection spot size, the relevant values were the focused beam diameter, W_y, and the Rayleigh range, $Z_R(y)$.

Table 3.4: Comparison of focused beam size and intensity for varied focal lengths.

Lens	$W_x(\mu m)$	$W_y(\mu m)$	Int. $(\frac{W}{cm^2})$	$Z_R(x)$ (cm)	$Z_R(y)$ (cm)
200 mm	199	125	4.8E9	3.90	1.52
175 mm	174	109	6.3E9	3.00	1.17
150 mm	150	93	8.6E9	2.19	0.86
125 mm	124	78	1.2E10	1.52	0.59
100 mm	99	62	1.9E10	0.98	0.38
75 mm	75	47	3.5E10	0.55	0.21
50 mm	50	31	7.8E10	0.24	0.10

As mentioned in the previous section, it is important that the detector cannot see the edges of the cuvette in order to detect the accurate polarization and magnitude of the scattering. This can be achieved by placing an aperture between the sample and the first collection lens. Additionally, a limiting aperture can be placed further in the collection optics.

In the case of the focused beam, the limiting aperture was used to both prevent detection of edge-wall scattering as well as limit the imaging area to the size of the beam. Since the beam was focused into the sample, the optimal collection spot size was one that was smaller than the cross-section of the focused beam. The size of the collection spot size was primarily determined by the size of the limiting aperture and the magnification of the system. The ideal magnification of the system was as large as possible in order to loosen the tolerances on the positioning of the limiting aperture. However, an increase in the magnification can also increase the amount of polarization leakage. Table 3.5 shows this tradeoff. Based on the calculated values, an iris with a diameter of 5 mm and a initial focusing lens of f = 50 mm were chosen.

Table 3.5: Comparison of lenses for collection magnification, assuming f2 = 150 mm.

Lens, f1	Mag.	Iris dia. (mm)	Angle, θ	Solid angle, $d\Omega$	Pol. Leak (%)
150 mm	x1	10	0.033°	2.78E-4	0.050%
		5	0.017°	6.94E-5	0.010%
50 mm	x3	10	0.100°	2.50E-3	0.500%
		5	0.050°	6.25E-4	0.120%
		3	0.033°	2.25E-4	0.045%
25 mm	x6	10	0.200°	1.00E-2	2.020%
		5	0.100°	2.50E-3	0.500%
		3	0.060°	9.00E-4	0.180%
		1	0.020°	1.00E-4	0.020%

After comparing the tradeoff between the collection spot size and the percentage of possible polarization leakage, the arrangement of optics shown in figure 3.17 was decided upon. Figure 3.18 shows that this arrangement, where the use of a 75 μm pinhole yielded a collection spot size of $\sim$25 μm in diameter. In this arrangement, the collection spot size was limited by the pinhole as long as the pinhole was smaller than $\sim$3 mm.

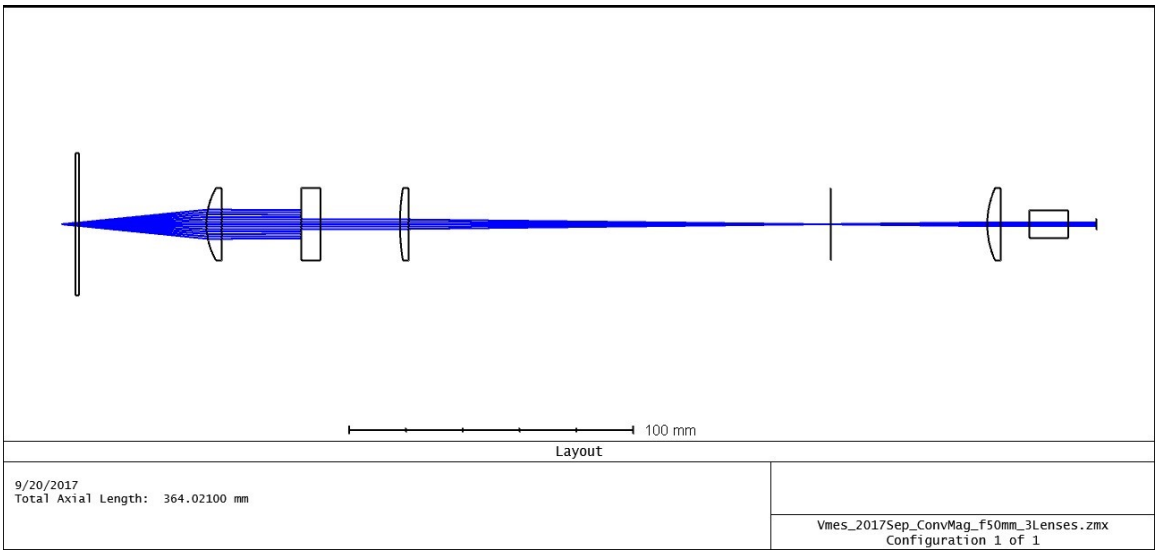

Figure 3.17: Zemax model of collection optics: f1 = 50 mm, f2 = 150 mm, f3 = 60 mm, iris diameter = 5mm, pinhole diameter = 75 μm.

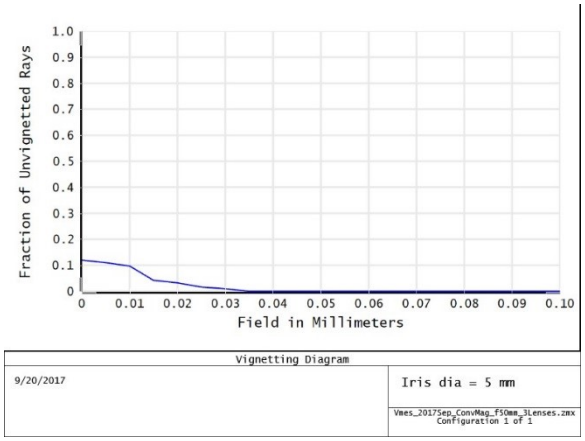

Figure 3.18: Zemax vignetting model of collection optics: f1 = 50 mm, f2 = 150 mm, f3 = 60 mm, iris diameter = 5mm, pinhole diameter = 75 μm.

3.1.4 Signal detection limits

In addition to the calibration described in section 3.1.2.3, the detection system limits were also verified. Figure 3.4 shows that the detection system was capable of detecting changes in the average intensity of the main laser beam.

To test the response to changes in peak power, Rhodamine 590 in methanol and glass of varied thicknesses were used. The 2-photon fluorescence of Rhodamine 590 depends on the square of the incident field intensity. Using a 1:1 collection system (f1 = f2 = 150 mm) and a beam focusing lens of 12.5 mm, the values in table 3.6 were obtained. Note that the values were adjusted to account for the different Fresnel reflection losses of each dispersing glass. Figure 3.19 shows this graphically as a function of both pulse length and average intensity. This calibration means that if M-E scattering depends on changes in peak power, it is possible to observe it if the signal is above the noise limits of the detection system.

Table 3.6: Verification of detection of changes in peak power using the 2-photon fluorescence signal from Rhodamine 590 dissolved in methanol.

Pulse length	V_v (mV)	V_h (mV)	H_h (mV)	H_v (mV)
~40 fs	307.6 (±2.9)	269.6 (±0.3)	255.0 (±0.4)	254.8 (±0.4)
~48 fs	281.3 (±0.2)	241.8 (±0.2)	230.3 (±0.3)	229.6 (±0.2)
~52 fs	272.9 (±0.5)	228.5 (±0.2)	217.5 (±0.3)	217.2 (±0.2)
~80 fs	182.5 (±7.7)	143.0 (±0.2)	136.5 (±0.2)	136.0 (±0.2)

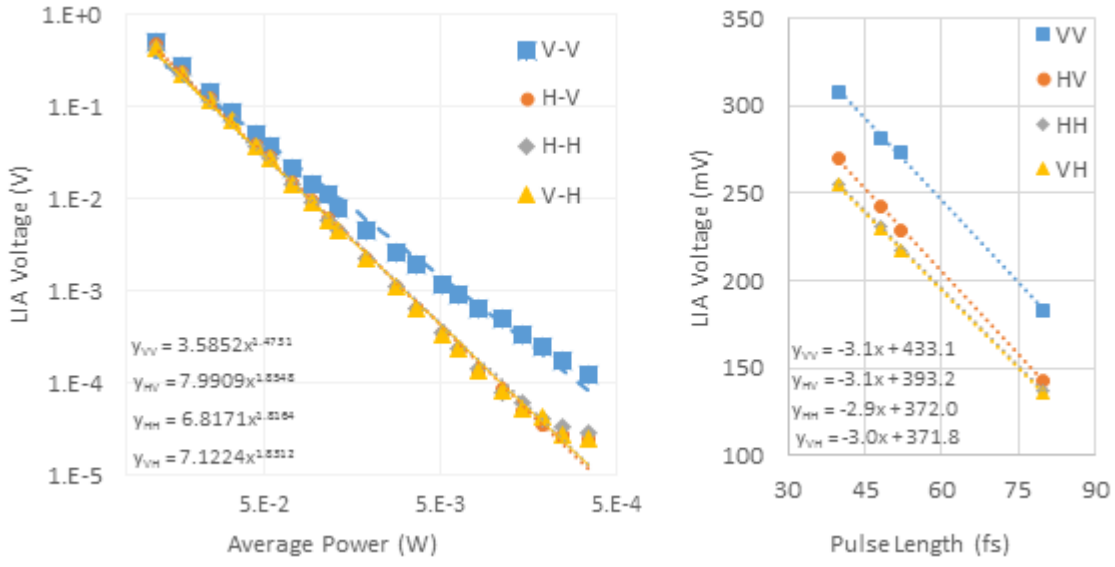

Figure 3.19: Verification of detection of changes in (l) average power and (r) peak power using the 2-photon fluorescence signal from Rhodamine 590 dissolved in methanol.

3.2 Data acquisition procedure and analysis

In each intensity-dependent magneto-electric scattering experiment, the data was collected using the programmatic procedure shown in figure 3.20. Note that there are three loops within the program as determined by the number of different polarizations and intensity points desired. For example, collecting data on one sample over one decade of intensity required 11 intensity loops, 2 dipole loops, and 36 input polarization loops resulting in near to 800 sets of data points. Due to this large number of data points, data collection consisted of a MATLAB program that controlled the input intensity, input polarization, and output polarization via computer-controlled rotation stages. The complete MATLAB program is included in appendix B.

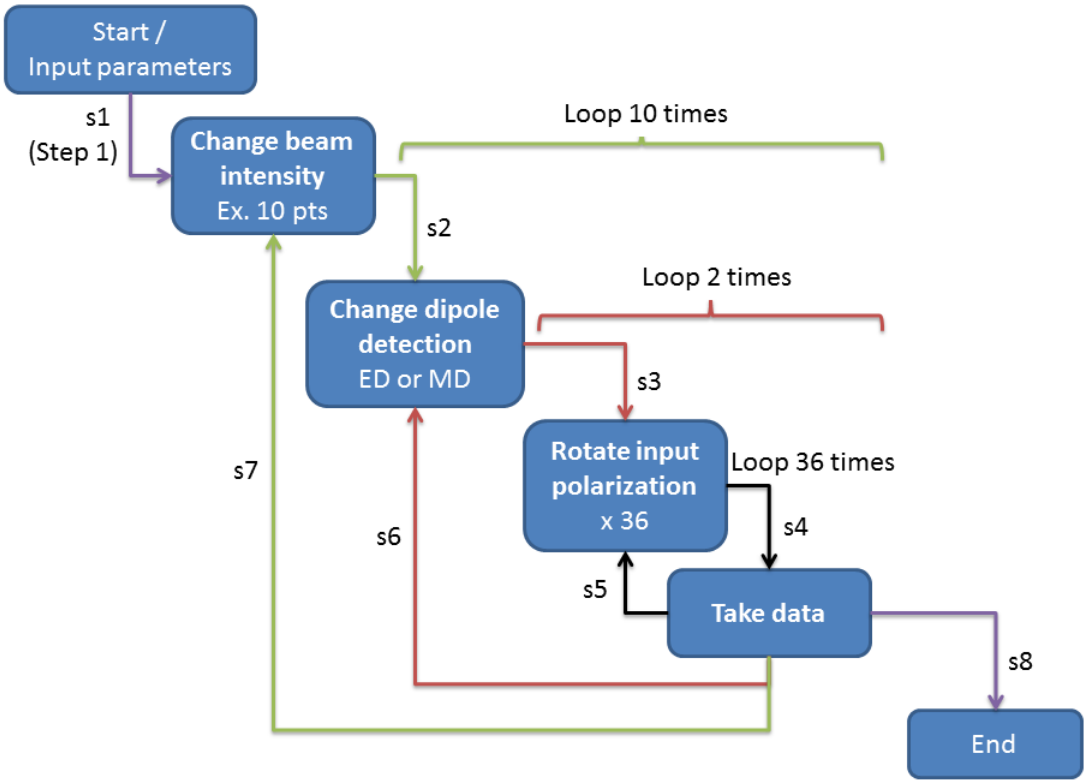

Figure 3.20: Flowchart depicting the steps used by the data collection computer program.

The data collection program wrote the data to a text file for easy analysis. The master data file was split into individual text files for each intensity and dipole point. For example, an experiment consisting of 11 intensity loops and 2 dipole loops (ED, MD) resulted in 22 individual files. Each file contained data for a complete set of input polarization states.

For analysis, the data was loaded into a MATLAB program. For each file, the raw data was extracted and plotted versus input polarization state / waveplate angle. Each set of data was fitted with a dipole pattern as shown in figure 3.21 [162].

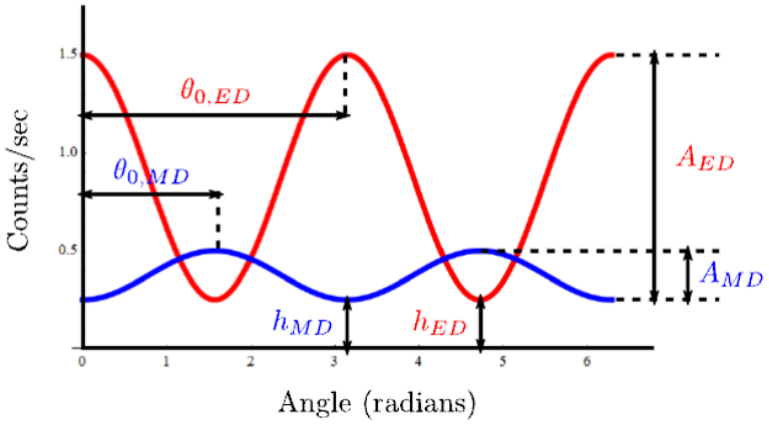

Figure 3.21: Schematic of dipole components for analysis.

The curves used to fit the data were standard cosine squared functions.

$$I_{ED} = A_{ED}\cos^2(\theta + \theta_{0,ED}) + h_{ED} \tag{3.7}$$

$$I_{MD} = A_{MD}\cos^2(\theta + \theta_{0,MD}) + h_{MD} \tag{3.8}$$

Each function had an amplitude, a vertical offset (waist) and a phase offset. In the next chapter, the amplitude and waist of the fitted data are referred to as the *polarized* and *unpolarized* dipole components, respectively. The MATLAB analysis program extracted the amplitude, maximum, and minimum for each data set, plotting versus intensity. By analyzing the dipole responses as a function of intensity, one can observe the nonlinear response of each material system.

Recalling the discussion in section 3.1, the maximum of the electric dipole signal ($A_{ED} + h_{ED}$) will be observed when the input polarization state and detected polarization state are vertical (V_v). The minimum of electric dipole signal (h_{ED}) will be observed when the input polarization state is horizontal and detected polarization state is vertical (V_h). Likewise, the magnetic dipole signal maximum ($A_{MD} + h_{MD}$) will be observed when the input polarization state and detected polarization state are horizontal (H_h) and the minimum (h_{MD}) when the input polarization state is vertical and detected polarization state is horizontal (H_v).

3.3 Sample selection and preparation

As in previous studies, the primary objective of sample selection was to provide a way to systematically vary important material parameters. As will be discussed in section 4.1.4, moment of inertia and rotation frequency, ω_ϕ, were hypothesized to be important. The first series examined was the tetrachloride series of CCl_4 (carbon tetrachloride), $SiCl_4$ (silicon tetrachloride), $SnCl_4$ (tin tetrachloride) and $GeCl_4$ (germanium tetrachloride) [136]. In this series, the rotation frequency decreased as the central atom was substituted.

$$CCl_4 \rightarrow SiCl_4 \rightarrow SnCl_4 \rightarrow GeCl_4$$

The second series examined was the orthosilicate series composed of $SiCl_4$ (silicon tetrachloride), $SiBr_4$ (silicon tetrabromide), $Si(OCH_3)_4$ (tetramethyl orthosilicate), $Si(OC_2H_5)_4$ (tetraethyl orthosilicate), and $Si(OC_2H_7)_4$ (tetrapropyl orthosilicate). In this series, the rotation frequency decreased as the peripheral atoms in the tetrahedral structure were changed.

$$SiCl_4 \rightarrow SiBr_4 \rightarrow Si(OC2H3)_4 \rightarrow Si(OC2H5)_4 \rightarrow Si(OC2H7)_4$$

Additional criteria for liquid sample selection were for experimental convenience rather than scientific inquiry. First, samples were selected that were non-polar and centrosymmetric. The centrosymmetry excluded all second-order all-electric nonlinear optical processes, while the non-polar nature prohibited electric-torque phenomena such as depolarized-light orientation scattering (see section 1.2.1.3). Second, ideal samples had a low number of impurities which limited the possibility of multiple scattering. Third, samples were chosen that did not have an optical resonance anywhere near the excitation wavelengths. This enabled the electric dipole response to be compared to the induced magnetic dipole response without having to account for absorption phenomena.

Solid samples were also investigated during this work. As with liquid samples, it was desirable to have samples with a low number of impurities (internal and surface) and either centrosymmetric or amorphous structure. For their availability and structure, Quartz and GGG (Gadolinium Gallium Garnet) were examined. Quartz has a tetrahedral structure where each silicon atom is linked to four oxygen atoms accounting for the chemical formula of SiO_2. GGG has a cubic crystal structure with the base unit of $Gd_3Ga_5O_{12}$ [163].

3.3.1 Procedure for cleaning cuvettes

In order to maintain the integrity of the experiments and prevent mixing of chemicals, great care was taken to completely clean the quartz sample cuvettes. The quartz sample cuvettes were 10 mm Flourometer cells from Starna Cells, Inc. Each cuvette held ∼3.5 mL of liquid. Cuvettes were filled with liquid samples for optical study. The necessary equipment needed to clean is shown below in table 3.7. The procedure varied depending on the sample

Table 3.7: Supplies needed to clean cuvettes.

Equipment	Source	Details	#
Fluorometer 10mm Quartz Cuvette	Starna Cells	23-Q-10	1
Cuvette Concentrated Detergent	Starna Cells	-	1
De-Ionized Water	-	-	1
Acetone	-	-	1
Isopropanol	-	-	1
Small Oven	-	-	1
Cuvette Storage Container	Fisher Scientific	Heat Resistant	1
Aluminum Foil	-	-	1
Waste Beaker	-	-	1
Misc. PPE	-	-	-

that was in the cuvette. Table 3.8 is an overview by solvent and material type taken from http://www.starnacells.com/d_tech/tech01.html. The majority of the samples that were used in this work were alcohol-based solutions and organic solvents. The procedure for cleaning organic solvents with alcohol and acidic solutions is as follows:

1. Gather the needed equipment listed in the table above.
2. Don protective equipment. Refer to specific SDS and glove compatibility charts.
3. Empty any samples remaining in the cuvette into a labeled waste container.
4. Rinse with DI water once to remove any traces of chemical sample.
5. Place one drop of detergent into the cell. The detergent is concentrated and one drop is really all that is needed.
6. Rinse repeatedly with DI water until no soap bubble remain. At least 12 rinses are often necessary.
7. Rinse cuvette with Acetone from the acetone squeeze bottle. Collect any excess and transfer to waster container.

8. Rinse cuvette with IPA from IPA squeeze bottle. Collect any excess and transfer to waster container.

9. Immediately transfer cuvettes to the heat-resistant cuvette holder. Wrap cuvette holder in aluminum foil and place in oven at 82 °C until no IPA remains on the cells. This is necessary to prevent drying marks on the cells.

10. Remove the cuvette holder from oven and place in a clean container for transport.

11. Store cells in a clean area until ready to be filled.

12. Remove gloves and wash hands.

Table 3.8: Suggested cleaning methods from Starna Cells, Inc.

Solvent	Material	Suggested Cleaning Methods
Aqueous	Protein, DNA, Biologics	Warm water with detergent, Dilute acid rinse, Copious water rinse
Aqueous	Salt sols.	Warm water Acid rinse, Copious water rinse
Aqueous	Basic sols.	Warm water with detergent, Dilute acid rinse, Copious water rinse
Organic	Oil based	Rinse with solvent, Warm water with detergent, Dilute acid rinse, Copious water rinse
Organic	Alcohol sols.	Rinse with solvent, Copious water rinse
Organic	Acidic sols.	Rinse with solvent, Copious water rinse
Organic	Basic sols.	Rinse with solvent, Dilute acid rinse, Copious water rinse
Fluorescence		Clean cells in Nitric Acid (5M) use a copious water rinse immediately before use

3.3.2 Preparation procedure: Liquids

All liquid samples were tested inside quartz Fluorometer cells. Each sample was filtered using 0.9 μm IC-Millex-LG PTFE filters from Millipore Corp. The preparation procedure is detailed below.

1. Gather the needed equipment.

2. Don protective equipment. Refer to specific SDS and glove compatibility charts. For example, carbon tetrachloride should be handled using Nitrile gloves.

3. If the sample comes in a large opentop bottle,

(a) Attach two Millipore filters to the plastic syringe.

(b) Move large bottle of chemical sample into the fume hood and lower sash to working height to protect user.

(c) Use large volume pipette to move chemical sample into filtering syringe. Move only what is required. Approx. 4 mL.

4. If the sample comes in a bottle with the protective top,

   (a) Attach hypodermic needle to plastic syringe.

   (b) Carefully withdraw approximately 3 mL from the container.

   (c) Turn syringe upside down, remove needle, and attach two Millipore filters to the end of the plastic syringe.

5. Push slowly on the plunger of the plastic filtering syringe to gently force the chemical sample through the Millipore filters into the quartz cuvette. Do NOT use excessive force! It can damage the filters causing them to lose their filtering properties, put fibers into sample, and may spray chemicals in hood. Slow pressure reduces bubble formation.

6. Place labeled stopper on cuvette and allow bubbles to settle. This can take hours.

7. Remove plunger, filters from filtering syringe, and allow MINIMAL chemical sample to evaporate. Pour any excessive chemical sample and filters into waste bucket in the fume hood.

8. Return the large bottle of chemical sample to the chemical cabinet.

9. Remove gloves and wash hands.

3.4 Simulation methods

The dipole moments described in subsection 2.1.2 were simulated by applying finite time steps in a MATLAB program that integrated equation 2.16. See appendix C for the complete MATLAB code. For the *n*th iteration, the electron position $\overline{\xi}(t_{n+1})$ was calculated from $\overline{\xi}(t_n)$ and inserted into equation 2.17 to update torque components. Angular velocities from equations 2.10-2.12 were then similarly used to obtain the change in the "tether" position, $\Delta\overline{r}_A(t_n)$, from equation 2.18. This yielded a new value of $\overline{r}_A$, given by $\overline{r}_A(t_{n+1}) = \overline{r}_A(t_n) + \Delta\overline{r}_A(t_n)$, to be inserted into equation 2.16 to iterate the procedure.

3.4.1 Numerical solving techniques

Specifically, the Ordinary Differential Equation (ODE) solver function built into MATLAB was used to solve the system of first-order ODEs. MATLAB was chosen as the solving program specifically because of its robust library of ODE solvers and ease of analyzing the results. Initial simulations were run in Mathematica but that course was abandoned due to its limited capability to iterate through a set of values. For MATLAB, the equations had to be written explicitly as first-order ODEs by using generic substitutions. These equations were the following:

$$\overline{\xi}(t) = [x_1, y_1, z_1] \tag{3.9}$$

$$\overline{r}_A(t) = [x_2, y_2, z_2] \tag{3.10}$$

$$\frac{dx_1(t)}{dt} = xd(t) \tag{3.11}$$

$$\frac{dy_1(t)}{dt} = yd(t) \tag{3.12}$$

$$\frac{dz_1(t)}{dt} = zd(t) \tag{3.13}$$

$$\frac{dx_2(t)}{dt} = z_2(t)\,\Omega_y(t) - y_2(t)\,\Omega_z(t) \tag{3.14}$$

$$\frac{dy_2(t)}{dt} = -z_2(t)\,\Omega_x(t) + x_2(t)\,\Omega_z(t) \tag{3.15}$$

$$\frac{dz_2(t)}{dt} = y_2(t)\,\Omega_x(t) - x_2(t)\,\Omega_y(t) \tag{3.16}$$

$$\frac{d\Omega_x(t)}{dt} = \frac{m}{I_{//}}\omega_0^2\left[y_2(t)\,z_1(t) - y_1(t)\,z_2(t)\right] \tag{3.17}$$

$$\frac{d\Omega_y(t)}{dt} = \frac{m}{I_\perp}\omega_0^2\left[-x_2(t)\,z_1(t) + x_1(t)\,z_2(t)\right] \tag{3.18}$$

$$\frac{d\Omega_z(t)}{dt} = \frac{m}{I_\perp}\omega_0^2\left[x_2(t)\,y_1(t) - x_1(t)\,y_2(t)\right] \tag{3.19}$$

$$\frac{d[xd(t)]}{dt} = \frac{e}{m}E(t) - \omega_0^2\left[x_1(t) - x_2(t)\right] - \gamma xd(t) - \frac{ek_z}{mc}E(t)\,zd(t) \tag{3.20}$$

$$\frac{d[yd(t)]}{dt} = -\omega_0^2\left[y_1(t) - y_2(t)\right] - \gamma yd(t) \tag{3.21}$$

$$\frac{d[zd(t)]}{dt} = -\omega_0^2\left[z_1(t) - z_2(t)\right] - \gamma zd(t) + \frac{ek_z}{mc}E(t)\,xd(t) \tag{3.22}$$

MATLAB has eight basic solvers available [164]. The solvers vary based on their accuracy and ability to handle *stiff* problems, or problems that are difficult to solve due to a difference in scaling somewhere in the problem. ode23 was chosen because of the moderately stiff nature of the problem. The numerical accuracy of ode23 is determined by the error tolerances of the ODE. If the tolerance is too low, rounding errors will accumulate in the solver and lead to an erroneous solution. In this case, the absolute error was set to 1e-22 and the relative error to 1e-20. These values were found to be small enough to minimize the errors in the solution, but large enough as to allow for efficient solving.

3.4.2 Dimensionless equations

Dimensionless equations in numerical simulations allow numbers that have a high probability of causing errors in the ODE solution, namely numbers that are either very large or very small, to be avoided. Additionally, they allow greater understanding of the system by relating it to "intrinsic" or "natural" scales rather than arbitrary ones such as meters or seconds. The choice of scaling values is important because it also will affect how the system responds.

To start, values for the time, space, charge, and mass scales were chosen from which to normalize the system [165]. For this case, the scale values were

Time scale:	$t_0 = 1/\omega_0$	(ω_0 = Oscillator resonance frequency),
Space scale:	$r_0 = \sqrt{\hbar/(\omega_0 \times m_e)}$	($\hbar$ = Reduced Plank constant),
Charge scale:	$e_0 = q_0$	(q_0 = Fundamental charge of an electron), and
Mass scale:	$m_0 = m_e$	(m_e = Mass of an electron).

This implied typical values for

$E_0 = m_e r_0/t_0^2 q_0$ (electric field),

$v_0 = r_0/t_0$ (velocity), and

$I_0 = m_e r_0 r_0$ (moment of inertia).

The substitutions for the fundamental equations were then the following:

$$t = \tilde{t}/\omega_0 \tag{3.23}$$

$$x = \tilde{x} r_0 \tag{3.24}$$

$$e = \tilde{e} q_0 \tag{3.25}$$

$$m = \tilde{m} m_e \tag{3.26}$$

$$E = \tilde{E} m_e r_0 / t_0^2 q_0 \tag{3.27}$$

$$\frac{dx}{dt} = \frac{d\tilde{x}}{dt}\frac{r_0}{t_0} \tag{3.28}$$

$$I = \tilde{I} m_e r_0 r_0 \tag{3.29}$$

$$\omega = \tilde{\omega}/t_0 \tag{3.30}$$

$$\gamma = \tilde{\gamma}/t_0 \tag{3.31}$$

$$\Omega = \tilde{\Omega}/t_0 \tag{3.32}$$

$$\frac{d^2x}{dt^2} = \frac{d^2\tilde{x}}{dt^2}\frac{r_0}{t_0^2} \tag{3.33}$$

$$c = \tilde{c} r_0/t_0 \tag{3.34}$$

These were substituted into the fundamental equations (equations 3.11 to 3.22). For example, equation 3.14 then transformed as $\frac{dx_2(t)}{dt} = z_2(t)\,\Omega_y(t) - y_2(t)\,\Omega_z(t) \Rightarrow \frac{d\tilde{x}_2(t)}{dt}\frac{r_0}{t_0} = \frac{r_0}{t_0}\left[\tilde{z}_2(t)\,\tilde{\Omega}_y(t) - \tilde{y}_2(t)\,\tilde{\Omega}_z(t)\right] \Rightarrow \frac{d\tilde{x}_2(t)}{dt} = \tilde{z}_2(t)\,\tilde{\Omega}_y(t) - \tilde{y}_2(t)\,\tilde{\Omega}_z(t)$. Doing a similar substitution for all of the equations resulted in a final set of dimensionless equations that were ready to be analyzed using MATLAB.

$$\frac{d\tilde{x}_1(t)}{dt} = \widetilde{xd}(t) \tag{3.35}$$

$$\frac{d\tilde{y}_1(t)}{dt} = \widetilde{yd}(t) \tag{3.36}$$

$$\frac{d\tilde{z}_1(t)}{dt} = \widetilde{zd}(t) \tag{3.37}$$

$$\frac{d\tilde{x}_2(t)}{dt} = \tilde{z}_2(t)\,\tilde{\Omega}_y(t) - \tilde{y}_2(t)\,\tilde{\Omega}_z(t) \tag{3.38}$$

$$\frac{d\tilde{y}_2(t)}{dt} = -\tilde{z}_2(t)\,\tilde{\Omega}_x(t) + \tilde{x}_2(t)\,\tilde{\Omega}_z(t) \tag{3.39}$$

$$\frac{d\tilde{z}_2(t)}{dt} = \tilde{y}_2(t)\,\tilde{\Omega}_x(t) - \tilde{x}_2(t)\,\tilde{\Omega}_y(t) \tag{3.40}$$

$$\frac{d\tilde{\Omega}_x(t)}{dt} = \frac{\tilde{m}}{\tilde{I}_{//}}\tilde{\omega}_0^2\left[\tilde{y}_2(t)\,\tilde{z}_1(t) - \tilde{y}_1(t)\,\tilde{z}_2(t)\right] \tag{3.41}$$

$$\frac{d\tilde{\Omega}_y(t)}{dt} = \frac{\tilde{m}}{\tilde{I}_{\perp}}\tilde{\omega}_0^2\left[-\tilde{x}_2(t)\,\tilde{z}_1(t) + \tilde{x}_1(t)\,\tilde{z}_2(t)\right] \tag{3.42}$$

$$\frac{d\tilde{\Omega}_z(t)}{dt} = \frac{\tilde{m}}{\tilde{I}_{\perp}}\tilde{\omega}_0^2\left[\tilde{x}_2(t)\,\tilde{y}_1(t) - \tilde{x}_1(t)\,\tilde{y}_2(t)\right] \tag{3.43}$$

$$\frac{d[\tilde{xd}(t)]}{dt} = \frac{\tilde{e}}{\tilde{m}}\tilde{E}(t) - \tilde{\omega}_0^2\left[\tilde{x}_1(t) - \tilde{x}_2(t)\right] - \tilde{\gamma}\tilde{xd}(t) - \frac{\tilde{e}\tilde{k}_z}{\tilde{m}\tilde{c}}\tilde{E}(t)\,\tilde{zd}(t) \tag{3.44}$$

$$\frac{d[\tilde{yd}(t)]}{dt} = -\tilde{\omega}_0^2\left[\tilde{y}_1(t) - \tilde{y}_2(t)\right] - \tilde{\gamma}\tilde{yd}(t) \tag{3.45}$$

$$\frac{d[\tilde{zd}(t)]}{dt} = -\tilde{\omega}_0^2\left[\tilde{z}_1(t) - \tilde{z}_2(t)\right] - \tilde{\gamma}\tilde{zd}(t) + \frac{\tilde{e}\tilde{k}_z}{\tilde{m}\tilde{c}}\tilde{E}(t)\,\tilde{xd}(t) \tag{3.46}$$

3.4.3 Physical meaning of initial conditions

The initial conditions had a dramatic effect on the response of the system. In most cases, the initial conditions were defined as $I_{//} = \hbar/\omega_0$, $I_{\perp} = \hbar/\omega_{\phi}$, $\overline{\xi}(t) = [0,0,0]$, and $\overline{r}_A(t) = [0, y_2, 0]$, where ω_0 and ω_{ϕ} were the optical driving and molecular rotation frequencies, respectively. Refer to table 3.9 for comparison to dimensionless values.

Table 3.9: Constants of the Lorentz Oscillator Model equations for (top) real-scale values in their common units and (bottom) dimensionless values.

ω_0	ω	γ	e	m	$I_{//}$	$I_{\perp}$	E_x
$2.6e15$	$2.34e15$	$0.26e15$	$1.6e$-19	$9.11e$-31	$6.47e$-51	$6.47e$-48	$1e9$
1	0.9	0.1	1	1	1	1000	0.31

3.4.3.1 Reduction to the atomic Lorentz Oscillator Model

The enhancement achieved by extending the model into the molecular domain only could occur if certain initial conditions were selected. In this section, two cases for when the molecular Lorentz oscillator model (LOM) reduces to the atomic LOM in behavior are described. The cases are when $I_{//} = I_{\perp} = \infty$ and $\overline{\xi}(t) = \overline{r}_A(t) = [0,0,0]$. In each of these cases, the enhancement was removed due to the suppression of the effects of torque.

When $I_{//} = I_{\perp} = \infty$, the equations for the angular velocity of the electron are reduced to zero,

$$\frac{d\Omega_x(t)}{dt} = \frac{m}{\infty}\omega_0^2 \left[y_2(t) z_1(t) - y_1(t) z_2(t)\right] \Rightarrow \frac{d\Omega_x(t)}{dt} = 0. \tag{3.47}$$

This means that the applied electromagnetic wave is unable to facilitate the transfer of internal angular momentum to external angular momentum. Essentially, the infinitely large moment of inertia prevents the system from undergoing any rotation and no enhancement is observed.

When $\overline{\xi}(t) = \overline{r}_A(t) = [0,0,0]$, the applied electromagnetic wave is unable to begin motion in the y- or z- directions. There is no initial lever for the wave to torque upon. Similarly to the previous case, the angular velocity is zero around all three axis. Around the x-axis this is,

$$\frac{d\Omega_x(t)}{dt} = \frac{m}{I_{//}}\omega_0^2 \left[(0) z_1(t) - y_1(t)(0)\right] \Rightarrow \frac{d\Omega_x(t)}{dt} = 0, \tag{3.48}$$

and is similarly zero around the y- and z- axes. A non-zero angular velocity must be created for any enhancement to occur.

3.4.3.2 Non-zero equilibrium point

For a non-zero initial position of the point of equilibrium, r_A, enhancement to the second-order magnetization and polarization can be observed. The magnitude of the enhancement increases with the distance from the origin until it reaches a critical threshold. This threshold is a result from the relationship between angular velocity components in the system. Assuming that $\overline{r}_A(t) = [0, y_2, 0]$, the system is stable if Ω_x is larger than Ω_y. When Ω_x becomes smaller than Ω_y, the point of equilibrium moves from oscillating in the y-z plane to oscillating in the x-y plane, signifying an unstable rotation of the homonuclear diatomic molecule. If the rotation frequency, ω_ϕ, is kept constant, one finds that $\Omega_x \propto 1/y_2$ and $\Omega_y \propto y_2$. With this in mind, most simulations took the position of the equilibrium to be at the largest distance as dictated by the system molecular parameters. One example of this behavior is shown in table 3.10, where the simulation values are $\omega_0 = 1, \omega = 0.9, \gamma = 0.1, c = 1, e = 1, I_{\perp} = 10^{-5}, I_{\perp}/I_{//} = 1000, E = 0.0002$, and $\xi = [0,0,0]$, unless otherwise noted.

3.4.3.3 Comparisons of molecular properties

When comparing simulations that use different molecular properties, such as ω_ϕ, it was necessary to scale the time and magnitudes accordingly. One example, is that the maximal

Table 3.10: Dependence of dipole moments on initial position of equilibrium point.

$r_A(y)$	ED	MD	MD/ED
0	1.75E-29	5.21E-37	2.98E-8
1E-7	1.75E-29	5.21E-37	2.98E-8
1E-6	1.75E-29	8.04E-36	4.59E-7
1E-5	1.75E-29	7.92E-35	4.52E-6
1E-4	1.75E-29	7.85E-34	4.49E-5

stable location of the equilibrium point changes with the square of the rotation frequency. If the rotation frequency, ω_ϕ, is decreased by a factor 100, the equilibrium point ought to increase by a factor of 10. This is due to the moment of inertia relationship where $I_\perp = \hbar/\omega_\phi = mr^2$. The normalizing distance is $r_A = 2c/\omega$, where ω is the driving frequency of the applied electric field.

For measurements of the steady-state value of the dipole moments, a snapshot time was chosen. This is the time at which the magnetization reaches an equilibrium in its evolution and is defined as $\tau_{ss} = 1/\omega_\phi$. When the rotation frequency is decreased, the snapshot time must increase by the same amount in order to capture the same scale of system dynamics.

Additionally, for the classical model, the conversion between photon number and electric field strength in Volts/meter is taken as

$$n = \frac{V}{\hbar\omega c} I = \frac{V\epsilon_0}{2\hbar\omega}|E|^2, \tag{3.49}$$

where the volume in question was arbitrarily taken to be V = 5×10^{-18} m^3.

CHAPTER 4

Results

This chapter covers the main experimental and theoretical results relevant to determining the dependence of magneto-electric scattering on material composition. The first section covers the experiments whose methods are described in section 3.1. Liquid and solid samples were examined and found to exhibit large radiant optical magnetization. The magnitudes of the magnetization are compared with theoretical predictions in subsection 4.1.4. The materials with the largest magnetization are those with a low rotation frequency. Lastly, the spectrum of the magneto-electrically scattered light was examined and it was determined that the MD (H_h) spectrum contains a red-shifted spectral feature that is dependent on the rotation frequency of the molecule. This supports the quantum theory described earlier in section 2.2.

Results from the torque-enhanced classical Lorentz oscillator model are presented in the second section. Refer to section 2.1 for discussion of the origin of the model and section 3.4 for the background on the MATLAB simulation. First, comments on limits to the symmetry of the electron motion are presented. It was found that at high applied field strengths, the symmetry of the electron displacement is reduced. Second, the dependence of the dipole moments on certain input parameters is explored. It was found that the magnitude of the second order electric dipole moment and the total magnetic moment were increased by increasing the ratio between the moment of inertias in the diatomic molecular system. Additionally, if the system was driven at too high of an applied electric field strength, a pulsing in the magnetization and DC polarization arises. Lastly, the results of the classical model were compared with those of the quantum theory and it was found that the two models are in good agreement.

4.1 Experimental results

The data presented in this section are from the three laser systems described in table 3.2. When a result is presented, the specific experimental parameters used to obtain that data are described. The intensity dependent experiments were primarily obtained using the Clark-MXR CPA-2001 system. All of the spectroscopy experiments were done using the Amplitude Aurora system. All experiments relied on a 90 degree scattering geometry and polarization analysis to distinguish between electric and magnetic dipole radiation.

4.1.1 Magneto-electric scattering in liquids

Although many different materials were examined during the time frame of this thesis, only a subset of the results is presented. Other materials are omitted either for clarity or because they are presented in depth in other places such as reference [136].

4.1.1.1 Tetrachlorides

Since the initial magneto-electric scattering experiments, carbon tetrachloride has served as the model system. Not only does its isotropic structure prohibit second-order all-electric nonlinear effects, but it is relatively easy to work with experimentally. It is easy to obtain and can be filtered for impurities. It is also optically transparent. Refer to the introduction for a description of the first experiments using CCl_4.

Here, a comparison of unpolarized ED (V_h) scattering for the tetrachloride series is presented. The tetrachloride series was of interest because it allowed for probing of the effect that the center atom has on the magnetization. The data was obtained using the Clark-MXR CPA-2001 system. The raw data was normalized to counts per second and plotted logarithmically versus input intensity in figure 4.1. The solid curves are quadratic + linear fits to the data. The fits are for CCl_4, y=4.71e-17*x^2+3.28e-8*x; for $SiCl_4$, y=9.00e-15*x^2+4.57e-7*x; for $GeCl_4$, y=4.76e-16*x^2+5.16e-8*x; and for $SnCl_4$, y=1.01e-16*x^2+6.20e-8*x. The figure is broken into three scattering regimes. The blue represents detector noise. Data points in this regime have a signal-to-noise ratio less than one and should be disregarded. The red regime represents leakage of light with orthogonal polarization into the signal channel due to the size of the collection solid angle. The final regime (white) shows quadratic fits to the data. This regime is the area where magneto-electric scattering can be detected. Analysis of the trend in scattering intensities is included in section 4.1.4 as a discussion of the material parameters involved in magnetization.

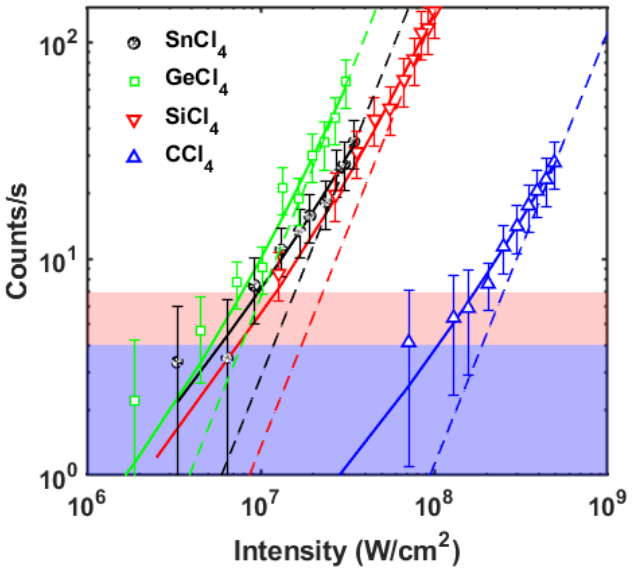

Figure 4.1: Unpolarized ED (V_h) scattering for CCl_4, $SiCl_4$, $GeCl_4$, and $SnCl_4$. Solid curves are quadratic fits to the data, with the dashed lines showing only the I^2 component.

4.1.1.2 Orthosilicates

Orthosilicates are a class of materials where a central Silicon atom is connected to four Oxygen atoms in a tetrahedral structure. Three orthosilicate compounds were examined in the experiments: Tetramethyl Orthosilicate (TMOS), Tetraethyl Orthosilicate (TEOS), and Tetrapropyl Orthosilicate (TPOS). Figure 4.2 shows the molecular structure of these three materials.

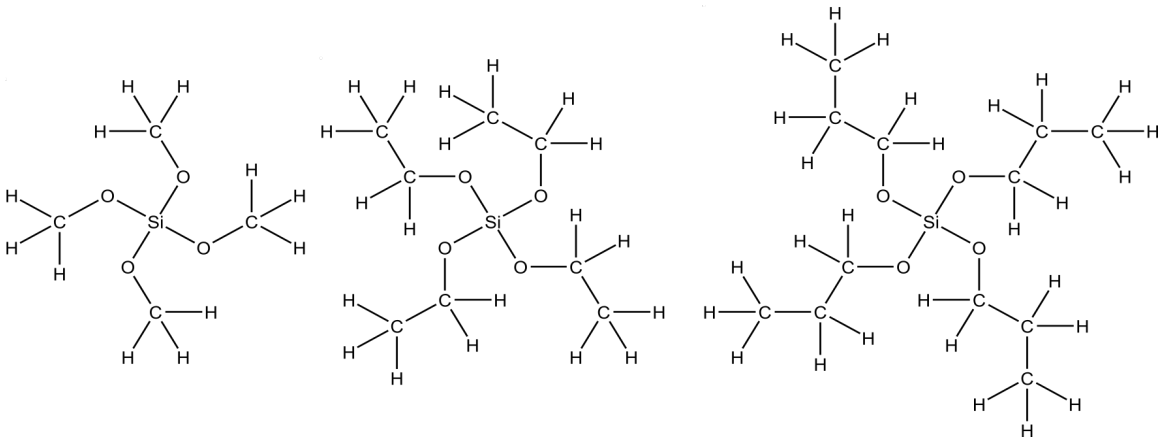

Figure 4.2: Molecular structure of TMOS (l), TEOS (c), and TPOS (r).

The orthosilicate series was tested using the Coherent Vitara-HP system. In this case, the beam was unfocused resulting in the lower intensities. Figure 4.3 shows the total MD response (H_h) of the three orthosilicates as compared to carbon tetrachloride. TMOS shows a larger MD response while TEOS and TPOS show a smaller one as compared to CCl_4. Error bars indicate a ten percent experimental uncertainty.

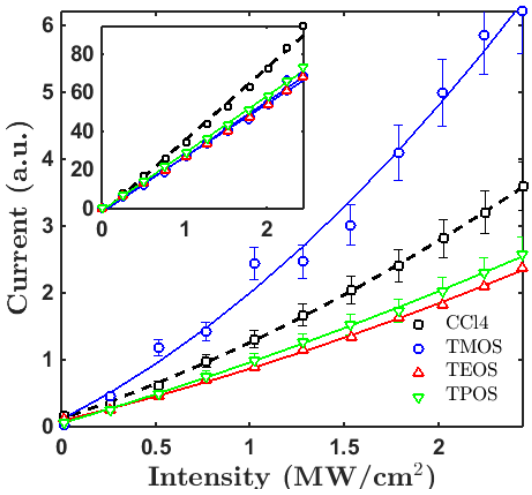

Figure 4.3: Total magnetic dipole scattering of CCl_4, TMOS, TEOS, and TPOS. Inset shows electric dipole scattering for reference.

4.1.2 Magneto-electric scattering in solids

Seeing the dependence on rotation frequency, solids are a natural experimental extension of liquids. Whereas rotation frequency in liquids can be thought of as the rate at which a molecule tumbles around, solids are fixed in place. Instead, rotation frequency in solids can be thought of as a libration frequency, or rather the rate at which a molecular unit of a solid wiggles back and forth. Presented in this section are the polarized and unpolarized magneto-electric scattering intensities from the isotropic solids, Gadolinium Gallium Garnet (GGG) and Quartz. Discussion of the significance of these results is reserved for Chapter 5.

4.1.2.1 Gadolinium Gallium Garnet

Gadolinium Gallium Garnet (GGG, $Gd_3Ga_5O_{12}$) is a synthetic garnet crystal commonly used in optics. It is a body-centered cubic crystal with space group $O_h^{10} = Ia\bar{3}d$ that includes inversion symmetry [163]. It is non-magnetic (in the conventional sense) and

does not support second-order, all-electric nonlinearities. Figure 4.4 shows a strong cross-polarized radiation pattern with a quadratic intensity dependence for the unpolarized ED (V_h) and MD (H_v) components. The ratio of unpolarized MD and ED scattering intensities is less than unity ($I_{MD}/I_{ED} \sim 0.9$). At higher intensity (2×10^{10} W/cm^2), the ratio of polarized intensity is approximately unity.

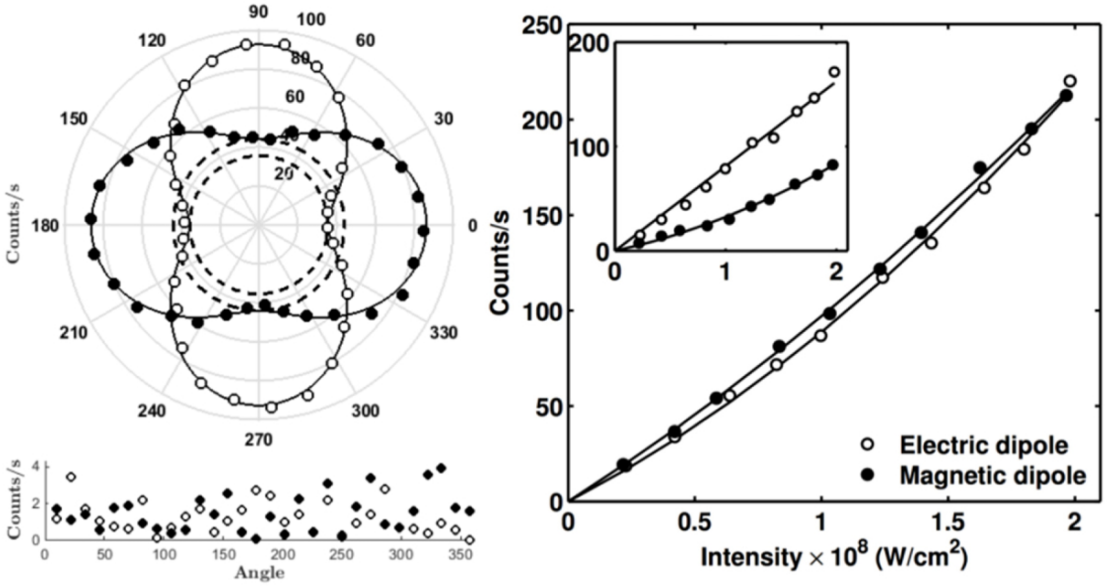

Figure 4.4: (a) Polar plot of raw data on co-polarized (open circles) and cross-polarized (filled circles) radiation patterns in GGG at I=1.4×10^7 W/cm^2 obtained at a repetition rate of 1 kHz. Dashed circles anticipate fits to the unpolarized background signal intensities. Residuals from the best fit of a circle plus a squared cosine curve to the raw data are shown below the polar plot. (b) Comparative plots in crystalline GGG of unpolarized ED (open circles) and MD (filled circles) scattering. Solid curves are quadratic fits to the data. Inset: corresponding data for polarized scattering components on the same scale. Reprinted with permission from reference [130].

4.1.2.2 Quartz

Quartz is the crystalline form of SiO_2, where the molecular unit of SiO_2 forms a SiO_4 silicon-oxygen tetrahedra. This sample was an Ultraviolet (UV) grade fused silica with a very low metallic impurity content and optical range of 170 to 2700 nm. Quartz was tested using the Coherent Vitara-HP system and a tightly focused beam to give an input intensity of $\sim2.2\times10^{10}$ W/cm^2. A polar plot of the raw data is shown in figure 4.5 and results versus input intensity are shown in figure 4.6. Note that the ratio of polarized intensities has reached the upper limit of unity ($I_{MD}/I_{ED} = 1$).

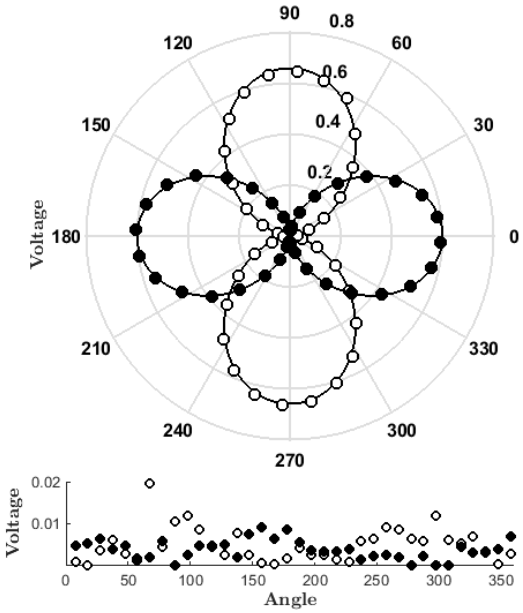

Figure 4.5: Polar plots of the radiation patterns for polarized ED and MD scattering in fused quartz at an input intensity of $\sim 2.2 \times 10^{10}$ W/cm^2 obtained at a repetition rate of 80 MHz. At this intensity, in this sample, the unpolarized component is negligible compared to the polarized component. Note that peak intensities in the two plots are equal. Residuals from the best fit of a squared cosine curve to the raw data are shown below the polar plot. Reprinted with permission from reference [130].

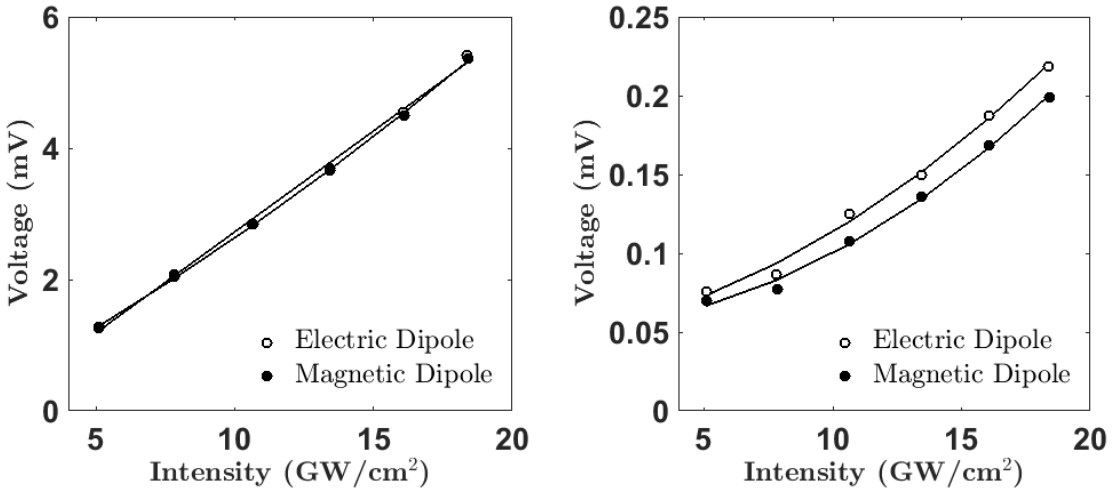

Figure 4.6: Measurements of polarized (l) and unpolarized (r) components of ED (open circle) and MD (closed circle) scattered light versus input intensity for Quartz. Solid curves are quadratic fits to the data.

4.1.3 Spectrally-resolved magnetic scattering

Another way to explore magneto-electric scattering is by analyzing the spectrum of the scattered light for elastic and inelastic processes. Using the set-up in figure 3.11, with an average power of 10-1000 mW, the spectrum was obtained for scattered light from a carbon tetrachloride sample. From the spectra in figures 4.7 and 4.8, it is apparent that the ED spectrum consists of the main laser peak without any other spectrally-shifted features of measurable intensity. It is representative of the instrumental lineshape. This lack of features shows that no all-electric Raman processes are taking place. Note that the ED spectrum has been made 5 times larger in order to compensate for experimental acquisition time and noise levels in figure 4.8. The MD spectrum is different from the ED spectrum and has three components: a red-shifted feature on the shoulder of the main peak, a red-shifted feature peaking near 850 nm, and a blue-shifted feature at 780 nm. These features can be more easily examined as the difference between the ED and MD spectra in figure 4.9.

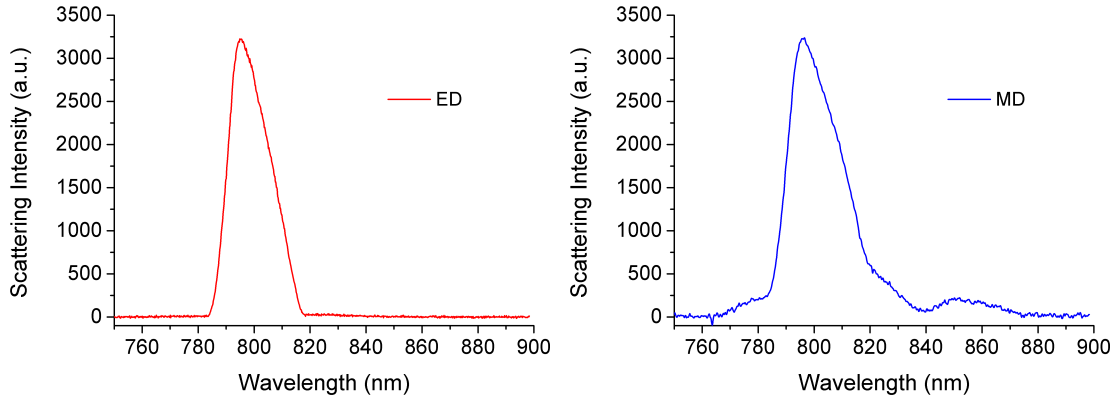

Figure 4.7: Normalized scattered light spectrum for V_v (l) and H_h (r) geometries for CCl_4.

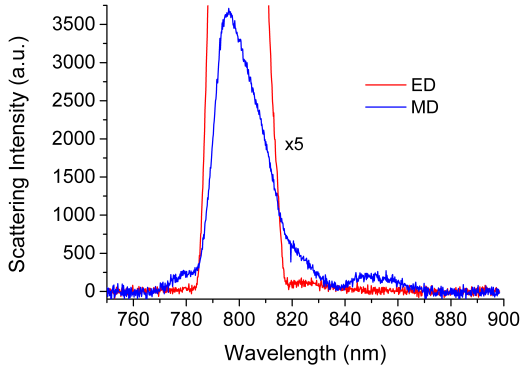

Figure 4.8: Comparative scattered light spectrum for electric (red) and magnetic (blue) dipole radiation for CCl_4.

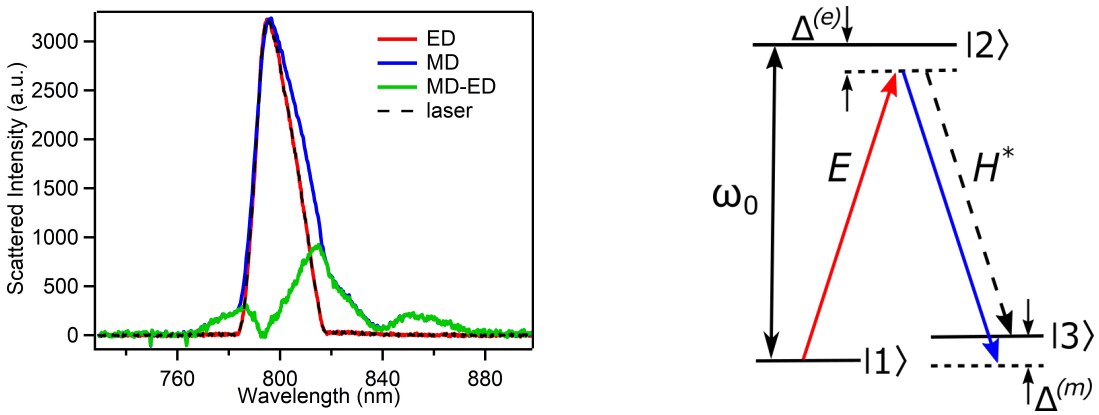

Figure 4.9: (l) Difference between ED and MD scattered light. (r) Quantum model for M-E processes.

Now, it is beneficial to re-examine the quantum picture of magneto-electric effects. Referring to figure 4.9, the ED spectrum corresponds to the red-line transition between the ground state and the virtual excited state detuned from state $|2\rangle$ by the one-photon detuning, $\Delta^{(e)} = \omega - \omega_0$. This is Rayleigh scattering. The MD spectrum corresponds to the two-photon process involving the red-line and blue-line transitions, where the blue-line transition is between the virtual excited state and the virtual ground state detuned from state $|3\rangle$ by the two-photon detuning, $\Delta^{(m)} = \omega_\phi$. Taking the difference between MD and ED spectra, processes that support the quantum theory for magneto-electric effects can be seen in figure 4.10.

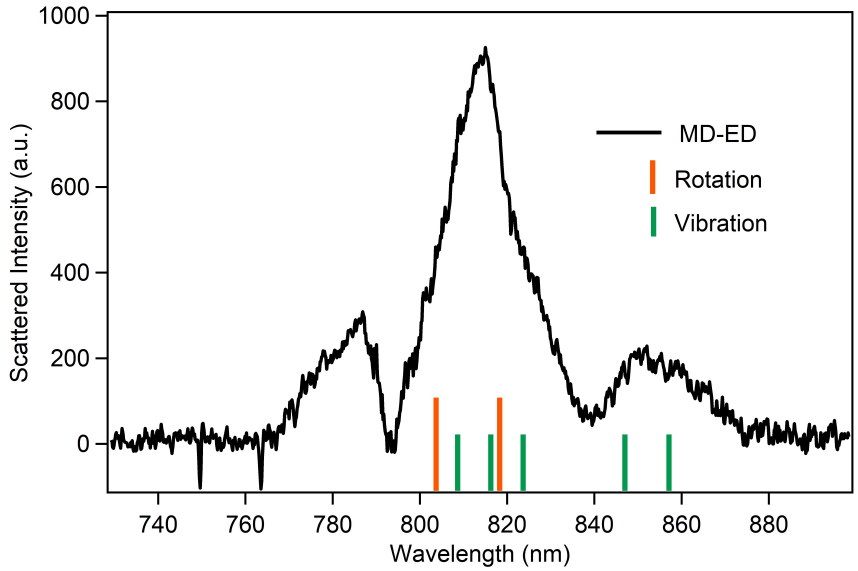

Figure 4.10: Difference between MD and ED spectrums of light scattered from CCl_4.

The polarized-light scattering experiment was repeated for silicon tetrachloride, silicon tetrabromide, tetramethyl orthosilicate, and tetraethyl orthosilicate. The Stokes energy shift observed via the spectral broadening for each sample was analyzed with respect to rotation frequency. The comparison is shown in figure 4.11.

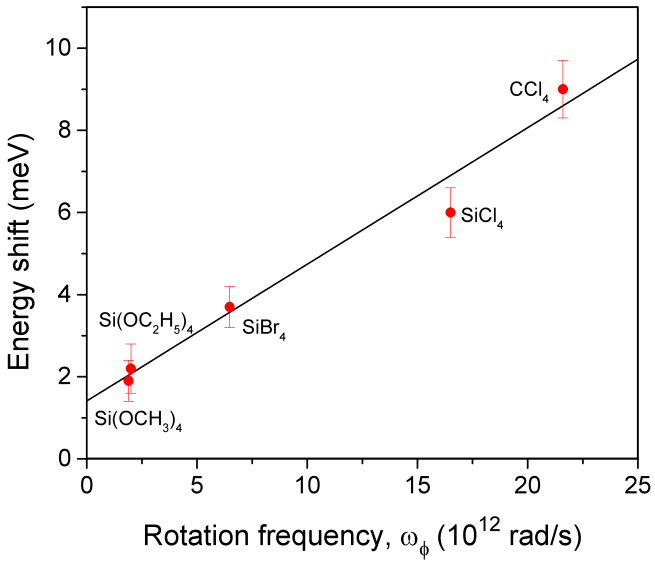

Figure 4.11: Comparison of magneto-electrically induced energy shift with molecular rotation frequency.

From figure 4.11, a linear relationship is observed between the energy shift and rotation frequency. Molecules with a higher rotation frequency, i.e. those which are easier to rotate, give a larger spectral broadening. For completeness, the raw data from spectrally-resolved ED and MD scattering observations for $SiCl_4$, $SiBr_4$, TMOS, and TEOS are shown in figures 4.12, 4.13, 4.14, and 4.15, respectively. Note that each spectrum has been normalized for easier comparison. Additionally, the vibrational energies are listed in tables 4.2, 4.3, 4.4, and 4.5.

Table 4.1: Vibration frequencies of Carbon Tetrachloride [46].

Mode	Frequency (cm^{-1})	Energy (meV)	Shifted λ (@ 800 nm)
$\nu 1$	459	56.9	830.5
$\nu 2$	217	26.9	814.1
$\nu 3$	779	96.6	853.2
$\nu 4$	314	39.0	820.6

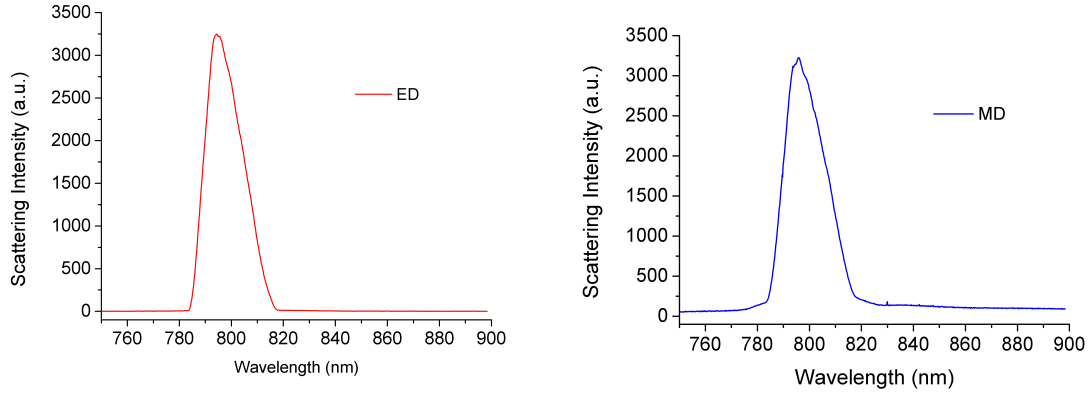

Figure 4.12: Normalized scattered light spectrum for V_v (l) and H_h (r) geometries for $SiCl_4$.

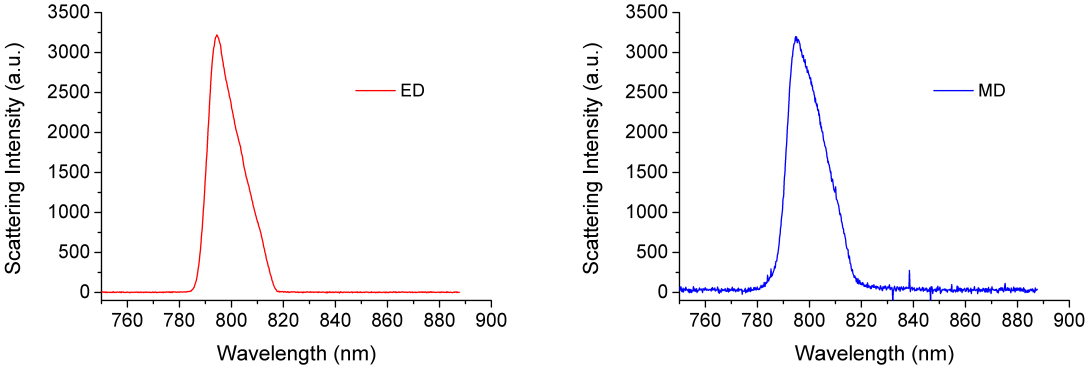

Figure 4.13: Normalized scattered light spectrum for V_v (l) and H_h (r) geometries for $SiBr_4$.

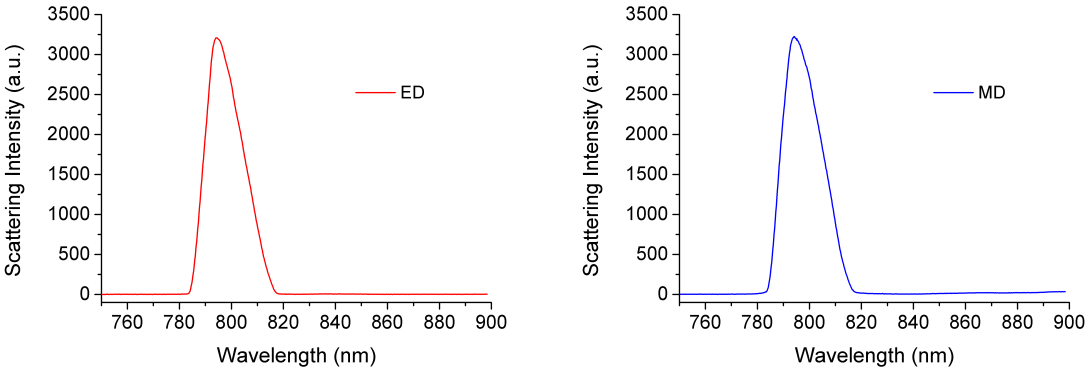

Figure 4.14: Normalized scattered light spectrum for V_v (l) and H_h (r) geometries for Tetramethyl Orthosilicate (TMOS).

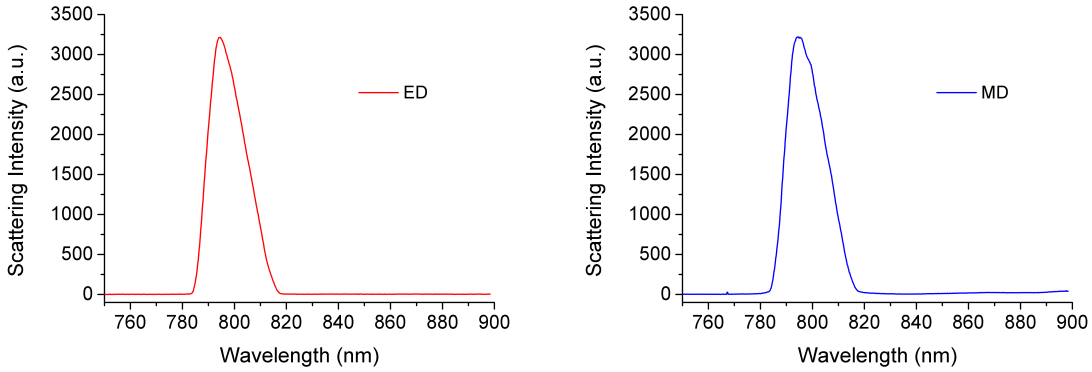

Figure 4.15: Normalized scattered light spectrum for V_v (l) and H_h (r) geometries for Tetraethyl Orthosilicate (TEOS).

Table 4.2: Vibration frequencies of Silicon Tetrachloride [46].

Mode	Frequency (cm^{-1})	Energy (meV)	Shifted λ (@ 800 nm)
$\nu 1$	424	52.6	828.1
$\nu 2$	150	18.6	809.7
$\nu 3$	610	75.7	841.0
$\nu 4$	221	27.4	914.4

Table 4.3: Vibration frequencies of Silicon Tetrabromide [46].

Mode	Frequency (cm^{-1})	Energy (meV)	Shifted λ (@ 800 nm)
$\nu 1$	249	30.9	816.3
$\nu 2$	90	11.2	805.8
$\nu 3$	487	60.4	832.4
$\nu 4$	137	17.0	808.9

Table 4.4: Vibration frequencies of Tetramethyl Orthosilicate [166].

Frequency (cm^{-1})	Energy (meV)	Shifted λ (@ 800 nm)
202	25.1	813.1
309	38.3	820.3
379	47.0	825.0
406	50.4	826.9
423	52.5	828.0
440	54.6	829.2
642	79.7	843.3
820	101.7	856.2
846	105.0	858.1
1094	135.7	876.7
1115	138.3	878.4
1161	144.0	881.9
1196	148.4	884.6
1460	181.1	905.8
1466	181.9	906.3
1478	183.4	907.3
2849	353.5	1036.2
2912	361.3	1043.0
2951	366.1	1047.2
2979	369.6	1050.3

Table 4.5: Vibration frequencies of Tetraethyl Orthosilicate [167].

Mode	Frequency (cm^{-1})	Energy (meV)	Shifted λ (@ 800 nm)
CH3 torsion	250	31.0	816.3
SiO4 deform	304	37.7	819.9
SiO4 deform	400	49.6	826.5
CCO deform	478	59.3	831.8
SiO4 asym. stretch	655	81.3	844.2
SiO4 asym. stretch	792	98.3	854.1
CH2 rock	811	100.6	855.5
CC stretch	935	116.0	864.7
CH3 rock	960	119.1	866.6
CO asym. stretch	1083	134.4	875.9
CO sym. stretch	1092	135.5	876.6
CO asym. stretch	1110	137.7	878.0
CH3 rock	1170	145.2	882.6
CH2 twist	1298	161.0	892.7
CH3 sym. def.	1368	169.7	898.3
CH2 wag	1393	172.8	900.3
CH3 asym. def.	1445	179.3	904.6
CH3 asym. def.	1458	180.9	905.6
CH2 deform	1485	184.2	907.9
CH2 sym. stretch	2890	358.5	1040.6
CH3 sym. stretch	2929	363.4	1044.8
CH2 asym. stretch	2973	368.8	1049.7
CH3 asym. stretch	2977	369.3	1050.1

4.1.4 Analysis

From the outset, a key interest in this research was to predict which materials are capable of producing a large magneto-electric magnetization. Existing quantum mechanical theory suggests that the second-order M-E magnetization, $M_y^{(2)}(\omega)$, depends on specific material properties as well as the strengths of the electric and magnetic field components of light. The dependence of $M_y^{(2)}(\omega)$ on field strength, transition moments, frequencies, and molecular parameters is given by [7, 136]

$$M_y^{(2)}(\omega) \propto \frac{\eta \mu_0^m \mu_0^e E H^*}{\left(\omega_0 - \omega + i\Gamma^{(e)}\right)\left(\omega_\phi + i\Gamma^{(m)}\right)}, \tag{4.1}$$

where μ_0^e is the electric dipole moment; μ_0^m the magnetic dipole moment; $\omega_0 - \omega$ the one-photon detuning between the driving optical frequency and the resonance frequency of the molecule; $\Gamma^{(e)}$ the electronic relaxation rate; $\Gamma^{(m)}$ the magnetic relaxation rate; ω_ϕ the rotation frequency of the molecule; η the magnetization enhancement factor; and E and H^* the strengths of the electric and magnetic fields. The material properties in equation 4.1 are detailed fully in the next section.

To compare the magnetization response of different materials, a simplified form of equation 4.1 is used as a "figure of merit (FOM)." The electric and magnetic field strengths are dropped as well as the magnetic moment. This gives a FOM of

$$F.O.M. = \left\| \frac{\eta \mu^{(e)}}{\left(\omega_0 - \omega + i\Gamma^{(e)}\right)\left(\omega_\phi + i\Gamma^{(m)}\right)} \right\|^2. \tag{4.2}$$

4.1.4.1 Material comparisons and procedures

The parameters in the FOM are defined as the following:

1. ω_ϕ is the rotation frequency of the molecule. The rotation frequency is calculated from the moment of inertia as $\omega_\phi = \hbar / I$. For spherical molecules, the moment of inertia can be approximated as $I = mr^2$, where m is the mass of a particle and r is the distance of the molecule from the center of mass. For non-spherical molecules, the moment of inertia is given based on internal coordinates.

2. ω_0 is the resonance frequency of the molecule. It can be experimentally measured using Ultraviolet-Visible (UV-VIS) spectroscopy. It is the first resonance in the UV, commonly known as either the b-band or Soret resonance. It is calculated from the wavelength of maximum molar absorption as $\omega_0 = 2\pi c / \lambda_{max}$ [168].

3. $\Gamma^{(m)}$ is the magnetic relaxation rate. It is related to the light scattering reorientational relaxation time as $\Gamma^{(m)}\left(rad/s\right) = 2\pi/\left(\tau_{reor}\right)$. τ_{reor} is experimentally measured as the time it takes for the molecule to reorient one radian.

4. $\Gamma^{(e)}$ is the electronic relaxation rate. It is defined in radians per second in relation to the half-width half-max Lorentzian bandwidth around ω_0 in an expression like $1/\left(\left(\omega_0-\omega\right)^2+\left(\Gamma^{(e)}\right)^2\right)$. It is also related to the Einstein A coefficient, A_{12}, by $\Gamma^{(e)} = \Delta\nu_{FWHM}\left(s^{-1}\right)/2 = c\left(cm/s\right)\Delta\nu_{FWHM}\left(cm^{-1}\right)/2 = A_{12}/2$.

5. $\mu^{(e)}$ is the electronic transition dipole moment. It is calculated from the UV-VIS spectrum as being directly proportional to the square root of the oscillator strength and inversely proportional to the square root of the center frequency: $f = \frac{2m_e\pi\nu}{3e^2\hbar}\mu_{12}^2$.

6. η is the magnetization enhancement factor. It is the ratio between the resonance frequency and the rotation frequency: $\eta = \omega_0/\omega_\phi$.

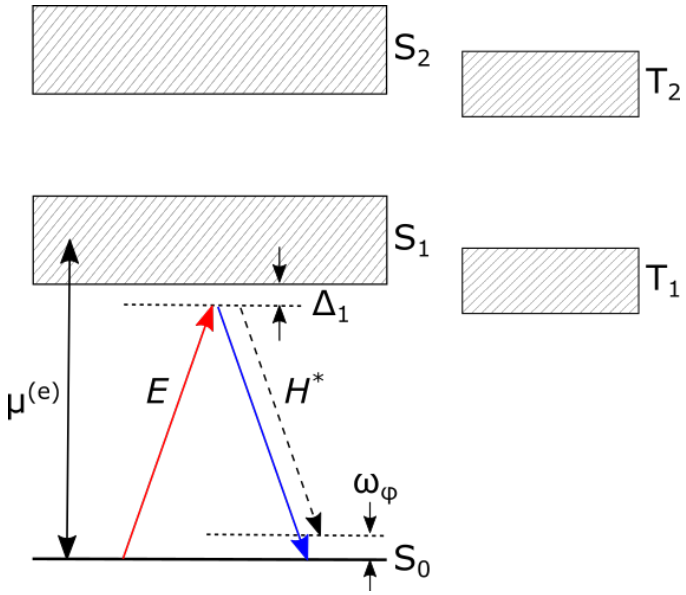

Figure 4.16: Energy level diagram showing magneto-electric magnetization. Δ_1 is the one-photon detuning where $\Delta_1 = \omega_0 - \omega$. ω_ϕ is the two-photon detuning.S_1 and T_1 are the singlet and triplet resonance bands, respectively.

For the calculation of the FOM, the parameters needed to be found in the literature, calculated from known quantities, or experimentally measured. While most of the values were able to be found using the Google Scholar or Reaxys databases, a small number had to be measured.

The first necessary data set is the UV-VIS spectrum. The UV-VIS spectrum provides data for the transition dipole moment, $\mu^{(e)}$, the resonance frequency, ω_0, and the electronic

relaxation rate, $\Gamma^{(e)}$. The UV-VIS spectrum should be obtained as far into the UV/x-ray as possible since many resonances for organic molecules are located around 200 nm. After the spectrum is obtained, the resonance frequency can be identified by locating the first resonance in the UV (the Soret resonance). At this location, the oscillator strength (and thus the transition dipole moment) should be calculated by integrating the absorption strength underneath the resonance frequency curve.

The next parameter is the light scattering reorientational relaxation time, which provides the magnetic relaxation rate $\Gamma^{(m)}$. Depending on the anisotropy of the molecule, it can be measured by either nuclear magnetic resonance [169], Rayleigh light scattering [170], or beam deflection [171]. All remaining parameters, such as the moment of inertia, can be calculated or found in existing literature databases.

4.1.4.2 Tetrachloride series

FOMs for the tetrachloride series were calculated from tabulated literature values for the parameters involved. For ease of presentation, the parameters for the FOM are broken up into tables 4.6 and 4.7. Where possible, each number includes its error in calculation and reference. See section 4.1.4.4 for full details on the error calculations. Lastly, table 4.8 provides additional physical parameters for this series of compounds. The FOMs can be directly compared to the data collected on individual Tetrachlorides shown in figure 4.1 as a test of the quantum mechanical theory. The absorption spectra of the tetrachlorides are shown in figure 4.17.

Table 4.6: Tetrachloride figure of merit: Part one.

Chem.	ω_ϕ (10^{12}rad/s)	$\mu^{(e)}$ (10^{30}C.m)	$\Gamma^{(e)}$ (10^{15}rad/s)	$\Gamma^{(m)}$ (10^{12}rad/s)
CCl_4	21.6[172]	4.1($\pm$0.2)[173]	0.548($\pm$0.015)[173]	3.70($\pm$0.21)[174, 175]
$SiCl_4$	16.5[176]	11.3($\pm$0.6)[173]	0.654($\pm$0.024)[173]	2.86($\pm$0.29)[176]
$GeCl_4$	15.5[169]	12.1($\pm$0.6)[173]	0.596($\pm$0.015)[173]	0.898($\pm$0.09)[174]
$SnCl_4$	12.3[172]	13.2($\pm$0.7)[173]	0.585($\pm$0.012)[173]	1.26($\pm$0.13)[174]

4.1.4.3 Orthosilicate series

FOMs were also calculated for the majority of the orthosilicate series. The parameters for the FOM are presented in tables 4.10 and 4.11. Table 4.12 provides additional relevant physical parameters. Since $\Gamma^{(e)}$ was unable to be located in the literature for TMOS and TEOS, the complete FOMs were unable to be calculated for those molecules.

Table 4.7: Tetrachloride figure of merit: Part two.

Chem.	ω (10^{15}rad/s)	ω_0 (10^{15}rad/s)	λ_0 (nm)	η (unitless)	FOM
CCl_4	2.35($\pm$0.17)	10.7($\pm$0.015)[173, 177]	176($\pm$0.5)	497	0.122($\pm$0.11)
$SiCl_4$	2.35($\pm$0.17)	13.6($\pm$0.047)[173, 177]	139($\pm$0.5)	825	2.46($\pm$0.21)
$GeCl_4$	2.35($\pm$0.17)	10.7($\pm$0.015)[173, 177]	176($\pm$0.5)	890	4.08($\pm$0.36)
$SnCl_4$	2.35($\pm$0.17)	9.47($\pm$0.012)[173, 177]	199($\pm$0.5)	771	13.3($\pm$1.3)

Table 4.8: Additional physical constants for Tetrachlorides.

Chem.	Refr. Index	Density ($g.cm^{-3}$)	Molecular Weight ($g.mol^{-1}$)	Vapor Pressure (mmHg)	Melting Point (C)	Boiling Point (C)
CCl_4	1.460	1.594	153.82	143	-23	76.5
$SiCl_4$	1.412	1.483	169.90	419.9	-70	57.6
$GeCl_4$	1.464	1.844	214.50	75.99	-49.5	83
$SnCl_4$	1.512	2.226	260.52	9.998	-33	114

One item that had to be measured was the reorientation correlation time, τ_θ, for $SiBr_4$. This quantity was calculated from the measured Spin-Lattice and Spin-Spin relaxation times, which are represented as T_1 and T_2 respectively. The relaxation times were measured at the University of Michigan Chemistry Nuclear Magnetic Resonance (NMR) facility using a Varian vnmrs 700 system. The sample, neat $SiBr_4$, was filled inside a Nitrogen-filled glove box to prevent reaction with the air. Although the lack of a Si solvent made it more difficult to lock into the Si NMR signal, an optimal signal was obtained by varying the shims on the magnets.

T_1 was measured using the common 5T1-π-τ-π/2-FID (free-induction decay) pulse sequence. T_2 was measured using the CPMG-PROJECT multipulse sequence. For an explanation of these methods, refer to T. James' Fundamentals of NMR [179] or another NMR textbook. Table 4.9 shows the raw data obtained from the T_1 and T_2 pulse sequences. This data is plotted in figures 4.18 and 4.19 respectively. The exponential curve fits gave the times of $T_1 \approx 107.4 \pm 9.3$ s and $T_2 \approx 178.2 \pm 2.3$ ms.

From these times, it is possible to calculate to reorientational correlation time, τ_{reor}, for a silicon tetrabromide molecule. One simple way to estimate τ_{reor} is by the Debye-Stokes-Einstein formula,

$$\tau_{reor} = \frac{4\pi\eta a^3}{3kT} f_r, \tag{4.3}$$

where η is the viscosity, a is the molecular radius, and f_r is the microviscosity factor [176].

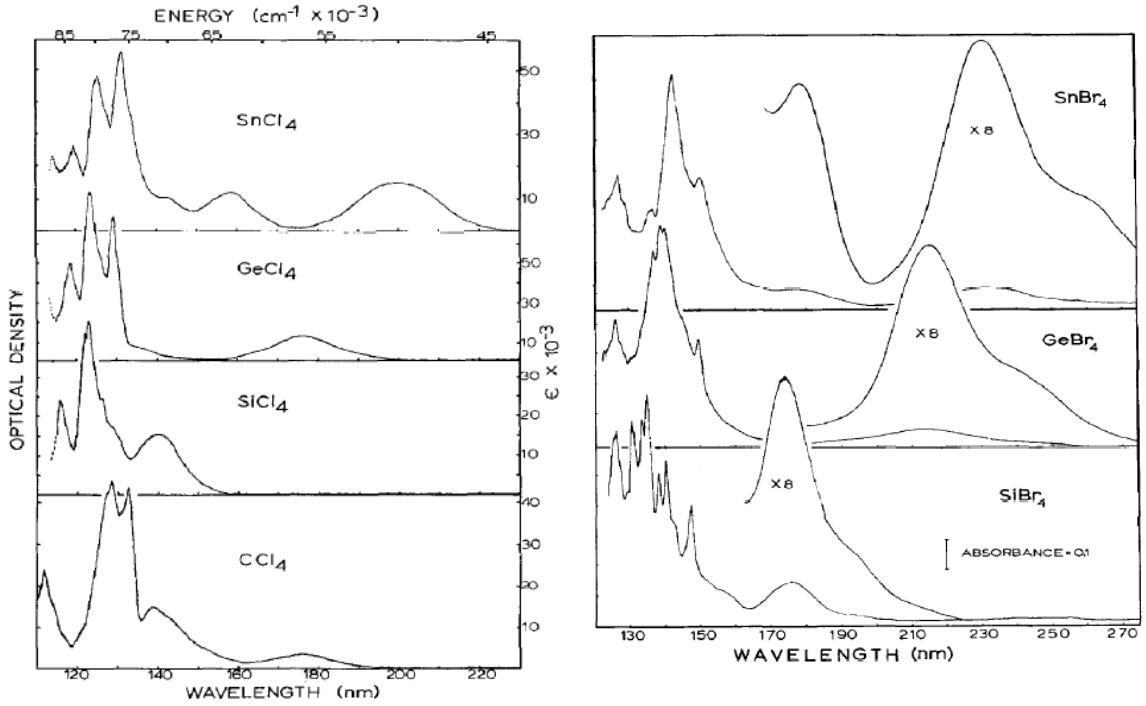

Figure 4.17: The vapor phase vacuum UV spectra of the group IVA tetrachlorides (l) and group IVA tetrabromides (r). Reprinted with permission from references [173] and [178], respectively.

Table 4.9: Raw NMR data for Spin-Lattice (l) and Spin-Spin (r) relaxation times.

$T_1 \approx 107.4 \pm 9.3$ s	
Time (s)	Strength (a.u.)
3.75	-52.2
7.5	-43.3
15	-36.3
30	-23.9
60	-1.84
120	31.7
240	57.8

$T_2 \approx 178.2 \pm 2.3$ ms	
Time (ms)	Strength (a.u.)
1.25	132
40	107
100	75.7
200	43.7
400	15.0
800	1.63

f_r equals 1/6 for close-packed spherical molecules. Taking the value of f_r at 25 °C, the viscosity for $SiBr_4$ at 0.00916 P and the radius as a=2.15 Å, then τ_{reor} = 1.54 ± 0.04 ps.

Although this is a good estimate of the reorientational correlation time, it is preferrable to measure it experimentally, especially since equation 4.3 is only valid if rotational and translational motion of a molecule are highly coupled [180].

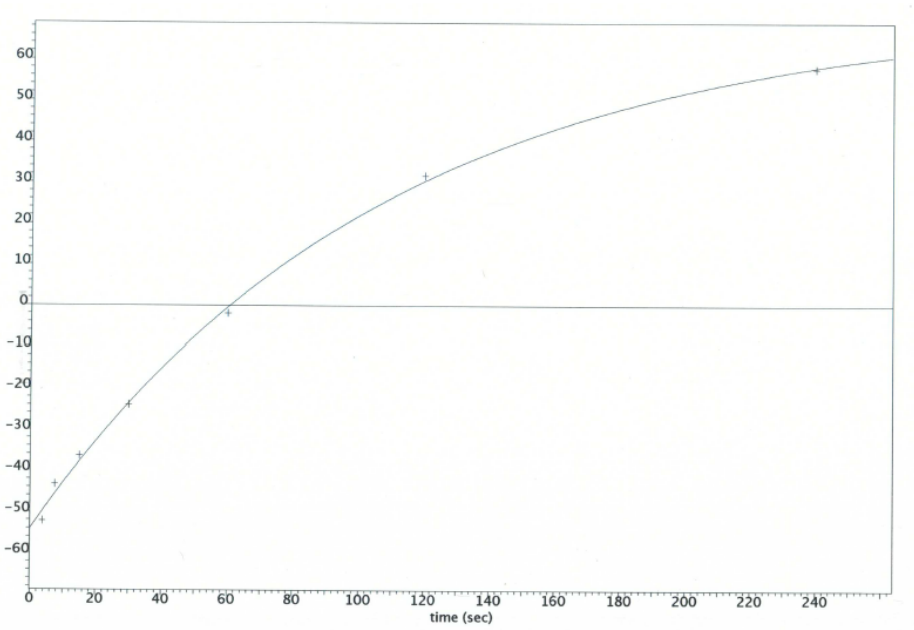

Figure 4.18: Raw NMR data with exponential fit for $SiBr_4$ Spin-Lattice relaxation time, T_1.

Table 4.10: Orthosilicate figure of merit: Part one.

Chem.	ω_ϕ (10^{12}rad/s)	$\mu^{(e)}$ (10^{30}C.m)	$\Gamma^{(e)}$ (10^{15}rad/s)	$\Gamma^{(m)}$ (10^{12}rad/s)
CCl_4	21.6[172]	4.1($\pm$0.2)[173]	0.548($\pm$0.015)[173]	3.70($\pm$0.21)[174, 175]
$SiCl_4$	16.5[176]	11.3($\pm$0.6)[173]	0.654($\pm$0.024)[173]	2.86($\pm$0.29)[176]
$SiBr_4$	6.48[172]	4.8($\pm$0.3)[178]	0.188($\pm$0.012)[178]	4.08
$Si(OCH_3)_4$	1.99[181]	6.09[182]	-	0.47[181]
$Si(OC_2H_5)_4$	2.00[181]	5.76[182]	-	0.17[181]

Table 4.11: Orthosilicate figure of merit: Part two.

Chem.	ω (10^{15}rad/s)	ω_0 (10^{15}rad/s)	λ_0 (nm)	η (unitless)	FOM
CCl_4	2.35($\pm$0.17)	10.7($\pm$0.015)[173, 177]	176($\pm$0.5)	497	0.122($\pm$0.11)
$SiCl_4$	2.35($\pm$0.17)	13.6($\pm$0.047)[173, 177]	139($\pm$0.5)	825	2.46($\pm$0.21)
$SiBr_4$	2.35($\pm$0.17)	9.67($\pm$0.024)[178, 177]	195($\pm$0.5)	1490	16.4($\pm$1.8)
$Si(OCH_3)_4$	2.35($\pm$0.17)	-	-	-	-
$Si(OC_2H_5)_4$	2.35($\pm$0.17)	10.7[183]	189.8	5357	-

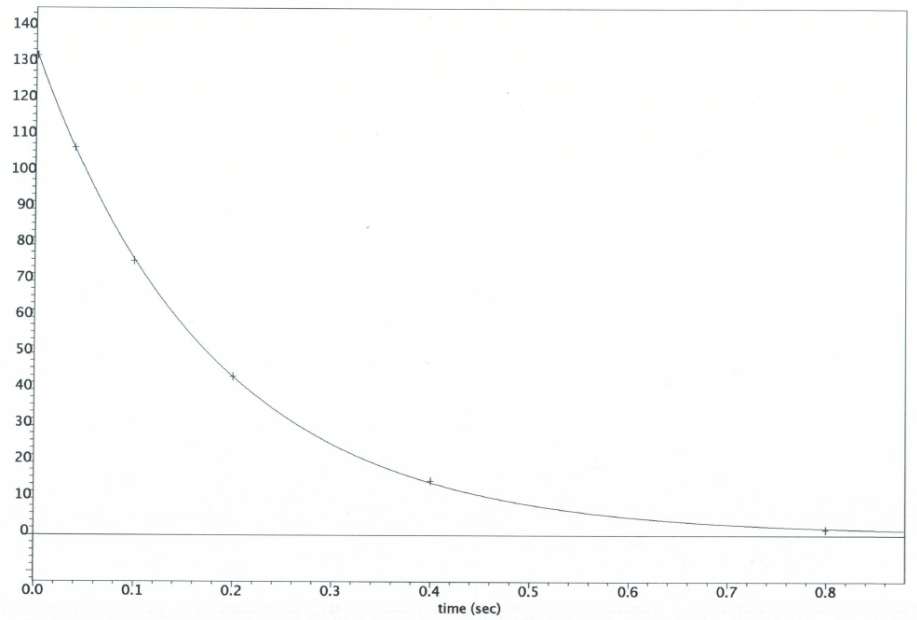

Figure 4.19: Raw NMR data with exponential fit for $SiBr_4$ Spin-Spin relaxation time, T_2.

Table 4.12: Additional physical constants for Orthosilicates.

Chem.	Refr. Index	Density $(g.cm^{-3})$	Molecular Weight $(g.mol^{-1})$	Vapor Pressure (mmHg)	Melting Point (C)	Boiling Point (C)
CCl_4	1.460	1.594	153.82	143	-23	76.5
$SiCl_4$	1.412	1.483	169.90	419.9	-70	57.6
$SiBr_4$	1.5685	2.800	347.70	4.2	5	153
$Si(OCH_3)_4$	1.368	1.023	152.221	173.2	-4	121.5
$Si(OC_2H_5)_4$	1.382	0.934	208.327	0.9998	-85.5	168

4.1.4.4 Errors in FOM calculations

As with any calculation, it is important to keep track of errors in the measurements. These errors are given as resolution of the measurement instrument as either a percentage or a range.

$$\frac{\Delta FOM}{FOM} = \sqrt{2\left(\frac{\Delta\mu_e}{\mu_e}\right)^2 + 2\left(\frac{\Delta\eta}{\eta}\right)^2 + \left(\frac{\Delta\left(\left(\omega_0-\omega\right)^2+\left(\Gamma^{(e)}\right)^2\right)}{\left(\omega_0-\omega\right)^2+\left(\Gamma^{(e)}\right)^2}\right)^2 + \left(\frac{\Delta\left(\omega_\phi^2+\left(\Gamma^{(m)}\right)^2\right)}{\omega_\phi^2+\left(\Gamma^{(m)}\right)^2}\right)^2} \tag{4.4}$$

$$\Delta f = 2\frac{4m_e\pi\nu}{3e^2\hbar}\mu_{12}\Delta\mu_{12} \tag{4.5}$$

$$\frac{\Delta\eta}{\eta} = \frac{\Delta\left(\omega_0/\omega_\phi\right)}{\omega_0/\omega_\phi} = \frac{\omega_\phi}{\omega_0}\sqrt{\left(\frac{\Delta\omega_0}{\omega_0}\right)^2 + \left(\frac{\Delta\omega_\phi}{\omega_\phi}\right)^2} \tag{4.6}$$

$$\Delta\omega_\phi = \frac{\hbar}{I^2}\Delta I \tag{4.7}$$

$$\frac{\Delta\left(\left(\omega_0-\omega\right)^2+\left(\Gamma^{(e)}\right)^2\right)}{\left(\omega_0-\omega\right)^2+\left(\Gamma^{(e)}\right)^2} = \sqrt{2\left(\Delta\omega_0\right)^2\omega_0^2 + 4\omega_0^2\omega^2\left(\left(\Delta\omega_0/\omega_0\right)^2+\left(\Delta\omega/\omega\right)^2\right) + 2\left(\Delta\omega\right)^2\omega^2 + 2\left(\Delta\Gamma^{(e)}\right)^2\left(\Gamma^{(e)}\right)^2} \Big/ \left(\left(\omega_0-\omega\right)^2+\left(\Gamma^{(e)}\right)^2\right) \tag{4.8}$$

$$\frac{\Delta\left(\omega_\phi^2+\left(\Gamma^{(m)}\right)^2\right)}{\omega_\phi^2+\left(\Gamma^{(m)}\right)^2} = \frac{\sqrt{2\left(\Delta\omega_\phi\right)^2\omega_\phi^2 + 2\left(\Delta\Gamma^{(m)}\right)^2\left(\Gamma^{(m)}\right)^2}}{\omega_\phi^2+\left(\Gamma^{(m)}\right)^2} \tag{4.9}$$

$$\Delta\Gamma^{(m)} = \frac{\Delta\tau_{reor}}{\tau_{reor}^2} \tag{4.10}$$

$$\Delta\Gamma^{(e)} = c\left(cm/s\right)\Delta\left[\Delta\widetilde{\nu}_{FWHM}\left(cm^{-1}\right)\right]/2 \tag{4.11}$$

4.2 Simulation results

The results in the following subsections illustrate several features of a *molecular*, as opposed to *atomic*, model of magneto-electric dynamics. Section 4.2.1, for example, shows electron motion at high-field strengths that are qualitatively similar to those of an atomic oscillator model, but that are *quantitatively* superior because they include strong enhancement by magnetic torque. The figures in section 4.2.2 explicitly show that the magnitudes and temporal dynamics of $P_z^{(2)}(0)$ and $M_y^{(2)}(\omega)$ depend on molecular structure, torque, and internal damping. Section 4.2.3 compares the predictions of the induced magnetic dipole directly to the electric dipole. Finally, the classical model is compared to the quantum model in section 4.2.4 and found to be in good agreement.

4.2.1 Electron motion at high-field strengths

Since the electric and magnetic dipole moments are functions of the trajectory of the electron motion, it is important to understand the thresholds at which the electron trajectory becomes abnormal. For reliable simulations, work should be done below this threshold. Figure 4.20 shows one such dependence on electric field strength. In the case of the atomic model, the trajectory of the electron shows the transition of the path from a broken symmetry (c-shaped path) to a less broken symmetry (figure-8 path). Note that in the atomic case, all electron motion is restricted to the x-z plane.

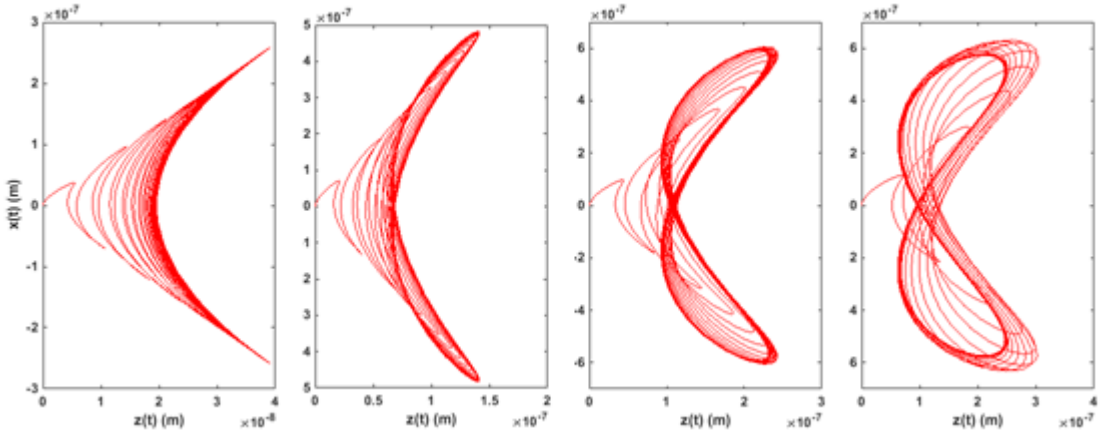

Figure 4.20: Trajectory of electron motion calculated by integration of the equations of motion for an incident electric field of arbitrary strengths. From left to right, the electric field strengths are 1e12, 2e12, 3e12, and 4e12 V/m. Simulation values are $\omega_0 = 1.63e16$rad/s$, \omega = 0.9\omega_0, \gamma = 0.1\omega_0, I_{//} = \hbar/\omega_0, I_\perp/I_{//} = 1000, \xi = [0,0,0]$, and $r_A = [0, 15pm, 0]$.

4.2.2 Charge separation

The electron trajectory in figure 4.20 shows evidence of two magneto-electric processes. The first is a second-order DC polarization, $P_z^{(2)}(0)$, also referred to as charge separation. This is the displacement of the electron along the z-axis, or "separation", as a function of time. Note how the average location of the electron along the z-axis increases with applied electric field strength. The second process is a second-order magnetization, $M_y^{(2)}(\omega)$. The magnetization is induced by electron motion via Ampere's Law: $0 = \partial P/\partial t + \hat{\nabla} \times \hat{M}$.

The dependence of charge separation and magnetization on molecular structure, torque, and internal damping are described in the following figures. In figures 4.21 and 4.22, the moments of inertia $I_{//}$ and $I_{\perp}$ have been assigned arbitrary but representative values that are inversely proportional to optical and rotation frequencies of the molecule respectively. More specifically, the reference values of the momenst of inertia are chosen to representative of a diatomic hydrogen molecule. In figure 4.21, the average offset in motion of the electron away from its initial equilibrium point is seen to increase a thousand-fold when $I_{\perp}/I_{//}$ is increased from a value of 1 to 1000. Similarly, in figure 4.22, magnetization is enhanced by a factor of 500 for the same evolution of the molecular moment of inertia from $I_{//}$ to $I_{\perp}$ as the result of magnetic torque. Figure 4.23 shows that an increase of librational damping removes the long-period nutation transients (Rabi oscillations) and tends to reduce the amplitude of response for magnetization. Figure 4.24 shows that the charge separation and magnetization reach steady state sooner at elevated field strengths. The amplitude of response is reduced for the magnetization but not for the charge separation.

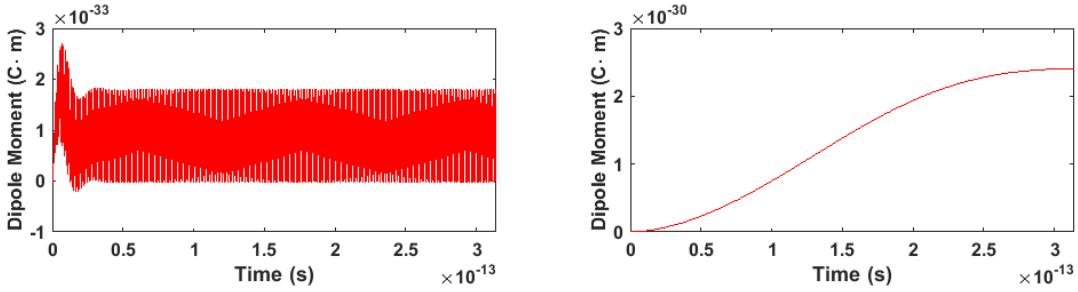

Figure 4.21: Evolution of the charge separation, $P_z(0)$, of the test charge versus time for $I_{\perp}/I_{//} = 1$ (left) and $I_{\perp}/I_{//} = 1000$ (right). Simulation values are $\omega_0 = 1.63e16$rad/s, $\omega = 0.9\omega_0$, $\gamma = 0.1\omega_0$, $I_{//} = \hbar/\omega_0$, $E = 1e9$V/m, $\xi = [0, 0, 0]$, and $r_A = [0, 15pm, 0]$.

At elevated field strengths, pulsing appears in the temporal evolution of the system. This is a reflection of the susceptibility of the Drude-Lorentz model (including magnetic forces) to parametric instabilities [6]. This is a direct result of extending the model to include magnetic torque. Figure 4.25 shows traces of the electric and magnetic moments

versus time for high values of the optical field, with and without strong librational damping.

The behavior predicted in figure 4.25 exhibits an interesting trend. As shown in figure 4.26, the periodicity of the pulsing is linearly dependent on the applied electric field strength. Temporal behavior and pulsing was also analyzed while varying the librational damping. Pulsing behavior seemed to be relatively robust against changes in the γ parameter, but damping had little effect on the amplitude of either magnetization or charge separation.

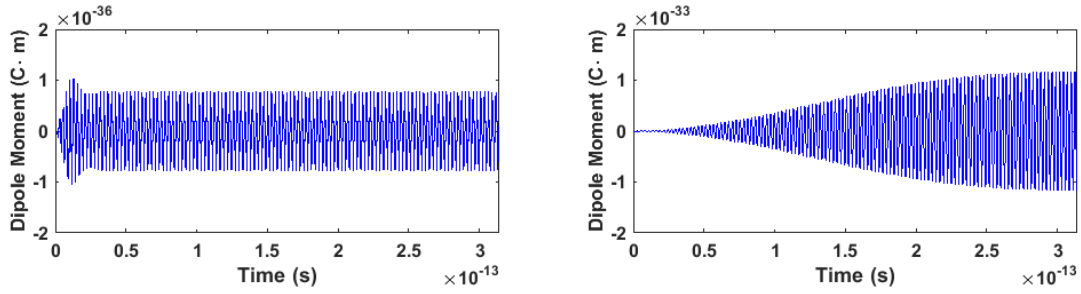

Figure 4.22: Evolution of the magnetic moment of the test charge divided by light speed, $M_y(\omega)/c$, versus time for $I_\perp/I_{//} = 1$ (left) and $I_\perp/I_{//} = 1000$ (right). Simulation values are $\omega_0 = 1.63e16$rad/s, $\omega = 0.9\omega_0, \gamma = 0.1\omega_0, I_{//} = \hbar/\omega_0, E = 1e9$V/m, $\xi = [0, 0, 0]$, and $r_A = [0, 15pm, 0]$.

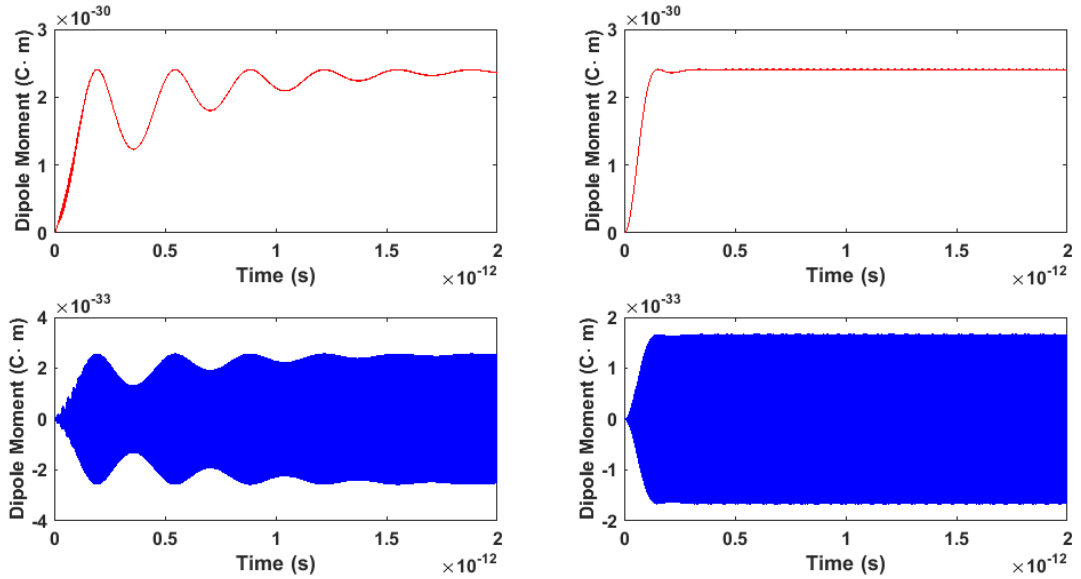

Figure 4.23: Evolution of charge separation (top) and magnetization/c (bottom) versus time for different values of the magnetic (librational) damping. The damping coefficient is $\gamma = 0.025\omega_0$ (left) and $\gamma = 0.25\omega_0$ (right). Simulation values are $\omega_0 = 1.63e16$rad/s, $\omega = 0.9\omega_0, I_{//} = \hbar/\omega_0, I_\perp/I_{//} = 1000, E = 2e9$V/m, $\xi = [0, 0, 0]$, and $r_A = [0, 15pm, 0]$.

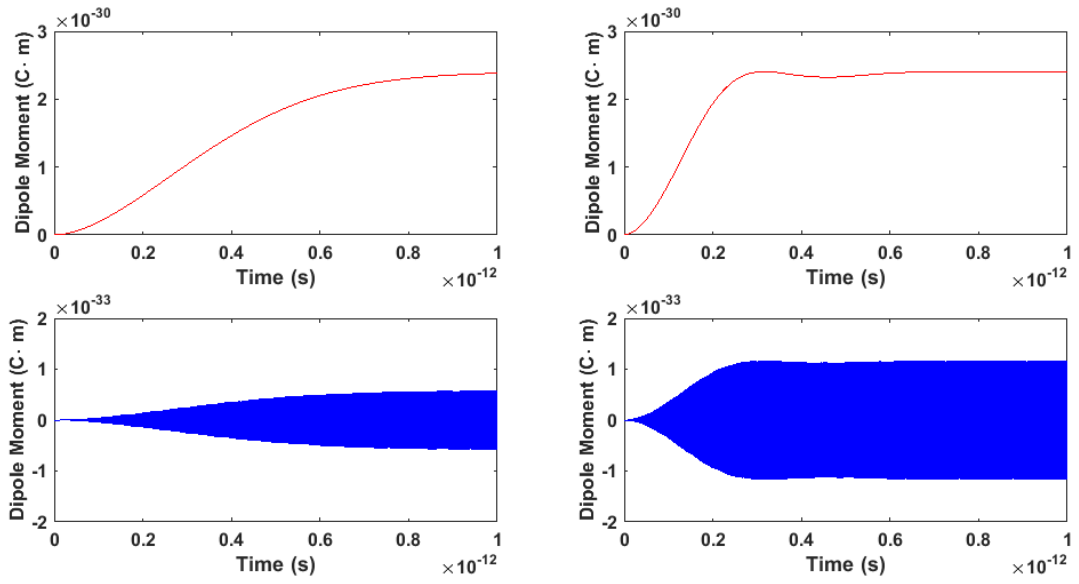

Figure 4.24: Evolution of the charge separation (top) and magnetization/c (bottom) versus time for different values of the applied electric field. The electric field strength is $E = 5e8$V/m (left) and $E = 1e9$V/m (right). Simulation values are $\omega_0 = 1.63e16$rad/s, $\omega = 0.9\omega_0, \gamma = 0.1\omega_0, I_{//} = \hbar/\omega_0, I_\perp/I_{//} = 1000, \xi = [0, 0, 0]$, and $r_A = [0, 15pm, 0]$.

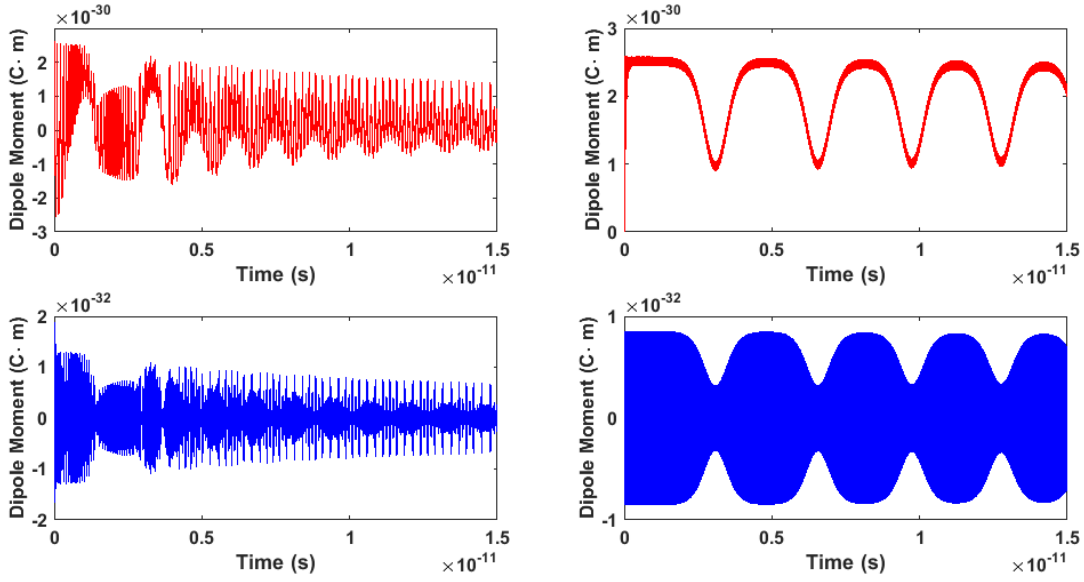

Figure 4.25: High-field charge separation (top) and high-field magnetization/c (bottom) versus time for different values of the magnetic (librational) damping. The damping coefficient is $\gamma = 0.025\omega_0$ (left) and $\gamma = 0.25\omega_0$ (right). Simulation values are $\omega_0 = 1.63e16$rad/s, $\omega = 0.9\omega_0, E = 1e10$V/m, $I_{//} = \hbar/\omega_0, I_\perp/I_{//} = 1000, \xi = [0, 0, 0]$, and $r_A = [0, 15pm, 0]$.

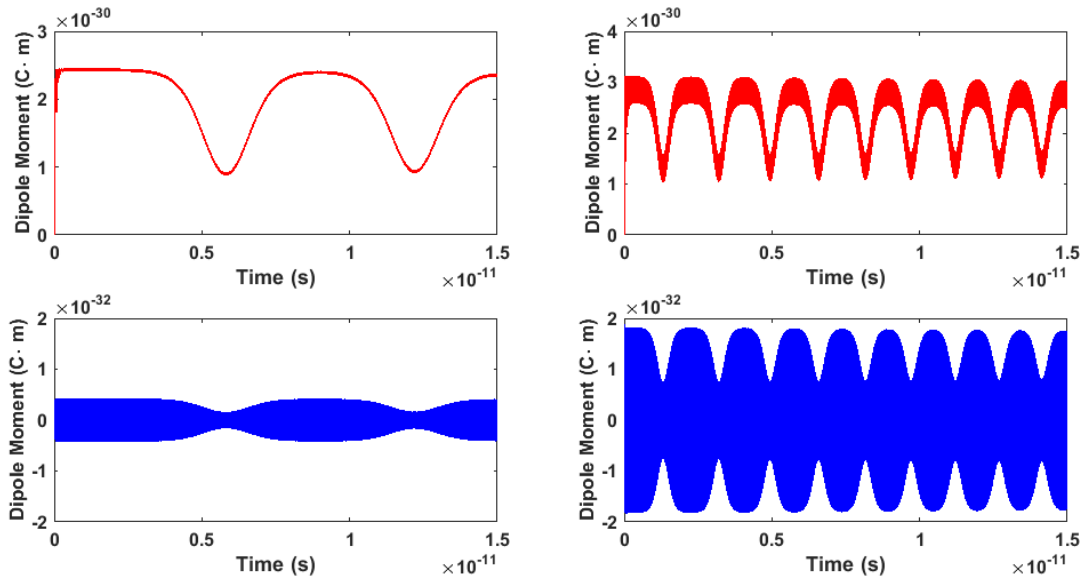

Figure 4.26: High-field charge separation (top) and high-field magnetization/c (bottom) versus time computed for large magnetic (librational) damping, $\gamma = 0.25\omega_0$, and $E = 5e9$V/m (left) and $E = 20e9$V/m (right). Simulation values are $\omega_0 = 1.63e16$rad/s, $\omega = 0.9\omega_0, I_{//} = \hbar/\omega_0, I_\perp/I_{//} = 1000, \xi = [0, 0, 0]$, and $r_A = [0, 15pm, 0]$.

4.2.3 Magnetization and electric polarization

In order to relate the simulations to experiments, the relative magnitude of scattering from an induced magnetic dipole moment to that from the electric dipole moment was predicted versus time for the full molecular model. Figure 4.27 shows an example of the electric polarization and the magnetization oscillating at the driving frequency, ω.

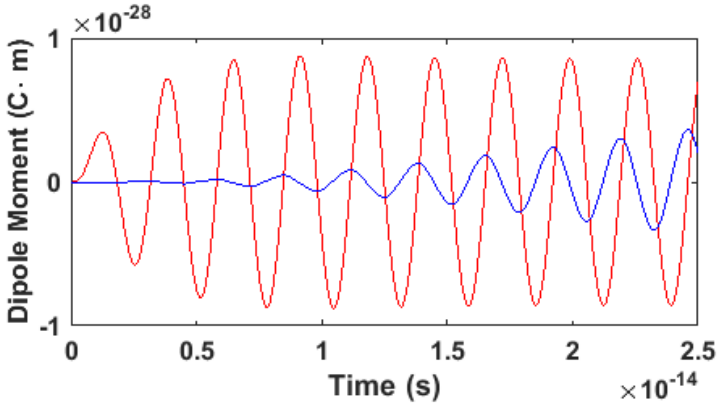

Figure 4.27: Electric polarization (red) and magnetization/c (blue) versus time showing both oscillate at ω. Simulation values are $\omega_0 = 1.63e16$rad/s, $\omega = 0.9\omega_0, I_{//} = \hbar/\omega_0, I_\perp/I_{//} = 1000, E = 6e9V/m, \xi = [0, 0, 0]$, and $r_A = [0, 15pm, 0]$.

In the case of the *atomic* Lorentz oscillator model, the ratio of the magnetic dipole moment to the electric dipole moment is invariably less than 10^{-5}, whereas in the molecular model much larger ratios - similar to those measured in our experiments - are obtained. Figure 4.28 compares the atomic model to the molecular model, showing that the magnetization is enhanced by over 3 orders of magnitude. This enhancement can be even larger depending on the molecular constants used in the simulation.

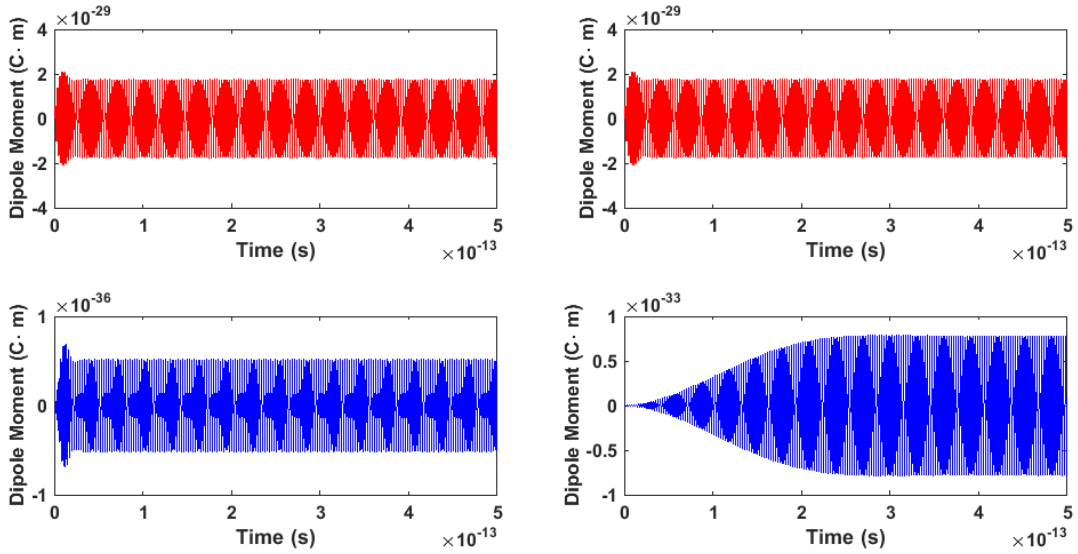

Figure 4.28: Electric polarization (top) and magnetization/c (bottom) versus time computed for atomic (left) and molecular (right) models. Simulation values are $\omega_0 = 1.63e16$rad/s, $\omega = 0.9\omega_0$, $I_{//} = \hbar/\omega_0$, $I_\perp/I_{//} = 1000$, $\xi = [0, 0, 0]$, and $r_A = [0, 15pm, 0]$.

4.2.4 Comparison to quantum theory

By examining the steady-state values of classically simulated dipole moments, a direct comparison can be made between the quantum mechanical and classical theory. Figure 4.29 compares the magnitudes of the dipole moments as a function of intensity (or the number of incident photons). For close comparisons with experiments, the squared value of the total magnetic moment (figure 4.30) and the second order electric dipole moment (figure 4.31) versus incident number of photons and rotation frequencies have been computed, since scattering intensity is proportional to the squared moments.

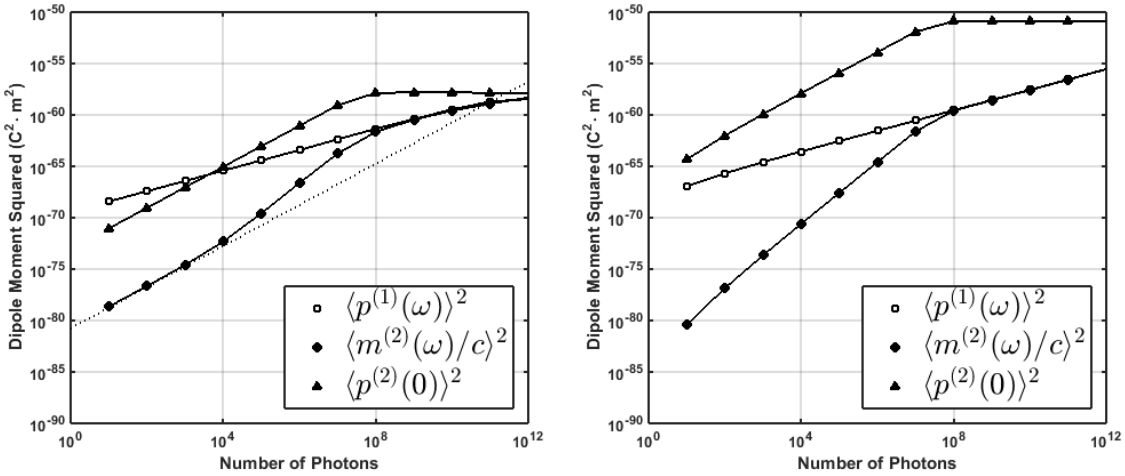

Figure 4.29: Values of the total magnetic moment, second order electric moment, and first order electric dipole moment versus the number of incident photons in the (l) 4-state quantum model and (r) molecular torque-enhanced Lorentz oscillator model. In both figures, the rotation frequency is $\omega_\phi/\omega_0 = 10^{-5}$.

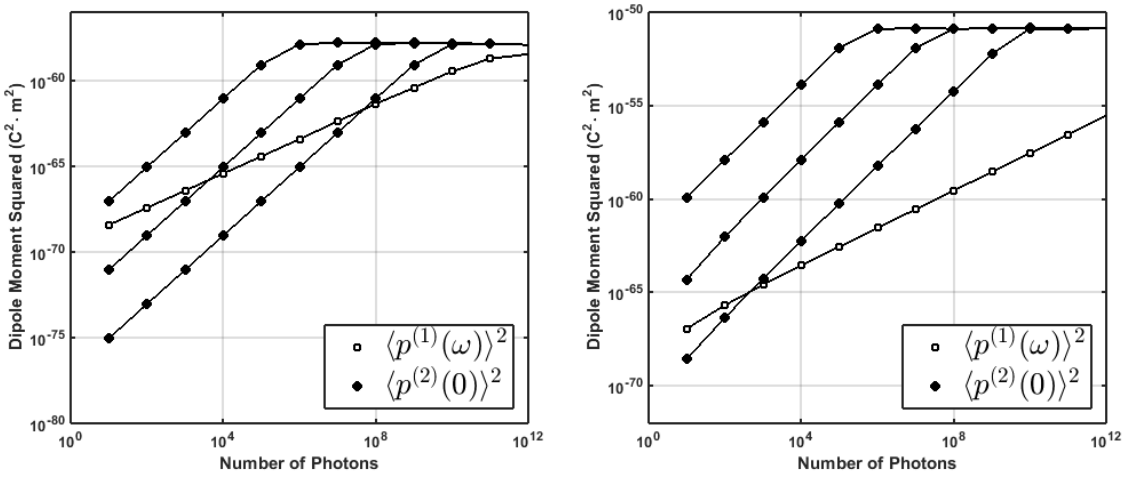

Figure 4.30: Squared values of the total magnetic moment and first order electric dipole moment versus the number of incident photons in the (l) 4-state quantum model and (r) molecular torque-enhanced Lorentz oscillator model. In both figures, the rotation frequencies from left to right are ω_ϕ/ω_0=10^{-7}, 10^{-5}, 10^{-3}.

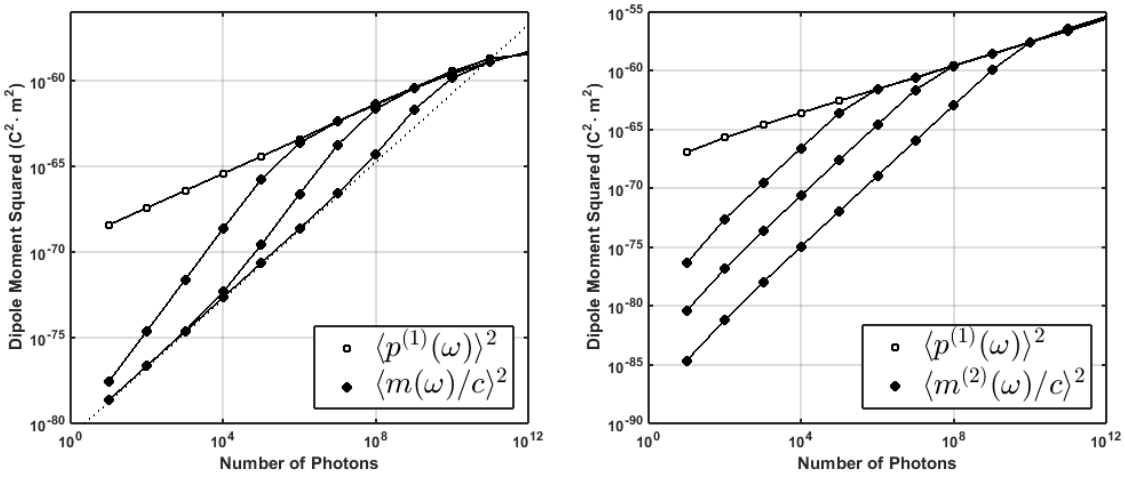

Figure 4.31: Squared values of the second order electric moment and first order electric dipole moment versus the number of incident photons in the (l) 4-state quantum model and (r) molecular torque-enhanced Lorentz oscillator model. In both figures, the rotation frequencies from left to right are ω_ϕ/ω_0=10^{-7}, 10^{-5}, 10^{-3}.

CHAPTER 5

Conclusion

This chapter presents the conclusions and future directions for this research. The chapter is split into five sections. The first section summarizes the main experimental findings of the magneto-electric scattering experiments, including their intensity dependence and spectral response. Studies of the intensity dependence confirmed the expected quadratic variation of scattering intensity versus input intensity, together with the anticipated polarizations, radiation patterns, and rotational frequency dependence of scattering signals. From the spectroscopy experiments, it was found that second-order magneto-electric dynamics can account for scattering from high-frequency librations characteristic of each sample. The spectral features cannot be assigned to all-electric Raman transitions, as either first-order collision-induced or third-order all-electric processes. The results from the torque-enhanced Lorentz oscillator model as well as implications of the PT symmetry in the quantum mechanical model are also discussed. Additionally, the results from the classical and quantum mechanical models are compared and found to be in good agreement.

The second section compares the experimental results to the predictions made by the quantum mechanical and classical theories. The third section provides additional context on depolarized light scattering. The fourth section analyzes applications to material design of the nonlinear optical susceptibility relationships discussed earlier in chapter 2 are explored. Lastly, the fifth section presents ideas for future experimental and theoretical work in magneto-electric scattering.

5.1 Summary of results

Linearly-polarized magnetic dipole (MD) scattering on the same order of magnitude as electric dipole (ED) radiation is reported in molecular liquids (CCl_4, $SiCl_4$, $GeCl_4$, $SnCl_4$, $SiBr_4$, TMOS, TEOS, TPOS) and transparent crystalline solids (GGG, Quartz). Magneto-electric magnetization for the tetrachloride and orthosilicate series was shown in the earlier

figures 4.1 and 4.3, respectively. These molecular liquids display a quadratic dependence on optical incident intensity, as predicted by theory.

The quantum theory derived in section 2.2 predicts the presence of one 1-photon and three 2-photon processes during magneto-electric scattering. These four processes, as displayed in figure 5.1 are dependent on the 1-photon ($\Delta^{(e)} \equiv \omega_0 - \omega$) and 2-photon ($\Delta^{(m)} \equiv \omega_\phi$) detunings. Experimentally, these four processes correspond to measurements using the following polarization configurations: electric polarization (E), V_v; optical magnetization (EH*), H_h; unpolarized electric dipole radiation (HE*), V_h; and unpolarized magnetic dipole radiation (EH*), H_v.

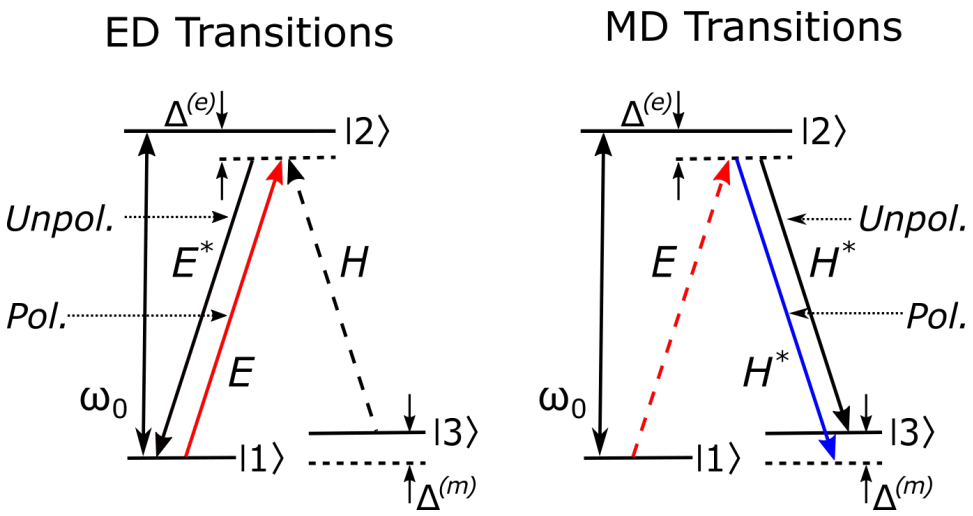

Figure 5.1: Diagram showing the 4 M-E quantum processes as solid arrows: two electric transitions on the left and two magnetic transitions on the right. $\Delta^{(e)}$ is the 1-photon detuning, $\omega_0 - \omega$. $\Delta^{(m)}$ is the 2-photon detuning, ω_ϕ.

The magnitude of the optical magnetization in GGG and Quartz at $\sim 2{\times}10^{10}$ W/cm^2 was found to be just as intense as Rayleigh scattering (figures 4.4 and 4.5, respectively). This is the strongest optical magnetization relative to electric polarization ever reported [130]. The intensity dependent measurements for GGG presented in figure 4.4 demonstrate the four magneto-electric processes predicted by theory and described above with no systematic residuals. The unpolarized ED, unpolarized MD and polarized MD signals each display a quadratic dependence on input intensity. Each quadratic fit to the data also has a significant linear component arising from leakage of orthogonal polarization through the analyzer and a small background from collision depolarization. The presence of minor linear components is not surprising in solid samples because an increased number of scattering centers (defects, etc.) are unavoidably included during crystal growth. These can be expected to produce a larger linear component than in the liquid samples. The polarized

ED signal is purely linear, but, in this case, linearity is expected because the polarization is first-order with respect to the input fields. It is also worth noting that the data taken with the photodiode and lock-in amplifier also have a constant offset due to electronic noise.

By spectrally resolving scattered light, additional evidence of the 2-step magneto-electric process was obtained. Key spectral features that appear in figure 4.10 during the magnetic scattering process are explained as originating from magneto-electrically induced rotations of the molecule. Here, the fundamental rotational shift energy is defined as $E_{rot} = \hbar \times \omega_{\phi}$. For one rotation in CCl_4, the energy is 14.2 meV. The second rotational energy level corresponds to $E_{rot} = 3 * \hbar \times \omega_{\phi}$, consistent with the well-known rigid rotor model [45]. Other red-shifted spectral features appear at shifts corresponding to vibrational excitations, which are attributable to "knock-on" collisions with rotating molecules. In other words, the light induces magneto-electric rotations and when the rotating molecules knock into nearby molecules, vibrations are induced. The small anti-Stokes component is interpreted as a reverse sequence (see Figure 5.1a) of the 2-photon transition, drawing on the population of rotations established in the sample for thermal equilibrium at temperature T. It is noteworthy that vibrational features are absent on the anti-Stokes side of the spectrum. This is consistent with the reverse processes (Figure 5.1a) because rotations are annihilated in the optical interaction, thereby eliminating the possibility of subsequent knock-on collisions.

The results shown in the spectrum are unique in the literature. Others have looked at H_h scattering, but never at these intensities. Stevens et al. measured the central Lorentzian in the depolarized Rayleigh spectra of liquid CCl_4 and $GeCl_4$ in 1982 [63]. Using a 514.5 nm CW laser with an average power of 700 mW, they noted that "the HH and HV spectral shape was compared with the pure HV spectral shape at one temperature and found to be identical." This is not surprising because their peak intensity was less than 0.1 kW/cm^2 whereas in the present experiments it was around 100 MW/cm^2. The effects reported here are truly nonlinear processes, but not of the all-electric variety. Neither collisional depolarization nor the optical Kerr effect can explain the dipolar component in cross-polarized scattering on the timescale of the experiments which utilized pulses much shorter than collisional reorientation times.

Two theoretical descriptions of radiant optical magnetization were presented in this dissertation. The first was an extension of the classical Lorentz Oscillator Model from an atomic to a molecular picture. This model included the effect of torque exerted by the optical magnetic field on excited state orbital angular momentum, resulting in an enhancement in the magnetization. Temporal dynamics were explored along with dependence on material properties. Secondly, results from the quantitatively-exact doubly-dressed state

quantum theory of induced optical magnetization were also discussed. Analysis showed that the magnetic-interaction Hamiltonian obeys Parity-Time (PT) symmetry, indicating that magneto-electric effects should occur universally. Lastly, the results from the classical and quantum mechanical models, which contain the same kinematic elements, were compared and found to be in very reasonable agreement.

The classical molecular model developed in section 2.1 showed very different behavior from the elementary Drude-Lorentz model [34], as the result of including magnetic torque. This added feature of the extended model mediated the appearance and the enhancement of two magneto-electric effects driven by the optical fields. Magneto-electric rectification and magnetization were predicted to be substantially enhanced by torque when the ratio of transverse to parallel moments of inertia, $I_{\perp}/I_{//}$, is large. The longitudinal ED moment can also exceed the linear ED moment driven by the electric field. For values of the ratio exceeding the fine structure constant ($I_{\perp}/I_{//} > 1/\alpha$) the calculations showed that the magnetization can be as large as the linear electric polarization under non-relativistic conditions. The physical explanation for this is shown in figure 2.5, where the area enclosed by charge libration in a molecule is seen to grow as the result of torque-mediated dynamics. The effect of magnetic torque is to convert orbital angular momentum to rotational angular momentum (similar to the Einstein-de Haas effect [144]), causing the area enclosed by displacement current to increase dramatically. The magnitude of the magnetization is equal to the product of induced electric current and the enclosed area. For this reason, for both rectification and magnetization, the maximum enhancement depends on the ratio of the moments of intertia $I_{\perp}/I_{//}$, reflecting the importance of the ratio of the rotational and optical frequencies in these dynamic magneto-electric processes.

Regarding temporal behavior, the classical model predicted that the time required to reach steady-state behavior is strongly affected by optical field strength, librational damping rate, and the $I_{\perp}/I_{//}$ ratio of the molecular model. High field strengths speed up torque dynamics (See figure 4.24). Small damping rates result in under-damped Rabi oscillations that persist in time (See figure 4.23). High ratios of $I_{\perp}/I_{//}$ result is a reduction of the intensity needed to achieve a specified ratio of magnetic to electric scattering intensity (See figures 4.21 and 4.22).

The quantum mechanical model described in section 2.2 showed that the magneto-optical interaction is driven by dual optical fields E and H^{*}, and gives rise to an optical magnetization oriented perpendicularly to the propagation direction of linearly-polarized light in dielectric materials. The simulation results presented in this thesis suggest that an accompanying static electric dipole moment oriented along the propagation direction of linearly-polarized light is induced as well. Both these two-photon processes are to be

expected at high-intensities whenever an electric polarization is established and the duration of the interaction permits the magnetic field to exert torque on the orbital angular momentum of the excited state of a molecule.

The magnetic portion of the interaction Hamiltonian (equation 2.25) that governs the second step of the magneto-electric interaction was shown in chapter 2 to obey Parity-Time symmetry. This in itself showed that the M-E process is universally allowed at the molecular level despite the fact the interaction is second-order with respect to the incident field. Although the susceptibility for transverse magnetic moments is zero in unperturbed, centrosymmetric systems, it becomes non-zero in the face of Parity-Time symmetry. The initial parity of the system is broken dynamically by the action of the optical magnetic field.

By comparing the two theoretical models one notices that each classical dipole moment behaves similarly to its quantum counterpart. As seen in figure 4.29, the first order electric dipole moment is linear in the incident electric field. The second order electric dipole moment is quadratic in the incident electric field until it reaches a point of saturation where it stops growing. The total magnetic moment, however, displays different behavior between the two models at low intensities. In the quantum model, the magnetic moment begins growing quadratically, becomes cubic at higher intensities, and then saturates linearly to follow the progression of the electric dipole moment. In the classical model, the quadratic growth is absent and only the cubic region of growth is seen. This difference between models is because the quadratic portion in the quantum model is from a 2-photon coherence between states 1 and 3 in figure 5.1 [7]. Such states do not exist in classical physics.

In summary, the unexpected and comparatively large magnetic scattering reported here can be fully accounted for by magnetic torque dynamics in the excited states of molecules at the field strengths used in our experiments. Rotation/libration features shown in cross-polarized spectra are qualitatively consistent with a theoretical picture of magneto-electrically induced molecular rotations. Additionally, fair agreement was found between theoretical expectations and comparative magnitudes of scattering in different tetrachlorides based on fundamental properties of these molecules, such as their rotation frequencies and transition moments. This is discussed further in section 5.2. In contrast to these points of agreement, none of these features can be explained by all-electric processes on the ultrafast timescale of our experiments.

Portions of the results of this thesis appear in the following publications. The intensity-dependent magneto-electric scattering for GGG and Quartz from Chapter 4 are detailed in "Optical magnetization, Part I: Experiments on radiant optical magnetization in solids" [130]. The quantum theory introduced in Chapter 2 and analyzed in Chapter 4 initially appeared in "Optical magnetization, Part II: Theory of induced optical magnetism" [7]. An

earlier atomic version was published in "Dynamic symmetry-breaking in a simple quantum model of magneto-electric rectification, optical magnetization, and harmonic generation" [134]. PT-symmetry analysis of the quantum theory (Chapter 2) along with results of the torque-enhanced Lorentz oscillator model are presented in "Optical magnetization, Part III: Theory of molecular magneto-electric rectification" [139]. The nonlinear optical susceptibility derivation from Chapter 2 appeared in "Molecular Design Principles for Magneto-Electric Materials: All-Electric Susceptibilities Relevant to Optimal Molecular Chromophores" and its supplementary information [138].

5.2 Detailed experimental comparisons of materials

Based on figure 4.30, the intensity at which the magnetization saturates, I_{sat}, is proportional to rotation/libration frequency ω_ϕ in both quantum and classical theory. In molecular liquids the rotation frequency is $\omega_\phi = \hbar/I_\perp$, so an inverse dependence on moment of inertia is expected. In solids there is no well-defined moment of inertia at the molecular level. Nevertheless librational frequencies associated with localized optical centers are well-defined and may be represented by ω_ϕ, or a distribution of librational frequencies. Hence the intensity requirement for saturated magnetization can be expected to drop in proportion to such characteristic frequencies both in liquids and solids. Other structural and chemical aspects of the medium, such as the strength of the transition dipole, orientational damping and electron delocalization can be expected to affect magneto-electric magnetization as well.

More explicitly, predictions for the magnitude of magneto-electric magnetization were developed in section 4.1.4. A "figure of merit" based on the quantum theory developed here was shown to be in substantial agreement with experimental trends in scattering strengths among tetrachloride compounds (figure 4.1). This provided support for the theoretical implication that magnetization has inverse proportionality to rotation frequency and direct proportionality to the strength of the transition dipole. It was also consistent with a proportionality to the number of electrons in the system. The level of magnetization from smallest to largest was $CCl_4 \rightarrow SiCl_4 \rightarrow GeCl_4 \rightarrow SnCl_4$. It was possible to compare experimental values of magnetization for the tetrachloride series with the theoretical values predicted by the FOM in table 4.6. The experimental ratios are taken as the ratio between the quadratic extrapolations for each molecule at a fixed incident intensity. The theoretical ratios are the squared value of the FOMs from table 4.6. From the comparison in table 5.1, there is reasonable agreement for the ratios of $SiCl_4/CCl_4$ and $GeCl_4/SiCl_4$. A discrepancy appears in the comparison for $SnCl_4/GeCl_4$, but this is ascribed to the very large uncertainty associated with both the FOM and parameter determinations for these materials.

Table 5.1: Comparison of theoretical and experimental values of magnetization in Tetrachloride molecules.

	Predicted	Measured
$SiCl_4/CCl_4$	400	140
$GeCl_4/SiCl_4$	3	5
$SnCl_4/GeCl_4$	11	0.4

For the orthosilicate series, molecular properties needed to calculate the FOM were not available in the literature, but some conclusions can still be drawn. Experimentally, it was seen that the level of magnetization from smallest to largest was $TEOS \rightarrow TPOS \rightarrow CCl_4 \rightarrow TMOS$. Looking at the available parameters listed in tables 4.10, 4.11, and 4.12, this progression suggests that the strength of the transition dipole constitutes an important factor. By looking at just the rotation frequency, one would expect TEOS to have just as large a response as TMOS, but this is not the case. This suggests an effective rotation frequency may have to be calculated for molecules which have multiple axes of rotation, such as in TEOS and TPOS.

5.3 Additional discussion on depolarized light scattering

Although there are many causes of depolarized light scattering in the literature, only induced magnetization due to a 2-photon magneto-electric interaction at the molecular level is consistent with all aspects of our ultrafast light-scattering experiments. This section discusses many possible depolarized contributions and seeks to dispel any doubt on the origin of the experimental results of this thesis.

The electric dipole approximation is well-obeyed at low intensities in liquids like CCl_4. The small amount of depolarization observed in early polarized light scattering experiments, described in section 1.2.1.4, is ascribed in the literature to electric dipole-dipole coupling in collisions [55]. In some cases, an unknown reorientation contribution was supposed [74, 184]. The early light scattering literature (and our data) shows no evidence of induced magnetic scattering at low intensities [73, 74, 80], apart from one report in CCl_4 of low-intensity magnetic scattering that is inconsistent with prior experimental findings as well as our own experiments [53].

Prior definitions, measurements, and analysis of depolarization ratio were published without any consideration of the resulting radiation patterns. Even to this day, depolarized light scattering is used to refer to the specific case of fixed, vertically-polarized incident light that scatters from a sample and is subsequently analyzed using a horizontal polarizer

at 90 degrees to the direction of propagation, notated as I_{VH} or H_v [79]. Hence, information is not generally available for earlier experiments regarding whether "depolarization" of scattering referred to completely unpolarized signal components or dipole radiation that was cross-polarized. An important experimental advance in this work was the explicit mapping and separation of these components in scattered light measurements (as in figure 3.21). In this work, the scattered light was separated into "polarized" and "unpolarized" components. The polarized component is one that is transmitted by a horizontal analyzer but displays a $\cos^2(\theta)$ dependence on the orientation of the input field. The unpolarized component is a special case of depolarized light scattering where the entire radiation pattern is mapped and found to be independent of angle.

Many mechanisms for depolarization were already considered in the introduction of this thesis. They are summarized for convenience and then discussed in greater depth below. Depolarization mechanisms include:

i. Dipole-induced dipole effect [61, 55],

ii. Collision-induced molecular frame distortion [62],

iii. Anisotropy induced by changes in microscopic stress (shear waves) [67],

iv. Electric torque-induced reorientation of an anisotropic molecule (reorientational optical Kerr effect) [65],

v. Electric torque acting on Kerr-induced anisotropy in isotropic molecules (generalized optical Kerr effect) [185, 186],

vi. Third-order anisotropy in which depolarized input is regarded as a cross-polarized probe field in a four-wave-mixing process [187], and

vii. Reorientation induced by a magneto-electric process at the molecular level [7].

The depolarization mechanisms enumerated above can be compared with experimental and theoretical results reported in chapter 4. It is helpful to remember the depolarization ratio, where $\rho_u = (H_h + H_v) / (V_v + V_h)$. A lower value of ρ_u indicates that less light is being "depolarized" into the cross-polarization channel. At low-powers of incident light, where the electric-dipole approximation is well-obeyed, isotropic liquids have been shown to have very small depolarization ratios such as in CCl_4 ($\rho_u = 0.053$) and n-hexane ($\rho_u = 0.085$). Slightly anisotropic liquids have moderate depolarization ratios such as in $CHCl_3$ ($\rho_u = 0.22$) and C_6H_6 ($\rho_u = 0.43$). Highly anisotropic liquids have large depolarization ratios such as in CS_2 ($\rho_u = 0.67$) and $(C_6H_5)_2CO$ ($\rho_u = 0.72$) [80].

In carbon tetrachloride, dipole-induced dipole effect accounts for very little depolarization even when the optical excitation is continuous. However, the depolarization ratios observed in this work at intensities near 2×10^8 W/cm^2 (such as figure 2a of reference [130]) are closer to $\rho_u \approx 0.24$ and are observed on a timescale ($<$ 150 fs) much shorter than any collision-related reorientation ($\tau_{reor} > 1$ ps). Therefore, reorientational collision effects play a negligible role in the large cross-polarized signal reported here.

In anisotropic molecules, the effects of molecular frame distortion, shear waves, and electric torque-induced reorientation dominate at low to mid-intensities. Since all of the materials presented in this work were isotropic, these effects are also not the cause of the large cross-polarized signals observed here.

The next two possible contributions are the electric torque acting on Kerr-induced anisotropy in isotropic molecules and a third-order anisotropy seen as part of a four-wave-mixing process. All-electric third-order nonlinearities require higher intensities than in the present work. The experiments presented here are in the range of 10^6-10^{10} W/cm^2. The third-order anisotropy shown by Benis et al. [187] used an incident intensity of 2.5×10^{11} W/cm^2 and the optical Kerr effect reported by Yu et al. [186] was for 1.2×10^{11} W/cm^2. The Yu experiment in GGG used an incident laser intensity 1000 times larger than those used here, shown in figure 4.4. Therefore, it is reasonable to expect that third-order optical Kerr effects can be neglected as contributions to the cross-polarized scattering observed here on the basis of intensity requirements alone. However, let us suppose that we *could* detect a third-order signal and continue with our analysis.

These third-order processes can be expressed in the general form

$$P^{(3)}(\omega) = \epsilon_0 \chi^{(3)} E_{probe} E_{pump} E^*_{pump}, \tag{5.1}$$

where ϵ_0 is the electric permittivity of free space, $\chi^{(3)}$ the third-order nonlinear optical susceptibility tensor, and E_i the electric field strength of either the pump or probe fields. Since polarization mapping onto the detection plane is what is measured in our scattering experiments, we first consider terms which theoretically contribute to $P^{(3)}_x(\omega)$, which is the co-polarized signal detected with a (vertical) linear polarizer transmitting along $\hat{x}$, and thus expand equation 5.1 as

$$\begin{aligned} P^{(3)}_x(\omega) =& \epsilon_0 \big[\chi^{(3)}_{xxxx} E_{probe,x} E_{pump,x} E^*_{pump,x} + \chi^{(3)}_{xxyy} E_{probe,x} E_{pump,y} E^*_{pump,y} \\ &+ \chi^{(3)}_{xyxy} E_{probe,y} E_{pump,y} E^*_{pump,y} + \chi^{(3)}_{xyyx} E_{probe,y} E_{pump,y} E^*_{pump,x}\big]. \end{aligned} \tag{5.2}$$

Equation 5.2 can be re-written in terms of direction cosines for the electric field vectors of the pump and probe fields. Since the pump field is confined to being linearly polarized in

the $\hat{x}$-$\hat{y}$ plane, it can be written as $E_{pump,x} = |E_{pump}|\cos(\theta)$ and $E_{pump,y} = |E_{pump}|\sin(\theta)$. The probe is due to a random collisional dipole-dipole interaction. Consequently, the angle α makes with respect to the $\hat{x}$-axis is random. Therefore, equation 5.2 reduces to

$$\begin{aligned} P_x^{(3)}(\omega) =& \epsilon_0 \big[\chi_{xxxx}^{(3)}|E_{probe}||E_{pump}|^2\cos(\alpha)\cos^2(\theta) \\ &+ \chi_{xxyy}^{(3)}|E_{probe}||E_{pump}|^2\cos(\alpha)\sin^2(\theta) \\ &+ \chi_{xyxy}^{(3)}|E_{probe}||E_{pump}|^2\sin(\alpha)\cos(\theta)\sin(\theta) \\ &+ \chi_{xyyx}^{(3)}|E_{probe}||E_{pump}|^2\sin(\alpha)\cos(\theta)\sin(\theta)\big] \end{aligned} \tag{5.3}$$

Collecting the cosine terms, $P_x^{(3)}(\omega)$ simplifies further to

$$\begin{aligned} P_x^{(3)}(\omega) =& \epsilon_0\chi_{xxyy}^{(3)}|E_{probe}||E_{pump}|^2\big[3\cos(\alpha)\cos^2(\theta) \\ &+ \cos(\alpha)\sin^2(\theta) + \sin(\alpha)\sin(2\theta)\big]. \end{aligned} \tag{5.4}$$

To the extent that random collisions randomize α over its range from 0 to 2π, the polarization in equation 5.4 must be summed over possible values of α and reduce equation 5.4 further.

$$\left\langle P_x^{(3)}(\omega)\right\rangle_\alpha = \epsilon_0\chi_{xxyy}^{(3)}|E_{probe}||E_{pump}|^2\big[0\big] = 0, \tag{5.5}$$

since $\langle\cos(\alpha)\rangle_\alpha = \langle\sin(\alpha)\rangle_\alpha = 0$. Similarly for the cross-polarized signal, detectable with a (horizontal) linear polarizer transmitting along $\hat{z}$, the angle-averaged polarization is zero.

$$\left\langle P_z^{(3)}(\omega)\right\rangle_\alpha = \epsilon_0\chi_{zzxx}^{(3)}|E_{probe}||E_{pump}|^2\left\langle\cos(\alpha)\right\rangle_\alpha = 0 \tag{5.6}$$

The third case of $P_y^{(3)}(\omega)$ does not radiate in the direction of the detector and is hence ignored in this analysis. Therefore, this shows that to the extent that the collisional interactions are random, the optical Kerr effect does not contribute to measured signals under the conditions of our experiments.

Overall, the scattered light radiation intensities potentially observable from a Kerr-induced anisotropy have cubic dependence on the intensity of the pump field. Their contributions to the radiation patterns depend on the exact origin of the probe field. Since the probe field is derived from the pump field, the detected radiation intensity would show a dependence $\left\langle\bar{S}_x\right\rangle \propto |I_{pump}|^3$ for a vertical analyzer. The vertically-analyzed signals observed in this thesis were consistently linearly dependent on incident intensity however. Any possible contribution of a pump field acting as its own probe field is therefore negligibly small on an experimental basis. Moreover, if the probe is of collisional origin, the polarization due to the Kerr effect averages to zero as shown by equations 5.5 and 5.6, as-

suming a perfectly randomized set of angles, α: $\langle \bar{S}_x \rangle = \langle \bar{S}_z \rangle = 0$. Therefore, we conclude that the optical Kerr effect does not contribute to either the co- or cross-polarized radiation patterns when the probe is purely of collisional origin, at the relatively low intensities in our experiments.

The only candidate process that can explain the depolarized scattering seen here is reorientation induced by a magneto-electric process at the molecular level. This is a unique stimulated process driven by simultaneous action of the E and H components of light. The magnetic field component of the incident light torques upon the molecules, causing prominent rotational features that are uniquely visible in the cross-polarized light spectrum in section 4.1.3. One is lead to the conclusion that induced magnetization due to a 2-photon magneto-electric interaction at the molecular level is the only process consistent with all aspects of the ultrafast light-scattering experiments reported here.

5.4 Application of theoretical models to material design

The theory developed in this thesis, is applicable to future material design. The following subsection discusses the results from the nonlinear optical susceptibility and possible future designs for nonlinear materials. The subsequent subsection presents a discussion of quantum mechanical predictions of magnetization, making connections to viscosity and relaxation rate.

5.4.1 Predictions from nonlinear optical susceptibility for design of nonlinear materials

The connection between M-E susceptibilities and third-order all-electric susceptibilities established in section 2.3 makes it possible to develop design criteria for enhanced M-E magnetization and rectification by maximizing their respective third-order tensor components. In order to formulate practical design guidelines, a sum-over-states expression for the elements of χ^3 to valence-bond charge-transfer (VB-CT) models was applied. A complete description is given in reference [138].

In order to enhance magnetization, M_{NL}, the diagonal tensor component $\chi^{(3)}_{xxxx}$ (or the second hyperpolarizability element γ_{xxxx}) needs to be maximized. Fortunately, γ_{xxxx} governs the response of many third-order Nonlinear Optics (NLO) molecules. Chromophores, a type of molecule that has a electronic transition resonance in the visible spectrum, are known to have an easily-manipulated and large hyperpolarizability element [188]. Based on equation 2.70, it can be assumed that molecules which exhibit large diagonal third-order

nonlinearities are likely to also have a large M-E magnetization coefficient. For example, cyanines and typical 1-D-donor-π-acceptor chromophores are predicted to be good candidates, given their very large values of $\chi^{(3)}_{xxxx}$.

In the case of M-E rectification, P_{NL}, the guidelines for optimal material synthesis are more challenging to formulate. Historically, little attention has been given to off-diagonal elements of γ since they have had no specific use in conventional NLO, resulting in a need for new analysis. The analysis of γ_{zzxx} in VB-CT models has identified rational design criteria for three common structures, which are by no means exhaustive [138]. Specifically,

i. For Λ-shaped, X-shaped, and octopolar molecules, γ_{zzxx} is proportional to the fourth power of the static electric dipole moment. Including strong donor and acceptor moieties and extending the charge transfer spatial length will increase the response insofar as it does not negatively impact valence band / charge transfer mixing.

ii. For Λ-shaped and X-shaped chromophores, moderate to large conjugation length leads to large, positive γ_{zzxx}. For octopolar molecules, the conjugation length simply needs to be maximized. In both cases, it is clear that enhanced charge transfer character in the ground state must be controlled by either lowering the charge transfer state energy or raising the energy of the valence band state.

iii. Disrupting conjugation shows promise in all geometries as a tool for controlling the charge transfer character of the molecule.

Excited state charge transfer dynamics have not been addressed in this analysis, although they are likely to be an important component of the M-E response. It is also worth re-emphasizing that the equivalence relations given in equations 2.56 and 2.70 imply that magneto-electric rectification and magnetization are universally allowed in dielectric materials, no matter the symmetry of the system.

5.4.2 Predictions from quantum and classical theory

Additional insight can be drawn into material response from the quantum and classical theories. By further exploring the dependence on rotation frequency and magnetic damping for simple molecular liquids, a connection can be drawn between the magnetic relaxation and that of viscosity and microviscosity [176]. τ_{reor} can be calculated from the Debye-Stokes-Einstein formula as $\tau_{reor} = (4\pi\eta a^3 f_r) / (3kT)$, where η is the viscosity, a is the molecular radius, and f_r is the microviscosity factor. Since $\Gamma^{(m)} = 2\pi / (\tau_{reor})$, then $\Gamma^{(m)} = (3kT) / (2\eta a^3 f_r)$. Therefore, the more viscous the material, the smaller the magnetic relaxation.

Additionally, the PT symmetry of the magnetic interaction Hamiltonian implies that magneto-electric rectification and magnetization are universally allowed in dielectric materials, regardless of the phase and state of the matter. Magneto-electric effects ought to be able to occur in liquids *and solids*, regardless of their crystallographic symmetry.

Now, to bring everything together, the major conclusions from this thesis can be summarized as the following:

i. Torque is required for the enhancement of magnetization.

ii. Experimental evidence supports the exact quantum mechanical theory for these effects.

iii. By spectrally resolving magneto-electric interactions, it is possible to observe an energy shift that is correlated with molecular rotations.

iv. Due to the parity-time symmetry of the magnetic interaction, magneto-electric effects should occur universally.

v. By employing a classical model, the temporal dynamics of magneto-electric effects at the molecular level can be predicted.

5.5 Future work

Although this dissertation advanced the theory of and experimental evidence for dynamic magneto-optic effects, including radiant optical magnetization, there is still a wealth of areas left to explore. To conclude, suggestions are given for future work on the theory of magneto-electric effects at the molecular level and experimental efforts to understand them.

5.5.1 Theory

The classical molecular model developed here, which includes the Lorentz force and magnetic torque, permits the prediction of temporal dynamics of magneto-electric scattering. The major drawback from this model, however, is the assumption that the applied electromagnetic wave is a step function rather than a pulse as in our experiments. Currently, the pulse function (line 26 in section C.B) used in the ODE is defined as $pulseFunc = sin(\omega * t)$. In future work, the pulse function should capture the ultrafast dynamics of femtosecond laser systems.

One way to accommodate simulations with ultrashort pulses would be to incorporate an envelope factor in the specified pulse function. For example, one possible pulse function

could be

$$pulseFunc = exp(-2*log(2)*(t-2.5*tauP).^2/tauP^2).*cos(w*(t-2.5*tauP)), \quad (5.7)$$

where $tauP$ is the pulse duration. This would enable the oscillator model to provide more realistic simulations of response to Dirac delta-like input. Preliminary simulations were run with the pulse function listed in equation 5.7 and resulted in the dynamics depicted in figures 5.3 and 5.4. Note the delay between ED and MD in figure 5.3b as well as the relaxation of the charge separation is figure 5.4a. Additional simulations should be run in order to more fully understand the effect different pulsed input has on the torque-enhanced Lorentz oscillator model presented here.

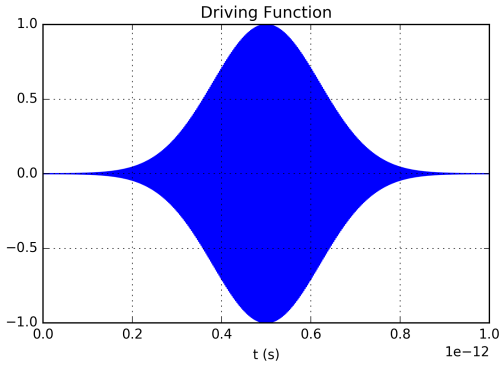

Figure 5.2: Example of pulse function for Lorentz oscillator model.

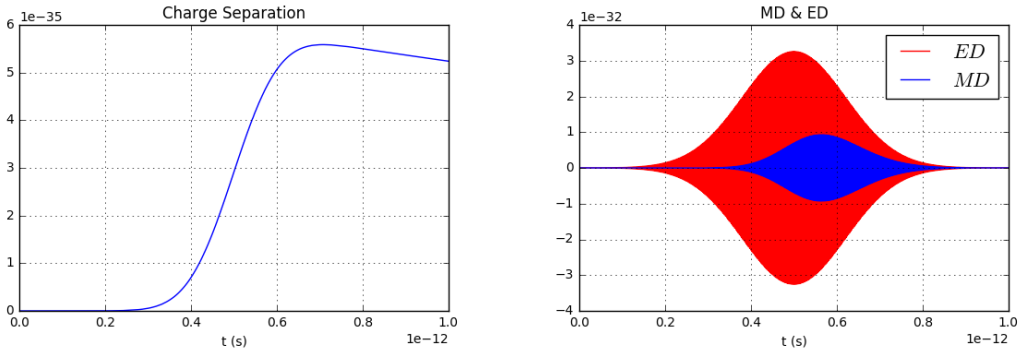

Figure 5.3: Comparison of ED, MD (l) and charge separation (r) for LOM driven by a femtosecond pulse.

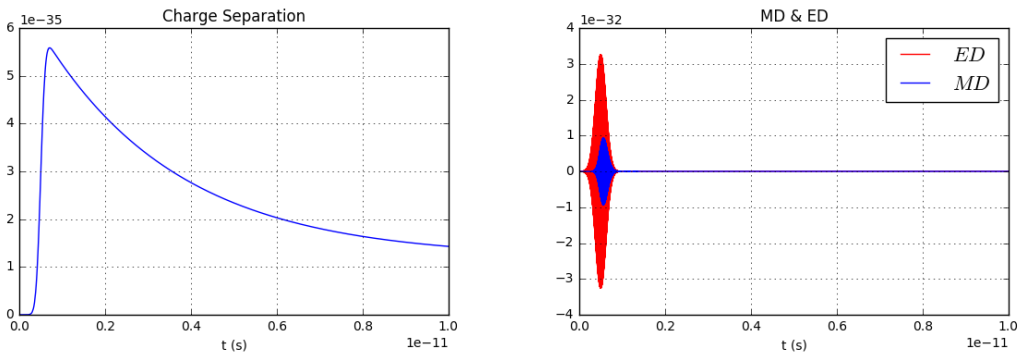

Figure 5.4: Comparison of ED, MD (l) and charge separation (r) for LOM driven by a femtosecond pulse.

5.5.2 Experiments

For future studies of magneto-electric magnetization at the molecular level, the most promising path of further exploration is spectrally-resolved experiments along the lines of those presented earlier in section 4.1.3. Without the necessity of time-resolving the scattering dynamics, they reveal frequency-domain aspects of the dynamics. Thus, they enable important tests of the material dependence of radiant optical magnetization and should be extended to new compounds.

Spectroscopy experiments could be undertaken on materials at different temperatures in order to better understand the role viscosity has upon the magnetic relaxation rate of molecular compounds. Finally, in view of the substantial enhancement of dynamic magnetization that is provided by the coupling of orbital and angular momentum, it would be interesting to extend experiments to systems with non-zero spin.

Appendix A

Initialization of SMC100PP rotation stages

The SMC100PP are rotation stages from Newport. For the experiment to run properly, "zero" locations for each rotation stage must be recorded and entered into the data acquisition control program.

A.A Polarizers

The most important quality of a polarizer is how well it extinguishes unwanted polarizations. In this case, the polarizer claims 10^5:1 polarization extinction. After the polarizer is mounted in a PR50PP rotation stage and controlled by a SMC100PP motor controller, the location where the polarizer passes horizontally polarized light needs to be calibrated.

A.A.1 Verify Extinction Rate

For this procedure, one needs a polarizer, a linearly polarized source and a power meter.

i. Mount polarizer in a manual or automatic rotation stage.

ii. Arrange set-up as seen in Figure A.1.

iii. Turn polarizer and measure the maximum and minimum power transmitted.

iv. Compare the power extrema. If the ratio is approximately 10^5:1, the polarizer is correct.

A.A.2 Calibrate Polarizer Zero for SMC100PP

For this calibration, one needs a polarizer, a iris or pinhole, and a laser.

i. Mount polarizer in the PR50PP rotation stage.

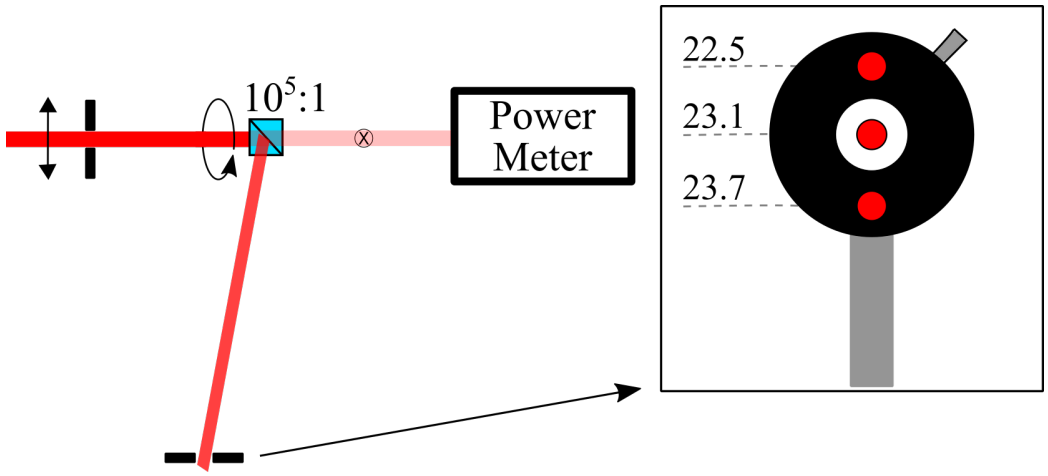

Figure A.1: Set-up for verification of the extinction rate of the polarizer and for locating the zero position on the mounted rotatable polarizer. Inset shows three example beam locations on the alignment iris, where 23.1 is the optimal SMC position. The "Analyzer Zero" value is then 113.1.

ii. Arrange set-up as seen in Figure A.1.

iii. Use the SMC100PP rotation controller to rotate the polarizer to where the rejected beam of light is directed about parallel to the table.

iv. Take the iris which is at the same height as the input beam and place it down the table in the path of the rejected beam.

v. Slowly rotate the polarizer until the rejection beam passes through the pinhole. If the polarizer is rejecting vertical light, this arbitrary rotation unit is the "polarizer zero for passing horizontal light".

vi. To get the Analyzer Zero location for detecting an Electric Dipole, add or subtract 90 units to this number and save it as the default value in the computer control program (detailed in figure 3.20).

A.B Waveplates

Just as with the polarizer, once the waveplates are mounted into the PR50PP rotation stage and controlled by a SMC100PP motor controller, the internal zero location needs to be initialized. The waveplate used for dipole mapping (WP2) needs the location of where the fast axis is at zero (the position where horizontal polarization is rotated to be vertical

polarization). The waveplate used for intensity adjustments (WP3) needs the location of where the horizontally polarized beam is undeviated.

The items needed for this initialization are the mounted waveplates, a horizontally polarized laser source, a polarizer, and a power meter.

i. Arrange the equipment as shown in Figure A.2. If laser is not horizontally polarized, use a second polarizer to make it so.

ii. Set the analyzing polarizer to pass horizontally polarized light. Rotate the waveplate until the maximum amount of power transfered is observed. Note this number.

iii. Change the analyzing polarizer to pass vertically polarized light. Rotate the waveplate until the maxium amount of power transfered is observed. This location should be 45 units away from the previous location.

iv. Repeat procedure with other waveplate.

v. Save the location that maximally passes horizontally polarized light as the zero for WP3. Save the location that maximally passes vertically polarized light as the zero for WP 2.

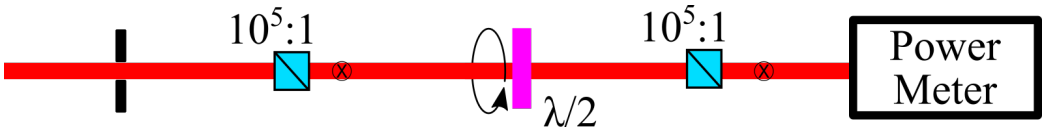

Figure A.2: Set-up for locating the zero position on the mounted rotatable wave plate, where the half-wave plate does not rotate the polarization of the incident laser beam.

Appendix B

MATLAB code for data acquisition

B.A Main program

```
1 %% Vmes_experimentMasterCode_LargeCountsXYRT
2 % Elizabeth Dreyer
3 % 2017-04-12
4 % Vitara Magneto-Electric Scattering Experiment
5 % Purpose: The purpose of this program is to control the magneto-
      electric scattering
6 % experiment.
7 % Input Variables:
8 %  Header Input (File name, Sample, PMT Voltage, PMT
      Amplification...)
9 %  Intensity Input(Waveplate address, zero location, points on
      intensity sweep, intensity minimum, intensity maximum)
10 %  Zeroing (Analyzer Address, Waveplate Address, Analyzer Zero,
      Waveplate Zero)
11 %  Movement (Points on Analyzer Sweep, Points on Waveplate sweep,
       Half Analyzer)
12 %  Data Collection (Discriminator level, Collection Time, Number
      of Periods)
13 %  Instrument locations (Sr400, SMC, PM100D, Shutter)
14 % Output Variables: Experiment time, Matlab data file
15 % Needed files:
16
17 %% Clear workspace
18 clc, clear;
19 Vmes_PiUsb_func(0)  %Start with shutter closed
```

```
20 zeroLIA = 11;   %Set all dark counts to zero and don't wait for
       them.
21 tic
22
23 %% non-GUI input of variables
24 % Header Input
25 folderName = uigetdir('C:\Users\eecs-rand-02\Documents\
       Vitara_Experiment\MES_Data');
26 recipient = {'efcloos@umich.edu'};
27 sampleName = 'CCl4-Oct9'; %Sample name
28 chopFreqHz = '1100';  %Chopper frequency in Hz
29 timeConstant = '1s';  %Time constant of Lock-In Amplifier
30 fwhmTFemtoSec = '15.7'; %Pulse duration at sample
31 fwhmXMillimeter = '.050'; %FWHM of pulse at sample
32 fwhmYMillimeter = '.031'; %FWHM of pulse at sample
33 irisINMillimeter = '5mm'; %Size of clipping iris
34 irisSAMillimeter = 'open';  %Size of solid angle iris
35 preAmp = '9'; %Amplification from preamp
36 otherNotes = 'PD_100umSlit';  %Any other notes
37
38 % SMC Input
39 smcAnalyzerAdd = 1; %SMC Address for Analyzer
40 smcAnalyzerZer = 42;  %Location for passing vertical pol.
41 smcRotationAdd = 2; %SMC Address for Pol. Rotation WP
42 smcRotationZer = 27.4;  %Switches Horiz. to Vert. pol.
43
44 % Intensity Input
45 % Note: 1 point equals 0.5 degree rotation
46 GWheelHighStart = 585;
47 GWheelHighEnd = 806;
48 GWheelLowStart = 1;
49 GWheelLowEnd = 378;
50 dN = 806/360;
51
52 intensityODdelta = .1;  %Change in intensity in OD
53 intensityOD1 = 0; %Max. intensity in OD
54 intensityOD2 = 2.6; %Min. intensity in OD
55 intensitySweepPts = (intensityOD2 - intensityOD1)/
```

```
    intensityODdelta;
intStr = strcat(num2str(intensityOD1),32,'to',32,num2str(
    intensityOD2),32,'by',32,num2str(intensityODdelta));

% Movement Input
analyzerSweepPts = 4; %No. of analyzer points, e.g. 4
analyzerHalf = 1; %Do you want half the number of analyzer pts? Y
    : 1, N: 0
rotationSweepPts = 36;  %No. of WP rotation points, e.g. 36

% Data Collection Input
sr830CollPts = 30;  %No. of LIA points to average
sr830timeConstantSec = 1; %Time constant of LIA
sr830timeConstantNum = '10';
% Note: 0=10us; 1=30us; 2=100us; 3=300us; 4=1ms; 5=3ms; 6=10ms;
    7=30ms; 8=100ms; 9=300ms; 10=1s; 11=3s; 12=10s; 13=30s;
% Note: If gain is greater than 1 second, the autogain will do
    nothing!

pause(1e-2);
%% Instrument Locations
% sp = instrhwinfo('serial'); gp.ObjectConstructorName
% Display serial location
sr830Location = 'com6';
smcInstrLoc = 'com5';

%% Initialize Data File
fileStartTime = datestr(now,'yyyymmdd_HHMM');
fileName = strcat(sampleName,'_',otherNotes,'_',fileStartTime,'.
    txt');
pathName = strcat(folderName,'\',fileName);
fileID = fopen(pathName,'wt');

% Note: tabs are added in to make data file into a table
tab1Str = '%s\t';
for loc2 = 1:(4*sr830CollPts+3)
    tab1Str = strcat(tab1Str,'\t');
end
```

```
88 tab1Str = strcat(tab1Str,'\r\n');   %Create number of initial
       tabs
89 fprintf(fileID,tab1Str,fileName);
90
91 %% Initialize Equipment
92 % Here we initialize and zero all SMC controllers and pause for
       the correct amount of time to zero the devices
93 smcAnalyzerCurrentPos = Vmes_Smc_func(smcAnalyzerAdd,strcat(
       num2str(smcAnalyzerAdd),'TP?'),1);
94 smcAnalyzerDiff = abs(smcAnalyzerCurrentPos - smcAnalyzerZer);
95 if smcAnalyzerDiff ~= 0
96     smcAnalyzerTime = Vmes_Smc_func(smcAnalyzerAdd,strcat(num2str
           (smcAnalyzerAdd),'PT',num2str(smcAnalyzerDiff),'?'),1);
97 else
98     smcAnalyzerTime = 0;
99 end
100
101 smcRotationCurrentPos = Vmes_Smc_func(smcRotationAdd,strcat(
       num2str(smcRotationAdd),'TP?'),1);
102 smcRotationDiff = abs(smcRotationCurrentPos - smcRotationZer);
103 if smcRotationDiff ~= 0
104     smcRotationTime = Vmes_Smc_func(smcRotationAdd,strcat(num2str
           (smcRotationAdd),'PT',num2str(smcRotationDiff),'?'),1);
105 else
106     smcRotationTime = 0;
107 end
108
109 % Zero rotators
110 Vmes_Smc_func(smcAnalyzerAdd,strcat(num2str(smcAnalyzerAdd),'PA',
       num2str(smcAnalyzerZer)),0);
111 Vmes_Smc_func(smcRotationAdd,strcat(num2str(smcRotationAdd),'PA',
       num2str(smcRotationZer)),0);
112
113 % Pause
114 pause(max(smcAnalyzerTime,smcRotationTime));
115
116 % Move wheel to initial intensity position
117 intensityNowOD = intensityOD1;
```

```
118 intStr = strcat(num2str(intensityOD1),32,'to',32,num2str(
      intensityOD2),32,'by',32,num2str(intensityODdelta));
119 intDelta = round(360/4*intensityNowOD);
120 if (0 <= intDelta) && (intDelta <= (GWheelHighEnd-GWheelHighStart
      )/dN)
121     intensityTheta = GWheelHighStart+dN*intDelta;
122 elseif ((GWheelHighEnd-GWheelHighStart)/dN < intDelta) && (
      intDelta <= 360)
123     intensityTheta = dN*intDelta-(GWheelHighEnd-GWheelHighStart);
124 end
125 Vmes_PiWheel_func(1,intensityTheta);
126
127 % Send initial SR830 commands to configure
128 Vmes_PiUsb_func(1);
129 pause(sr830timeConstantSec*30); %Pause to stabilize the one light
      count
130 Vmes_sr830_config_func(sr830timeConstantNum,sr830timeConstantSec)
      ;
131
132 %% Take Data Loop
133
134 % Intensity while loop
135 % Decide Loop parameters
136 AnNum = 0; WpNum = 0;
137 if (analyzerSweepPts==1) && (rotationSweepPts==1)
138   AnNum = 1; WpNum = 1;
139 elseif (analyzerSweepPts==1) && (rotationSweepPts~=1)
140   AnNum = 1; WpNum = rotationSweepPts;
141 elseif (analyzerSweepPts~=1)&&(rotationSweepPts==1)&&(
      analyzerHalf==0)
142   AnNum = analyzerSweepPts; WpNum = 1;
143 elseif (analyzerSweepPts~=1)&&(rotationSweepPts==1)&&(
      analyzerHalf==1)
144   AnNum = analyzerSweepPts/2; WpNum = 1;
145 elseif (analyzerSweepPts~=1)&&(rotationSweepPts~=1)&&(
      analyzerHalf==0)
146   AnNum = analyzerSweepPts; WpNum = rotationSweepPts;
147 elseif (analyzerSweepPts~=1)&&(rotationSweepPts~=1)&&(
```

```
    analyzerHalf==1)
148   AnNum = analyzerSweepPts/2; WpNum = rotationSweepPts;
149 end
150
151 % Write data file header
152 fileHeader2 = [{'Sample Name';'FWHM_t (fs)';'FWHM_x (mm)';...
153 'FWHM_y (mm)';'Amp (E-x)';'Iris In (mm)';'Iris SA (mm)';...
154 'Chop Freq (Hz)';'Time Const.';'Coll. Pts';...
155 'Wave Plate Pts';'Analyzer Pts';'Anazlyer 0';'Rot. WP 0';'Int. #'
    ;'Intensity'},...
156 {sampleName;fwhmTFemtoSec;fwhmXMillimeter;fwhmYMillimeter;preAmp;
    irisINMillimeter;...
157 irisSAMillimeter;chopFreqHz;timeConstant;num2str(sr830CollPts)
    ;...
158 num2str(WpNum);num2str(AnNum);num2str(smcAnalyzerZer);num2str(
    smcRotationZer);...
159 num2str(intensitySweepPts);intStr}];
160
161 tab2Str = '%s\t%s\t';
162 tab0Str = '\t\t';
163 for loc = 1:(4*sr830CollPts+2)
164   tab2Str = strcat(tab2Str,'\t');
165   tab0Str = strcat(tab0Str,'\t');
166 end
167 tab2Str = strcat(tab2Str,'\r\n');      %Create number of header
    tabs
168 tab0Str = strcat(tab0Str,'\r\n');      %Create number of blank row
     tabs
169
170 [nrows,ncols] = size(fileHeader2);
171 for row = 1:nrows
172   fprintf(fileID,tab2Str,fileHeader2{row,:});
173 end
174
175 %% Intensity Loop
176 % Calculate Intensity loop parameters
177 cnt = 0;
178 while intensityNowOD <= (intensityOD2)
```

```
179   cnt = cnt+1;
180   if zeroLIA == 1
181     drkArray = zeros([sr830CollPts,1]);
182     xDataDrkCnt=drkArray;yDataDrkCnt=drkArray;rDataDrkCnt=
          drkArray;thDataDrkCnt=drkArray;
183     Vmes_PiUsb_func(0)  %Double check that the shutter is closed
184     pmBufferclear = Vmes_Pm100USB_func;
185     pmPowerDrk = Vmes_Pm100USB_func;
186   else
187     % Take dark counts
188     Vmes_PiUsb_func(0)  %Double check that the shutter is closed
189     pause(sr830timeConstantSec*30); %Pause to stabilize the one
          dark count
190     pmBufferclear = Vmes_Pm100USB_func;
191     pmPowerDrk = Vmes_Pm100USB_func;
192     [xDataDrkCnt,yDataDrkCnt,rDataDrkCnt,thDataDrkCnt,chopFreqNow
          ]=Vmes_sr830_data_func(sr830CollPts,sr830timeConstantSec);
193   end
194   pause(1);
195
196   % Write intensity value to file
197   fprintf(fileID,tab0Str);
198   intensityNowStr = sprintf('%1.2g',intensityNowOD);
199   fprintf(fileID,tab2Str,'Intensity OD',intensityNowStr);
200
201   % Change intensity
202   intDelta = round(360/4*intensityNowOD);
203   if (0 < intDelta) && (intDelta <= (GWheelHighEnd-
        GWheelHighStart)/dN)
204     intensityTheta = GWheelHighStart+dN*intDelta;
205   elseif ((GWheelHighEnd-GWheelHighStart)/dN < intDelta) && (
        intDelta <= 360)
206     intensityTheta = dN*intDelta-(GWheelHighEnd-GWheelHighStart);
207   end
208   if intensityTheta < 1
209     Vmes_PiWheel_func(1,1); %Set position
210   else
211     Vmes_PiWheel_func(1,intensityTheta); %Set position
```

```
212   end
213   pause(sr830timeConstantSec*5);
214
215   %% Data loop Analyzer
216   smcAnalyzerDelta = 360/analyzerSweepPts;      % Calc An. delta
217   smcRotationDelta = 180/rotationSweepPts;      % Calc WP delta
218   for i = 1:AnNum
219     if AnNum ~= 1
220       % Zero waveplate
221       smcRotationCurrentPos = Vmes_Smc_func(smcRotationAdd,strcat
            (num2str(smcRotationAdd),'TP?'),1);
222       smcRotationDiff = abs(smcRotationCurrentPos-smcRotationZer)
            ;
223       if smcRotationDiff ~= 0
224         try
225           smcRotationTime = Vmes_Smc_func(smcRotationAdd,strcat(
                num2str(smcRotationAdd),'PT',num2str(smcRotationDiff
                ),'?'),1);
226         catch err
227           smcRotationTime = 10;
228         end
229       else
230         smcRotationTime = 0;
231       end
232
233       Vmes_Smc_func(smcRotationAdd,strcat(num2str(smcRotationAdd)
            ,'PA',num2str(smcRotationZer)),0);
234       pause(max(1,smcRotationTime));
235     end
236
237     % Find analyzer relative position wrt zero and determine if
          ED or MD or other (NA)
238     smcAnalyzerCurrentPos = Vmes_Smc_func(smcAnalyzerAdd,strcat(
          num2str(smcAnalyzerAdd),'TP?'),1);
239     smcAnalyzerDiffPos = smcAnalyzerCurrentPos - smcAnalyzerZer;
240     fprintf(strcat('An',num2str(smcAnalyzerDiffPos),'\n'))
241
242     if ((smcAnalyzerDiffPos < 1)&&(smcAnalyzerDiffPos > -1))
```

```
243       dipoleAbbrv = 'ED';
244     elseif ((smcAnalyzerDiffPos < 91)&&(smcAnalyzerDiffPos > 89))
245       dipoleAbbrv = 'MD';
246     elseif ((smcAnalyzerDiffPos < 181)&&(smcAnalyzerDiffPos >
          179))
247       dipoleAbbrv = 'ED';
248     elseif ((smcAnalyzerDiffPos < 271)&&(smcAnalyzerDiffPos >
          269))
249       dipoleAbbrv = 'MD';
250     else
251       dipoleAbbrv = 'NA';
252     end
253
254     % Write analyzer relative position wrt zero to file
255     tab3Str = '%s\t%s\t%s\t';
256     for loc3 = 1:(4*sr830CollPts+1)
257       tab3Str = strcat(tab3Str,'\t');
258     end
259     tab3Str = strcat(tab3Str,'\r\n');
260     smcAnalyzerDiffPosStr = strcat(num2str(smcAnalyzerDiffPos)
          ,32,32,32,32,32,32);
261     fprintf(fileID,tab3Str,'Analyzer',smcAnalyzerDiffPosStr,
          dipoleAbbrv);
262
263     % Write data header
264     xDataHdr = '';
265     yDataHdr = '';
266     rDataHdr = '';
267     thDataHdr = '';
268     for k = 1:sr830CollPts
269       xDataHdr{k} = strcat('X',num2str(k),32,32,32,32,32,32);
270       yDataHdr{k} = strcat('Y',num2str(k),32,32,32,32,32,32);
271       rDataHdr{k} = strcat('R',num2str(k),32,32,32,32,32,32);
272       thDataHdr{k} = strcat('Th',num2str(k));
273     end
274
275     fprintf(fileID,'WP\tShutter\tPower\tChop(Hz)\t');
276     for col = 1:sr830CollPts
```

```
277         fprintf(fileID,'%s\t',xDataHdr{col});
278       end
279       for col = 1:sr830CollPts
280         fprintf(fileID,'%s\t',yDataHdr{col});
281       end
282       for col = 1:sr830CollPts
283         fprintf(fileID,'%s\t',rDataHdr{col});
284       end
285       for col = 1:sr830CollPts
286         fprintf(fileID,'%s\t',thDataHdr{col});
287       end
288       fprintf(fileID,'\r\n');
289
290      %% Take data Waveplate loop
291       for j = 1:WpNum
292         % Find waveplate relative position wrt zero
293         smcRotationCurrentPos = Vmes_Smc_func(smcRotationAdd,strcat
              (num2str(smcRotationAdd),'TP?'),1);
294         smcRotationDiffPos = smcRotationCurrentPos - smcRotationZer
              ;
295         % Write waveplate relative position wrt zero to file
296         fprintf(fileID,'%3.3g\t',smcRotationDiffPos);
297         % Open shutter
298         Vmes_PiUsb_func(1);
299         % Pause to stabilize lock-in signal
300         pause(sr830timeConstantSec*10)
301         % Write shutter position to file (Open = 1)
302         fprintf(fileID,'%s\t','1');
303         % Write power level
304         pmBufferclear = Vmes_Pm100USB_func;
305         pmPowerNum = Vmes_Pm100USB_func;
306         fprintf(fileID,'%6.4g  \t',pmPowerNum);
307         % Collect data from SR830
308         [xData,yData,rData,thData,chopFreqNow]=Vmes_sr830_data_func
              (sr830CollPts,sr830timeConstantSec);
309         % Write chopper freq
310         fprintf(fileID,'%s   \t',chopFreqNow);
311         % Write transposed data to file
```

```
312         fprintf(fileID,'%-5.3g  \t', xData', yData', rData', thData
                ');
313         fprintf(fileID,'\r\n');
314         % Write waveplate relative position wrt zero to file
315         fprintf(fileID,'%3.3g\t',smcRotationDiffPos);
316
317         % Close shutter and wait to Lock-in to stabilize
318         Vmes_PiUsb_func(0)
319         % Pause to stabilize lock-in signal
320         pause(sr830timeConstantSec*10)
321         % Write shutter position to file (Closed = 0)
322         fprintf(fileID,'%s\t','0');
323         % Write power level
324         pmBufferclear = Vmes_Pm100USB_func;
325         pmPowerNumDrk = Vmes_Pm100USB_func;
326         fprintf(fileID,'%6.4g  \t',pmPowerDrk);
327         % Collect data from SR830
328         if zeroLIA ~= 1
329         [xDataDrk,yDataDrk,rDataDrk,thDataDrk,chopFreqNowDrk]=
                Vmes_sr830_data_func(sr830CollPts,sr830timeConstantSec);
330         end
331         % Write chopper freq
332         fprintf(fileID,'%s   \t',chopFreqNowDrk);
333         fprintf(fileID,'%s   \t',chopFreqNow);
334         % Write transposed data to file
335         fprintf(fileID,'%-5.3g  \t', xDataDrkCnt', yDataDrkCnt',
                rDataDrkCnt', thDataDrkCnt');
336         fprintf(fileID,'\r\n');
337
338         % Relative move waveplate
339         if j ~= WpNum
340           smcRotationCurrentPos = Vmes_Smc_func(smcRotationAdd,
                  strcat(num2str(smcRotationAdd),'TP?'),1);
341           smcRotationTarget = j*smcRotationDelta+smcRotationZer;
342           smcRotationDiff = abs(smcRotationCurrentPos -
                  smcRotationTarget);
343           if smcRotationDiff ~= 0
344             smcRotationTime = Vmes_Smc_func(smcRotationAdd,strcat(
```

```
                num2str(smcRotationAdd),'PT',num2str(smcRotationDiff
                ),'?'),1);
345           else
346             smcRotationTime = 0;
347           end
348           Vmes_Smc_func(smcRotationAdd,strcat(num2str(
                smcRotationAdd),'PA',num2str(smcRotationTarget)),0);
349           pause(smcRotationTime);
350         end
351       end
352
353       % Relative move analyzer
354       if i ~= AnNum
355         smcAnalyzerCurrentPos = Vmes_Smc_func(smcAnalyzerAdd,strcat
              (num2str(smcAnalyzerAdd),'TP?'),1);
356         smcAnalyzerTarget = i*smcAnalyzerDelta+smcAnalyzerZer;
357         smcAnalyzerDiff = abs(smcAnalyzerCurrentPos -
              smcAnalyzerTarget);
358         if smcAnalyzerDiff ~=0
359           try
360             smcAnalyzerTime = Vmes_Smc_func(smcAnalyzerAdd,strcat(
                  num2str(smcAnalyzerAdd),'PT',num2str(smcAnalyzerDiff
                  )),1);
361           catch err
362             smcAnalyzerTime = 20;
363           end
364         else
365           smcAnalyzerTime = 0;
366         end
367         Vmes_Smc_func(smcAnalyzerAdd,strcat(num2str(smcAnalyzerAdd)
              ,'PA',num2str(smcAnalyzerTarget)),0);
368         pause(smcAnalyzerTime);
369       end
370     end
371
372     %% Reset rotation stages and change intensity and send email
373
374     % Send email update
```

```
375   emailTitle = strcat('MES Run -',32,fileName);
376   emailMessage = strcat('Intensity sweep OD',32,num2str(
          intensityNowOD),32,'has completed.');
377   try
378     mes_send_gmail_func(recipient,emailTitle,emailMessage,'');
379   catch err
380     errEmailMsg = strcat('Email for intensity sweep',32,num2str(
            intensityNowOD),32,'did not send.');
381     disp(errEmailMsg);
382   end
383   disp(emailMessage);
384
385   % Change intensity
386   intensityNowOD = intensityNowOD + intensityODdelta;
387   if intensityNowOD ~= intensityOD2
388     % Zero Analyzer and waveplate
389     smcAnalyzerCurrentPos = Vmes_Smc_func(smcAnalyzerAdd,strcat(
            num2str(smcAnalyzerAdd),'TP?'),1);
390     smcAnalyzerDiff = abs(smcAnalyzerCurrentPos - smcAnalyzerZer)
            ;
391     if smcAnalyzerDiff == 0
392       smcAnalyzerTime = Vmes_Smc_func(smcAnalyzerAdd,strcat(
              num2str(smcAnalyzerAdd),'PT',num2str(smcAnalyzerDiff),'?
              '),1);
393     else
394       smcAnalyzerTime = 0;
395     end
396
397     smcRotationCurrentPos = Vmes_Smc_func(smcRotationAdd,strcat(
            num2str(smcRotationAdd),'TP?'),1);
398     smcRotationDiff = abs(smcRotationCurrentPos - smcRotationZer)
            ;
399     if smcRotationDiff ~=0
400       smcRotationTime = Vmes_Smc_func(smcRotationAdd,strcat(
              num2str(smcRotationAdd),'PT',num2str(smcRotationDiff),'?
              '),1);
401     else
402       smcRotationTime = 0;
```

```
403       end
404
405       Vmes_Smc_func(smcAnalyzerAdd,strcat(num2str(smcAnalyzerAdd),'
              PA',num2str(smcAnalyzerZer)),0);
406       Vmes_Smc_func(smcRotationAdd,strcat(num2str(smcRotationAdd),'
              PA',num2str(smcRotationZer)),0);
407
408       pause(max(smcAnalyzerTime,smcRotationTime));
409     end
410 end %end intensity loop
411
412 % Add two empty lines to file
413 fprintf(fileID,tab0Str);
414 fprintf(fileID,tab0Str);
415
416 % Send conclusion email
417 try
418     mes_send_gmail_func(recipient,emailTitle,'The experiment has
            finished.',pathName);
419 catch err
420     disp('Final email did not send.');
421 end
422 disp('The experiment is finished.');
423
424 % Split apart file to sub files
425 Vmes_TextFileSplitter_func(pathName)
426
427 % Close files
428 fclose all;
429 toc    %Print program runtime
```

B.B Vmes_PiUsb_func(a)

```
1 function[] = Vmes_PiUsb_func(shutter_SetState)
2 %% mes_PiUsb_func
3 %% Elizabeth Dreyer
4 %% 2015-02-20
5 %% Vitara Magneto-Electric Scattering Experiment
```

```
6 %% Purpose: The purpose of this program is to open/close the USB
      shutter from Picard Industries
7 %% Input Variables : shutter_Status (1 - open, 0 - closed)
8
9 shutter_Status = shutter_SetState;
10
11 %% Load piUsb.dll ... Make sure to copy PiUsb.h and PiUsb.lib are
       in the project source code folder and piUsb.dll to executable
       folder. Build as a 32 - bit program.
12
13 % We use the dll and the header file (piUsb.dll, piSUB.h)
14 fullpathToHeader = 'C:\Users\eecs-rand-02\Documents\Lab
      Documentation\usb-shutter\Shutter DLL and Docs\PiUsb.h';
15 fullpathToDll = 'C:\Users\eecs-rand-02\Documents\Lab
      Documentation\usb-shutter\Shutter DLL and Docs\x64\PiUsb.dll';
16
17 % Use below code if you need to re-write the Header to remove
      errors
18 % See MATLAB help for "Why does MATLAB crash when I make a
      function call on a DLL
19 %[notfound, warnings] = loadlibrary(fullpathToDll,
      fullpathToHeader,'mfilename','mHeader');
20 % unloadlibrary('PiUsb');
21 try
22   %[notfound, warnings] = loadlibrary(fullpathToDll, @mHeader);
23   [notfound, warnings] = loadlibrary(fullpathToDll,
        fullpathToHeader);
24 catch err
25   disp('library not found')
26 end
27
28 % The libfunctionsview function show the MATLAB prototype of the
      Dll exported functions
29 % libfunctionsview PiUsb
30
31 libLoadedTf = libisloaded('PiUsb');
32 ptError = libpointer('int32Ptr',0);
33 pUsbl = libpointer('voidPtr');
```

```
34
35 shutterSerialNumber = int32(361);  % serial number from shutter
36
37 pUsbl = calllib('PiUsb','piConnectShutter', ptError,
       shutterSerialNumber);
38
39 if ptError.Value == 1 %'PI_DEVICE_NOT_FOUND'
40   disp('Unable to find Shutter ...')
41 else
42   %disp('Shutter Connected.')
43 end
44
45 %% Set shutterState (Commands PI_SHUTTER_OPEN and PI_SHUTTER
       _CLOSED)
46 if shutter_Status == 1
47   ptError = calllib('PiUsb','piSetShutterState',1,pUsbl);
48   if ptError == 1 %'PI_DEVICE_NOT_FOUND'
49     disp (' Shutter was disconnected.')
50     pUsbl = []; % Pointer is invalid after disconnecting
51   else
52     disp('Shutter open.')
53   end
54 elseif shutter_Status == 0
55   ptError = calllib('PiUsb','piSetShutterState',0,pUsbl);
56   if ptError == 1 %'PI_DEVICE_NOT_FOUND'
57     disp (' Shutter was disconnected.')
58     pUsbl = []; % Pointer is invalid after disconnecting
59   else
60     disp('Shutter closed.')
61   end
62 else
63   disp ('Invalid shutter open/close command.')
64 end
65
66 %% Disconnect Shutter
67 if isempty (pUsbl) == 0
68   calllib('PiUsb', 'piDisconnectShutter', pUsbl)
69   pUsbl = []; % Pointer is invlaid after disconnecting
```

```
70 end
71
72 %% Unload library
73 unloadlibrary('PiUsb')
74
75 end %end function
```

B.C Vmes_PiWheel_func(a,b)

```
1 function[posGradient] = Vmes_PiWheel_func(GWheel_Action,
    GWheel_Position)
2 %% Vmes_PiWheel_func
3 %% Elizabeth Dreyer
4 %% 2017-02-09
5 %% Magneto-Electric Scattering Experiment
6 %% Purpose: The purpose of this program is to control the filter
    wheel from Picard Industries
7 %% Input Variables : GWheel_Action (0 - Get Position, 1 - Set
    Position)
8
9 %% Load piUsb.dll ... Make sure to copy PiUsb.h and PiUsb.lib are
    in the project source code folder and piUsb.dll to executable
    folder. Build as a 32 - bit program.
10
11 % We use the dll and the header file (piUsb.dll, piSUB.h)
12 fullpathToHeader = 'C:\Users\eecs-rand-02\Documents\Lab
    Documentation\usb-gradientwheel\Gradient DLL and Docs\PiUsb2.h
    ';
13 fullpathToDll = 'C:\Users\eecs-rand-02\Documents\Lab
    Documentation\usb-gradientwheel\Gradient DLL and Docs\x64\
    PiUsb.dll';
14
15 % Use below code if you need to re-write the Header to remove
    errors
16 % See MATLAB help for "Why does MATLAB crash when I make a
    function call on a DLL
17 % [notfound, warnings] = loadlibrary(fullpathToDll,
    fullpathToHeader,'mfilename','mGWHeader2');
```

```
18 % unloadlibrary('PiUsb');
19 try
20   %[notfound, warnings] = loadlibrary(fullpathToDll, @mGWHeader);
21   [notfound, warnings] = loadlibrary(fullpathToDll,
        fullpathToHeader);
22 catch err
23   disp('library not found')
24 end
25 % The libfunctionsview function show the MATLAB prototype of the
     Dll exported functions
26 % libfunctionsview PiUsb
27
28 libLoadedTf = libisloaded('PiUsb');
29
30 %% Connect to a Gradient Wheel
31 ptError = libpointer('int32Ptr',0);
32 pUsbl = libpointer('voidPtr');
33 ptrDevice = libpointer('int32Ptr',0);
34 ptGradient = libpointer('int32Ptr',0);
35 posGradient = int32(-1);
36
37 GradientSerialNumber = int32(50);  % serial number from shutter
38
39 pUsbl = calllib('PiUsb','piConnectGWheel', ptError,
     GradientSerialNumber);
40
41 if ptError.Value == 1 %'PI_DEVICE_NOT_FOUND'
42   disp('Unable to find GWheel ...')
43 else
44   %disp('GWheel Connected.')
45 end
46
47 %% Get and Set GWheel Position
48 if GWheel_Action == 0 %Get Position Only
49   [posGradient,ptrGradient,ptError] = calllib('PiUsb','
       piGetGWheelPosition',ptGradient,pUsbl);
50   if ptError == 1 %'PI_DEVICE_NOT_FOUND'
51     disp (' Wheel was disconnected.')
```

```
52      pUsbl = []; % Pointer is invalid after disconnecting
53    else
54      sprintf('Wheel is at position %d',ptrGradient);
55      posGradient = ptrGradient;
56    end
57  elseif GWheel_Action == 1 %Set Position then Get
58    [posGradient,ptError] = calllib('PiUsb','piSetGWheelPosition',
          GWheel_Position,pUsbl);
59    if ptError == 1 %'PI_DEVICE_NOT_FOUND'
60      disp (' Wheel was disconnected.')
61      pUsbl = []; % Pointer is invalid after disconnecting
62    else
63      pause(3.5);
64      [posGradient,ptrGradient,ptError] = calllib('PiUsb','
            piGetGWheelPosition',ptGradient,pUsbl);
65      if ptError == 1 %'PI_DEVICE_NOT_FOUND'
66        disp ('Wheel was disconnected.')
67        pUsbl = [];% Pointer is invalid after disconnecting
68      else
69        sprintf('Wheel is now at position %d',ptrGradient);
70        posGradient = ptrGradient;
71      end
72    end
73  else
74    disp ('Invalid gradient wheel command.')
75  end
76
77  %% Disconnect Wheel
78  if isempty (pUsbl) == 0
79      calllib('PiUsb','piDisconnectGWheel', pUsbl)
80      pUsbl = []; % Pointer is invlaid after disconnecting
81  end
82
83  %% Unload library
84  unloadlibrary('PiUsb')
85
86  end %"end function"
```

B.D Vmes_smc_func(a,b,c)

```
1 function[smcPos] = Vmes_Smc_func(smcAxis,smcCmnd,smcQuery)
2 %% Vmes_Smc_func
3 % Elizabeth Dreyer
4 % 2015-02-20
5 % Vitara Magneto-Electric Scattering Experiment
6 % Purpose: The purpose of this program is to send the control
      command to the SMC, wait, and read back the response.
7 % Input Variables: SMC Axis (1,2,3); SMC command, Smc Query (1/0)
8 % Output Variables: smcResult (usually position)
9
10 %% Variables to use if ran as not a function
11 % smcAxis = 3;
12 % smcCmnd = '3TP'; %PA - Abs. Move; TP? - Tell postion; TS - Get
      position error and controller state
13 % smcQuery = 1; %1 = true, 0 = false %Decides query or fprintf
14
15 %% Initialize position
16 smcPos = -1;
17
18 %% Open communication via Serial
19 % Close previously open serial
20 oldSerial = instrfind('Port','COM5');
21 if ~isempty(oldSerial)
22   fclose(oldSerial);
23   delete(oldSerial);
24   clear oldSerial;
25 end
26
27 % Create serial object and configure properties to match smc
28 smc = serial('com5','BaudRate',57600,'DataBits',8,'Parity','None'
      ,'Terminator','CR/LF');
29 clear err;
30 try
31   fopen(smc); %open communication
32   pause(1e-3);
33 catch err
```

```
34    smcPos = -999;
35    fprintf('SMC controller %s communication did not open on %s
          command \r\n',smcAxis,smcCmnd)
36    return
37  end
38
39  %% Send and Read Command
40  % Verify smc is ready
41  status = smc.Status;  %Check status to see if connected
42  if strcmp(status,'open')==0
43    fopen(smc);
44    pause(1e-3);
45  end
46
47  % Check for errors -- 0000 = No errors
48  smcReady = 0;
49  smcErr = '';
50  while smcReady == 0
51    smcErrCmnd = strcat(num2str(smcAxis),'TS?');
52    smcErr = query(smc,smcErrCmnd);
53    pause(1e-3);
54    smcErrResult1 = '';
55    smcErrResult2 = '';
56    for i = (4):(7)
57      smcErrResult1 = strcat(smcErrResult1,smcErr(i));
58    end
59    for i = (8):(9)
60      smcErrResult2 = strcat(smcErrResult2,smcErr(i));
61    end
62
63    %error handling -- See page 65 of user manual
64    switch smcErrResult2
65      case {'0A','0B','0C','0D','0E','0F','10','11'}
66        smcErrCmndFix = strcat(num2str(smcAxis),'OR');
67        smcErr = fprintf(smc,smcErrCmndFix);
68      case {'14'}
69        fprintf('SMC is in configuration mode and cannot execute
              command. \r\n')
```

```
70        smcErrCmndFix = strcat(num2str(smcAxis),'PW0');
71        smcErr = fprintf(smc,smcErrCmndFix);
72        smcErrCmndFix2 = strcat(num2str(smcAxis),'OR');
73        smcErr = fprintf(smc,smcErrCmndFix2);
74      case {'1E','1F'}
75        fprintf('SMC is currently homing. \r\n');
76        pause(3);
77      case {'28'}
78        pause(3);
79        fprintf(' SMC is moving right now. \r\n ')
80      case {'32','33','34','35'}
81        smcReady = 1;
82      case {'3C','3D','3E'}
83        fprintf('smc is disabled \r\n')
84      case {'46','47'}
85        fprintf('SMC is jogging \r\n')
86      otherwise
87        disp('Unknown error \r\n');
88    end
89 end
90
91 % Use the smcQuery boolean to decide if reading needs to be done
92 if smcQuery == 1
93    smcAns = query(smc,smcCmnd);
94    pause(1e-3);
95    % fprintf(smcAns); %Display full answer for debugging purposes.
96 elseif smcQuery == 0
97    fprintf(smc,smcCmnd);
98    pause(1e-3);
99 else
100   disp('error in query')
101 end
102
103 % If reading occured, discard first part of response and return a
        number.
104 % In example, 1PA0.00 returns that axis 1 is at position zero.
105 if smcQuery == 1
106   smcResult = '';
```

```
107    for i = (4):length(smcAns)
108      smcResult = strcat(smcResult,smcAns(i));
109    end
110  else
111    smcResult = '';
112  end
113  smcPos = str2double(smcResult);
114
115  %% Close communication
116  fclose(smc); pause(1e-3);
117  delete(smc); pause(1e-3);
118  clear smc;
119
120  end %end function
```

B.E Vmes_sr830_config_func(a,b)

```
1  function Vmes_sr830_config_func(sr830timeConstantNum,
       sr830timeConstantSec)
2  % Elizabeth Dreyer
3  % 2015-03-26
4  % Vitara Magneto-Electric Scattering Experiment
5  % Purpose: To control and set-up the SR830 lock-in amplifier
6  % Input Variables: sr830timeConstantNum
7  % Output Variables: none
8
9  %% Initialize sr830
10 % Make sure it is set to REMOTE physically and is on RS232
       communication.
11
12 % Open Communication
13 % Close previously open serial
14 oldSerial = instrfind('Port','COM6');
15 if ~isempty(oldSerial)
16   fclose(oldSerial);
17   delete(oldSerial);
18   clear oldSerial;
19 end
```

```
20 sr830 = serial('com6','BaudRate',9600,'DataBits',8,'StopBits', 2,
       'Parity','None', 'Terminator', 'CR');
21
22 try
23   fopen(sr830); %open communication
24   pause(1e-3);
25 catch err
26   fprintf('Error')
27   return
28 end
29
30 %% Send and Read Command
31 % Verify sr830 is ready
32 status = sr830.Status;  %Check status to see if connected
33 if strcmp(status,'open')==0
34   fopen(sr830);
35   pause(1e-3);
36 end
37
38 % Initial commands
39 fprintf(sr830,'OUTX0'); %Set com mode to RS232
40 pause(1e-3);
41 fprintf(sr830,'LOCL1'); %Set the Local/Remote state to remote
42 pause(1e-3);
43 fprintf(sr830,'FMOD0'); %Set the SR830 to external reference
44 pause(1e-3);
45 fprintf(sr830,'RSLP0'); %Set the external reference slope to Sine
46 pause(1);
47 if sr830timeConstantSec <= 1
48   fprintf(sr830,'AGAN');  %Set gain to auto
49   pause(sr830timeConstantSec*30);
50   sr830timecmd = strcat('OFLT',sr830timeConstantNum);
51   fprintf(sr830,sr830timecmd);  %Set time constant
52   pause(1e-3);
53   sr830SENS = query(sr830,'SENS?');
54   pause(1e-3);
55   sr830SENSnew = str2num(sr830SENS)+2; %Add 2 for fluctuations
56   sr830SENScmd = strcat('SENS',num2str(sr830SENSnew));
```

```
57    fprintf(sr830,sr830SENScmd); %Set sensitivity to 2 more than
          auto
58 else %Do this when autogain won't work - ie. cases of 3s and 10s
59    sr830SENSnew = 2;
60    sr830SENScmd = strcat('SENS',num2str(sr830SENSnew));
61    fprintf(sr830,sr830SENScmd); %Set sensitivity to lowest
          possible one
62    sr830SENSovld = query(sr830,'LIAS?2');
63    sr830SENSovld = query(sr830,'LIAS?2');
64    sr830SENSovldNum = str2num(sr830SENSovld);
65    while sr830SENSovldNum == 1
66       sr830SENSnew = sr830SENSnew+2;
67       sr830SENScmd = strcat('SENS',num2str(sr830SENSnew));
68       fprintf(sr830,sr830SENScmd); %Set sensitivity to 2 more than
             auto
69       sr830SENSovld = query(sr830,'LIAS?2');
70       sr830SENSovldNum = str2num(sr830SENSovld);
71    end
72 end
73 fprintf(sr830,'DDEF110'); %Set the CH1 display to R,Theta
74
75 %Clear buffer
76 sr830Buffer = query(sr830,'SPTS?');
77 sr830BufferCellStr = cellstr(sr830Buffer);
78 sr830ClearedBuffer = cellstr('0');
79 while strcmp(sr830BufferCellStr(1),sr830ClearedBuffer(1)) == 0
80    fprintf(sr830,'REST');  %Clear buffer command
81    sr830Buffer = query(sr830,'SPTS?');
82    sr830BufferCellStr = cellstr(sr830Buffer);
83 end
84
85 %% Close communication
86 fclose(sr830); pause(1e-3);
87 delete(sr830); pause(1e-3);
88 clear sr830;
89 end %End function
```

B.F Vmes_sr830_data_func(a,b)

```
1 function[xData,yData,rData,thData,chopFreqNow]=
      Vmes_sr830_data_func(dataPts,timePause)
2 % Elizabeth Dreyer
3 % 2015-03-26
4 % Vitara Magneto-Electric Scattering Experiment
5 % Purpose: To get a certain number of data points from the SR830
      lock-in amplifier
6 % Input Variables: Number of points, time to pause
7 % Output Variables: x, y, r, theta, chopper frequency
8
9 %% Initialize sr830
10 % Make sure it is set to REMOTE physically and is on RS232
      communication.
11
12 % Open Communication
13 % Close previously open serial
14 oldSerial = instrfind('Port','COM6');
15 if ~isempty(oldSerial)
16   fclose(oldSerial);
17   delete(oldSerial);
18   clear oldSerial;
19 end
20 sr830 = serial('com6','BaudRate',9600,'DataBits',8,'StopBits', 2,
      'Parity','None', 'Terminator', 'CR');
21
22 % Initialize space for data points
23 xData = double(-1*ones(dataPts,1)); % DO NOT USE int16
24 yData = double(-1*ones(dataPts,1)); % DO NOT USE int16
25 rData = double(-1*ones(dataPts,1)); % DO NOT USE int16
26 thData = double(-1*ones(dataPts,1)); % DO NOT USE int16
27
28 try
29   fopen(sr830); %open communication
30 catch err
31   for i = 1:dataPts
32     xData(i) = -1;
```

```
33      yData(i) = -1;
34      rData(i) = -1;
35      thData(i) = -1;
36    end
37    return
38 end
39
40 %% Send and Read Command
41 % Verify sr830 is ready
42 status = sr830.Status;  %Check status to see if connected
43 if strcmp(status,'open')==0
44    fopen(sr830);
45    pause(1e-3);
46 end
47
48 % Initial commands
49 chopFreqNow = query(sr830,'FREQ?');
50 chopFreqNow = str2double(chopFreqNow);
51 chopFreqNow = num2str(chopFreqNow);
52
53 % Clear buffer
54 sr830Buffer = query(sr830,'SPTS?');
55 sr830BufferCellStr = cellstr(sr830Buffer);
56 sr830ClearedBuffer = cellstr('0');
57 while strcmp(sr830BufferCellStr(1),sr830ClearedBuffer(1)) == 0
58    fprintf(sr830,'REST');  %Clear buffer command
59    sr830Buffer = query(sr830,'SPTS?');
60    sr830BufferCellStr = cellstr(sr830Buffer);
61 end
62
63 % Select data
64 clear k
65 clear sr830output
66 clear sr830outSplit
67 for k=1:dataPts
68    pause(timePause);
69    errTemp = 0;
70    try
```

```
71      sr830output = query(sr830,'SNAP?1,2,3,4');
72    catch err
73      errTemp = 1;
74    end
75    if errTemp == 1
76      disp('error in sr830 collection')
77    else
78      sr830outSplit = strsplit(sr830output,',');
79      sr830X = char(sr830outSplit(1));
80      sr830Y = char(sr830outSplit(2));
81      sr830R = char(sr830outSplit(3));
82      sr830Th = char(sr830outSplit(4));
83
84      xData(k) = str2double(sr830X);
85      yData(k) = str2double(sr830Y);
86      rData(k) = str2double(sr830R);
87      thData(k) = str2double(sr830Th);
88    end
89 end
90
91 %% Close communication
92 fclose(sr830); pause(1e-3);
93 delete(sr830); pause(1e-3);
94 clear sr830;
95 end %end function
```

B.G Vmes_Pm100USB_func

```
1 function[pmPower] = Vmes_Pm100USB_func
2 % Vmes_Pm100USB_func
3 % Elizabeth Dreyer
4 % 2015-03-18
5 % Magneto-Electric Scattering Experiment
6 % Purpose: The purpose of this program is to read out the value
     on the ThorLabs PM100USB power meter
7 % Input Variables: none
8 % Output Variables: pmPower (W)
9
```

```
%% Open communication via USB
% Clear any old visa-usb instrument files
oldUSB = instrfind('typ','visa-usb');
if ~isempty(oldUSB)
   fclose(oldUSB);
   delete(oldUSB);
   clear oldUSB;
end

% Try connecting to it manually --> instrhwinfo('visa','ni') -->
% ObjectConstructorName
pm100USB = visa('ni','USB0::0x1313::0x8072::P2004423::INSTR');

%% Initialize PM100USB
% Open VISA
   try
      fopen(pm100USB);
   catch err
      fopen(pm100USB);
   end
pause(1e-3);

% Configure readout
fprintf(pm100USB,'CONF:POW');  %Power readout
pause(0.01);
fprintf(pm100USB,'INIT');

%% Take measurement
% MEASure[:POWer]     %Performs a power measurement
pmPower=0;
pause(0.01)
pmPower = query(pm100USB,'FETC?');
pmPower = str2double(pmPower);

%% Close communication
fclose(pm100USB);
delete(pm100USB);
clear pm100USB
```

```
48 end %end function
```

B.H mes_send_gmail_func(a,b,c,d)

```
1 function[] = mes_send_gmail_func(emailAddress,messageName,
      messageText,attachPathName)
2 %% mes_send_gmail_func
3 % Elizabeth Dreyer
4 % 2014-07-29
5 % Magneto-Electric Scattering Experiment
6 % Purpose: The purpose of this program is to send email to the
      researcher
7 % Input Variables: Email of recipient, Name of message, body of
      message
8 % Output Variables: None
9
10 % Modify these two lines to reflect your account and password.
11 % Note - You must use an insecure email address
12 myaddress = 'email@website.com';
13 mypassword = 'password';
14
15 setpref('Internet','E_mail',myaddress);
16 setpref('Internet','SMTP_Server','smtp.gmail.com');
17 setpref('Internet','SMTP_Username',myaddress);
18 setpref('Internet','SMTP_Password',mypassword);
19
20 props = java.lang.System.getProperties;
21 props.setProperty('mail.smtp.auth','true');
22 props.setProperty('mail.smtp.socketFactory.class', ...
23                   'javax.net.ssl.SSLSocketFactory');
24 props.setProperty('mail.smtp.socketFactory.port','465');
25
26 if isempty(attachPathName)
27   sendmail(emailAddress, messageName, messageText);
28 else
29   sendmail(emailAddress, messageName, messageText,attachPathName)
       ;
30 end
```

```
31 end %end function
```

B.I Vmes_TextFileSplitter_func(a)

```
1 function[]=Vmes_TextFileSplitter_func(filePath)
2 %% mes_TextFileSplitter_func
3 % Elizabeth Dreyer
4 % 2014-07-30
5 % Magneto-Electric Scattering Experiment
6 % Purpose: The purpose of this program is to split apart the text
      file
7 % generated in the MES experiment
8 % Input Variables: filepath to textfile
9 % Output Variables: text files saved
10
11 % Split file path into name and folder
12 [pathstr,name,ext] = fileparts(filePath) ;
13
14 % Create new folder but first check that it does not exist
15 folderPath = strcat(pathstr,'\',name);
16 folderExists = exist(folderPath,'dir');
17 if folderExists == 0
18   mkdir(pathstr,name)
19 end
20
21 [filesub,dateExtra] = regexp(strcat(name,ext),'_20','split');
22 fileNameNew = '';
23
24 % Load textfile data
25 try
26   textfileTable = readtable(filePath,'delimiter','\t');
27 catch err
28 end
29 [len,wid]=size(textfileTable);
30 textfileTable(:,wid)=[];
31 textfileCells = table2cell(textfileTable);
32
33 % Size of table
```

```
34 [len,wid]=size(textfileTable);
35
36 % Create header block
37 textfileTableHeader = textfileTable(1:17,:);
38
39 % Find rows with Intensity breakpoints
40 locBreak = 1;
41 for i = 18:len
42   intTF = strcmp(textfileTable{i,1},'Intensity OD');
43   if intTF == 1
44     intBreak(locBreak)=i;
45     locBreak = locBreak +1;
46   end
47 end
48
49 % Split apart each intensity block
50 [lenInt,widInt]=size(intBreak);
51
52 for j = 1:widInt
53   clear tempTable
54   %Initialize ED/MD/NA counters
55   anEDctr = 0; anMDctr = 0; anNActr = 0; anDstr = '';
56
57   if widInt>(j)    %Is this not the last intensity block
58     tempTable = cell2table(cell((intBreak(j+1)-intBreak(j)),wid))
         ;
59     tempTable = textfileTable(intBreak(j):(intBreak(j+1)-1),:);
60
61     % Grab Intensity header
62     intHeader = tempTable(1,:);
63
64     % Find Analyzer breakpoints
65     [lenTable,widTable] = size(tempTable);
66
67     locAnBreak = 1;
68     for ii = 1:lenTable
69       anTF = strcmp(tempTable{ii,1},'Analyzer');
70       if anTF == 1
```

```
71          anBreak(locAnBreak)=ii;
72          locAnBreak = locAnBreak +1;
73        end
74      end
75
76      % Split apart each analyzer block
77      [lenAn,widAn] = size(anBreak);
78
79      for jj = 1:widAn
80        if jj < widAn %Is this not the last analyzer block?
81          tempAnTable = tempTable(anBreak(jj):(anBreak(jj+1)-1),:);
82
83          % Stitch together Header, Intensity header, and Analyzer
84          tableNew = [textfileTableHeader;intHeader;tempAnTable];
85
86          % Print tableNew to a new file
87          if strcmp(tempAnTable{1,3},'ED')
88            anEDctr = anEDctr + 1;
89            anDstr = strcat('ED',num2str(anEDctr));
90          elseif strcmp(tempAnTable{1,3},'MD')
91            anMDctr = anMDctr + 1;
92            anDstr = strcat('MD',num2str(anMDctr));
93          elseif strcmp(tempAnTable{1,3},'NA')
94            anNActr = anNActr + 1;
95            anDstr = strcat('NA',num2str(anNActr));
96          end
97
98          fileNameNew = strcat(filesub{1},'_',anDstr,'_',num2str(j)
                ,ext);
99          pathNameNew = strcat(folderPath,'\',fileNameNew);
100         writetable(tableNew,pathNameNew,'delimiter','\t')
101
102       else %This is the last analyzer block
103         tempAnTable = cell2table(cell((lenTable-anBreak(jj)),wid)
              );
104         tempAnTable = tempTable(anBreak(jj):(lenTable-1),:);
105
106         % Stitch together Header, Intensity header, and Analyzer
```

```
107         tableNew = [textfileTableHeader;intHeader;tempAnTable];
108
109         % Print tableNew to a new file
110         if strcmp(tempAnTable{1,3},'ED')
111           anEDctr = anEDctr + 1;
112           anDstr = strcat('ED',num2str(anEDctr));
113         elseif strcmp(tempAnTable{1,3},'MD')
114           anMDctr = anMDctr + 1;
115           anDstr = strcat('MD',num2str(anMDctr));
116         elseif strcmp(tempAnTable{1,3},'NA')
117           anNActr = anNActr + 1;
118           anDstr = strcat('NA',num2str(anNActr));
119         end
120
121         fileNameNew = strcat(filesub{1},'_',anDstr,'_',num2str(j)
              ,ext);
122         pathNameNew = strcat(folderPath,'\',fileNameNew);
123         writetable(tableNew,pathNameNew,'delimiter','\t')
124       end
125     end
126
127   else %This is the last intensity block
128     tempTable = cell2table(cell((len-intBreak(j)),wid));
129     tempTable = textfileTable(intBreak(j):(len-1),:);
130
131     % Grab Intensity header
132     intHeader = tempTable(1,:);
133
134     % Find Analyzer breakpoints
135     [lenTable,widTable] = size(tempTable);
136     locAnBreak = 1;
137       for ii = 1:lenTable
138         anTF = strcmp(tempTable{ii,1},'Analyzer');
139         if anTF == 1
140           anBreak(locAnBreak)=ii;
141           locAnBreak = locAnBreak +1;
142         end
143       end
```

```
144
145     % Split apart each analyzer block
146     [lenAn,widAn] = size(anBreak);
147
148     for jj = 1:widAn
149       if widAn>(jj) %Is this not the last analyzer block?
150         tempAnTable = cell2table(cell((anBreak(jj+1)-anBreak(jj))
                ,wid));
151         tempAnTable = tempTable(anBreak(jj):(anBreak(jj+1)-1),:)
                ;
152
153         % Stitch together Header, Intensity header, and Analyzer
154         tableNew = [textfileTableHeader;intHeader;tempAnTable];
155
156         % Print tableNew to a new file
157         if strcmp(tempAnTable{1,3},'ED')
158           anEDctr = anEDctr + 1;
159           anDstr = strcat('ED',num2str(anEDctr));
160         elseif strcmp(tempAnTable{1,3},'MD')
161           anMDctr = anMDctr + 1;
162           anDstr = strcat('MD',num2str(anMDctr));
163         elseif strcmp(tempAnTable{1,3},'NA')
164           anNActr = anNActr + 1;
165           anDstr = strcat('NA',num2str(anNActr));
166         end
167
168         fileNameNew = strcat(filesub{1},'_',anDstr,'_',num2str(j)
                ,ext);
169         pathNameNew = strcat(folderPath,'\',fileNameNew);
170         writetable(tableNew,pathNameNew,'delimiter','\t')
171
172         else %This is the last analyzer block
173           tempAnTable = cell2table(cell((lenTable-anBreak(jj)),
                  wid));
174           tempAnTable = tempTable(anBreak(jj):(lenTable-1),:);
175
176           % Stitch together Header, Intensity header, and
                Analyzer
```

```
177             tableNew = [textfileTableHeader;intHeader;tempAnTable];
178
179             % Print tableNew to a new file
180             if strcmp(tempAnTable{1,3},'ED')
181               anEDctr = anEDctr + 1;
182               anDstr = strcat('ED',num2str(anEDctr));
183             elseif strcmp(tempAnTable{1,3},'MD')
184               anMDctr = anMDctr + 1;
185               anDstr = strcat('MD',num2str(anMDctr));
186             elseif strcmp(tempAnTable{1,3},'NA')
187               anNActr = anNActr + 1;
188               anDstr = strcat('NA',num2str(anNActr));
189             end
190
191             fileNameNew = strcat(filesub{1},'_',anDstr,'_',num2str(
                    j),ext);
192             pathNameNew = strcat(folderPath,'\',fileNameNew);
193             writetable(tableNew,pathNameNew,'delimiter','\t')
194           end
195         end
196       end
197     end
198 end %End of function
```

Appendix C

MATLAB code for Lorentz oscillator model

C.A Main program

```
% ME_ClassicalTheory_v1_RealVals_NoDim
% Elizabeth Dreyer
% 2017-07-10
% Magneto-Electric Scattering Experiment
% Purpose: Simulate the classical equations for the Magneto-
    electric
% scattering
% Needed files: mes_ODE_func.m

my_save = 0;
plots = 11;

%% Define Intitial Conditions and Parameters for System
% Raw Parameter Values
var = 1;
hbar = 1.0545718e-34;
hh = 6.6261e-34;
freq = 80.0E6;      %Laser Rep Rate
tauP = 15.0e-15;    %Pulse Duration
w0 = 2.594e15;      %Arbitrary Oscillator 1/s
w0R = 1.6299e16;    %w0 in radians per second
w = 0.9*w0;         %Wave Frequency 1/s
g = 0.1*w0;         %Gamma E of CCl4 0.0872E15 1/s
c = 299792458;      %Speed of Light in m/s
e = 1.61e-19;       %Electron charge in C
```

```
25 m = 9.11e-31;      %Electron mass in kg
26 eps0 = 8.85e-12;   %Electric permitivity in Vacuum
27 M = 1.674e-27;     %Mass of Hydrogen in Kg
28 R = 2*0.0375e-9;   %Bond length of diatomic Hydrogen
29 rb = 5.292e-11;    %Bohr Radius
30 iPar = hbar/w0R;   %Moment of inertia - Parallel
31 iPer = iPar*1e5;   %Moment of inertia - Perpendicular
32 n1 = 1;            %Refractive index of CCl4 1.45355
33 lightInt = 1.3266e9;       %Watts / cm^2
34 Ex = sqrt(2*lightInt*1e4/(c*eps0*n1)); %Electric field strength
35 kz = 1;
36
37 %Scaling factors
38 t0 = 1/w0;
39 r0 = sqrt(hbar/(w0R*m));
40 q0 = e;
41 me = m;
42 E0 = me*r0/(t0*t0*q0);
43
44 %Substitutions
45 tauPn = tauP/t0;
46 w0n = w0*t0;
47 wn = w*t0;
48 gn = g*t0;
49 cn = c*t0/r0;
50 en = e/q0;
51 mn = m/me;
52 Mn = M/me;
53 Rn = R/r0;
54 iParn = iPar/(me*r0*r0);
55 iPern = iPer/(me*r0*r0);
56 Exn = Ex/E0;
57 freqn = freq*t0;
58
59 %Unitless Initial Conditions
60 % x1, y1, z1 are the position of the electron wrt. the foot point
61 x1 = 0.0;
62 y1 = 0.0;
```

```
63 z1 = 0.0;
64 % x2, y2, z2 are the initial displacement of the footpoint wrt.
       the COM
65 x2 = 0.0;
66 y2 = 0.1*sqrt(pi);
67 z2 = 0.0;
68 % ox, oy, oz are the initial angular momentums of the electron
69 ox = 0.0;
70 oy = 0.0;
71 oz = 0.0;
72 % xd, yd, zd are the initial velocities of the electron
73 xd = 0.0;
74 yd = 0.0;
75 zd = 0.0;
76
77 %% ODE Set-up
78 % ODE solver parameters
79 abserr = 1.0e-22;
80 relerr = 1.0e-20;
81 cycles = 1297*385/500; %1297 ~ 500 fs
82 stoptime = round(cycles/w0,3, 'significant'); %Cycles
83 numpoints = cycles*50;
84
85 % Create the time samples for the output of the ODE solver.
86 t = linspace(0,stoptime*w0,numpoints);
87
88 % Pack up the parameters and initial conditions:
89 pn = [w0n, wn, gn, cn, en, mn, iParn, iPern, Exn, kz, freqn,
       tauPn, t0, q0, me, r0];
90 s0n = [x1, y1, z1, x2, y2, z2, ox, oy, oz, xd, yd, zd];
91
92 syms s
93
94 %% Run ODE 23
95 options = odeset('RelTol',relerr,'AbsTol',abserr);
96 wsol = ode23(@(t,s) mes_ODE_func(t,s,pn),t,s0n);
97
98 %% Define Solutions
```

```
 99 % Assign solution to separate arrays
100 tSoln = wsol.x;
101 x1sn = wsol.y(1,:);
102 y1sn = wsol.y(2,:);
103 z1sn = wsol.y(3,:);
104 x2sn = wsol.y(4,:);
105 y2sn = wsol.y(5,:);
106 z2sn = wsol.y(6,:);
107 oxsn = wsol.y(7,:);
108 oysn = wsol.y(8,:);
109 ozsn = wsol.y(9,:);
110 xdsn = wsol.y(10,:);
111 ydsn = wsol.y(11,:);
112 zdsn = wsol.y(12,:);
113
114 % Assign solution to separate arrays
115 tSol = tSoln*t0;
116 x1s = x1sn*r0;
117 y1s = y1sn*r0;
118 z1s = z1sn*r0;
119 x2s = x2sn*r0;
120 y2s = y2sn*r0;
121 z2s = z2sn*r0;
122 oxs = oxsn/t0;
123 oys = oysn/t0;
124 ozs = ozsn/t0;
125 xds = xdsn*r0/t0;
126 yds = ydsn*r0/t0;
127 zds = zdsn*r0/t0;
128
129 % Define Magnetization and other vectors
130 m2xn = en/2*(-z1sn.*ydsn+y1sn.*zdsn);
131 m2yn = en/2*(z1sn.*xdsn-x1sn.*zdsn); %MD
132 m2zn = en/2*(-y1sn.*xdsn+x1sn.*ydsn);
133 m2xnC = en/2*(-z1sn.*ydsn+y1sn.*zdsn)/cn;
134 m2ynC = en/2*(z1sn.*xdsn-x1sn.*zdsn)/cn; %MD/c
135 m2znC = en/2*(-y1sn.*xdsn+x1sn.*ydsn)/cn;
136 p0xn = en*x1sn; %ED
```

```
137 p0yn = en*y1sn;
138 p0zn = en*z1sn; %Charge Separation
139
140 % Dimensionalize the vectors
141 m2x = e/2*(-z1s.*yds+y1s.*zds);
142 m2y = e/2*(z1s.*xds-x1s.*zds); %MD
143 m2z = e/2*(-y1s.*xds+x1s.*yds);
144 m2xC = e/2*(-z1s.*yds+y1s.*zds)/c;
145 m2yC = e/2*(z1s.*xds-x1s.*zds)/c; %MD/c
146 m2zC = e/2*(-y1s.*xds+x1s.*yds)/c;
147 p0x = e*x1s; %ED
148 p0y = e*y1s;
149 p0z = e*z1s; %Charge Separation
150
151 %% Plot Values
152  plottime = round(stoptime*w0);
153  plt_str = strcat('_',num2str(plottime));
154  date_str = datestr(now,'yymmddHHMMSS');
155  saveloc = 'C:...';
156  plotH=500;
157  plotW=250;
158
159 ... %Plots as needed
```

C.B ODE Function

```
1 function[dy] = mes_ODE_func(t,s,p)
2 % mes_ODE_func
3 % Elizabeth Dreyer
4 % 2016-11-21
5 % Magneto-Electric Scattering Experiment
6 % Purpose: System of normalized ODEs for solving
7 % Input Parameters: t = time, s = functions, p = parameters
8
9 % Initialize dy
10 dy = zeros(12,1);
11
12 % Expand s and p in terms of other variables
```

```
13 % pn = [w0n, wn, gn, cn, en, mn, iParn, iPern, Exn, kz, freqn,
       tauPn, t0, q0, me, rb];
14 % s0n = [x1, y1, z1, x2, y2, z2, ox, oy, oz, xd, yd, zd];
15 x1n = s(1); y1n = s(2); z1n = s(3);
16 x2n = s(4); y2n = s(5); z2n = s(6);
17 oxn = s(7); oyn = s(8); ozn = s(9);
18 xdn = s(10); ydn = s(11); zdn = s(12);
19
20 w0n = p(1); wn = p(2); gn = p(3); cn = p(4);
21 en = p(5); mn = p(6); iParn = p(7); iPern = p(8);
22 Exn = p(9); kz = p(10); freqn = p(11); tauPn = p(12);
23 t0 = p(13); q0 = p(14); me = p(15); rb = p(16);
24
25 % Define pulse function
26 pulseFunc = sin(wn*t);
27
28 % Write the equations
29 dy(1,1) = xdn;
30 dy(2,1) = ydn;
31 dy(3,1) = zdn;
32 dy(4,1) = (z2n*oyn - y2n*ozn);
33 dy(5,1) = (-z2n*oxn + x2n*ozn);
34 dy(6,1) =  (y2n*oxn - x2n*oyn);
35 dy(7,1) = mn/(iParn) * w0n*w0n *(y2n*z1n-y1n*z2n);
36 dy(8,1) = mn/(iPern) * w0n*w0n *(-x2n*z1n+x1n*z2n);
37 dy(9,1) = mn/(iPern) * w0n*w0n *(x2n*y1n-x1n*y2n);
38 dy(10,1) = en/mn*Exn*pulseFunc-w0n*w0n*(x1n-x2n)-en*Exn*kz/(cn*mn
       )*pulseFunc*zdn-gn*xdn;
39 dy(11,1) = -w0n*w0n*(y1n-y2n)-gn*ydn;
40 dy(12,1) = -w0n*w0n*(z1n-z2n)+en*Exn*kz/(cn*mn)*pulseFunc*xdn-gn*
       zdn;
41
42 end %End function
```

BIBLIOGRAPHY

[1] E. Kheirandish, *The Arabic Version of Euclids Optics: Edited and Translated with Historical Introduction and Commentary*, vol. 1. Springer Science & Business Media, 2012.

[2] L. Romero, *Ibn Al-Haytham: The Man Who Discovered How We See*. National Geographic Kids: Leve, National Geographic, 2016.

[3] I. Newton, *Opticks, or a treatise of the reflections, refractions, inflections and colours of light*, vol. 678. William Innys, 1730.

[4] C. Huygens, F. Arago, A. J. Fresnel, and T. Young, *The Wave Theory of Light: Memoirs by Huygens, Young and Fresnel*, vol. 10. American Book Company, 1900.

[5] L. D. Landau, J. Bell, M. Kearsley, L. Pitaevskii, E. Lifshitz, and J. Sykes, *Electrodynamics of continuous media*, vol. 8. Pergamon Press Ltd: New York, 1984.

[6] W. M. Fisher and S. C. Rand, "Light-induced dynamics in the lorentz oscillator model with magnetic forces," *Physical Review A*, vol. 82, no. 1, p. 013802, 2010.

[7] A. A. Fisher, E. F. C. Dreyer, A. Chakrabarty, and S. C. Rand, "Optical magnetization, part ii: Theory of induced optical magnetism," *Opt. Express*, vol. 24, pp. 26064–26079, Nov 2016.

[8] D. R. Smith, J. B. Pendry, and M. C. Wiltshire, "Metamaterials and negative refractive index," *Science*, vol. 305, no. 5685, pp. 788–792, 2004.

[9] G. Singh and A. Marwaha, "A review of metamaterials and its applications," *International Journal of Engineering Trends and Technology*, vol. 19, Jan 2015.

[10] D. R. Smith, W. J. Padilla, D. Vier, S. C. Nemat-Nasser, and S. Schultz, "Composite medium with simultaneously negative permeability and permittivity," *Physical review letters*, vol. 84, no. 18, p. 4184, 2000.

[11] V. M. Shalaev, "Optical negative-index metamaterials," *Nature photonics*, vol. 1, no. 1, p. 41, 2007.

[12] B. Gralak, S. Enoch, and G. Tayeb, "Anomalous refractive properties of photonic crystals," *JOSA A*, vol. 17, no. 6, pp. 1012–1020, 2000.

[13] C. Luo, S. G. Johnson, J. Joannopoulos, and J. Pendry, "Subwavelength imaging in photonic crystals," *Physical Review B*, vol. 68, no. 4, p. 045115, 2003.

[14] N. Caselli, F. Intonti, F. La China, F. Riboli, A. Gerardino, W. Bao, A. W. Bargioni, L. Li, E. H. Linfield, F. Pagliano, *et al.*, "Ultra-subwavelength phase-sensitive fano-imaging of localized photonic modes," *Light: Science & Applications*, vol. 4, no. 9, p. e326, 2015.

[15] R. Ghosh, K. Ghosh, and R. Chakraborty, "Design of electro-optic photonic crystal structure for subdiffraction imaging over the entire visible wavelength range," *Optical Engineering*, vol. 55, no. 12, p. 127101, 2016.

[16] A. Alù and N. Engheta, "Optical nanotransmission lines: synthesis of planar left-handed metamaterials in the infrared and visible regimes," *JOSA B*, vol. 23, no. 3, pp. 571–583, 2006.

[17] S. Zhang, W. Fan, B. Minhas, A. Frauenglass, K. Malloy, and S. Brueck, "Midinfrared resonant magnetic nanostructures exhibiting a negative permeability," *Physical review letters*, vol. 94, no. 3, p. 037402, 2005.

[18] G. Dolling, M. Wegener, C. M. Soukoulis, and S. Linden, "Negative-index metamaterial at 780 nm wavelength," *Optics letters*, vol. 32, no. 1, pp. 53–55, 2007.

[19] U. K. Chettiar, A. V. Kildishev, T. A. Klar, and V. M. Shalaev, "Negative index metamaterial combining magnetic resonators with metal films," *Optics Express*, vol. 14, no. 17, pp. 7872–7877, 2006.

[20] J. Zhou, L. Zhang, G. Tuttle, T. Koschny, and C. M. Soukoulis, "Negative index materials using simple short wire pairs," *Physical Review B*, vol. 73, no. 4, p. 041101, 2006.

[21] R. A. Shelby, D. R. Smith, and S. Schultz, "Experimental verification of a negative index of refraction," *science*, vol. 292, no. 5514, pp. 77–79, 2001.

[22] T.-J. Yen, W. Padilla, N. Fang, D. Vier, D. Smith, J. Pendry, D. Basov, and X. Zhang, "Terahertz magnetic response from artificial materials," *Science*, vol. 303, no. 5663, pp. 1494–1496, 2004.

[23] C. Enkrich, M. Wegener, S. Linden, S. Burger, L. Zschiedrich, F. Schmidt, J. Zhou, T. Koschny, and C. Soukoulis, "Magnetic metamaterials at telecommunication and visible frequencies," *Physical review letters*, vol. 95, no. 20, p. 203901, 2005.

[24] M. W. Klein, C. Enkrich, M. Wegener, and S. Linden, "Second-harmonic generation from magnetic metamaterials," *Science*, vol. 313, no. 5786, pp. 502–504, 2006.

[25] K. Busch, G. Von Freymann, S. Linden, S. Mingaleev, L. Tkeshelashvili, and M. Wegener, "Periodic nanostructures for photonics," *Physics reports*, vol. 444, no. 3-6, pp. 101–202, 2007.

[26] A. V. Kildishev, W. Cai, U. K. Chettiar, H.-K. Yuan, A. K. Sarychev, V. P. Drachev, and V. M. Shalaev, "Negative refractive index in optics of metal-dielectric composites," *JOSA B*, vol. 23, no. 3, pp. 423–433, 2006.

[27] S. Linden, C. Enkrich, M. Wegener, J. Zhou, T. Koschny, and C. M. Soukoulis, "Magnetic response of metamaterials at 100 terahertz," *Science*, vol. 306, no. 5700, pp. 1351–1353, 2004.

[28] R. W. Boyd, *Nonlinear optics*. Academic Press, 2003.

[29] B. E. A. Saleh and M. C. Teich, *Fundamentals of photonics*. Canada, Wiley Interscience, 2nd ed., 2008.

[30] P. A. Franken, A. E. Hill, C. W. Peters, and G. Weinreich, "Generation of optical harmonics," *Physical Review Letters*, vol. 7, no. 4, p. 118, 1961.

[31] T. H. Maiman, "Stimulated optical radiation in ruby," *nature*, vol. 187, no. 4736, pp. 493–494, 1960.

[32] G. S. He, "Stimulated scattering effects of intense coherent light," *Progress in Optics*, vol. 53, pp. 201–292, 2009.

[33] Y.-R. Shen, *The principles of nonlinear optics*. Wiley-Interscience: New York, 1984.

[34] E. Hecht, *Optics*. Addison-Wesley world student series, Addison-Wesley, 1998. See p. 69 for example.

[35] M. D. Williams, J. S. Ford, and D. L. Andrews, "Hyper-rayleigh scattering in centrosymmetric systems," *The Journal of Chemical Physics*, vol. 143, no. 12, p. 124301, 2015.

[36] R. Terhune, P. Maker, and C. Savage, "Measurements of nonlinear light scattering," *Physical Review Letters*, vol. 14, no. 17, p. 681, 1965.

[37] R. Bersohn, Y.-H. Pao, and H. L. Frisch, "Double-quantum light scattering by molecules," *The Journal of Chemical Physics*, vol. 45, no. 9, pp. 3184–3198, 1966.

[38] D. A. Long, "The raman effect: a unified treatment of the theory of raman scattering by molecules," *West Sussex*, 2002.

[39] C. Cho, N. Foltz, D. Rank, and T. Wiggins, "Stimulated rayleigh scattering," *Physical Review Letters*, vol. 18, no. 4, p. 107, 1967.

[40] D. Mash, V. Morozov, V. Starunov, and I. Fabelinskii, "Stimulated scattering of light of the rayleigh-line wing," *ZhETF Pisma Redaktsiiu*, vol. 2, p. 41, 1965.

[41] D. Rank, C. Cho, N. Foltz, and T. Wiggins, "Stimulated thermal rayleigh scattering," *Physical Review Letters*, vol. 19, no. 15, p. 828, 1967.

[42] C. V. Raman and K. S. Krishnan, "A new type of secondary radiation," *Nature*, vol. 121, no. 3048, pp. 501–502, 1928.

[43] L. Brillouin, "Diffusion de la lumière et des rayons x par un corps transparent homogène-influence de l'agitation thermique," *Annales de physique*, vol. 9, no. 17, pp. 88–122, 1922.

[44] W. Struve, *Fundamentals of Molecular Spectroscopy*. Wiley, 1989.

[45] G. Herzberg, "Molecular spectra and molecular structure. vol. 1: Spectra of diatomic molecules," *New York: Van Nostrand Reinhold, 1950, 2nd ed.*, 1950. p. 129.

[46] T. Shimanouchi, *Tables of Molecular Vibrational Frequencies*. No. v. 1 in NSRDS-NBS, National Bureau of Standards, 1972.

[47] D. Cotter, D. Hanna, W. Tuttlebee, and M. Yuratich, "Stimulated hyper-raman emission from sodium vapour," *Optics Communications*, vol. 22, no. 2, pp. 190–194, 1977.

[48] W. P. Acker, D. H. Leach, and R. K. Chang, "Stokes and anti-stokes hyper-raman scattering from benzene, deuterated benzene, and carbon tetrachloride," *Chemical physics letters*, vol. 155, no. 4-5, pp. 491–495, 1989.

[49] A. Mooradian, S. Brueck, and F. Blum, "Continuous stimulated spin-flip raman scattering in insb," *Applied Physics Letters*, vol. 17, no. 11, pp. 481–483, 1970.

[50] M. Born and E. Wolf, *Principles of optics: electromagnetic theory of propagation, interference and diffraction of light*. Cambridge university press, 1999.

[51] H. A. Bethe and E. E. Salpeter, *Quantum mechanics of one-and two-electron atoms*. Springer Science & Business Media, 2012.

[52] N. H. List, J. Kauczor, T. Saue, H. J. A. Jensen, and P. Norman, "Beyond the electric-dipole approximation: A formulation and implementation of molecular response theory for the description of absorption of electromagnetic field radiation," *The Journal of chemical physics*, vol. 142, no. 24, p. 244111, 2015.

[53] N. L. Sharma, "Nondipole optical scattering from liquids and nanoparticles," *Physical review letters*, vol. 98, no. 21, p. 217402, 2007.

[54] G. W. Mulholland, C. F. Bohren, and K. A. Fuller, "Light scattering by agglomerates: coupled electric and magnetic dipole method," *Langmuir*, vol. 10, no. 8, pp. 2533–2546, 1994.

[55] J. Bucaro and T. Litovitz, "Rayleigh scattering: collisional motions in liquids," *The Journal of Chemical Physics*, vol. 54, no. 9, pp. 3846–3853, 1971.

[56] J. Van Vleck, "On the role of dipole-dipole coupling in dielectric media," *The Journal of Chemical Physics*, vol. 5, no. 7, pp. 556–568, 1937.

[57] H. H. Uhlig and F. Keyes, "The dependence of the dielectric constants of gases on temperature and density," *The Journal of Chemical Physics*, vol. 1, no. 2, pp. 155–159, 1933.

[58] A. Buckingham and J. Pople, "The dielectric constant of an imperfect non-polar gas," *Transactions of the Faraday Society*, vol. 51, pp. 1029–1035, 1955.

[59] W. Baylis, "Collisional depolarization in the excited state," in *Progress in Atomic Spectroscopy*, pp. 1227–1297, Springer, 1979.

[60] J. McTague and G. Birnbaum, "Collision-induced light scattering in gaseous ar and kr," *Physical Review Letters*, vol. 21, no. 10, p. 661, 1968.

[61] L. Frommhold, "Collision-induced scattering of light and the diatom polarizabilities," *Adv Chem Phys*, vol. 46, pp. 1–72, 1981.

[62] D. Shelton and G. Tabisz, "Molecular frame distortion and molecular pair polarizability," *Chemical Physics Letters*, vol. 69, no. 1, pp. 125–127, 1980.

[63] J. Stevens, G. Patterson, P. Carroll, and G. Alms, "The central lorentzian in the depolarized rayleigh spectra of liquid ccl4 and gecl4," *The Journal of Chemical Physics*, vol. 76, no. 11, pp. 5203–5207, 1982.

[64] M. Neumann and H. Posch, "Interaction induced light scattering from tetrahedral molecules," in *Phenomena Induced by Intermolecular Interactions*, pp. 475–496, Springer, 1985.

[65] S. Shapiro and H. Broida, "Light scattering from fluctuations in orientations of CS2 in liquids," *Physical Review*, vol. 154, no. 1, p. 129, 1967.

[66] P. Madden, "The depolarized rayleigh scattering from fluids of spherical molecules," *Molecular Physics*, vol. 36, no. 2, pp. 365–388, 1978.

[67] P. J. Chappell, M. P. Allen, R. I. Hallem, and D. Kivelson, "Theory of depolarized light scattering," *The Journal of Chemical Physics*, vol. 74, no. 11, pp. 5929–5941, 1981.

[68] D. Bauer, J. Brauman, and R. Pecora, "Depolarized light scattering from liquids," *Annual Review of Physical Chemistry*, vol. 27, no. 1, pp. 443–463, 1976.

[69] T. Keyes, B. M. Ladanyi, and P. A. Madden, "Is depolarized light scattered from simple liquids mainly double-scattered?," *Chemical Physics Letters*, vol. 64, no. 3, pp. 479–484, 1979.

[70] J. Weis and B. Alder, "Effect of multiple scattering on the intensity of depolarized light," *Chemical Physics Letters*, vol. 81, no. 1, pp. 113–114, 1981.

[71] W. Gelbart, "Collision-induced and multiple light scattering by simple fluids," *Phil. Trans. R. Soc. Lond. A*, vol. 293, no. 1402, pp. 359–375, 1979.

[72] O. Deutschbein, "Experimentelle untersuchungen über die vorgänge bei der lichtemission," *Annalen der Physik*, vol. 428, no. 2, pp. 183–188, 1939. Translation available via Google Translate's picture to translation feature.

[73] J. Kratohvil, M. Kerker, and L. Oppenheimer, "Light scattering by pure water," *The Journal of Chemical Physics*, vol. 43, no. 3, pp. 914–921, 1965.

[74] H. S. Gabelnick and H. L. Strauss, "Low-frequency motions in liquid carbon tetrachloride. ii. the raman spectrum," *The Journal of Chemical Physics*, vol. 49, no. 5, pp. 2334–2338, 1968.

[75] E. Moreels, W. De Ceuninck, and R. Finsy, "Measurements of the rayleigh ratio of some pure liquids at several laser light wavelengths," *The Journal of chemical physics*, vol. 86, no. 2, pp. 618–623, 1987.

[76] K. Saito, H. Kakiuchida, and A. Ikushima, "Investigation of the origin of the rayleigh scattering in SiO2 glass," *Journal of non-crystalline solids*, vol. 222, pp. 329–334, 1997.

[77] H. Wang, X. Zheng, W. Mao, Z. Yu, and Z. Gao, "Stimulated dynamic light scattering," *Physical Review A*, vol. 52, no. 2, p. 1740, 1995.

[78] R. Xu, "Light scattering: a review of particle characterization applications," *Particuology*, vol. 18, pp. 11–21, 2015.

[79] R. B. Miles, W. R. Lempert, and J. N. Forkey, "Laser rayleigh scattering," *Measurement Science and Technology*, vol. 12, no. 5, p. R33, 2001.

[80] H. Wahid, "Molecular scattering of light in pure liquids," *Journal of optics*, vol. 26, no. 3, p. 109, 1995.

[81] X. Chen, L. Ju, R. Flaminio, H. Lück, C. Zhao, and D. G. Blair, "Rayleigh scattering in fused silica samples for gravitational wave detectors," *Optics Communications*, vol. 284, no. 19, pp. 4732–4737, 2011.

[82] S. L. Oliveira and S. C. Rand, "Intense nonlinear magnetic dipole radiation at optical frequencies: Molecular scattering in a dielectric liquid," *Phys. Rev. Lett.*, vol. 98, p. 093901, Feb 2007.

[83] W.-K. Tung, *Group theory in physics: an introduction to symmetry principles, group representations, and special functions in classical and quantum physics*. World Scientific Publishing Company, 1985.

[84] A. Tureanu, "Cpt and lorentz invariance: Their relation and violation," in *Journal of Physics: Conference Series*, vol. 474, p. 012031, IOP Publishing, 2013.

[85] C. Malgrange, C. Ricolleau, and M. Schlenker, *Symmetry and Physical Properties of Crystals*. Springer, 2014. See Appendex 18A for discussion of axial tensors.

[86] G. New, *Introduction to nonlinear optics*. Cambridge University Press, 2011.

[87] O. Stenzel, "Some basic effects of nonlinear optics nonlinear optics," in *The Physics of Thin Film Optical Spectra*, pp. 303–327, Springer, 2016.

[88] R. Zawodny, "Nonlinear magneto-optics of magnetically ordered crystals," *Modern Nonlinear Optics*, vol. 180, p. 307, 2009.

[89] C. M. Bender and S. Boettcher, "Real spectra in non-hermitian hamiltonians having PT symmetry," *Physical Review Letters*, vol. 80, no. 24, p. 5243, 1998.

[90] C. E. Rüter, K. G. Makris, R. El-Ganainy, D. N. Christodoulides, M. Segev, and D. Kip, "Observation of parity–time symmetry in optics," *Nature physics*, vol. 6, no. 3, p. 192, 2010.

[91] S. Longhi, "Bloch oscillations in complex crystals with PT symmetry," *Physical review letters*, vol. 103, no. 12, p. 123601, 2009.

[92] A. Guo, G. Salamo, D. Duchesne, R. Morandotti, M. Volatier-Ravat, V. Aimez, G. Siviloglou, and D. Christodoulides, "Observation of p t-symmetry breaking in complex optical potentials," *Physical Review Letters*, vol. 103, no. 9, p. 093902, 2009.

[93] R. El-Ganainy, K. G. Makris, M. Khajavikhan, Z. H. Musslimani, S. Rotter, and D. N. Christodoulides, "Non-hermitian physics and pt symmetry," *Nature Physics*, vol. 14, no. 1, p. 11, 2018.

[94] C. Zheng, L. Hao, and G. L. Long, "Observation of a fast evolution in a parity-time-symmetric system," *Phil. Trans. R. Soc. A*, vol. 371, no. 1989, p. 20120053, 2013.

[95] S. Bittner, B. Dietz, U. Günther, H. Harney, M. Miski-Oglu, A. Richter, and F. Schäfer, "P t symmetry and spontaneous symmetry breaking in a microwave billiard," *Physical review letters*, vol. 108, no. 2, p. 024101, 2012.

[96] L. Feng, Z. J. Wong, R.-M. Ma, Y. Wang, and X. Zhang, "Single-mode laser by parity-time symmetry breaking," *Science*, vol. 346, no. 6212, pp. 972–975, 2014.

[97] H. Hodaei, M.-A. Miri, M. Heinrich, D. N. Christodoulides, and M. Khajavikhan, "Parity-time–symmetric microring lasers," *Science*, vol. 346, no. 6212, pp. 975–978, 2014.

[98] M. Liertzer, L. Ge, A. Cerjan, A. Stone, H. Türeci, and S. Rotter, "Pump-induced exceptional points in lasers," *Physical Review Letters*, vol. 108, no. 17, p. 173901, 2012.

[99] R. Fleury, D. Sounas, and A. Alù, "An invisible acoustic sensor based on parity-time symmetry," *Nature communications*, vol. 6, p. 5905, 2015.

[100] X. Zhu, H. Ramezani, C. Shi, J. Zhu, and X. Zhang, "PT-symmetric acoustics," *Physical Review X*, vol. 4, no. 3, p. 031042, 2014.

[101] L. Schwarz, H. Cartarius, Z. H. Musslimani, J. Main, and G. Wunner, "Vortices in bose-einstein condensates with pt-symmetric gain and loss," *Physical Review A*, vol. 95, no. 5, p. 053613, 2017.

[102] J. Wang, Y. Dong, and X.-T. Xie, "symmetry phase transition of the trimer lattices with balanced gain and loss," *EPL (Europhysics Letters)*, vol. 120, no. 2, p. 21002, 2018.

[103] X. Yin and X. Zhang, "Unidirectional light propagation at exceptional points," *Nature materials*, vol. 12, no. 3, p. 175, 2013.

[104] R. Fleury, D. L. Sounas, and A. Alù, "Negative refraction and planar focusing based on parity-time symmetric metasurfaces," *Physical review letters*, vol. 113, no. 2, p. 023903, 2014.

[105] B. Peng, Ş. K. Özdemir, F. Lei, F. Monifi, M. Gianfreda, G. L. Long, S. Fan, F. Nori, C. M. Bender, and L. Yang, "Parity–time-symmetric whispering-gallery microcavities," *Nature Physics*, vol. 10, no. 5, p. 394, 2014.

[106] A. Regensburger, C. Bersch, M.-A. Miri, G. Onishchukov, D. N. Christodoulides, and U. Peschel, "Parity–time synthetic photonic lattices," *Nature*, vol. 488, no. 7410, p. 167, 2012.

[107] H. Ramezani, T. Kottos, R. El-Ganainy, and D. N. Christodoulides, "Unidirectional nonlinear pt-symmetric optical structures," *Physical Review A*, vol. 82, no. 4, p. 043803, 2010.

[108] L. Feng, M. Ayache, J. Huang, Y.-L. Xu, M.-H. Lu, Y.-F. Chen, Y. Fainman, and A. Scherer, "Nonreciprocal light propagation in a silicon photonic circuit," *Science*, vol. 333, no. 6043, pp. 729–733, 2011.

[109] K. Konishi and G. Paffuti, *Quantum mechanics: a new introduction*. OUP Oxford: New York, 2009.

[110] A. Zyablovsky, A. P. Vinogradov, A. A. Pukhov, A. V. Dorofeenko, and A. A. Lisyansky, "PT-symmetry in optics," *Physics-Uspekhi*, vol. 57, no. 11, p. 1063, 2014.

[111] C. M. Bender, "PT-symmetric quantum theory," in *Journal of Physics: Conference Series*, vol. 631, p. 012002, IOP Publishing, 2015.

[112] C. M. Bender, "PT symmetry in quantum physics: From a mathematical curiosity to optical experiments," *Europhysics News*, vol. 47.2, pp. 17–20, 2016.

[113] M. Fiebig, D. Fröhlich, T. Lottermoser, V. Pavlov, R. Pisarev, and H.-J. Weber, "Second harmonic generation in the centrosymmetric antiferromagnet nio," *Physical review letters*, vol. 87, no. 13, p. 137202, 2001.

[114] C. Stanciu, F. Hansteen, A. Kimel, A. Kirilyuk, A. Tsukamoto, A. Itoh, and T. Rasing, "All-optical magnetic recording with circularly polarized light," *Physical review letters*, vol. 99, no. 4, p. 047601, 2007.

[115] J. C. Ginn, I. Brener, D. W. Peters, J. R. Wendt, J. O. Stevens, P. F. Hines, L. I. Basilio, L. K. Warne, J. F. Ihlefeld, P. G. Clem, *et al.*, "Realizing optical magnetism from dielectric metamaterials," *Physical review letters*, vol. 108, no. 9, p. 097402, 2012.

[116] R. Hertel, "Microscopic theory of the inverse faraday effect," *arXiv preprint cond-mat/0509060*, 2005.

[117] P. Pershan, J. Van der Ziel, and L. Malmstrom, "Theoretical discussion of the inverse faraday effect, raman scattering, and related phenomena," *Physical Review*, vol. 143, no. 2, p. 574, 1966.

[118] J. Van der Ziel, P. Pershan, and L. Malmstrom, "Optically-induced magnetization resulting from the inverse faraday effect," *Physical Review Letters*, vol. 15, no. 5, p. 190, 1965.

[119] D. Popova, A. Bringer, and S. Blügel, "Theory of the inverse faraday effect in view of ultrafast magnetization experiments," *Physical Review B*, vol. 84, no. 21, p. 214421, 2011.

[120] L. Le Guyader, M. Savoini, S. El Moussaoui, M. Buzzi, A. Tsukamoto, A. Itoh, A. Kirilyuk, T. Rasing, A. Kimel, and F. Nolting, "Nanoscale sub-100 picosecond all-optical magnetization switching in gdfeco microstructures," *Nature communications*, vol. 6, p. 5839, 2015.

[121] K. Vahaplar, A. Kalashnikova, A. Kimel, D. Hinzke, U. Nowak, R. Chantrell, A. Tsukamoto, A. Itoh, A. Kirilyuk, and T. Rasing, "Ultrafast path for optical magnetization reversal via a strongly nonequilibrium state," *Physical review letters*, vol. 103, no. 11, p. 117201, 2009.

[122] A. Arora, M.-A. Mawass, O. Sandig, C. Luo, A. A. Ünal, F. Radu, S. Valencia, and F. Kronast, "Spatially resolved investigation of all optical magnetization switching in tbfe alloys," *Scientific reports*, vol. 7, no. 1, p. 9456, 2017.

[123] M. S. El Hadri, P. Pirro, C.-H. Lambert, S. Petit-Watelot, Y. Quessab, M. Hehn, F. Montaigne, G. Malinowski, and S. Mangin, "Two types of all-optical magnetization switching mechanisms using femtosecond laser pulses," *Physical Review B*, vol. 94, no. 6, p. 064412, 2016.

[124] G. Glushkov, A. Tuchin, S. Popov, and L. Bityutskaya, "On the size-dependent magnetism and all-optical magnetization switching of transition-metal silicide nanostructures," *Semiconductors*, vol. 49, no. 13, pp. 1695–1697, 2015.

[125] M. Kasperczyk, S. Person, D. Ananias, L. D. Carlos, and L. Novotny, "Excitation of magnetic dipole transitions at optical frequencies," *Physical review letters*, vol. 114, no. 16, p. 163903, 2015.

[126] N. R. Brewer, Z. N. Buckholtz, Z. J. Simmons, E. A. Mueller, and D. D. Yavuz, "Coherent magnetic response at optical frequencies using atomic transitions," *Physical Review X*, vol. 7, no. 1, p. 011005, 2017.

[127] A. B. Evlyukhin, S. M. Novikov, U. Zywietz, R. L. Eriksen, C. Reinhardt, S. I. Bozhevolnyi, and B. N. Chichkov, "Demonstration of magnetic dipole resonances of dielectric nanospheres in the visible region," *Nano letters*, vol. 12, no. 7, pp. 3749–3755, 2012.

[128] Z. Wang, T. Senden, and A. Meijerink, "Photonic effects for magnetic dipole transitions," *The journal of physical chemistry letters*, vol. 8, no. 23, pp. 5689–5694, 2017.

[129] S. L. Oliveira and S. C. Rand, "Optical magnetism," in *Quantum Electronics and Laser Science Conference*, p. QMJ3, Optical Society of America, 2007.

[130] A. A. Fisher, E. F. Dreyer, A. Chakrabarty, and S. C. Rand, "Optical magnetization, part i: Experiments on radiant optical magnetization in solids," *Optics Express*, vol. 24, no. 23, pp. 26055–26063, 2016.

[131] S. C. Rand, W. Fisher, and S. L. Oliveira, "Optically induced magnetization in homogeneous, undoped dielectric media," *JOSA B*, vol. 25, no. 7, pp. 1106–1117, 2008.

[132] W. Fisher and S. Rand, "Dependence of optically induced magnetism on molecular electronic structure," *Journal of Luminescence*, vol. 129, no. 12, pp. 1407–1409, 2009.

[133] W. Fisher and S. Rand, "Optically-induced charge separation and terahertz emission in unbiased dielectrics," *Journal of applied physics*, vol. 109, no. 6, p. 064903, 2011.

[134] A. A. Fisher, E. F. Cloos, W. M. Fisher, and S. C. Rand, "Dynamic symmetry-breaking in a simple quantum model of magneto-electric rectification, optical magnetization, and harmonic generation," *Optics express*, vol. 22, no. 3, pp. 2910–2924, 2014.

[135] E. F. Cloos, A. A. Fisher, W. M. Fisher, and S. C. Rand, "Experiments & analysis of second-order magnetization in centrosymmetric ggg crystals," in *Laser Science*, pp. LTu1H–1, Optical Society of America, 2013.

[136] A. A. Fisher, *Experiments and Theory of Induced Optical Magnetization*. PhD thesis, The University of Michigan, 450 Church St., 1425 Randall Laboratory, Ann Arbor, MI 48109, 1 2016.

[137] S. C. Rand, *Lectures on light: nonlinear and quantum optics using the density matrix*. Oxford University Press, 2016.

[138] A. J.-T. Lou, E. F. C. Dreyer, S. C. Rand, and T. J. Marks, "Molecular design principles for magneto-electric materials: All-electric susceptibilities relevant to optimal molecular chromophores," *The Journal of Physical Chemistry C*, vol. 121, no. 30, pp. 16491–16500, 2017.

[139] E. F. Dreyer, A. A. Fisher, P. Anisimov, and S. C. Rand, "Optical magnetization, part iii: Theory of molecular magneto-electric rectification," *Optics Express*, in draft.

[140] M. Schubert, P. Kühne, V. Darakchieva, and T. Hofmann, "Optical hall effect—model description: tutorial," *J. Opt. Soc. Am. A*, vol. 33, pp. 1553–1568, Aug 2016.

[141] Y. Qin, Y. Li, H. He, and Q. Gong, "Measurement of spin hall effect of reflected light," *Opt. Lett.*, vol. 34, pp. 2551–2553, Sep 2009.

[142] G. R. Fowles and R. C. Whitten, "Analytical mechanics," *American Journal of Physics*, vol. 30, no. 12, pp. 938–938, 1962. See for example p. 206.

[143] P. Bruskiewich, "The time reversal operator and the quantum harmonic oscillator," *Canadian Undergraduate Physics Journal*, vol. VI, pp. 24–25, 2008.

[144] V. Y. Frenkel', "On the history of the einstein–de haas effect," *Physics-Uspekhi*, vol. 22, no. 7, pp. 580–587, 1979.

[145] F. Pedrotti, L. Pedrotti, and L. Pedrotti, *Introduction to Optics*. Cambridge University Press, 2017. See p. 124 for example.

[146] P. E. Powers and J. W. Haus, *Fundamentals of nonlinear optics*. CRC Press, 2017. For example, see pages 25-26.

[147] K. Gottfried and T.-M. Yan, *Quantum mechanics: fundamentals*. Springer Science & Business Media, 2013. For example of commutation rules, see page 450.

[148] K. F. Riley, M. P. Hobson, and S. J. Bence, *Mathematical methods for physics and engineering: a comprehensive guide*. Cambridge university press, 2006.

[149] C. Bosshard, R. Spreiter, M. Zgonik, and P. Günter, "Kerr nonlinearity via cascaded optical rectification and the linear electro-optic effect," *Physical review letters*, vol. 74, no. 14, p. 2816, 1995.

[150] R. DeSalvo, H. Vanherzeele, D. Hagan, M. Sheik-Bahae, G. Stegeman, and E. Van Stryland, "Self-focusing and self-defocusing by cascaded second-order effects in ktp," *Optics letters*, vol. 17, no. 1, pp. 28–30, 1992.

[151] W. K. Panofsky and M. Phillips, *Classical electricity and magnetism*. Courier Corporation, 2005.

[152] P. E. Powers, *Field Guide to Nonlinear Optics*. SPIE Press, 2013.

[153] W. Fisher, *Transvere Optical Magnetization*. PhD thesis, The University of Michigan, 450 Church St., Randall Laboratory, Ann Arbor, MI 48109, 9 2012.

[154] C. M. Penney, "Light scattering in terms of oscillator strengths and refractive indices," *JOSA*, vol. 59, no. 1, pp. 34–40, 1969.

[155] E. Collett, *Field guide to polarization*, vol. 15. SPIE, 2005.

[156] BURLE Electron Tubes, *C31034 Series Photomultipliers Datasheet*.

[157] Stanford Research Systems, 1290-D Reamwood Avenue Sunnyvale, CA 94089, *MODEL SR400 Gated Photon Counter Manual*.

[158] D. R. W. Emerson, *Photomultiplier Handbook*. PMT-62, Lancaster, PA: RCA, Solid State Division, Electro Optics and Devices, 1980.

[159] Y. Coello, V. V. Lozovoy, T. C. Gunaratne, B. Xu, I. Borukhovich, C.-h. Tseng, T. Weinacht, and M. Dantus, "Interference without an interferometer: a different approach to measuring, compressing, and shaping ultrashort laser pulses," *JOSA B*, vol. 25, no. 6, pp. A140–A150, 2008.

[160] V. V. Lozovoy, I. Pastirk, and M. Dantus, "Multiphoton intrapulse interference. iv. ultrashort laser pulse spectral phase characterization and compensation," *Optics letters*, vol. 29, no. 7, pp. 775–777, 2004.

[161] M. Cardamone, J. Hunt, and J. Stevens, "Depolarization ratios of rayleigh scattering for several organic liquids," *Chemical Physics Letters*, vol. 12, no. 4, pp. 628–630, 1972.

[162] A. Chakrabarty, A. Fisher, E. F. Dreyer, and S. C. Rand, "Four-fold enhancement of transverse optical magnetism in unstructured solids," in *CLEO: QELS_Fundamental Science*, pp. FW3D–4, Optical Society of America, 2015.

[163] G. GIBBS, "The crystal chemistry of the silicate garnets," *The American Mineralogist*, vol. 56, 1971.

[164] The MathWorks, Inc., *Choose an ODE Solver - MATLAB & Simulink*. Available at https://www.mathworks.com/help/matlab/math/choose-an-ode-solver.html (10/12/2017).

[165] E. A. Johnson, "Nondimensionalization of plasma equations," February 2011. Available at http://www.danlj.org/eaj/math/summaries/units/nondimensionalization.pdf (10/13/2017).

[166] I. Ignatyev, A. Lazarev, T. Tenisheva, and B. Shchegolev, "Molecular structure, force field and vibrational spectra of tetramethoxysilane," *Journal of molecular structure*, vol. 244, pp. 193–202, 1991.

[167] M. Van der Vis, R. Konings, A. Oskam, and T. Snoeck, "The vibrational spectra of gaseous and liquid tetraethoxysilane," *Journal of molecular structure*, vol. 274, pp. 47–57, 1992.

[168] D. Pavia, G. Lampman, G. Kriz, and J. Vyvyan, *Introduction to Spectroscopy*. Cengage Learning, 2014.

[169] R. R. Sharp, "Field dependence of nuclear magnetic relaxation of 119sn in sncl4, snbr4, and sni4," *The Journal of Chemical Physics*, vol. 60, no. 3, pp. 1149–1157, 1974.

[170] H. A. Ahmed and G. Thyagarajan, "Rotational relaxation studies in benzene derivatives from rayleigh scattering," *Proc Natl Acad Sci India Sect A*, vol. 55, pp. 661–669, Jan 1989.

[171] P. Zhao, M. Reichert, T. R. Ensley, W. M. Shensky, A. G. Mott, D. J. Hagan, and E. W. V. Stryland, "Nonlinear refraction dynamics of solvents and gases," *Proc.SPIE*, vol. 9731, pp. 9731 – 9731 – 8, 2016.

[172] T. Shinoda, "Qualitative classification of tetrahedral molecular crystals," *Molecular Crystals and Liquid Crystals*, vol. 76, no. 3-4, pp. 191–197, 1981.

[173] G. Causley and B. Russell, "The vacuum ultraviolet absorption spectra of the group iva tetrachlorides," *Journal of Electron Spectroscopy and Related Phenomena*, vol. 11, no. 4, pp. 383–397, 1977.

[174] T. Harazono, K. Tanaka, Y. Takeuchi, and H. Fukutomi, "Relaxation mechanism of germanium-73 nuclei in tetrahalogermanes," *Inorganic Chemistry*, vol. 26, no. 23, pp. 3851–3854, 1987.

[175] F. Bartoli and T. Litovitz, "Raman scattering: Orientational motions in liquids," *The Journal of Chemical Physics*, vol. 56, no. 1, pp. 413–425, 1972.

[176] A. Briguet, J. Duplan, and J. Delmau, "Molecular reorientation of liquid silicon tetrachloride," *Molecular Physics*, vol. 39, no. 6, pp. 1541–1546, 1980.

[177] M. B. Robin, "{CHAPTER} i - a catalog of orbitals and excitations in polyatomic molecules," in *Higher Excited States of Polyatomic Molecules* (M. B. Robin, ed.), pp. 1 – 47, Academic Press, 1985.

[178] J. Clark and B. Russell, "Vacuum ultraviolet absorption spectra of several group iva tetrabromides," *Journal of Electron Spectroscopy and Related Phenomena*, vol. 11, no. 4, pp. 371–382, 1977.

[179] T. L. James, "Fundamentals of nmr," 1998. Available at http://www.biophysics.org/portals/1/PDFs/Education/james.pdf (2/10/18).

[180] C. R. Lassigne and E. Wells, "Nuclear magnetic resonance relaxation and anisotropic reorientation in liquid dimethylmercury," *Canadian Journal of Chemistry*, vol. 55, no. 8, pp. 1303–1313, 1977.

[181] W. Phadungsukanan, S. Shekar, R. Shirley, M. Sander, R. H. West, and M. Kraft, "First-principles thermochemistry for silicon species in the decomposition of tetraethoxysilane," *The Journal of Physical Chemistry A*, vol. 113, no. 31, pp. 9041–9049, 2009.

[182] J. Nagy, F. S, R. Farkas, I. Barta, and B. A, "Study of molecular structure of alkyl-alkoxysilanes and aryl-alkoxysilanes. 2. dielectric study of monoalkoxysilanes dialkoxysilanes andtrialkoxysilanes," *ACTA CHIMICA ACADEMIAE SCIENTARIUM HUNGARICAE*, vol. 69, no. 4, p. 397, 1971.

[183] É. Kirichenko, A. Ermakov, N. Pimkin, and V. Kopylov, "Ultraviolet-radiation absorption by siloxane bond in region of 186-220 nm," *Russian Journal of Organic Chemistry*, vol. 50, no. 7, pp. 1576–1580, 1980.

[184] J. A. Bucaro and T. A. Litovitz, "Molecular motions in ccl4: Light scattering and infrared absorption," *The Journal of Chemical Physics*, vol. 55, no. 7, pp. 3585–3588, 1971.

[185] S. R. Vigil and M. G. Kuzyk, "Absolute molecular optical kerr effect spectroscopy of dilute organic solutions and neat organic liquids," *JOSA B*, vol. 18, no. 5, pp. 679–691, 2001.

[186] Z. Yu, L. Gundlach, and P. Piotrowiak, "Efficiency and temporal response of crystalline kerr media in collinear optical kerr gating," *Optics letters*, vol. 36, no. 15, pp. 2904–2906, 2011.

[187] S. Benis, D. J. Hagan, and E. W. Van Stryland, "Cross-propagating beam-deflection measurements of third-order nonlinear optical susceptibility," in *Nonlinear Frequency Generation and Conversion: Materials and Devices XVI*, vol. 10088, p. 100880N, International Society for Optics and Photonics, 2017.

[188] D. R. Kanis, M. A. Ratner, and T. J. Marks, "Design and construction of molecular assemblies with large second-order optical nonlinearities. quantum chemical aspects," *Chemical Reviews*, vol. 94, no. 1, pp. 195–242, 1994.